Development of a Gamma-Ray Detector for Z-Selective Radiographic Imaging

Thesis submitted for the degree of

"Doctor of Philosophy"

By **Michal Brandis**

Submitted to the Senate of the Hebrew University of Jerusalem

November 2013

This work was carried out under the supervision of:

Dr. David Vartsky – Soreq NRC

Prof. Eliahu Friedman – The Hebrew University of Jerusalem

Dr. Israel Mardor – Soreq NRC

Acknowledgements

I would like to express my sincere gratitude to Dr. David Vartsky who worked very closely with me throughout my time as his student and contributed more than anyone else to the success of this work. His continuous support, patience, motivation, enthusiasm and immense knowledge helped me in every step. I could not have imagined having a better supervisor and mentor for my Ph.D. study.

The contribution of my supervisors, Prof. Eliahu Friedman of the Hebrew University of Jerusalem and Dr. Israel Mardor of Soreq NRC, was invaluable. I thank them for their guidance and remarkable patience throughout all stages of the work.

Very special thanks are due to Dr. Mark B. Goldberg, who invented the patent that was the base for this work and accompanied me in the experiments, giving excellent advice.

The thesis work has been carried out in close collaboration with Dr. Volker Dangendorf from Physikalisch-Technische Bundesanstalt (PTB), whose scientific knowledge and technical understanding were irreplaceable.

I would like to thank all members of the Soreq and PTB groups: Doron Bar, Benjamin Bromberger, Kai Tittelmeier, Ilan Mor and Mathias Weierganz. I thank the people of RoentDek for their cooperation and response to the requirements of this research, especially Achim Czasch, Sven Schossler and Ottmar Jagutzki.

I would like to thank the members of the thesis committee, Prof. Amos Breskin and Prof. Michael Paul, for their encouragement and insightful comments.

This research would not have been possible without the financial assistance of the Israeli Ministry of Science and Technology (MOST) and the German Ministry of Education and Research (BMBF) within the joint program "Research for Civil Security".

Finally, I thank my husband and my parents for supporting and even pushing me to pursue my Ph.D.

ABSTRACT

Dual-Discrete Energy Gamma-Radiography (DDEGR) is a method for Special Nuclear Materials (SNM) detection. DDEGR utilizes 15.11 and 4.43 MeV gamma-rays produced in the ^{11}B(d,n)^{12}C reaction, in contrast to the conventional use of continuous Bremsstrahlung radiation.

The clean and well separated gamma-rays result in high contrast sensitivity, enabling detection of small quantities of SNM. The most important aspects of a DDEGR system were discussed, simulated, measured and demonstrated.

An experimental measurement of gamma-ray yields from the ^{11}B(d,n)^{12}C reaction showed that the yields from deuterons with 3–12 MeV energy are 2–20$\times10^{10}$ N_γ/sr/mC 4.4 MeV gamma-rays and 2–5$\times10^{9}$ N_γ/sr/mC 15.1 MeV gamma-rays. The measured neutron yields show that the neutron energies extend to 15-23 MeV for the same deuteron energy range.

A simplified inspection system was simulated with GEANT4, showing that the effect of scattering on the signal measured in the detector is acceptable. Considering the reaction gamma yields, 1.8 mA deuteron current is required for separation of high-Z materials from medium- and low-Z materials and a 4.5 mA current is required for the additional capability of separating benign high-Z materials from SNM.

The main part of the work was development of a detector suitable for a DDEGR system — Time Resolved Event Counting Optical Radiation (TRECOR) detector. TRECOR detector is a novel spectroscopic imaging detector for gamma-rays within the MeV energy range that uses an event counting image intensifier with gamma-rays for the first time.

Neutrons that accompany the gamma radiation enable to implement, in parallel, Fast Neutron Resonance Radiography (FNRR), a method for explosives detection. A second generation detector, TRECOR-II, is capable of detecting gamma-rays and neutrons in parallel, separating them to create particle-specific images and energy-specific images for each particle, thus enabling simultaneous implementation of the two detection methods.

A full DDEGR laboratory prototype was constructed using the specially-developed TRECOR-II detector and the ^{11}B(d,n)^{12}C nuclear reaction as a source. The separation of SNM from other materials including benign high-Z materials was demonstrated.

The results of the simulations, calculations and experimental studies support the viability of the proposed DDEGR inspection method and constitute a proof-of-principle.

CONTENTS

List of Abbreviations

COG	Centre Of Gravity
CSDA	Continuous Slowing Down Approximation
CT	Computed Tomography
CTF	Contrast-Transfer-Function
DDEGR	Dual Discrete Gamma Energy Radiography
DER	Dual Energy Radiography
DR	Digital Radiography
DOI	Depth Of Interaction
DU	Depleted Uranium
ECII	Event-Counting Image-Intensifier
FWHM	Full Width at Half Maximum
HCNO	Hydrogen, Carbon, Nitrogen, Oxygen
HEU	Highly Enriched Uranium
II	Image Intensifiers
LINAC	Linear Accelerator
MCP	Micro Channel Plate
NRF	Nuclear Resonance Florescence
PFNTS	Pulsed Fast Neutron Transmission Spectroscopy
PMT	Photo Multiplier Tube
PSD	Pulse Shape Discrimination
PSF	Point Spread Function
PSPMT	Position Sensitive Photomultiplier Tube
PTB	Physikalisch Technische Bundesanstalt
SD	Standard Deviation
SNM	Special Nuclear Material
TDC	Time to Digital Converter
TOF	Time Of Flight
TRECOR	Time Resolved Event Counting Optical Radiation (detector)
TRION	Time-Resolved Integrative Optical Neutrons (detector)
ULD	Unit Load Device
WGPu	Weapon Grade Plutonium
XRD	X-Ray Diffraction

Part I

Introduction

CHAPTER

1

MOTIVATION

1.1 The Challenge

1.1.1 Preamble

If you asked a government or a shipping company what the ideal aviation cargo mass-screening system should do, the answer would be simple: it should detect everything and cost nothing.

In detail, an ideal air cargo mass-screening system should be able to detect automatically any threat, including Special Nuclear Materials (SNM, defined in detail in Section 1.1.2) and explosives, in any quantity and at any geometry. It should be able to detect other types of contraband being smuggled into a country such as narcotics. This ideal inspection system should be able to do all of the above fast (less than 5 minutes per container) and without unpacking the containers, while maintaining the safety of passengers and operators. It should be stable and have rare or no false alarms. Finally, this ideal system should do all of the above at a minuscule cost [1–3].

Even the most optimistic do not expect that all of the above requirements will be fulfilled. A more reasonable list of requirements includes:

1. Produce high quality, medium-resolution (5-10 mm or better) images that can be readily interpreted by operators;

2. Distinguish ordinary metals such as aluminium, iron, steel and copper from heavy metals such as lead, tungsten, uranium and plutonium that may be associated with SNM;

3. Differentiate between organic and inorganic materials and ideally discriminate between different classes of organic materials such as explosives, narcotics and benign substances;

4. Screen cargo containers in 1-2 minutes, without unpacking most of them;

5. Safe to use;

6. Reasonable cost;

In this work, a method for SNM detection named Dual-Discrete Energy Gamma Radiography (DDEGR) is proposed and discussed. The work focuses on the development of a suitable detector and its use in a DDEGR laboratory prototype.

Combining DDEGR with Fast Neutron Resonance Radiography (FNRR), a method for explosives detection, enables responding to both main civil security threats. Some fundamental aspects of combining both methods will be discussed here, but not the details of explosives detection with FNRR, which have been thoroughly discussed in previous publications [4–15].

The detector developed for DDEGR has been modified to fit the combined DDEGR/FNRR system and this aspect is within the scope of this work.

1.1.2 SNM Definitions

Nuclear weapons require fissile material, such as uranium, ^{235}U isotope and plutonium, ^{239}Pu isotope. The Atomic Energy Act of 1954 designates them as Special Nuclear Material (SNM) [16]. Uranium in nature is 99.3% ^{238}U and 0.7% ^{235}U. ^{235}U must be enriched to produce a bomb. Uranium enriched to 20% ^{235}U is termed Highly Enriched Uranium, or HEU, but nuclear weapons typically use uranium enriched to 90% or so. Weapons-Grade Plutonium, or WGPu, is also a mix of isotopes, at least 93% ^{239}Pu.

According to a report from Los Alamos National Laboratory [17], it would take 26 kg of HEU or 5 kg of WGPu to fuel a bomb, amounts that would fit into 11 or 6 cm cubes, respectively.

Between January 1993 and December 2003, the International Atomic Energy Agency (IAEA) reported 182 confirmed incidents of nuclear material smuggling, with 18 incidents involving HEU or WGPu [18]. The publicly reported ones are listed in Table 1.1.

Date	**Location**	**Quantity**	**Material**
July 2003	Sadkhlo, Armenia	0.173 kg	HEU
July 2001	Paris, France	0.005 kg	HEU
April 2000	Batumi, Georgia	0.7 kg	HEU
December 1994	Prauge, Czech Republic	2.7 kg	HEU
March 1994	St. Petersburg, Russia	3 kg	HEU
August 1994	Munich airport, Germany	0.36 kg	Pu

Table 1.1: Confirmed incidents involving SNM snuggling through borders [19]

These attempts have raised public concern [20, 21] and in response, the U.S. government passed a bill named "Implementing Recommendations of the 9/11 Commission Act" (Public Law 110-53, Aug. 3, 2007). This bill mandates that within five years, 100% of all maritime cargo and aviation cargo loaded onto passenger aircraft bound for the U.S. will be screened for the above threat materials in foreign ports prior to loading.

To counter the threat of improvised nuclear devices being assembled from small quantities of SNM that were smuggled in piecemeal, a minimal quantity of 500 g SNM is generally accepted as a goal for detection systems [22]. For, uranium, this quantity fits into a 3 cm cube.

In the CAARS project [1,23,24], the U.S. Domestic Nuclear Detection Office (DNDO) defined a minimal detection capability of a 100 cm^3 cube of SNM behind a 25.4 cm steel wall.

1.1.3 Detection Scenario

Air cargo is usually packaged into Unit Load Devices (ULDs), the most common of which are lightweight aluminium containers named LD3 containers [2]. The size of an LD3 container is typically 155×160×210 cm^3, with small variations between manufacturing companies [25, 26]. The LD3 container's content is commonly limited to a weight of 1600 kg, which often does not fill its volume.

Another common ULD is the palletized cargo, which is significantly larger, with widths up to 240 cm and maximum gross weights of up to 6800 kg [2]. The commonest pallets have dimensions of about 240×320×163 cm^3. Examples of both ULD types are shown in Fig. 1.1.

Based on a survey of over three weeks in Brisbane International Airport [2, 27], about 50% of cargo was loaded into LD3 containers and 50% on pallets.

Figure 1.1: Main types of aviation transported cargo. On the left: an LD3 container. On the right: an example of palletized cargo.

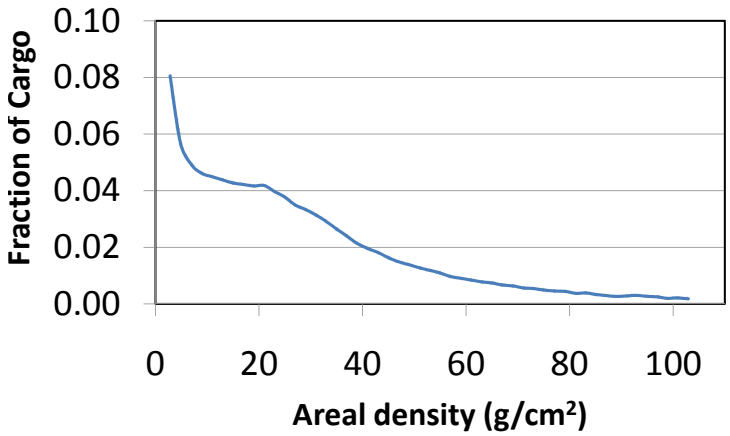

Figure 1.2: Areal density distribution in Brisbane International Airport [2, 27]. The graph excludes areal densities of less than 2 g/cm^2

The Brisbane survey included information about the content of the transported cargo. The distribution of the measured cargo areal density is presented in Fig. 1.2. The areal densities reach as high as 106 g/cm^2 and the average cargo areal density is 28 g/cm^2, calculated from this graph [2].

According to [28], air transported goods commonly include clothing, magazines, electronics, fresh fish, flowers, machine parts, etc. These goods can be divided into two groups, based on their material: the group of light (low-Z) elements, mainly hydrogen, carbon, nitrogen and oxygen. Materials from this group are commonly referred to as HCNO materials [28, 29]. The second group is the medium-Z materials, mainly iron. It is important to note that standard air cargo does not include significant amounts of high-Z materials.

1.2 Dual Discrete-Energy γ-Radiography (DDEGR)

In single energy radiography systems, a beam of gamma-rays/X-rays traverses the investigated object and impinges on the detector beyond it. Comparison of the attenuated and unattenuated signal intensities yields the areal density distribution of the investigated object. The goal in single energy radiography is to calculate the attenuation coefficients.

In dual energy photon radiography, the attenuation ratio of low- to high energy photons is imaged. Its main advantage over single energy radiography is that it enables differentiation of materials according to their atomic number. Discrimination is possible because different materials have different degrees of attenuation for high- and low-energy photons that enable identification of "organic" materials (low-Z) and "inorganic" (high-Z) materials in the controlled object.

The mass attenuation coefficient Z-dependence is different for each electromagnetic processes. The photoelectric effect dependence is the strongest, Z^4-Z^5. The Compton effect has a weak Z/A dependence and the pair-production dependence is $Z^2/A \sim Z$.

Therefore, the dominating process at each energy determines how the attenuation changes with Z. The energy range in which each process prevails is shown in Fig 1.3, as a function of atomic number Z.

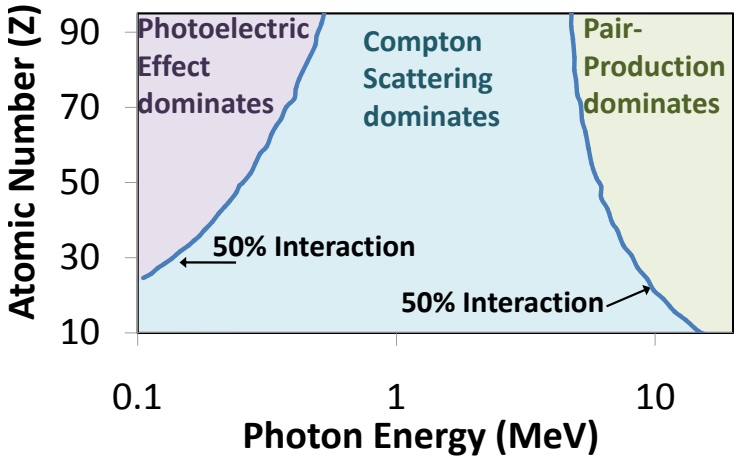

Figure 1.3: Dominance regions of photon attenuation processes, per atomic number and photon energy.

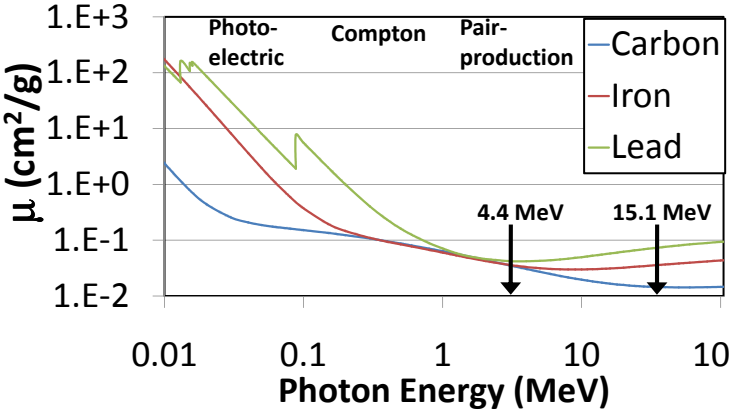

Figure 1.4: Mass attenuation coefficients as a function of energy for Pb, Fe and C [30]. The arrows mark the energies used in DDEGR with ^{11}B(d,n) reaction.

The dependence of the total mass attenuation coefficient (μ) on photon energy is shown in

Fig. 1.4 for an element from each material group: lead represents the high-Z materials, iron represents the medium-Z and carbon represents the low-Z – the last two consisting the absolute majority of transported cargo.

Today, dual energy radiography is widely used in X-ray inspection systems of hand luggage for customs and security purposes [31–36]. Typical X-ray energies of baggage inspection systems are usually up to 300 keV, where the prevailing photoelectric interaction has a strong Z dependence. However, the low penetrability of these low-energy photons makes them useless for inspection of aviation containers.

By choosing the two dual energy radiography energies judiciously, the Z-dependence of pair production can be utilized for efficient material discrimination. In Dual-Discrete Energy Gamma Radiography (DDEGR), the two photon energies are 4.43 and 15.1 MeV – gamma-rays from the ^{11}B(d,n+γ)^{12}C nuclear reaction [37].

The systems developed under the CAARS framework by SAIC (VACIS-Z) [32, 38] and the L-3 system (nameless at this point) [33] are the state of the art in dual energy radiography [1,23]. However, the Nuctech AC6015XN air cargo scanner is the only commercial dual energy system for aviation containers [35], but no units were sold thus far.

1.2.1 DDEGR Advantages

As of today, all systems intended for inspection of aviation containers are based on high-energy X-rays, where the lower energy is in the 3-6 MeV range and the higher energy is in the 6-10 MeV range [35, 39–41].

X-ray sources cause significant difficulties in implementation of dual energy radiography. Typical energy spectra of such sources are illustrated in Fig. 1.5b, showing that most of the X-ray photons are at energies lower than the end-point energy – for example, a 10 MV X-ray source generates photons with an average energy of only 3 MeV [42].

These spectra cause degradation of the measurement statistics because the penetration of most X-rays is not sufficient. Additionally, the attenuation difference between the two energies is masked by parts of the spectra that have identical energy. Using only the end-point energies (by filtering the lower energies) can improve on that at the cost of a very significant reduction of the measurement statistics.

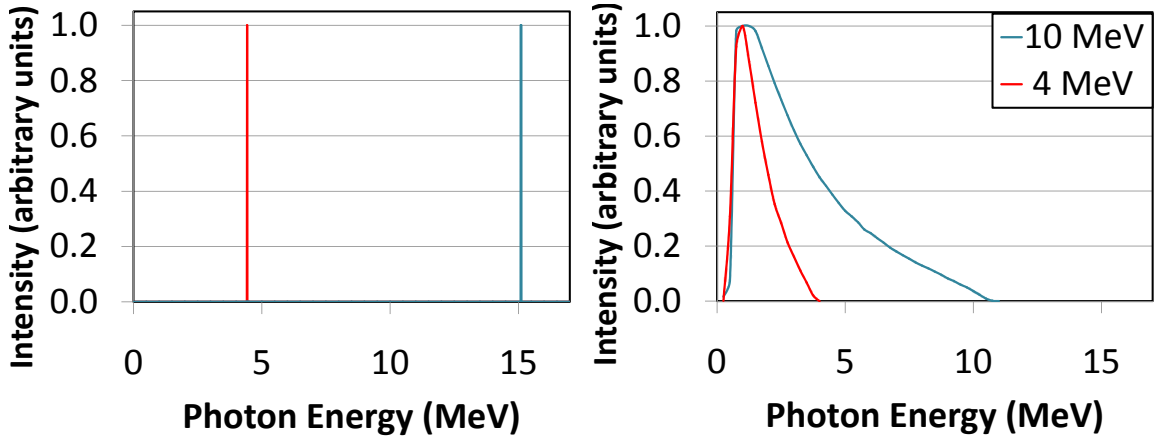

(a) Energy spectra of photons used in DDEGR - discrete energies of 4.4 and 15.1 MeV

(b) Typical Bremsstrahlung energy spectra for photons genrated in electron LINACS (X-ray sources). The legend shows the electron beam energies [42].

Figure 1.5: Typical energy spectra of photon sources for (a) DDEGR and (b) X-ray based dual-energy systems. The spectra are normalized such that the integral under each graph equals one.

The gamma-rays DDEGR relies on have higher, discrete energies, in contrast to the other realizations of dual energy radiography. The discrete nature of gamma-rays, compared with standard X-rays, provides a substantial advantage that simplifies detection and improves Z-differentiation.

The 4.4 MeV gamma-ray photons are on the threshold of the pair production energy regime, whereas the 15.1 MeV ones are well within it, thus taking advantage of its mass attenuation coefficient dependence on atomic number (Z^2/A). On the other hand, typical X-ray sources have average energies up to 3 MeV, leaving them in the energy regime where Compton scattering prevails, with its Z/A dependence that is almost constant.

Therefore, with DDEGR, high-Z materials can be efficiently distinguished, as a category, from low- and medium-Z materials. Details of material separation will be discussed in later chapters.

Moreover, SNM can be distinguished from benign high-Z materials (e.g., Hg, Tl, Pb, Bi) if several DDEGR projections are taken at different angles, enabling a 3D density reconstruction. Such reconstruction is under advanced stages of development [43, 44]. All the advantages of using discrete energy gamma-rays apply in the 3D density reconstruction as well.

1.2.2 Combined System for SNM & Explosives Detection

The operational requirements call for a system that will combine detection of high-Z materials with explosives detection. The explosives detection method of choice in this case is Fast-Neutron Resonance Radiography (FNRR).

FNRR is based on measurement of neutron transmission through an inspected object as a function of neutron energy. The inspected object is irradiated with neutrons having a wide energy spectrum extending up to 12 MeV. If the inspected object contains elements that exhibit sharp cross-section resonances, the transmission neutron spectrum will be modified such that it will exhibit dips and peaks at specific energies corresponding to these resonances.

FNRR offers determination of the elemental density distribution of C,N,O and possibly H within closed shipping containers or boxes of medium size, e.g. air-cargo or light trucks. Thus, FNRR is one of the most promising methods for fully automatic detection and identification of explosives concealed in passenger luggage and air-cargo [4, 6–8, 13].

The FNRR method that utilizes neutron Time-Of-Flight (TOF) techniques for determining the transmitted neutron spectrum is called Pulsed Fast Neutron Transmission Spectroscopy (PFNTS).

Since 2004 PTB and Soreq NRC have been developing a high spatial resolution (sub-mm) FNRR system based on a Time-Resolved Integrative Optical Neutrons (TRION) detector [9–15].

A pre-requisite for FNRR is the precise knowledge of the neutron energy, which is accomplished by Time-Of-Flight (TOF) spectroscopy. Thus, in order to implement FNRR, pulsed neutron beams and imaging systems with capability for TOF measurements are required.

DDEGR utilizes the 15.11 and 4.43 MeV gamma-rays produced in the $^{11}B(d,\gamma+n)^{12}C$ nuclear reaction with 3-8 MeV deuterons. The same reaction produces a continuous neutron spectrum of up to approximately 17 MeV that can be used for FNRR. The gamma-rays can be differentiated from the neutrons by TOF, enabling simultaneous DDEGR and FNRR [45–47]. The combined FNRR/DDER detection system is denoted FNDDER.

The combined nuclear-reaction-based system has the advantage of high sensitivity and specificity to the full range of threat materials in the contemporary arena. It permits employing the same accelerator, target and detectors for wide range of threat materials, reducing cost and

footprint.

The inspection system, illustrated in Fig. 1.6, is configured around a compact ns-pulsed deuteron accelerator. Fast neutrons and gamma-rays produced in the $^{11}B(d,\gamma+n)^{12}C$ reaction are collimated into fan-beams and detected by corresponding detector arrays. To generate multi-view data in a single pass and to shorten screening times of an object, several columnar detector arrays will be employed.

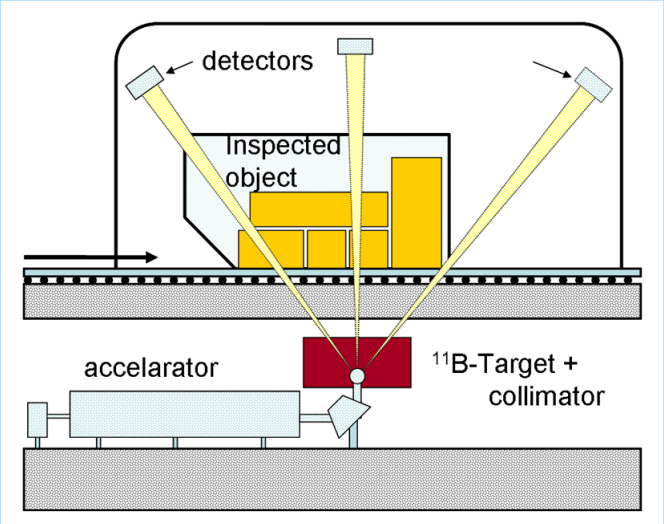

Figure 1.6: Illustration of operational FNDDER system

1.3 Objectives of This Research

- Proof-of-principle of the DDEGR method for SNM detection.
- Development of a gamma-ray detector suitable for a DDEGR system.
- Development of a gamma-ray/neutron detector suitable for a combined DDEGR/FNRR system.

1.4 Methodology

- Simulations of a DDEGR system.
- Experimental investigation of the radiation source (the nuclear reaction) properties.
- Design of a detector suitable for a DDEGR system.
- Investigation of detector properties by simulations.
- Experimental verification of detector properties.
- Experimental verification of material separation using a laboratory DDEGR prototype.

CHAPTER

2

DETECTION OF SNM – REVIEW

2.1 Preamble

This survey of detection methods is based on their interrogation principles, its structure illustrated in Fig. 2.1. First, radiographic interrogation methods are discussed. These are defined as the methods in which the detected ionizing radiation is the same radiation impinging on the inspected object, transmitted or scattered.

This definition excludes active interrogation methods in which ionizing radiation is sent unto the inspected object as well, but the detected radiation is the result fragments or secondary radiation created by interaction of the incident radiation in the inspected object.

The non-radiographic interrogation section discusses active and passive interrogation. The last does not include investigating radiation and relies on detecting the radiation emanating naturally from SNM.

2.2 Radiographic Interrogation Methods

Radiography, also known as transmission imaging, is a method in which an image is produced by penetrating radiation (other than visible light), especially by X-rays or γ-rays. Comparison of the attenuated and unattenuated signal intensities yields the areal density distribution of the inspected object.

Three types of radiation have been proposed for SNM detection in radiographic methods - gamma-rays, X-rays and cosmic muons. Gamma-ray radiation sources are radioactive isotopes such as ^{137}Cs and ^{60}Co. X-ray sources are usually Linear Accelerators (LINACs) with targets made of heavy materials, emitting Bremsstrahlung radiation.

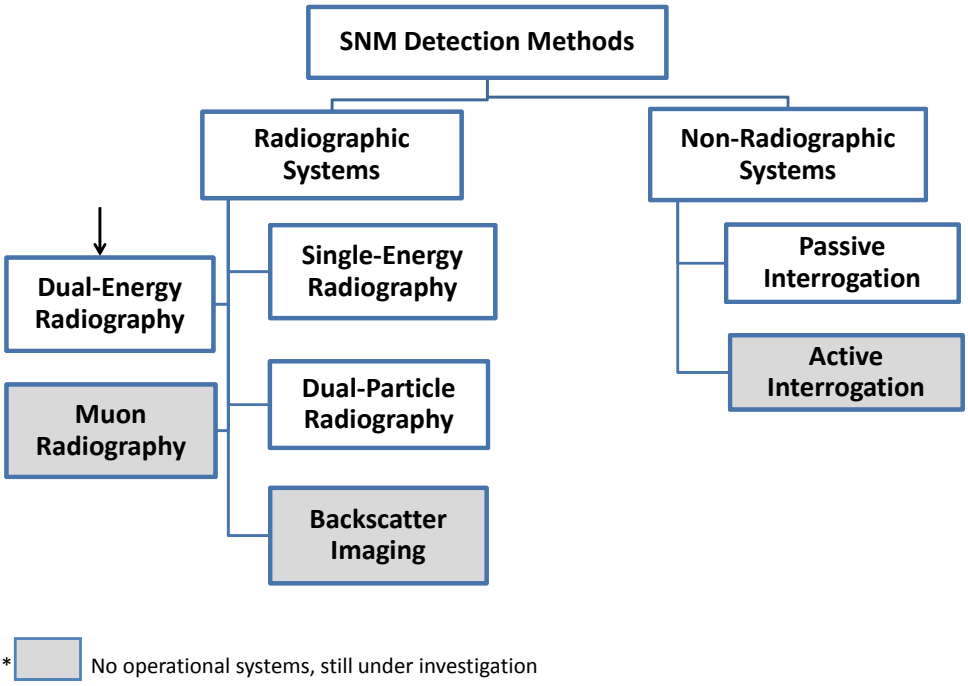

Figure 2.1: Illustration of the SNM detection survey logic, the group that DDEGR belongs to is marked by an arrow.

2.2.1 Single Energy Photon Radiography

A radiographic measurement integrates over the thickness of the inspected object [28, 48]. The simplest approach to transmission imaging is the single-energy photon radiography, which is based on attenuation in material, described by

$$I = I_0 \, e^{-\int \mu(x)\rho(x)dx} \tag{2.1}$$

where I is the intensity of the signal attenuated by the object (in our case, a cargo container), I_0 is the intensity of the unattenuated signal, μ is the object mass attenuation coefficient, ρ the object density and x the object thickness [49]. The goal here is to measure the macroscopic attenuation coefficient $\mu\rho$. Large differences between the macroscopic attenuation coefficients of benign materials and SNM will result in better system contrast. The mass attenuation coefficient depends on the atomic number Z of the medium that the photon transverses and on the incoming photon energy.

Since single energy radiography is a simple method and already often used for explosives detection, the first SNM detection systems were based on it [24, 50]. Quiter et al. [24] proposed that using only the part of the X-ray spectrum (reaching the detector) that is above 3 MeV will enable a reliable calculation of the mass attenuation coefficient and therefore the atomic number.

The Rapiscan Eagle P6000 is a cargo inspection system based on single energy X-ray radiography, the energy being 1,6 or 9 MeV, depending on the exact model. It uses an algorithm, "Auto-Z", that is designed to detect high-Z materials in cargo and indicate automatically the location of such material on a radiograph [36].

A more promising approach to single energy radiography for SNM detection is Z-Statistical Count-rate ANalysis (Z-SCAN), which is an X-ray inspection system under development at

Rapiscan. Z-SCAN offers an enhancement of the classic X-ray single-energy imaging radiography by using noise analysis rather than relying only on transmission calculations [51].
The principle of Z-SCAN is that the average energy of a Bremsstrahlung X-ray spectrum transmitted through an inspected object depends on the Z of that object. To put it simply, when traversing equivalent amounts of different materials the spectrum that traversed high-Z material will have a lower average energy. Z-SCAN determines the Z of the material from a combination of moments of the transmitted X-ray spectrum. It does so statistically, meaning that repeated measurements enable calculation of the variance of the average energy, $\mathrm{var}(\overline{\mathrm{E}}) =< \overline{\mathrm{E}}^2 >$.
The noise figure Y is defined by dividing the variance and the average energy. Lower average energy will have less fluctuations and a smaller noise figure because the Bremsstrahlung spectra have a larger number of low energy photons. This approach is denominated "noise spectroscopy". Langeveld et al. [51] demonstrated separation of 10" (25.4 cm) of steel from 3" (7.62 cm) of tungsten and 2" (5.08 cm) of depleted uranium.

2.2.2 Dual Energy Photon Radiography

The well-known dual energy method of material discrimination is widely used in X-ray inspection systems for scanning hand luggage for customs and other security purposes [31–34, 36].

In 1975, Alvarez and Maovski advanced the idea of using two X-ray spectra to separate the effects of photoelectric interaction and Compton scattering in order to improve medical diagnostic information extraction from computerized tomography systems [52].

In 1992, Eilbert and Krug described a baggage inspection system based on a single view, dual energy concept. The airport security system was designed to detect explosives and contraband via separation of bag contents based on atomic number calculated by comparing the relative attenuations of the 75 kV and 150 kV beams [53].

Later, a dual energy radiography system was proposed by Neale at el. [54], trying decomposition of transmitted X-ray spectrum onto the components resulting from the Compton effect and pair production. The ratio of the two processes in a transmitted spectrum determines the Z content of an irradiated sample. The proposed system was based on two linear accelerators arranged perpendicular to each other, each with its own detector array to enable reconstruction of a 3-dimensional image. Each beam consists of X-rays with energies up to 6 MeV that are separated to their components [54, 55].
Next, Bjorkholm [56] and Perion [57] proposed separately to use a filter to accumulate two attenuation profiles corresponding to two different energies between 1 and 10 MeV in one scan. The atomic number of the material is evaluated from a special reference table, which is created by a calibration procedure.
In the above two embodiments either the electron beam is deflected into two different targets [56] or two Bremsstrahlung filters are mechanically oscillated between the pulses of the accelerator [57]. The major disadvantage of this method is its low sensitivity due to the low degree of spectrum hardening by any existing materials. It therefore suffers from a low signal-to-noise ratio and can barely be realized with satisfactory image quality.

Ogorodnikov and Petrunin extended the idea to a dual energy, 4 and 8 MeV, cargo container inspection system suitable for full-size shipping containers [58–61]. Their laboratory prototype was based on a pulsed LINAC operated in an interlaced mode and $CdWO_4$ detectors $3{\times}3{\times}20$ mm^3 coupled to photodiodes. They scanned a real container and separated its content into 4 basic material groups, namely Hydrocarbons (Organics), Aluminium (Organic-Inorganic), Iron (Inorganics) and Lead (Heavy substances).

Later, Bjorkholm et al. tried using a pulsed LINAC emitting 5 and 9 MeV X-rays and operated in an interlaced mode [62–64]. They developed a real-time algorithm for detecting high atomic number materials claiming to have true detection rate in excess of 99% and false alarms of 1% or less.
Their most advanced published experimental results include separating tungsten from iron, both about 10 cm thick. Today, Varian sells the K9 Linatron, which is an interlaced 6/9 MeV LINAC suited for cargo inspection [39].

Other groups followed with similar approaches. Chen and Wang [65–67] employed 6 and 9 MeV X-rays, using one LINAC working in an interlaced mode and $CdWO_4$ detectors 6×6 mm^2. Later, in the same group, Duan et al. [44] used 3 and 6 MeV X-rays. Their work resulted in a commercial cargo inspection system sold today by Nuctech [35].

A recent simulation work by Gil et al. [68] proposes a single energy LINAC producing 9 MeV X-rays. The separation to low- and high- energy parts of the spectrum is implemented by using a double layered detector. Lee et al. [41] reported experimental results with a similar approach. They separated aluminium, iron and lead, but the LINAC maximal energy in their experiment was 950 keV, which is too low to penetrate cargo containers.

Rapiscan announced a plan to use dual energy radiography with 4 and 6 MeV energies at the currently under development Eagle MAX. They have demonstrated separation of material groups: low-Z organic (wood, water), low-Z inorganic (aluminium, water) and High-Z (steel and up) [40].

Currently developed commercial systems under the CAARS project of the U.S. Domestic Nuclear Detection Office (DNDO) are SAIC's VACIS-Z system [32] and the L-3 [33,69,70] system, currently nameless. In the CAARS project, materials with Z larger than 72 are considered high-Z materials.

The SAIC source is an interlaced accelerator that emits X-ray pulses with peak energies alternating between 6 MeV and 9 MeV. Each pulse is 3 μs long with 2.5 ms between pulses. Photons below 1 MeV are filtered out by a copper blocker located in the beam [1, 71]. After filtering, 6 - and 9 - MeV beams generate the greatest number of photons at about 2 and 3 MeV, respectively.
The system automatically flags for further inspection areas of high-Z material and areas with material too dense for the photons to penetrate. SAIC claims that the VACIS-Z system meets DNDO requirements such as scanning at 84 cm/sec (33 inches/sec), contrast sensitivity of 1%, spatial resolution of 0.7 cm (0.28 inches), penetration of 41 cm (16 inches) of steel, and automated detection of 100 cc of high-Z material shielded by 25.4 cm (10 inches) of steel. However, there are no published experimental results [1, 72].

The L-3 prototype includes two separate accelerators, producing 6 and 9 MeV Bremsstrahlung X-rays, each with its own dedicated detector array. A container remains stationary as the beam is moved on a gantry over it [23].

The CAARS systems were developed for maritime cargo containers but are suitable for aviation containers as well, as the former are larger.
The latest trial of the CAARS systems included detection definition of a 100 cm^3 cube of high-Z material behind 25.4 cm of steel anywhere in a container volume with a false alarm rate less than 3 occurrences per 100 scans. The real objects were larger, on the order of 100-400 cm^3. Approximately 8000 trials were conducted for each system, but to date no final report of the success rate was published.
The detection scenarios were divided by density and complexity. A representative test object – a central depleted uranium sphere surrounded by a lead-lined steel box was successfully detected

in several scenarios with ascending complexity. On a background of T-shirts, just one energy radiographic image was enough to detect the object. On a background of air compressors, the two energy ratio was necessary for detection and on a background of engines it was barely discernible with the two energy ratio image [23].

Our method (DDEGR) belongs to this family of applications, but differs from it by the nature of its source. The spectral shape of the nuclear-reaction-based gamma-ray source solves many of the problems arising from X-ray use.

2.2.3 Backscatter Imaging

When an object is irradiated by X-rays, the number of X-ray photons that scatter backwards (opposite to the beam direction) is strongly dependant on the object's Z. Backscatter imaging was originally used for imaging smaller objects (passengers carry-on luggage) with a source of 0.511 MeV gamma-rays, originating from positron annihilation [73].

When X-rays with sufficiently high energy strike a high-Z material, they produce electrons via Compton scattering and electron-positron pairs via pair-production. After the Compton scattering, the primary gamma-rays that are scattered in different directions and the charged secondary particles traverse the high-Z material creating new X-ray photons via Bremsstrahlung. It is possible to detect these scattered X-rays with detectors arranged in a backward angle in relation to the beam (larger than 90°). The number of these backscattered photons and their energy distribution is an indicator of the scattering material Z.

AS&E is developing a system that would utilize this principle [1, 31]. Its core technology is similar to EZ-3D developed by Passport Systems, Inc. [74, 75].
This technology is now under the final stages of becoming commercially available. The AS&E version is called Z-Backscatter and combines backscatter imaging with dual energy transmission imaging. Although the original research promised to differentiate between different types of high-Z materials, the final application promises to differentiate only low-Z from high-Z materials.

The Passport Systems version is based on a combination of backscatter imaging with transmission Nuclear Resonance Fluorescence (NRF, explained in the following section), back-angle NRF and transmission radiography. The combination of these methods is claimed to detect SNM, explosives and other contraband. It uses Bremsstrahlung X-rays with end energies of 2-8 MeV, depending on the size of the inspected object and the relevant NRF states [74, 75]. Passport Systems was expected to complete its experiments and determine the performance capabilities of the first system around March 2012 [76].

2.2.4 X-ray Diffraction (XRD)

XRD is a non-destructive technique that reveals information about chemical composition and crystallographic structure of materials. In XRD, an incoming beam of X-rays is diffracted by the atomic planes of the crystal it traverses. The structure of the crystal can then be determined by the interference pattern.

SNM detection in cargo with X-Ray Diffraction (XRD) was proposed by Harding in 2007 for explosive detection in small objects and later expanded to full cargo containers [77–79]. It is based on the fact that uranium and plutonium happen to have a non-cubic lattice structure, in contrast to all other non-SNM, high-density elements of the periodic table. The non-cubic structures of uranium and plutonium mean that their XRD profiles are densely populated with peaks compared to their cubic neighbours in the periodic table.

Currently, there is a parcel inspection device based on this technology, working at ∼100 keV X-ray energy. In this device the diffraction of the 1st order interference is exploited to get the third dimension, namely, the distance of the interfering molecules from the detector and the source.

Cargo inspection with XRD requires a coherent radiation source with at least 1 MeV X-rays energy. So far, published work includes diffraction calculations, showing that such a diffraction analysis is possible through cargo and that the energy resolution needed to distinguish uranium from innocuous high-Z elements is approximately 10%.

XRD for cargo container inspection is a problematic approach. At the much higher energies required to penetrate these large containers the wavelength becomes very short. As a result, the probability of getting interference from neighbouring lattice atoms that are characterized by inter-atomic distances of 2-10 Angstroms decreases sharply. Even if one is left with some effect at MeV probe energies, surely the whole diffraction pattern will be more and more forward-peaked, and eventually collapse into the forward transmission (no interference). That is also true for the 2nd and higher-order diffraction peaks, which will get even weaker than the 1st order as the probe energy increases.

2.3 Non-Radiographic Interrogation

2.3.1 Passive Interrogation

Out of all SNM detection methods, passive detection is the simplest to implement. It is also the safest, since unlike the other methods, no superfluous radiation is created in the process of detection. As a result, it is also relatively inexpensive and has seen by far the widest deployment.

In passive detection, the measured signal is the radiation emitted naturally from SNM isotopes. Each nuclei has a well known decay chain, that produces radiation at typical energies and intensities. Signatures that can be used are gamma-rays and neutrons. Alpha and beta radiations are also emitted, but these have limited value in nuclear threat detection because they are incapable of penetrating even thin shielding [19].

Neutrons are attractive not only because of their relatively high penetration capability, but also because the background is relatively small. High neutron fluxes are typical of Weapon-Grade Pu (WGPu) via the nuclear processes of spontaneous fission and (α,n) reactions on nearby light nuclei, but not of Highly Enriched Uranium (HEU). Depleted uranium (DU) is also a minor source of neutrons even when present in large quantities.
Typical neutron production values are 130 n/s/g for WGPu, 0.00136 n/s/g for HEU and 0.0135 n/s/g for DU. Significant amounts of these materials, organized in a sphere would have a 4-8 cm radius. Kouzes et al. published calculations of the number of neutrons leaving such spheres [80]. The average neuron energies are typically less than 10 MeV.
The published work of Kouzes et al. reports a simulations study and promises only detection of plutonium (not HEU) by detecting neutrons. The modelled system is based on ^{3}He detectors that are hard to come by at such quantities [80].

Cester et al. [81] reported on experimental detection of plutonium behind a 0.5 cm iron shield using neutron emission but it involved active interrogation methods in order to detect uranium.

Gamma-rays, on the other hand, are not only emitted by all types of SNM but also have discrete energies, enabling spectroscopy measurements. In addition, gamma-ray detection technology has betters energy, timing and directionality resolution than possible in neutron detection.

The passive detection challenge is to detect signals above background and after attenuation

by shielding. Even though passive detection is mostly assumed to be ineffective when the SNM is heavily shielded some work continues [82]. In fact, the operational cargo scanning devices prevailing today are the Radiation Portal Monitors (RPM) such as the SAIC portal monitors [38]. Manufacturers of commercial RPMs do not release specifics of detectable amounts.

2.3.2 Active Interrogation

The definition of active interrogation in this context is the use of ionizing radiation to induce nuclear reactions that uniquely identify SNM through fission or isotopic identification. Active interrogation has the advantage of good penetration into the inspected object, which makes it more likely to be effective in detecting shielded SNM than passive interrogation. Several active interrogation approaches incorporate radiographic methods to add imaging to their capabilities.

The most important reaction in active interrogation is fission, see Fig. 2.2 for typical cross sections. The second important reaction is Nuclear Resonance Florescence (NRF). Other nuclear interaction-related signatures are creation of prompt gamma-rays after neutron capture and production of gamma-rays from inelastic scattering of neutrons. The last two have not been thoroughly investigated yet. Unless otherwise stated, in the following discussion the emissions are the result of fission.

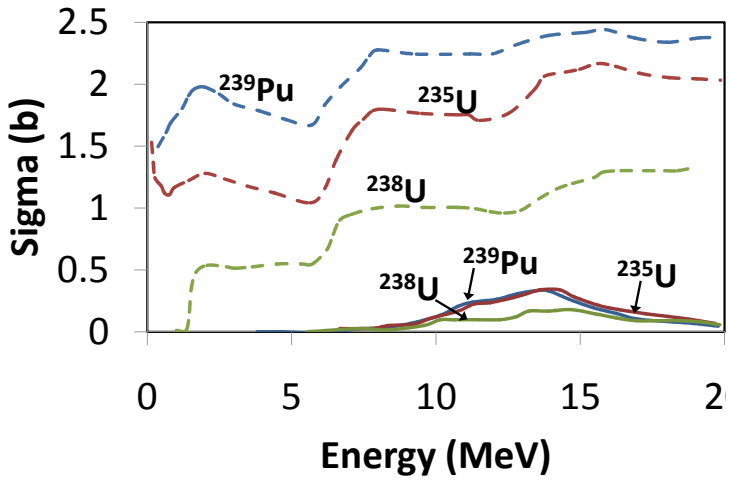

Figure 2.2: Neutron-induced (dotted lines) and photon-induced (solid lines) fission cross-sections as a function of particle energy [82, 83].

Neutrons and photons emitted following fission posses three properties of interest: their yield, their energy distribution and their temporal profile. The temporal profile, expressed in terms of decay constants, is important because of the need to distinguish between interrogating and induced radiation. The signatures are therefore divided into prompt and delayed emissions.

Prompt emission occurs immediately after the fission, within picoseconds, and is related to the scission of the nucleus. The detection can take longer because of the large system size involved. To differentiate the prompt emission from post-fission decays, it is defined as occurring up to 10 ns after a fission. Delayed signatures are those coming from decay of fission fragments and their daughter nuclei. Signatures up to 100 seconds later have been investigated [84].

Out of all possible combinations of radiation sources and induced radiation, most work on cargo inspection has been performed with incoming neutrons and induced gamma-ray emission. Examples of this approach are to be found in references [85–89]. The “nuclear car wash” used an accelerator-based pulsed neutron source, a large array of plastic scintillators as gamma-ray

detectors and recorded gamma-rays between 2.5 and 6 MeV. It detected a 5 kg ^{235}U sample concealed within wood or steel cargo in less than 30 s [88].
In these cases, pulsed neutron sources are used, making the delayed fission products gamma-rays easier to measure than the prompt gamma-rays. Most neutrons entering the inspected object will be thermalized within few ms and completely extinguished in a few tens of ms, leaving only the delayed gamma-rays behind [82].

An advantage of measuring the gamma-ray signatures is that in case the area surrounding the SNM is of low density, the fission gamma-rays (both prompt and delayed) are highly penetrating and easily reach the detector. Another advantage is that these gamma-ray signatures have higher intensities relative to neutron signatures.
A disadvantage is that for high density shields these gamma-rays are strongly absorbed, losing their edge on the neutron emissions whose intensities are lower but are much more penetrating.

Another leading approach is NRF, which uses incoming gamma-ray radiation to induce delayed gamma-rays emission. The target nucleus resonantly captures a photon and enters an excited state, which later emits one or more gamma-rays whose energies are as high as the energy of the incident photon. The emitted gamma-rays are isotope specific due to the distinct energy levels structure characteristic to each isotope.
The cargo inspection applications using NRF have mostly published proof-of-principal measurements [75, 90–93]. An example is the work of Kikuzawa et al. who used beam energies up to 5.7 MeV and mapped a 2×2×5 cm^3 lead block concealed behind a 1.5 cm lead plate - far from the final goal of scanning a cargo container [90].

The comprehensive study by Johnson et al. compared two possible NRF realizations [93]. In the first realization, reflection based, the reflected gamma rays are measured by detectors located upstream of the cargo and oriented at backward angles to the incident photon beam. This way, backgrounds from beam- related Compton scattering and other processes tend to be at lower energies than the NRF emission lines from materials of interest. The second realization is transmission based, in which the incident photon beam is analysed after passing through the cargo in an effort to detect a potential notch at the resonant frequency that might be associated with NRF absorption in a threat hidden in the cargo.

Although active interrogation for cargo containers screening is receiving a lot of attention, its role remains uncertain since the performance and costs of operational deployments remain unclear. A likely use of active interrogation will be as secondary detailed-inquiry system, after an alarm from a rough screening via a passive or radiographic system [82, 93–96].

2.4 Combined Interrogation, Multi-Purpose Detection

Up to this point, cargo interrogation techniques have been discussed one by one. However, the demands presented by realistic cargo inspection scenarios are so diverse that no technique can single-handedly meet all of them. Therefore, combined solutions are often suggested and being turned into commercial systems.

A very advanced development in air-cargo scanning is the dual neutron-photon system developed at the Commonwealth Science and Industrial Research Organisation (CSIRO) [2, 8, 27, 97–102]. In spirit it is dual-energy radiography translated into the dual-particle domain. The Fast Neutron-Gamma Radiography (FNGR) method forms 2D projection images by measuring the transmission of both 14-MeV neutrons from a DT generator and gamma rays from ^{60}Co.
An experimental FNGR system was installed in Brisbane airport. It used an intense DT source (10^{10} neutrons/s) and a ^{60}Co source emitting 10^{11} gamma-rays/s. The detection system con-

sisted of 700 plastic-scintillator neutron detectors and 350 CsI(Tl) gamma-ray detectors. This setup enabled complete scans of a ULD in 60-120 s.
In 2008, CSIRO signed a joint venture agreement with Nuctech [35] to develop and commercialize a new scanner incorporating CSIRO's technology with Nuctech's X-ray technology [44,67]. The first commercial unit of this air cargo scanner, the Nuctech AC6015XN Air Cargo Scanner [35], was commissioned in Beijing and after completing a program of trials to demonstrate the technology it is now available on the market.

The AC6015XN scanner uses a Nuctech 3/6 MeV dual-energy LINAC. The X-ray output is collimated into two vertical fan-beams separated by an angle of 9°. Alternate pulses from the LINAC are emitted at high and low energies. The dual-energy X-ray system is used to discriminate between organics and metals and the neutron radiography enables discrimination between different classes of organic materials.

Another photon/neutron system is the Eagle MaX, developed by Rapiscan systems [36, 40]. It is a combination of dual energy radiography and Z-SCAN [51] for SNM detection with thermal and fast neutron radiography for explosive detection.
In 2009, a U.S. patent was granted to Rothschild from AS&E [103] for a very similar concept, a combined X-ray CT/neutron material identification system. However, there is no published work or a commercial system.

A combined detection method technology that is on the market by AS&E is a combination of regular transmission imaging, dual-energy imaging, backscatter imaging and passive detection [31]. With all these technologies combined, AS&E claims only differentiation of low-Z and high-Z materials. Another company that combines passive detection with radiography is SAIC, in the VACIS IP6500 that utilises single energy radiography.

Another common approach is to combine radiography with active interrogation. Since active interrogation for cargo screening is problematic in terms of performance and costs, its potential is in alarm resolution whereby containers flagged by a combination of passive systems and radiographic inspection can be analysed using more elaborate equipment to assay the contents of a container [82].

Rapiscan is working towards a system based on this concept [104, 105]. In one possible implementation the first step will use standard X-ray radiography and Z-SCAN noise spectroscopy. The second, alarm clearing, step will take longer and will include activation of areas marked as high-Z with X-ray photons possessing energy from 6 MeV (the activation threshold) to 9 MeV [104].
In another approach by Rapiscan [105], neutrons are produced simultaneously with X-rays by the photo-nuclear interaction of the X-ray beam with a heavy-water converter. The active interrogation is combined with a radiography image obtained from the X-rays.

Passport Systems has developed another radiographic/active combination that has been previously discussed. It combines backscatter imaging with NRF and is currently in advanced experimental stage [74–76].

The detection method discussed in the present work is in itself a combination of dual energy radiography with fast neutron radiography. These two methods differ from other methods reviewed here by the nuclear-reaction based source, which has different characteristics and poses different challenges.

CHAPTER

3

GAMMA-RAY DETECTORS

3.1 Requirements from a DDEGR Detector

A detector for a DDEGR system should be able to perform gamma spectroscopy, imaging of a container (gamma-ray radiography) and separation of the gamma-rays from neutrons. These general requirements translate into:

Requirement		**Rational**
Gamma-ray energy resolution	∼3 MeV	To separate the 4.4 MeV from the 15.1 MeV γ-rays.
Image resolution	5-10 mm	To detect small objects and present a good quality image to the operator.
Timing resolution	50 ns	To separate gamma-rays from neutrons (for 8 m between the source and the detector).
Ability to work at high event rates	Up to 0.5 MHz	To minimize the time it takes to scan a container.
Large area detector	At least 10×10 cm^2	To enable a fast scan of containers.

Table 3.1: Requirements from a gamma-ray detector designed for a DDEGR system.

A detector for the combined DDEGR/FNRR system needs all of the above with the addition of the capability to perform neutron spectroscopy:

Requirement		**Rational**
Simultaneous detection of γ-rays and neutrons		
Timing resolution for neutron spectroscopy	5 ns	To distinguish the main feature of neutron transmission spectra.
Neutron imaging resolution	∼2 mm	The imaging resolution required for explosives detection by FNRR requirements.

Table 3.2: Requirements from a gamma/neutron detector designed for a DDEGR/FNRR system.

3.2 Scintillator Based Detectors

3.2.1 Gamma Spectroscopy

Gamma spectroscopy is the determination of a gamma-ray energy, usually through its interaction with the detector material. In gamma spectroscopy, the incoming gamma-ray is uncharged and does not create direct ionization or excitation in the material [49, 106].

The incoming gamma-ray undergoes an interaction that transfers all or part of its energy to a charged particle, an electron or a positron. That charged particle interacts with the material by consecutive ionizations and excitations. It may undergo Bremsstrahlung, creating photons that may re-interact to create new charged particles. If a positron is created, it annihilates into two 0.511 MeV photons that may interact with the material to deposit their energy via more excitation and ionization.

Electromagnetic interactions are the mechanisms by which a gamma-ray creates a charged particle. They include pair-production, Compton scattering and photoelectric absorption (see Fig. 1.3). The photoelectric absorption is dominant up to several hundred keV gamma energy, Compton scattering is dominant at higher energies up to about 5 MeV and above this value the dominant process is pair production.
In the photoelectric absorption process, a photon undergoes an interaction with an atom in which the photon is completely absorbed and a photo-electron is ejected. In Compton scattering the incoming gamma-ray is deflected by an electron with respect to its original direction. The gamma-ray transfers part of its energy to the electron, assumed to be initially at rest. In pair-production, the incident gamma-ray disappears and is replaced by an electron-positron pair. For pair production to be energetically possible, the gamma-ray energy has to exceed twice the rest-mass energy of an electron, 1.02 MeV.
Each of the three interaction processes can be characterized by a probability of occurrence per unit path length in the absorber. The Z-dependence of the probability of each process is detailed in Table 3.3.

Photoelectric absorption	**Compton scattering**	**Pair-production**
$\tau = \mu_{pe} \propto constant \times \frac{Z^n}{E_\gamma^{3.5}}$	$\sigma = \mu_C \propto \rho \frac{Z}{A} f_{KN}(E)$	$\kappa = \mu_{pp} \propto \rho \frac{Z^2}{A} f_{pp}(E)$
where n varies between 4 and 5, depending on the gamma-ray energy. [49]	where f_{KN} is the Klein-Nishina function.	where f_{pp} is calculated in [107]
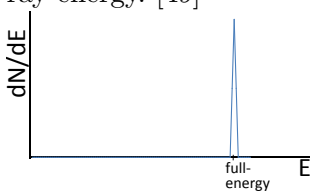	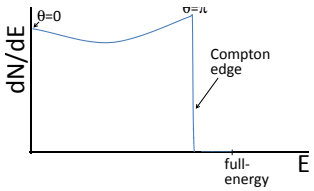	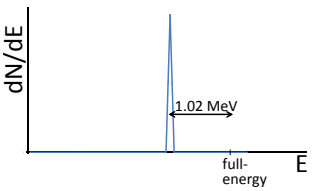
The full energy is the incoming gamma-ray energy.	θ is the scattering angle of the gamma-ray.	Assuming both annihilation photons escaped the detector.

Table 3.3: The Z-dependence of electromagnetic processes and the ideal detector response to mono-energetic gamma-rays undergoing each process.

A detector for gamma spectrometry must therefore be able to convert the incident gamma-rays into electrons with reasonable efficiency. The detector must be large enough for the secondary particles to leave all of their energy inside the detector, as a measure of the incident gamma-ray energy. For high-Z scintillator crystals an incident gamma-ray with several MeV energy will create energetic charged particles, with typical range of several millimetres.

The probability per unit path length for a gamma-ray to be absorbed or scattered is the sum of the individual probabilities:

$$\mu = \tau \text{ (photoelectric)} + \sigma \text{ (Compton)} + \kappa \text{ (pair production)} \tag{3.1}$$

and is called the linear attenuation coefficient. The transmitted intensity I is:

$$\frac{I}{I_0} = e^{-\mu\rho t} \tag{3.2}$$

where I_0 is the unattenuated intensity, ρ is the density and t is the thickness of the inspected object.

In the electromagnetic processes listed above photons lose their energy to electrons and positrons, which then transfer this energy to the absorbing material. The electron and positron masses are equal to that of the orbital electrons with which they interact, enabling large angle scattering. Because of theses large deflections along their path, the range of electrons and positrons is usually defined by the absorber thickness required to ensure that almost no electrons will penetrate it.

Electron-nuclear interaction also occur sometimes, abruptly changing the electron direction. The specific energy loss, also called linear stopping power, due to collisional processes (ionization and excitation of the absorbing material atoms) can be expressed by [49]:

$$-\left(\frac{\mathrm{d}E}{\mathrm{d}x}\right)_c = \frac{4\pi e^4 z^2}{m_0 v^2} NZ \left[\ln\left(\frac{2m_0 v^2}{I}\right) - \ln\left(1-\beta^2\right) - \beta^2\right] \tag{3.3}$$

In this expression, derived by Bethe-Bloch, v is the incoming electron velocity, N and Z are the number density and atomic number of the absorber atoms, m_0 is the electron rest mass, e is the electronic charge and β is defined as v/c, c being the speed of light. The parameter I represents the average excitation and ionization potential of the absorber and is normally an experimentally determined parameter. For non-relativistic electrons ($v << c$) only the first term on the right side of Eq. 3.3 is significant.

In addition to coulomb interactions, electrons and positrons may lose their energy in radiative processes such as Bremsstrahlung or synchrotron radiation, which can be created at any position along the electron track. The linear specific energy loss through radiative processes is:

$$-\left(\frac{\mathrm{d}E}{\mathrm{d}x}\right)_r = \frac{NEZ(Z+1)e^4}{137 m_0^2 c^4}\left(4\ln\frac{2E}{m_0 c^2} - \frac{4}{3}\right) \tag{3.4}$$

The factors E and Z^2 in the numerator of Eq. 3.4 show that radiative losses increase with electron energy and absorber material Z. The created Bremsstrahlung photon may be re-absorbed in the detector or escape from it, depending on the detector characteristics.

The ideal detector response to mono-energetic gamma-rays depends on its size. In a large detector the energy of an incident gamma-ray is transferred to the detector in its entirety and the response is a delta function at the full energy of the incident gamma rays. As the detector gets smaller, more particles escape.

The response of a realistic detector is more complex than that of the ideal detector. It is influenced by many phenomena: secondary electron escape, Bremsstrahlung escape, characteristic X-ray escape, effects of surrounding materials and summation effects as well as by the secondary radiation created near the source - Bremsstrahlung and annihilation radiation. The most feasible way to determine a detector response function in advance is through Monte-Carlo calculations. A typical response is presented in Fig. 3.1.

The response properties that are generally of interest are the ratio of the area under the photo-peak to the area under the entire response function. Large values of this ratio make identification of the gamma-ray energy easier.

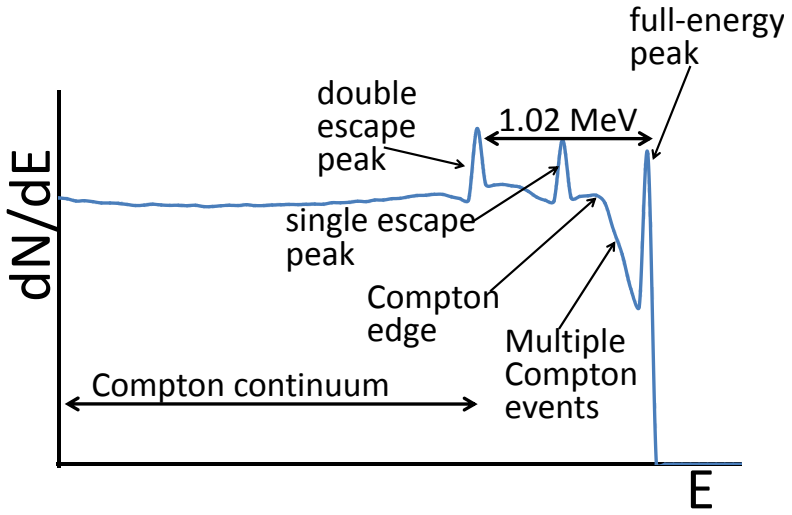

Figure 3.1: A typical, realistic detector response to gamma-rays. The single- and double-escape peaks are the result of one or two annihilation photons escaping the detector without leaving their energy.

3.2.2 High-Z Scintillators

One of the most common configurations in gamma spectroscopy and imaging is a scintillator optically coupled to a photo-detector. The scintillator converts gamma-ray energy deposited in the detector into a burst of optical (or near-optical) photons, which are read by the photo-detector that translates the light burst into an electrical signal.

Another common detector is Germanium, mostly used when excellent energy resolution is required. However, the main detector requirements in this thesis are high efficiency, fast response time and low cost, precluding the use of Germanium.

The ideal scintillator should have the following properties [49]:

1. High scintillation efficiency, meaning that the conversion of the incoming particle energy into detectable light is efficient.

2. Linear conversion of this deposited energy into detectable light.

3. Minimum self-absorption, meaning that the medium should be transparent to the wavelength of its own emission.

4. The material should be easily manufactured and shaped so that one can build a detector from it.

Other properties are commonly required but not always. For a DDEGR system detector these are:

5. The decay time of the emitted luminescence should be short enough so that fast signal pulses can be created.

6. For the combined neutron-gamma detector, the emission wavelength should be similar to that of plastic scintillator to enable a joint readout for the gamma and neutron detection.

No scintillator meets all these criteria. The choice of a scintillator for a certain application should be based on the specifics of the application.

The first decision when choosing a scintillator should be whether to use an organic or inorganic scintillator. Inorganic scintillators tend to have the best light output and linearity but a slow response time. Their high density and high-Z increase the efficiency for gamma-ray spectroscopy applications. Organic scintillators are generally faster but yield less light and have lower density. Their hydrogen content is suitable for fast neutron detection and beta spectroscopy. The DDEGR detector requires spectroscopic capability at high gamma energies (up to 15 MeV), so an inorganic scintillator is favourable.

A simple model of the scintillation process in inorganic crystals is that electron-hole pairs created in scintillators stay bound to each other as mobile pseudo-particles known as excitons. Excitons eventually find their way to luminescent (dopant) centres where they can re-combine via radiative transitions with energies lower than the band gap, emitting light in the process that is not reabsorbed by the crystal. In many scintillators this recombination can proceed through different intermediate excited states, leading these scintillators to exhibit fast and slow components in their light emissions [108]. All of these processes are generally well understood, although details for specific materials may still be lacking [106, 109].

Scintillation light emission can be defined as either fluorescence, phosphorescence or delayed fluorescence. Fluorescence is the prompt emission of light from a substance following its excitation. Phosphorescence is the emission of light at a longer wavelength than fluorescence and is usually much slower. Delayed fluorescence emits light at a similar wavelength to that of prompt fluorescence but at a longer time after the excitation.

The inorganic scintillators can of course be divided further into subgroups, the main ones being:

1. Alkali-halide scintillators such as NaI, CsI and LiI.

2. Slow response crystals such as BGO, $CdWO_4$, ZnS, CaF, etc.

3. Unactivated fast inorganics with low light yield such as BaF_2, CeF_3, etc.

4. Cerium activated fast inorganics such as GSO, YAP, YAG, LSO and LuAP.

5. Glass scintillators, which are silicate glasses containing lithium or boron and activated with cerium.

6. Scintillator gases such as xenon, argon and helium.

Table 3.4 lists physical properties of several common crystal scintillators from the different groups above. The values in this Table may vary somewhat between different manufacturers as the dopants and trace elements vary.

	NaI(Tl)	LSO	BGO	BaF_2	$LaBr_3$	$CdWO_4$	CsI(Na)
Effective atomic no.	51	66	74	54	47	64	54
Density(g/cm^3)	3.7	7.4	7.1	4.9	5.3	7.9	4.5
Index of refraction	1.9	1.8	2.1		1.9	2.2	1.8
Light yield (% of NaI(Tl))	100	75	15	5	160	20	85
Peak emission (nm)	410	420	480	220	370	480	420
Decay constant (ns)	230	40	300	0.8	25	5000	630

Table 3.4: Properties of popular inorganic scintillator crystals from different groups [110, 111]

The activation of certain crystals with cerium that produces crystals with reasonably good light yield started at the late 1980's. The principal decay time of the cerium luminescence ranges from about 20 to 80 ns, depending on the host crystal. These crystals timing characteristics are therefore faster than those of the classic inorganic crystals that are several hundreds nanoseconds, but are still slower than organic scintillators. The faster timing along with the good light-yield make this crystal group best suited for the DDEGR system detector. The selection of a specific crystal is described in detail in a later chapter, when describing the TRECOR detector design.

3.2.3 Photo-Detectors

To complete the discussion of the common scintillator – photo-detector assembly, the photo-detector side will be discussed in this section. Photo-detectors can be divided into the following main groups:

1. Vacuum: Photomultipliers (PMT), Multie-Anode PMT or Position-Sensitive PMT (PSPMT), Micro Channel Plate (MCP), MCP-PMT (ultra fast timing).

2. Solid state: PIN-diode, Avalanche Photodiode (APD), Geiger-mode APD (G-APD, also known as a Silicon Photo-multiplier or SiPM), Complementary MetalOxideSemiconductor (CMOS) and Charge-Coupled Device (CCD).

3. Hybrid detectors - combination of solid state and vacuum devices.

4. Gas: Photosensitive gas detectors such as Multi-wire Proportional Chambers (MWPC) or Micro Pattern Gas Detectors (MPGD), Gas Electron Multiplier (GEM).

The first group includes all instruments operating in a vacuum environment. All these devices have in common the photosensitive part, which absorbs light photons and emits electrons, which are the signal read by the electronics. These materials are used as the basis for all photo-detectors and the electron pulse they emit is then amplified and shaped. The statistics of the electron production in the photosensitive part determines the fluctuations in the outgoing signal.

The oldest, most common and reliable photo-detector is the PMT, which dates back to the 1930's. PMTs have very high gain (typically $\times 10^6$), low noise, fast response, and relatively low cost. The basic PMT is a vacuum tube consisting of a photo-cathode, several electrodes called dynodes and an anode. Each dynode is held at a positive voltage compared to the previous one. The photocathode is the photosensitive electrode that absorbs incident optical photons and emits electrons. These electrons are accelerated by the voltage, gaining sufficient energy to

create secondary electron emissions from collisions with each dynode stage, amplifying the signal. The signal is amplified at each dynode, until arriving at the anode. The main disadvantages of PMTs are their relatively bulky size and the high voltage of thousands of volts they require.

In 1985, Hamamatsu developed the multi-anode PMT with multiple dynode chains or channels (effectively multiple PMTs) inside a common vacuum envelope [112]. Each channel provides an essentially independent photodetector. For example, Hamamatsu H7546 with up to 8×8 channels, 2×2 mm^2 each and 41% active area. Since it carries several channels on one device it suffers from cross-talk between the channels, typically around 2%. The multi-anode PMTs enables gamma imaging with a single PMT [113].

Another development of the classic PMT is the flat-panel Position Sensitive PMT (PSPMT), which is basically a multi-anode PMT at a more compact size and a minimal peripheral dead zone, enabling to stack devices to image a larger area. For example, Hamamatsu H8500 with 8×8 channels, 5.8×5.8 mm^2 each, 89% active area and less than 1 mm peripheral dead area [114]. Using a PSPMT is essentially similar to working with many PMTs. It raises problems with the non-uniform response of different anodes that have to be compensated for by the electronics. The time response has to be coordinated between the different channels and light cross talk between different channels may add to the total noise.

Another veteran photo-detector is the Micro-Channel Plate (MCP). MCP is a thin glass plate with an array of pores, <10-100 μm diameter each. Each hole is coated with metal that essentially turns it into a continuous dynode structure. Due to the bias voltage applied electrons are accelerated down the channel toward the output end. An electron will be multiplied repeatedly upon hitting the walls along its path. The output signals are typically collected in any of several ways, including metal anodes, resistive anodes, wedge and strip anodes, delay-line readout or a phosphor screen deposited on a fiber-optic or other substrate. MCPs have high gain, fast response and a large active area.

Originally, MCP's were developed for use in Image Intensifiers (II). IIs consist of three main components: s photocathode, a MCP and a phosphor screen. Often two or three MCPs are stacked to increase the amplification. The photocathode turns the incoming photons to electrons that are amplified by the MCP and then turned back into photons by the phosphor on the output window. By using a fiber-optic plate on the output window, the imaging is maintained.

Another use of MCPs is in MCP-PMT that is similar to an ordinary PMT but with the dynode structure replaced by a micro-channel plate (MCP).

The second group includes the solid-state, mostly silicon, devices. They can be used either alone or in combination with a scintillator, where they are used to read the scintillation light.

When a photodiode is used in combination with a scintillator, it is similar to a regular semiconductor, a PN junction, but with an opening that permits penetration of light. The incoming photons create electron-hole pairs, the holes move toward the anode and the electrons toward the cathode, producing current [115].

A simple kind of photodiode is the PIN photodiode in which an intrinsic piece of semiconductor is sandwiched between two heavily (oppositely) doped regions. The two charge sheets (on the n+ and p+) sides produce a field that, even without an external field supplied, will tend to separate charges produced in the depleted region. The PIN diode is the simplest, most reliable and cheapest photo sensor. It has high quantum efficiency, typically up to 60% , and a small volume. However, its gain is unity and its timing resolution is inferior to that of PMTs [110].

Another popular device is the Avalanche Photo-Diode (APD). It has the advantage over PIN diodes that it has higher gain (10^2-10^3) and has faster timing, on the order of 1 ns.

It operates by applying a high reverse bias voltage (typically 100-200 V in silicon). An incoming photon creates electron-hole pairs in the thin p-layer (depletion layer) on top of the device and these move towards the respective PN junctions, colliding with atoms in the crystal lattice and creating more electron-hole pairs through ionization, which in turn induce more ionizations. The total effect of this avalanche is increase in gain.

As with PIN diodes, APDs can be found in single packages or as arrays. More recently, position-sensitive planar APDs (PS-APD) have been produced. These devices use signals from the four corners of the device to determine the position of an event much like the technique used in the original block detectors. One advantage of PS-APDs is that the number of data channels in the electronics (preamplifiers, ADCs, etc) are reduced compared to discrete arrays in most applications. However, the noise in PS-APDs is generally worse than standard APDs [110].

These APD can be operated in Geiger mode, in which the reverse bias voltage is higher than the APD's breakdown voltage. In this mode, every incoming photon triggers a self-sustaining avalanche, resulting in a very high gain but losing the information about light intensity.

To compensate for that, a development composed of an array of such diodes is used. These devices are also known as G-APD, SiPM (Silicon PMT) or Single-Photon Avalanche Diode (SPAD) [116–118].
The basic device is built around a series of APD micro-cells, where each cell is an independent Geiger-mode detector. Each cell is connected to the bias voltage by an individual resistor that results in the cell discharge being quenched. The cells are then connected to a common output. Ideally, a SiPM should produce the same size and shape of a current pulse from each cell, making each cell a digital detection device (on or off).

When coupled to a scintillator, the hundreds to thousands of light photons that are emitted by the scintillator interact in a large number of the micro-cells. The result is an output pulse similar to that seen in PMTs. Gains for typical devices range from 10^5 to 10^7 and produce a signal of several millivolts on a 50 ohm load, making it very similar to PMTs. The bias voltage is typically between 30 and 150 volts, and the devices are capable of good timing resolution.

One limitation of such devices is that contemporary designs have relatively large capacitance per unit area, which leads to problems in scaling up such devices to active detection areas greater than 3×3 mm^2 (in a single device) with present-day devices [110].

Charge-coupled devices (CCDs) and CMOS detectors have also found use as transducers for scintillator-based detectors. CCDs are read out in sequence after some integration period (integration mode) that is fundamentally different from PMT's or APDs in which each event is read out separately (event-counting mode). To differentiate single events the integration times should be short. Gamma spectroscopy is possible by integrating the signal across all pixels in an event, but the energy resolution is still poor.

In addition to cooling CCDs to reduce dark current, some CCD-based gamma-ray detector systems utilize electron-multiplying CCDs (EMCCDs) that employ a series of multiplying registers to amplify the charge signal during readout to minimize the impact of the readout noise on energy resolution [119, 120].

Alternatives to scintillator-based photon imaging systems are semiconductor radiation detectors. When a gamma-ray interacts in a semiconductor detector, one or more energetic electrons are created. Each electron loses energy as it propagates via two primary competing processes: ionization and phonon generation. The ionization creates electron-hole (e-h) pairs. Application of a bias voltage creates an electric field that causes the two types of charge carriers to drift in opposite directions. These moving charges induce transient current signals on the detector electrodes that can be sensed by an external electric circuit, thereby providing the means to

measure the detector's response to a gamma-ray interaction [108].

The next group, Hybrid Photon Detectors (HPDs) consists of a combination of vacuum photon detectors, such as an II or a PMT, and a solid state device, usually a PIN diode. HPDs have been developed for high-energy particle experiments.

HPDs are comprised of a photocathode that turns the incoming photon to an electron, which is then guided by focusing electrodes into the silicon detector. Similarly to the HPD there is the Hybrid Avalanche Photon Detector (HAPD) that is a combination of an II and an avalanche photodiode [121, 122].

The last group of photo-detectors, the gas detectors, rely on the following principle: the photons interact electromagnetically with the gas, creating a charged particle. The charged particle ionizes gas atoms/molecules along its track. An electric field transports electrons (and ions) towards electrodes where the electrons are multiplied in a strong electric field finally reaching the readout electrodes and creating current in them.

The gas photo detectors include three main groups: multi-wire Proportional Chambers (MWPC), Micro Pattern Gas Detectors (MPGD) and Gas Electron Multiplier (GEM).

A MWPC is constructed with alternating planes of high voltage wires and grounded sense wires, all placed in a gas environment. When a charged particle passes through the gas in the chamber, it ionizes gas molecules, freeing electrons that are accelerated towards the sense wire by the electric field, ionizing more of the gas.

MPGDs are characterized by the electrode structures that are manufactured via microelectronic technology, enabling to achieve a very high granularity and thus a position resolution much better than in the case of the MWPCs.

The GEM consists of a thin composite sheet with two metal layers separated by a thin insulator and pierced by a regular matrix of open channels. The GEM electrode, inserted on the path of the electrons, enables transfer of the charge with an amplification factor approaching ten.

Typical GEMs are constructed of a 50-70 μm thick Kapton foil clad in copper on both sides, with up to 50 μm diameter holes through both layers, kept within a gaseous environment. A voltage of 150-400 V is placed across the two copper layers, creating strong electric fields in the holes. A single electron entering any hole will create an avalanche containing 100-1000 electrons leaving the hole from the other side. Two or three GEMs may be stacked to increase the total gain. An interesting example is the Hadron Blind Detector (HBD), which is a Čerenkov radiator operated with pure CF4 directly coupled in a windowless configuration to a triple-GEM detector element [123].

The group of A. Breskin is currently trying to develop a thick-GEM gas detector for the dual particle DDEGR/FNRR system [124].

3.3 Position-Sensitive Detectors for MeV Gamma-rays – a Review

This survey will review spectroscopic gamma-ray detectors with imaging capability based on high-Z scintillators. Reviewing all detectors developed for gamma-spectroscopy applications is outside the scope of this work. Two types of detectors are discussed here.

The first type is detectors developed for similar cargo inspection applications. The second type is detectors developed for medical imaging.

Most of the development in gamma/X-ray imaging detectors in recent years has been mo-

tivated by medical imaging applications such as PET (Positron Emission Tomography), CT (Computed Tomography), X-radiography, SPECT (Single-Photon Emission CT), etc [108, 110, 113, 125–130]. There is a substantial difference though, as typical gamma-ray energies used in medical applications do not exceed 1 MeV, a low energy compared to DDEGR's 4.43 & 15.1 MeV. The different physical processes prevailing at higher energies compel detector concept and design that are intrinsically different.

TRECOR has exceptionally broad capabilities that include, in addition to gamma-spectroscopy and imaging, TOF capability enabling neutron detection in one of its versions.

3.3.1 Detectors in Similar Applications

Reliable published data on the detectors used in actual applications is hard to come by as many of them are trade secrets. The available published information on the detectors in the systems reviewed earlier is hereby presented.

3.3.1.1 Dual-Energy Radiography Detectors

The vast majority of applications use high-Z crystal scintillators attached to photodiodes, with one exception of CCD readout by Rushbrooke et al. [55]. The scintillators are divided into pixels and each pixel has an individual readout.

When the photodiode is properly protected from direct beam, such detectors have proven to work for many years without noticeable performance degradation. Detector size should be small enough to permit good spatial resolution but it usually needs to be thick enough to be efficient for relevant applications [69, 131].

Most recent applications use Cadmium Tungstate ($CdWO_4$) scintillators [41,58,64,67,69,70], with few mentions of CsI [41, 69].

TRECOR is designed to be a gamma-neutron detector with TOF to separate between them. As such, it cannot use the common $CdWO_4$ as a scintillator converter due to its very long decay time of 5000 ns (see Table 3.4).

Typical pixel sizes are several mm^2, for example 6×6 mm^2 pixel size is very common [44,67,68] as well as 5×5 mm^3 used by Budner et al. and Rushbrooke et al. [55, 64]. Ogorodnikov et al. were using the smallest pixels, 3×3 mm^2 [58]. In many cases, especially in simulation papers, the pixel size is discussed without mentioning the detector material or readout method [44, 68].

Of interest is a recent work by Rapiscan Systems for their Z-SCAN methodology that is similar to two-energy radiography [40, 51]. While at first they were using plastic scintillators with PMT, an effort to use a square LYSO crystal with few cm dimensions attached to a PMT has been reported lately. This setup severely limits the spatial resolution and the use of SiPMs or APDs was suggested.

An entirely different concept was developed by SAIC in support of the VACIS-Z system - a Čerenkov detector array. No details are provided on this detector, except for the claims that it provides significant advantages over scintillation detectors due to its inherent threshold energy that reduces scattered X-rays and enhances contrast sensitivity, it is a more affordable detector array and it has a wider dynamic range [1, 23, 72].

3.3.1.2 Dual-Particle Radiography Detectors

Dual-particle systems pose a different challenge, since there is a need to separate between the particle types. The most thorough description of such detectors was given by Eberhard et al.,

as they were developing the early concept of the system that is sold today by Nuctech [27].

In that system the neutron and gamma-ray detectors are separated into two arrays, each array comprised of discrete scintillator elements that are read out using photodiodes. The gamma-ray detector array uses CsI scintillator elements, 10×10 mm^2 each, with reflective coating intended to increase the proportion of the scintillator light reaching the photodiode.
The neutron detector array uses plastic scintillator elements, 20×20 mm^2. A wavelength shifting dye was added to the plastic to increase the peak emission wavelength and to better match the emitted wavelength to that of the photodiode (the plastic has a 420 nm emission that is a poor match to the photodiodes). A reflective coating was applied to each scintillator.

The electronic readouts of the gamma-ray and of the neutron detector systems are very similar: signals from each detector channel are integrated using a preamplifier and then amplified and shaped, counting pulses lying between lower and upper discriminator levels.
Blocks of 32 gamma-ray elements are mounted on a single circuit board and share a common power supply and communication connections. The scanner has a single column containing 6 boards, for a total of 192 detector elements.
Due to their larger size, blocks of 16 neutron elements are mounted onto a single circuit board that has the same footprint as a 32 channel gamma-ray board. The complete neutron detector array in the scanner has 2 columns of 6 boards, for a total of 192 detector elements.

Another example of a dual-particle detection system is by Rapiscan Systems, which has two detection concepts involving photons and neutrons together, although none of them is dual-energy radiography. The description of detector technology in published data is lacking. The basic concept for the photofission combined with Z-SCAN system is separate arrays: $CdWO_4$ with conventional current mode readout for gamma-rays and fluorocarbon scintillators for neutrons [104].

3.3.2 Similar Detectors in Medical Applications

Medical imaging with photons spans a large field of applications. Many of the technologies used or considered for our application have been originally developed for this purpose. The topic of detectors in medical imaging is very wide and this section will review only the work that is relevant to our imaging technique, most of which was developed for SPECT and PET that are the source of much of the latest developments in the field of gamma imaging.

In SPECT, the basic technique requires injection of a gamma-emitting radionuclide into the bloodstream of the patient. It is carried and bound to a place of interest in the body, which then enables the ligand concentration to be seen by a gamma-camera.

In PET, a positron-emitting radionuclide (tracer) is introduced into the patient body on a biologically active molecule. The positron it emits annihilates into two coincident photons, each with an energy of 0.511 MeV. The annihilation photon detector typically comprises a scintillation crystal coupled to a fast photo-detector [127].

The work-horse of medical imaging is a scintillator attached to a PMT. Typical medical imaging scintillators are the same type of scintillators considered for our application - NaI, BaF_2, BGO, LSO/LYSO, GSO, etc. They are measured by the same standard: density, decay time, high light output and cost [129].

The decay time of the scintillator plays a different role in medical imaging than in our application. The application that is most dependant on timing has the misleading name TOF-PET, but the TOF here is not used to determine particle energy but to correlate the two photons coming from the same annihilation. This correlation helps to reduce noise and, in theory, helps

to locate the positron position better. The timing correlation is in the range of several hundreds ps, which is much finer than required in our neutron TOF. This timing depends on the crystal decay time, as well as on the shape of the crystal and the coupling of the scintillator to the photodetector [127–129, 132, 133].

The classic gamma camera, also known as the Anger camera, is a well known imaging device first developed in 1952 and still prevalent today [134].

The basic design of gamma cameras of this type consists of a large-area bulk NaI scintillator coupled to an array of PMTs, generally with a light guide between the crystal and the PMTs and combined with an absorptive collimator. The collimator, most often an array of parallel holes resembling an assembly of lead straws, constrains the angles of incidence by which the decay photons can enter the detector material.

The energy is measured by summing the signal amplitudes of all PMTs, while spatial information is extracted based on estimating the distribution of signal amplitudes in all the PMT's, in what is also known as Centre-Of-Gravity (COG) method.

The PMTs in an Anger (gamma) Camera are positioned in a close-packed, hexagonal array and coupled to a fused-quartz light guide via index-of-refraction-matching optical grease or room-temperature-vulcanizing (RTV) silicone. The number of optical photons created following a gamma-ray interaction is generally proportional to the energy deposited [108, 135].

Typical performance values for present-day Anger cameras are 10% FWHM energy resolution for ^{99}Tc and 24 mm FWHM spatial resolution on an active camera face area of $21" \times 18"$. A camera can typically support event rates of up to 10^5 per second. Cameras last for many years and require daily checks in order to trim out drifts in PMT channel gains [108].

In a later commercial development of the Anger camera concept for PET scanners the bulk NaI scintillator is replaced by an array of GSO crystals coupled to a light pipe and viewed by an array of PMTs [136]. A later design uses LYSO in place of GSO [110, 137].

While the bulk scintillator with PMTs remains very popular in SPECT and PET, new configurations are on the rise. One such configuration replaces the scintillator bulk with an array of fibres with a reflecting material between them in order to minimize cross talk of light. This design has also been used in PET gamma detectors.

An alternative to fibres are the micro-columnar crystal arrays, typically CsI(Tl) [138–140]. These consist of needle-like crystals that are grown together. The small size of the individual crystals, down to 10 μm, can provide good intrinsic spatial resolution. The thickness of such arrays is limited to 3 mm to date so they are used primarily in low-energy gamma-rays and X-rays applications [108].

The size of PMTs limits the possible spatial resolution, especially in one photo-detector to one scintillator (one-on-one) configurations. Alternative solid-state photo-detectors that have been considered for PET include silicon PIN diodes, avalanche photodiodes, and SiPMs. In PET and many other medical imaging applications, the use of scintillator attached to semiconductor devices has become very common with the increasing use of SiPM [128, 141, 142].

The combination of LYSO with an advanced photo-detector is the basis for many of these detectors. A popular concept for PET detectors combines LYSO with PSPMT [133, 143–148]. This concept is the natural successor for the classic scintillator–PMT combination.

One-on-one configurations of LYSO with a PSPMT are meant to avoid light cross-talk between different PSPMT channels, and use a reflector between the different crystals. One example is the $2.9 \times 2.9 \times 20$ mm^3 LYSO crystals arranged in a 16×16 array with mirrors and air gaps between the different crystals used by Moriya et al [133]. Another example is the 13×12 crystal array composed of $1.93 \times 1.54 \times 10$ mm^3 blocks built by Ramiraz et al. [146]. Both report position

resolution similar to the size of an individual crystal.

One-on-one configurations of LYSO with photodiodes are frequent as well. Either LYSO with APDs or the increasing use of LYSO with SiPM [149–154]. One of the more complicated concepts is the three dimensional 1×1×1 mm^3 LGSO crystal blocks array read by SiPM from three sides.

The majority of the new PET detectors concepts focus on Depth-Of-Interaction (DOI) methods - an attempt to recognize the longitudinal location of the interaction inside the detector in order to improve the spatial resolution [142]. There is one DOI detector that is similar to TRECOR, at least externally: these are composed of a thick, large scintillator slab attached to a segmented position sensitive readout on one side [155]. These detectors rely on modelling of the Light Response Function (LRF, same as the Point Spread Function) shape as a function of depth in the scintillator. A recent module described by Lewellen et al. uses a 50×50×8 mm^3 crystal coupled to a 64-anode PSPMT (Hamamatsu H8500) to accomplish spatial resolution better than 1.4 mm [110, 156].

Other examples of a LYSO scintillator slab attached to PSPMT are given in [144, 145, 148, 157]. Carles et al. have built a small animal PET scanner prototype that consists of eight modules each made out of a bulk LYSO crystal and a 64 anode PSPMT. The spatial resolution is 1.5 mm and the energy resolution is 18% [144]. This group compared results obtained by three methods: without DOI information, with the DOI provided by the system and with the assumption that all the γ-rays interact at half depth of the crystal thickness. Results show an improvement of the mean resolution by 10% with the half thickness assumption and a 16% resolution improvement achieved using the DOI provided by the system [157].

A variation on the PSPMT-LYSO concept is the cylindrical PET detector of Domingo et al. It consists of a cylindrical LYSO slab with 76 mm diameter and 3 mm thickness and a Hamamatsu R2486 PSPMT. A reflector is attached to the polished outer surface of the crystal and the roughly finished lateral side is covered with black tape to optimize light collection. The scintillation crystal is thin compared to other biological imaging detectors in order to achieve a good spatial resolution. Indeed, the measured spatial resolution is better than 1 mm with detection efficiency of approximately 10% for 511 keV gamma-rays, with a threshold at 70 keV [145].

The same principle can be realized with LYSO and SiPM as the position sensitive detector [158–160]. Schaart et al. built a 4×4 SiPM array coupled to either the front or back surface (in relation to the beam direction) of a 13.2×13.2×10 mm^3 LYSO crystal. The front-side readout resulted in better performance than conventional back-side readout. They measured spatial resolutions better than 1.6 mm and energy resolution of approximately 14% [159].

A similar detector built by Llosa et al. was composed of a 12×12×5 mm^3 LYSO crystal (half the thickness of the Schaart et al. LYSO crystal) coupled to a 64 pixel SiPM matrix for small animal PET. They measured spatial resolutions better than 0.9 mm and energy resolution of approximately 16% [161].

Part II

SNM Detection with DDEGR

CHAPTER

4

INVESTIGATION OF RADIATION SOURCE PROPERTIES: THE ^{11}B(d,n)^{12}C REACTION

4.1 Preamble

Highly promising gamma-rays for DDEGR are the ^{12}C gamma-lines [37], E_{low} = 4.43 MeV and E_{high}=15.11 MeV, populated, in decreasing yield order, by the ^{11}B(d,n), ^{13}C(^{3}He,α) and ^{10}B(^{3}He,p) reactions at E_{beam} less than 8 MeV. The ^{11}B(d,n) gamma-spectrum is by far the cleanest (assuming fast-neutron rejection by shielding, TOF, using pulsed beam or PSD), so this is obviously the reaction of choice.

This reaction has been investigated by many groups over the years, starting from 1949 with most of the research conducted in the period 1950-1970. Most of the work was devoted to measuring the neutron groups of the first states and much less of the gamma-rays [162–177].

Recently, this reaction has gained a renewed interest, first by M.B. Goldberg's patent [22,37] and subsequently by our group [46, 178]. Lanza et al have later described a similar system, but provided little more than the initial proposition [179]. There have also been recent measurements of gamma-rays yields by Sziki [180], but only up to 2 MeV deuteron energy and a recent proposal of using ^{11}B(d,n+γ) as an active interrogation source [181].

4.2 Experimental Setup

Two experiments were performed to measure gamma-ray and neutron yields from the ^{11}B(d,n+γ) reaction. The first experiment took place in 2007 and the second in 2009.

In 2007 the yields were measured using the PTB Van-De-Graaff accelerator for E_d up to 3.5 MeV and the cyclotron for higher deuteron energies. In 2009, only the cyclotron was used. Both accelerators deliver pulsed deuteron beams ($\sim$1.5 ns FWHM, repetition time T<500 ns)

suitable for TOF measurements. Average beam intensities are several μA at the Van-De-Graaff and $\sim$10 μA at the cyclotron [46].

A NE213 liquid scintillator spectrometer, 2×4" in size, was positioned at 0° and several other angles, at a distance of 7 m from the thick ^{11}B target. Neutrons were distinguished from gamma-rays via PSD and TOF.

An illustration of the target is presented in Fig. 4.1. The target consisted of a 3 mm thick layer of compressed ^{11}B granules, contained between a water-cooled copper backing and a 5 μm thick molybdenum foil. The isotopically-enriched ^{11}B contained less than 5% ^{10}B and was 12 mm in diameter. Another molybdenum foil of the same thickness served as a safety valve between the target assembly and the accelerator beam line. The molybdenum was provided by Goodfellow [182] with diameter of 18±0.2 mm and a density of 10.21 g/cm^3.

The 15.5 mm gap between the two molybdenum windows was filled with helium gas, to avoid parasitic nuclear reactions with oxygen and nitrogen and to prevent in-beam degradation of the molybdenum foils by atmospheric oxygen. The helium gas pressure was 1 bar, leading to 0.179 g/cm^3 density and 2.78 g/cm^2 areal density.

The same target and detector were used in 2009, but this time the NE213 PMT was stabilized to prevent gain shift with increasing count rate. The detector was positioned 12 m from the target at 0° only. In 2009, the detection threshold was set to 175 keV, lower than the 2007 value of 220 keV.

A measurement with identical deuteron energy, 7.03 MeV, was performed in both experiments. The gamma-ray and neutron yields at this point could be compared to ensure that both experiments were in agreement.

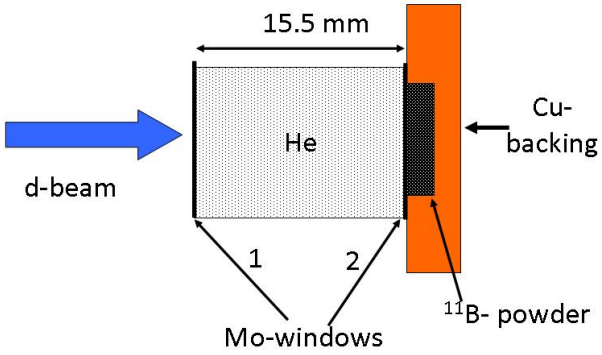

Figure 4.1: Sketch of the ^{11}B target. Measured parameters of molybdenum windows: Mo1: d = 5.85±0.13 μm and m=15.20±0.03 mg, Mo2: d = 5.49±0.12 μm and m=14.26±0.03 mg.

4.2.1 On-Target Deuteron Energies

The molybdenum foils and helium gas broaden the energy distribution of the incoming deuteron beam. SRIM2008 [183] calculations of the deuteron energy at the ^{11}B target, after traversing the molybdenum foils and the helium cell, are presented in Table 4.1 for the 2007 and 2009 experimental energies. The number of simulated deuterons at each energy is 2000. A SRIM image of the deuteron trajectories reaching the ^{11}B, in the plane perpendicular to the beam, is presented in Fig. 4.2b.

The total molybdenum film thickness is d = 11.34 μm ±0.18 μm. The resulting energy broadening was estimated using dE/dx tables from SRIM [183], amounting to 9–16 keV, decreasing with increasing deuteron energy. The total energy broadening (or the uncertainty on

the deuteron energy), is the combination of the broadening introduced by the molybdenum and the helium and the uncertainty on the actual molybdenum thickness.

The distributions of deflection angles relative to the beam direction are presented in Fig. 4.2a for three deuteron energies, normalized to a total integral of 1.

In the 2009 experiment the front molybdenum foil was distorted mid-experiment, changing the shape of the target. The effect on deuterons energy was assessed to be 5% using SRIM, by comparing the deuteron energy with and without the foil. It effected the measurements of deuterons with 7 MeV and lower.

The energy resolution of the accelerators is a constant 0.05% for the VDG. The energy broadening of the cyclotron should be determined separately for each cyclotron setup (each deuteron energy), but unfortunately that was not measured. The minimal cyclotron energy uncertainty is 20 keV, which was used in the uncertainty assessment.

2009 dataset			**2007 dataset**		
$\mathbf{E}_{acc}$ **(MeV)**	$\mathbf{E}_{target}$ **(MeV)**	σ **(MeV)**	$\mathbf{E}_{acc}$ **(MeV)**	$\mathbf{E}_{target}$ **(MeV)**	σ **(MeV)**
7.0	6.4	0.04	12.0	11.6	0.03
6.0	5.4	0.04	9.2	8.7	0.04
5.2	4.5	0.04	7.0	6.4	0.32
4.2	3.4	0.04	6.4	5.8	0.29
3.5	2.5	0.04	5.6	4.9	0.25
3.0	1.9	0.04	4.9	4.1	0.21
			3.9	3.0	0.16

Table 4.1: Energies of deuterons from the accelerator (E_{acc}), deuterons hitting the ^{11}B target after traversing the molybdenum foils and helium-cell (E_{target}) and the standard deviation (σ) calculated by SRIM [183] for the 2007 and 2009 measurements.

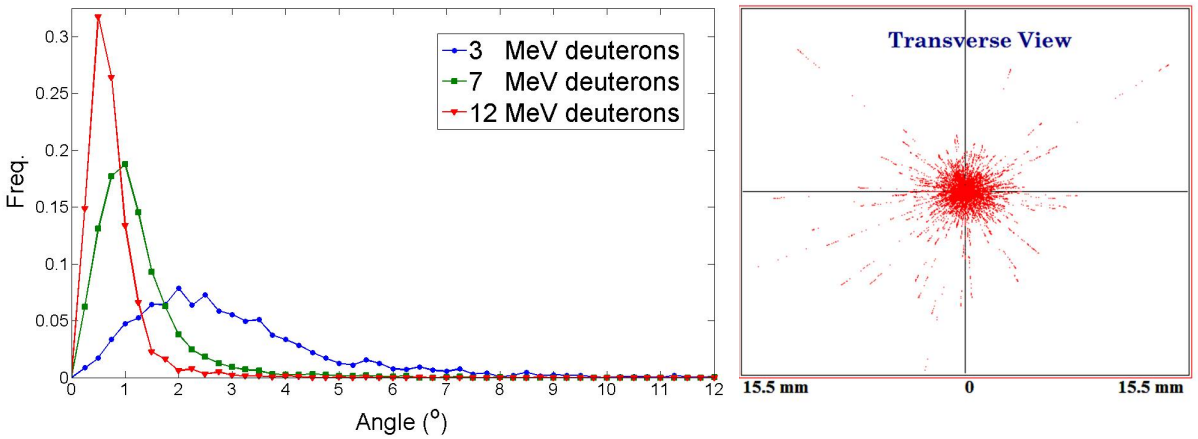

(a) Deflection angle as a function of energy.

(b) SRIM image of 3 MeV deuteron trajectories reaching the ^{11}B, in the plane perpendicular to the beam.

Figure 4.2: Deflection angle calculated from SRIM

4.3 Measured Gamma-ray Spectra

The energy of neutrons and gamma-rays following the ^{11}B(d,n)^{12}C reaction is determined by the structure of the residual nucleus, in this case ^{12}C. The energy level diagram of ^{12}C is presented in Fig. 4.3. The reaction ^{11}B(d,n)^{12}C creates an excited ^{12}C nucleus whose excitation is correlated with the energy of the emitted neutron. The neutron groups from ^{11}B(d,n)^{12}C that have been observed are from the ground state (g.s.) up to the 17.2 MeV [184].

The favoured decay from most ^{12}C lower states is into ^{8}Be+α that then decays into two more alphas. Out of all the energy levels between 4.4 and 15.1 MeV, only 7.7, 9.6 and 12.7 MeV states decay partially by gamma-rays. The 12.7 MeV state decays to the g.s. and to the 4.4 MeV state, with branching ratio of 87% and 13% of the gamma-rays, respectively [185]. However, the alpha decay of the 12.7 state into ^{8}Be+α prevails [186, 187] as with the 9.6 and 7.7 MeV states [184, 188].

The 4.4 MeV state is below the ^{8}Be g.s. energy (see Fig 4.3) and therefore it decays electromagnetically. The 15.1 MeV state is the first T=1 state, so the α-decay prominent in lower states is isopin-forbidden and therefore it decays electromagnetically. The 15.1 MeV state decay has a branching ratio of 92%, 2.3%, 2.6% and 1.4% into the g.s., 4.4, 7.7 and 12.7 MeV states, respectively [189].

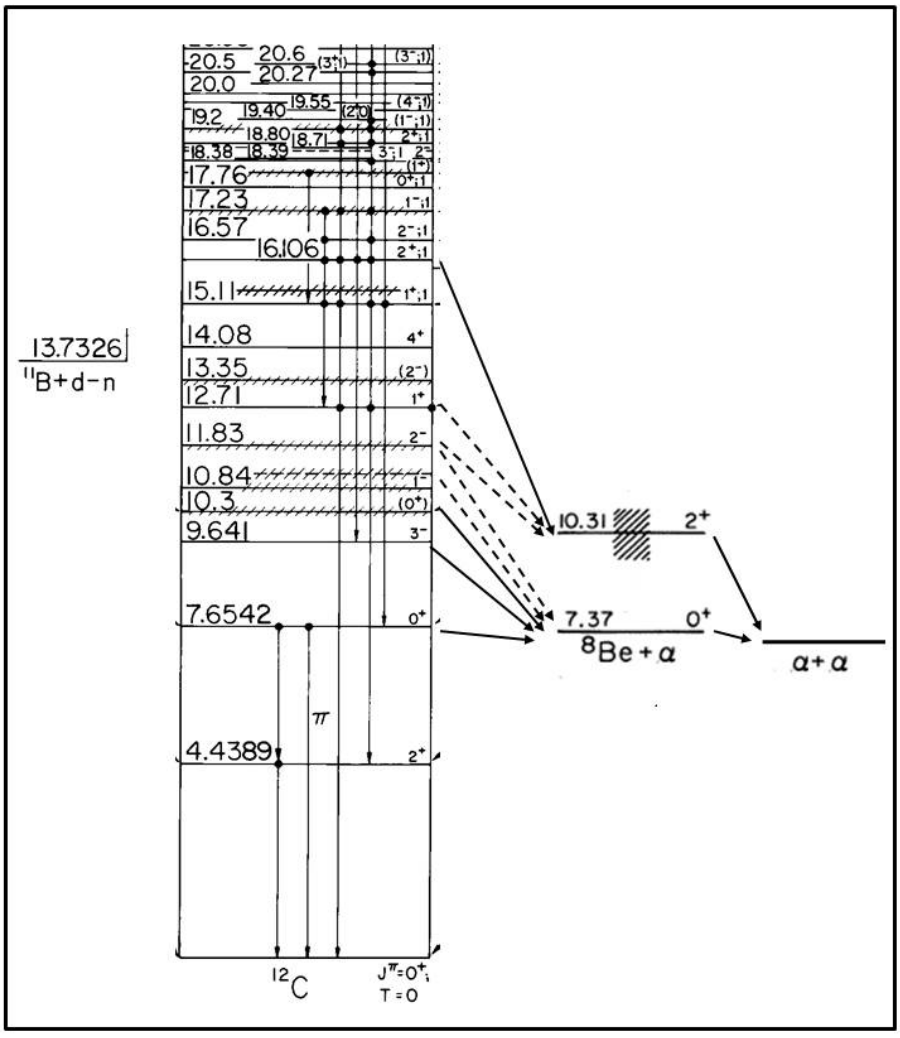

Figure 4.3: ^{12}C energy level diagram [184]

Our studies of the yields of gamma-rays and neutrons following the ^{11}B(d,n)^{12}C reaction were performed with an NE213 liquid scintillator detector, capable of γ,n discrimination by pulse-shape, in addition to the obvious TOF method. The interaction of gamma-rays with this detector is dominated by the Compton effect so that mono-energetic gamma-rays produce continuous pulse-height distributions, characterized by the Compton edge.

Our experiments are summarized in two datasets, from the 2007 and 2009 measurements. In 2009 the detector gain was stabilized, so that the energy calibration was the same for all deuteron energies. In 2007, there was no such stabilization and the energy calibration was performed for each spectrum separately.

Gamma spectra from the 2009 experiment are presented in Fig. 4.4, the area under each spectrum normalized to 1. This normalization is required to enable comparison of the spectral shapes even though the absolute number of gamma-rays depends on many factors such as the measurement time, the accelerator current etc.

The two main peaks above 4.5 MeV and below 15 MeV are the 5.03 and 6.8 MeV levels of ^{10}B, which constitutes less than 5% of the target. This explanation is supported by earlier measurements using a natural B target showing higher peaks at equivalent deuteron energies [22]. However, the rise in the spectra begins already at ~9 MeV, but there is no clear peak structure at that energy. This is the result of a combination between the ^{10}B gamma-rays at these energies (8.7, 8.3, 7.3 [190]) and ^{12}C from ^{11}B$(d,n)^{12}$C that produces gamma rays from partial decays of the 15.1 MeV level into the 4.4 and 7.7 MeV levels, with the branching ratio mentioned above.

The lower energy gamma-rays are coming from the competing reaction ^{11}B(d,p)^{12}B. The ^{12}B g.s. is the analogue of the 15.1 MeV state in ^{12}C, with T=1 and $J^{\pi}=1^{+}$. The relevant ^{12}B energy level diagram is presented in Fig. 4.5. The branching ratios of the gamma decays are listed in Table 4.2, which summarizes the gamma-rays produced by all participating reactions.

The peak just below the 4.4 MeV peak is a combination of the escapes and the 3.8 MeV level of ^{12}B that have been observed as a three-peaks structure in previous work using a NaI detector [175]. The NE213 detector resolution is too low to see this structure and instead we see this as a single broad peak.

The highest energy seen in the spectra shown in Fig. 4.4 is 15.1 MeV, since higher levels do not decay directly into the ground state.

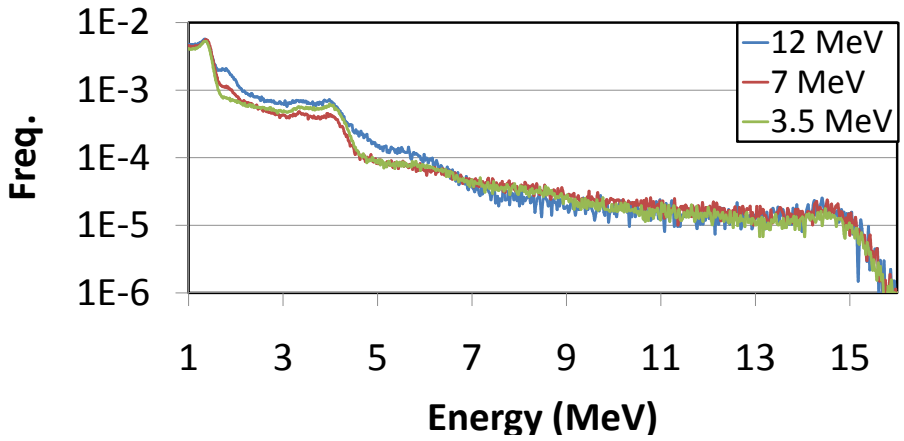

Figure 4.4: Pulse height spectra of gamma-rays acquired in the 2009 experiment at different deuteron energies. The area under each spectrum is normalized to 1.

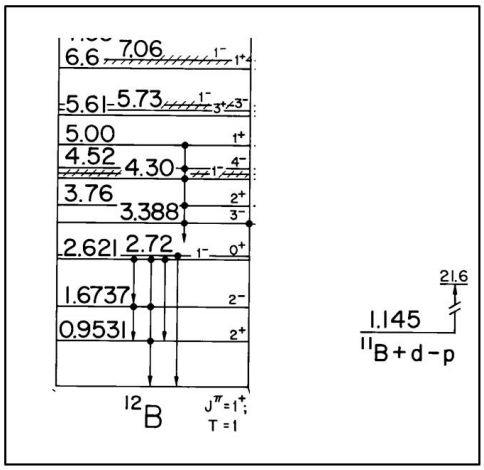

Figure 4.5: ^{12}B energy level diagram [184, 191]

Transition energy	$E_{compton}$	levels	branching ratio	reaction
0.72	0.53	1.67 → 0.95	3%	^{11}B(d,p)^{12}B
0.95	0.75	0.95 → 0	100%	^{11}B(d,p)^{12}B
0.95	0.75	2.62 → 1.67	14%	^{11}B(d,p)^{12}B
1.67	1.45	1.67 → 0	97%	^{11}B(d,p)^{12}B
1.67	1.45	2.62 → 0.95	80%	^{11}B(d,p)^{12}B
2.4	2.17	15.1 → 12.7	2.2%	^{11}B(d,n)^{12}C
2.62	2.39	2.62 → 0	6%	^{11}B(d,p)^{12}B
2.72	2.49	2.72 → 0	>85%	^{11}B(d,p)^{12}B
3.38	3.14	3.38 → 0		^{11}B(d,p)^{12}B
3.76	3.56	3.8 → 0		^{11}B(d,p)^{12}B
4.3	4.06	4.3 → 0		^{11}B(d,p)^{12}B
4.43	4.16	4.4 → 0		^{11}B(d,n)^{12}C
4.46	4.26			^{10}B
4.52	4.26	4.5 → 0		^{11}B(d,p)^{12}B
4.75	4.51			^{10}B
5	4.76	5 → 0		^{11}B(d,p)^{12}B
5.03	4.79			^{10}B
5.35	5.16			^{10}B
6.52	6.25			^{10}B
6.78	6.55			^{10}B
7.45	7.20	15.1 → 7.65	7.2%	^{11}B(d,n)^{12}C
7.29	7.05			^{10}B
8.27	8.05			^{10}B
8.87	8.65			^{10}B
10.7	10.45	15.1 → 4.4	2.3%	^{11}B(d,n)^{12}C
15.1	14.85	15.1 → 0	92%	^{11}B(d,n)^{12}C

Table 4.2: A summary of all the gamma-rays produced by the participating reactions [184, 190]. All energy values are in MeV. The $E_{compton}$ value is the energy at the centre of the Compton peak. For some levels there are some details missing - these are levels of different ^{10}B reactions that were measured by Sample [190] but without all the details.

4.4 Gamma-ray Yields

The extraction of gamma-ray yields is complicated by the nature of the Compton continuum and by overlap of the gamma-rays of interest (4.4 and 15.1 MeV) with other gamma-rays present in the spectrum.

The Compton spectrum of the 15.1 MeV gamma-rays has no interference with higher energies, but the Compton spectrum of the 4.4 MeV gamma-rays is masked by adjacent gamma-rays with higher and lower energies. Fortunately, our application permits some freedom concerning the gamma-ray energy: the difference between the attenuation coefficients of 4 and 5 MeV gamma-rays is less than 1%, 6% and 7% in Pb, Fe and C, respectively. Therefore, treating all the gamma-rays in the range of 4–5 MeV as 4.4 MeV gamma-rays (that constitute the majority) will result in a small error. However, in this analysis an effort was made to isolate the 4.4 MeV gamma-rays whereas in the final application, the amount of gamma-rays used may be slightly higher due to the contributions from adjacent gamma-rays.

To calculate the response of the detector to the different gamma-rays a detailed simulation of the cylindrical NE213 detector was performed using GEANT4 [192]. The simulated quantity is the energy deposited by the secondary electrons and positrons (not including the conversion into optical photons). The details of the detector can be seen in Fig. 4.6, showing the cross section of the simulated detector.

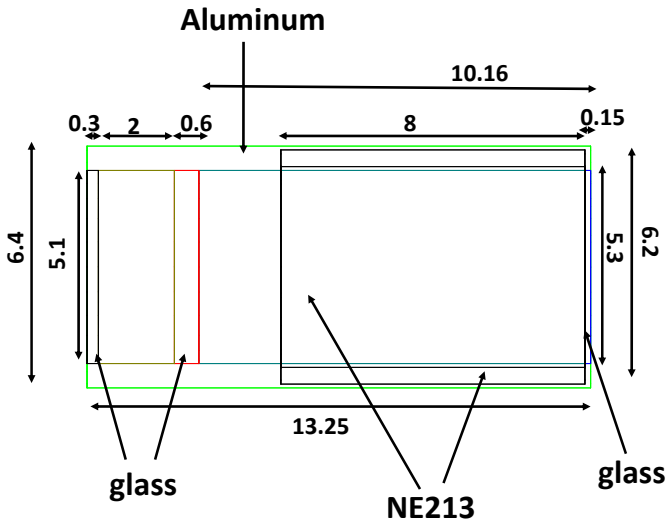

Figure 4.6: Cross section of the simulated cylindrical NE213 detector. Sizes are in cm.

The response of the detector to each discrete gamma-ray was simulated separately. Fig. 4.7 compares the response of the NE213 detector as measured with 7.0 MeV deuterons and the simulated response to 15.1 MeV gamma-rays. The single escape peak visible in the simulated spectrum is indistinct in the experimental spectrum due to effects of light creation and collection. Another effect of the light is that the experimental spectrum ends (at the high energies) with a Gaussian tail while the simulated spectrum ends abruptly at 15.1 MeV.

Since the lower energy Compton continuum of the 15.1 MeV distribution is overlapping with other gamma-rays, a comparison of the entire spectra was not possible. To compare the two spectra, we need to find a part of the spectrum that represents the same energy for both the simulated and experimental spectra. This was done by comparing only the part of the spectra that is free from the overlap with other gamma-rays. This part of the two spectra is marked in red in Fig. 4.7.

Several energy ranges were compared and the effect on the uncertainty of the yield was on average 1%. Finally, the region between 13 and 16 MeV was used.

The efficiency factor was calculated from the simulated spectrum by dividing the selected area by the area under the entire curve. This efficiency factor was used to calculate the number of 15.1 MeV gamma-rays per charge per solid angle unit, considering the dead time correction. The forward (0°) yields of 15.1 MeV gamma-rays are presented in Fig. 4.9 and Tables 4.3, 4.4.

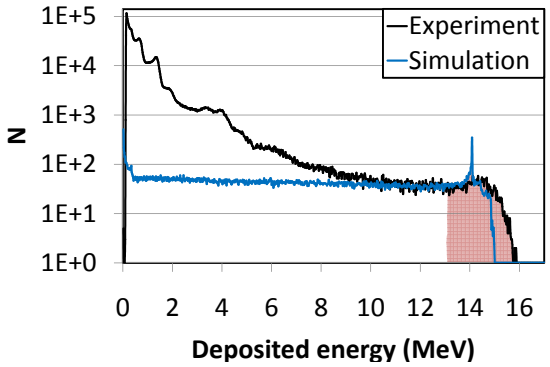

Figure 4.7: An experimentally measured gamma spectrum with 7 MeV deuterons and a simulated 15.1 MeV gamma-ray spectrum multiplied by a normalization factor. N is the number of gamma-ray counts. The area marked in red was used to compare the two spectra in the yield analysis.

A similar analysis was performed for the 4.4 MeV gamma-rays. However, the 4.4 MeV gamma-rays overlap with a step created by the Compton continuum of higher-energy gamma-rays. This step had to be subtracted in order to calculate the efficiency factor for 4.4 MeV gamma-rays. Again, a part of the spectrum that represents the same energy for both the simulated and experimental spectra was selected.

Fig. 4.8a presents the 4.4 MeV peak in the gamma spectrum (measured with 7.0 MeV deuterons) and the step due to higher energies, to be subtracted from the experimental spectra. The height of the step was chosen to be the experimental one, just above the 4.4 peak. The uncertainty on the gamma yields due to the choice of the step was evaluated to be ±15% by comparing several step choices.

The subtracted spectrum is presented in Fig. 4.8b along with the simulated 4.4 MeV gamma-ray spectrum. The part of the spectrum that was used for the yield calculation is marked in red. The selected region starts at the beginning of the peak below the 4.4 peak. It is a point easy to identify among the spectra of different energy calibrations, as is the case in the 2007 dataset where each measurement had to be calibrated separately. The selected region is therefore 3.1–4.5 MeV.

The measured and simulated spectra presented in Fig. 4.8b appear to be different. The reason is that the simulated spectrum includes only the effect of the energy deposited in the detector by gamma-rays via secondary charged particles, whereas the measured spectrum includes also the rest of the relevant physical and technical effects, such as light emission and collection and the electronic setup response. Nevertheless, the simulation of deposited energy is sufficient for the comparison to the measured results, as it is clear that the number of events in each peak are comparable, even though the resolutions are different.

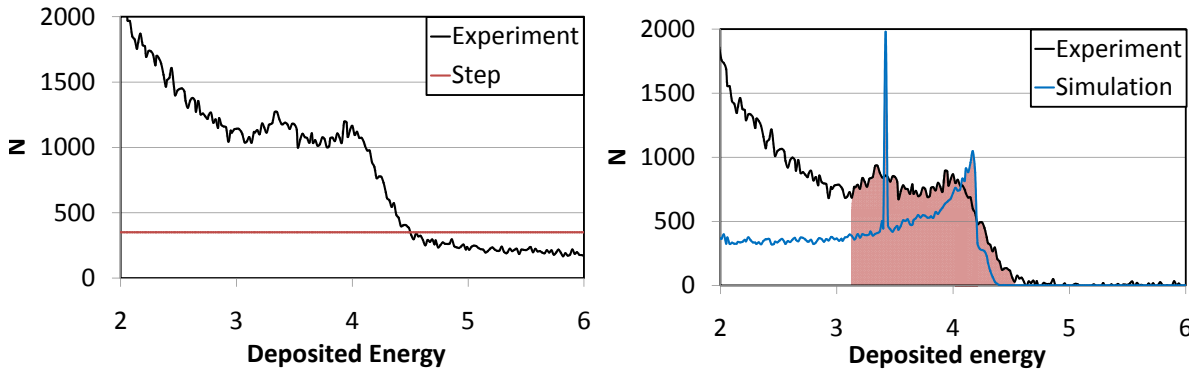

(a) 4.4 MeV spectrum and the linear fit to be subtracted.

(b) Exprimental spectrum after subtraction of higher energies, along with the simulated 4.4 MeV spectrum. The area marked in red was used to compare the two spectra in the yield analysis.

Figure 4.8: Spectrum of 4.4 MeV gamma rays created by 7.0 MeV deuterons. N is the number of gamma-ray counts.

The gamma-ray yields of 4.4 and 15.1 MeV gamma-rays as calculated from both the 2007 and 2009 datasets are presented in Tables 4.3, 4.4 and graphically in Fig. 4.9. The yields of both gamma-rays rise linearly with deuteron energy and the measurements of 2007 agree with the 2009 measurements.

For 4.4 MeV gamma-rays the statistical error is on average 1% of the yield, in addition to the 15% error caused by the subtraction of the step. The statistical error on the 15.1 MeV gamma-ray yields is up to 2% (there is no threshold selection in the 15.1 MeV gamma-ray calculation). The errors on deuteron energies (the X-axis of the graph presented in Fig. 4.9) are determined by the target as explained in the previous section.

A similar measurement made by Lanza et al. quotes 4.4 and 15.1 MeV gamma-rays yields an order of magnitude larger, measured with 3 MeV deuterons, but without describing target details such as isotopic fractions, density, diameter or thickness [179].

The gamma-ray yields define the required accelerator current that, for detection with DDEGR, is calculated in the next chapter.

		E_γ=4.4		**E_γ=15.1**	
d energy (MeV)	**±**	**N_γ/(sr mC)**	**±**	**N_γ/(sr mC)**	**±**
1.9	0.04	4.9×10^{9}	7.4×10^{8}	1.8×10^{8}	6.6×10^{6}
2.5	0.04	1.0×10^{10}	1.5×10^{9}	2.1×10^{9}	3.4×10^{7}
3.4	0.03	2.4×10^{10}	3.6×10^{9}	7.8×10^{9}	1.2×10^{8}
4.5	0.03	3.8×10^{10}	5.7×10^{9}	1.5×10^{10}	2.4×10^{8}
5.4	0.03	4.8×10^{10}	7.2×10^{9}	1.8×10^{10}	2.5×10^{8}
6.4	0.03	5.7×10^{10}	8.5×10^{9}	2.2×10^{10}	3.4×10^{8}

Table 4.3: Forward (0°) yields of 4.4 and 15.1 MeV gamma-rays as measured in 2007 at different deuteron bombarding energies.

		E_γ=4.4		E_γ=15.1	
d energy (MeV)	**±**	**N_γ/(sr mC)**	**±**	N_γ/(sr mC)	±
3	0.2	2.0×10^{10}	3.0×10^{9}	2.5×10^{9}	4.9×10^{7}
4.1	0.2	3.7×10^{10}	5.5×10^{9}	8.8×10^{9}	1.3×10^{8}
4.9	0.2	4.9×10^{10}	7.4×10^{9}	1.4×10^{10}	1.9×10^{8}
5.8	0.3	5.3×10^{10}	8.0×10^{9}	1.5×10^{10}	2.4×10^{8}
6.4	0.3	6.3×10^{10}	9.4×10^{9}	1.8×10^{10}	3.2×10^{8}
8.7	0.03	1.1×10^{11}	1.6×10^{10}	3.0×10^{10}	6.1×10^{8}
11.6	0.03	2.0×10^{11}	3.0×10^{10}	4.5×10^{10}	1.1×10^{9}

Table 4.4: Forward (0°) yields of 4.4 and 15.1 MeV gamma-rays as measured in 2009 at different deuteron bombarding energies.

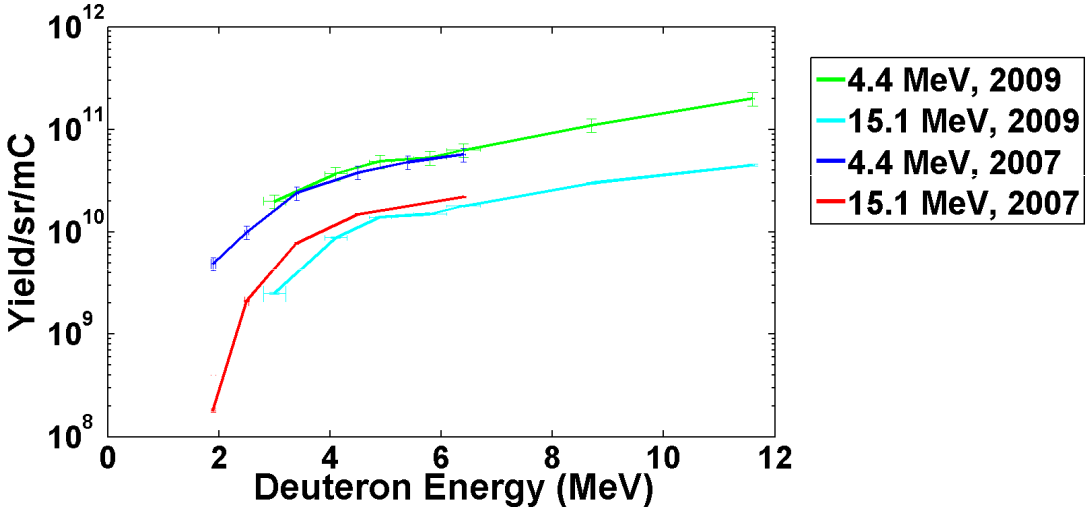

Figure 4.9: Comparison of the experimental forward (0°) yields of 4.4 and 15.1 MeV gamma-rays measured in 2007 and 2009.

4.5 Neutron Yields

To ensure that the 2007 and 2009 experiments are comparable, a measurement with identical deuteron energy – 7 MeV, was performed in both. The results are presented in Fig. 4.10, showing a reasonable agreement between the two experiments.

The main difference is the structure on the 2009 spectrum at energies below 4 MeV. This is the result of part of the beam missing the target and hitting the target surroundings.

The other difference between the two neutron yield curves is the slight difference in shape visible at the high energy peak. This is the result of the modified deuteron beam energy after traversing the MO foils and He. As explained in the previous sections, there is a 5% uncertainty for deuteron energies below 7 MeV in the 2009 experiment.

The neutron yield curves for selected deuteron bombarding energies between 3–12 MeV are presented in Fig. 4.11. The highest energy neutron groups leave ^{12}C in its ground state and first excited state at 4.43 MeV. Most of the continuum at energies < 7 MeV is due to neutrons leaving ^{12}C in higher excited states, along with deuterium breakup neutrons at energies below half the beam energy [193,194]. As deuteron energy increases, the spectral shape is qualitatively maintained, but all neutron groups progressively extend to higher energies.

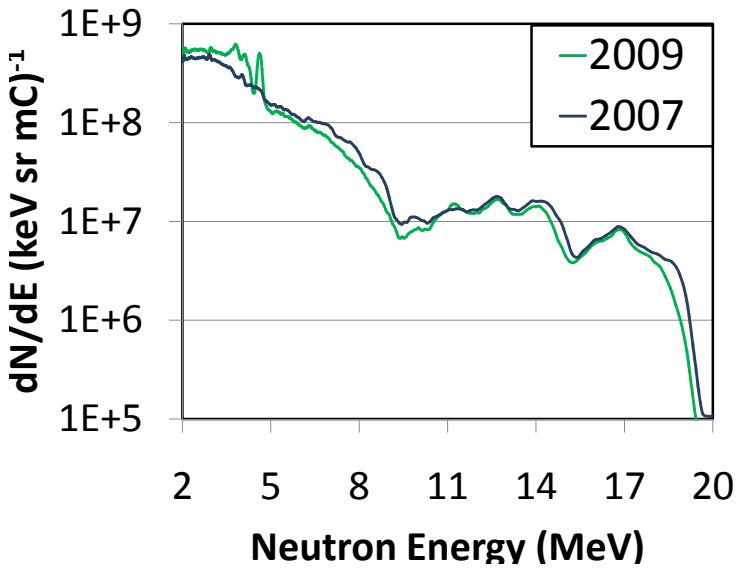

Figure 4.10: Comparison of neutron forward (0°) yields measured with a 7 MeV deuteron beam at the 2007 and 2009 experiments.

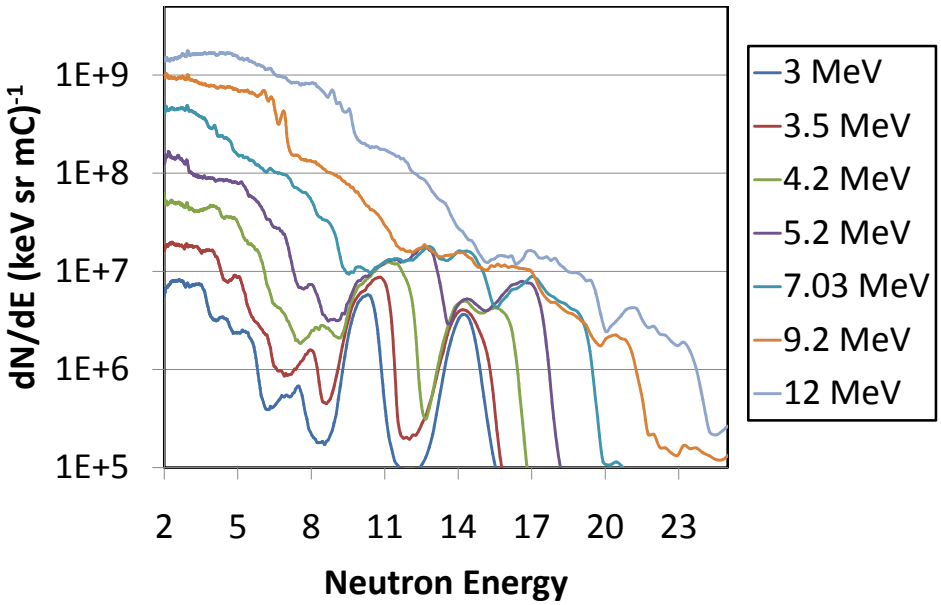

Figure 4.11: Neuron forward (0°) yields measured at different deuteron bombardment energies with a thick ^{11}B target and an NE213 detector. The deuteron energies in the legend are the on-target energies.

CHAPTER

5

SIMULATION OF THE SYSTEM

5.1 Simulation Details

The simulations were performed using the GEANT4 simulation toolkit, version 4.9.3, distributed by CERN [192,195]. For each primary gamma-ray event, the simulation tracks all the secondary, tertiary and further interactions, until all the energy dissipates into absorbing materials, or escapes the simulation "world". The simulations do not include many of the more complex phenomena involved in detection, such as light production in the scintillator, light collection in the detector, etc.

The prevailing physical processes in this energy range are the electromagnetic processes, namely pair production, Compton scattering and photoelectric absorption. Electron interactions in this simulation include ionization, multiple scattering and Bremsstrahlung. Positron processes include annihilation as well [49, 195].

The simulated geometry is assembled from three parts: the source area, the container and the detector. A rotated view of the assembled geometry with 100 gamma-rays emitted from the source is presented in Fig. 5.1 and a side view is presented in Fig. 5.2. In both images there are hidden inner features that will be described separately.

The point source emits 4.43 and 15.1 MeV gamma-rays at a ratio of 5:1 in favour of the former. The solid angle into which the source emits rays is adjusted to encompass the cargo container side. The point source is 20 cm away from a steel collimator, which has a 2 cm wide slit, allowing the relevant part of the beam through and stopping the rest. The entire source assembly is illustrated in Fig. 5.3.

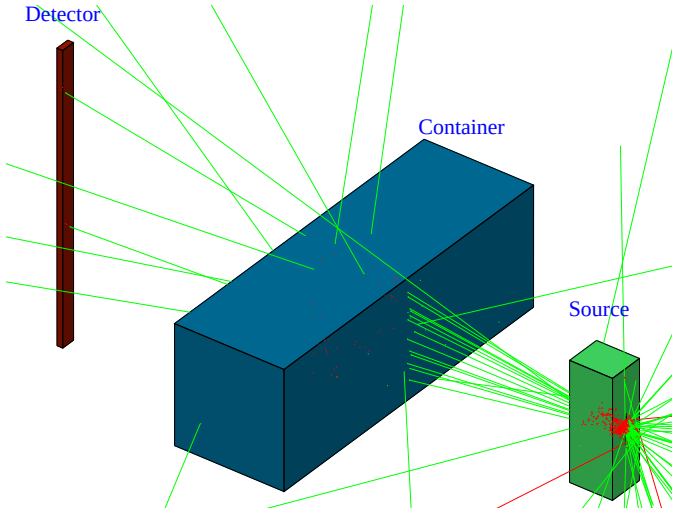

Figure 5.1: Illustration of simulation scenario to scale, rotated view, with 100 primary events. The red cuboid is the detector array, made of smaller LYSO detectors. The green lines are the gamma-rays coming from the source and the red lines are secondary electron tracks.

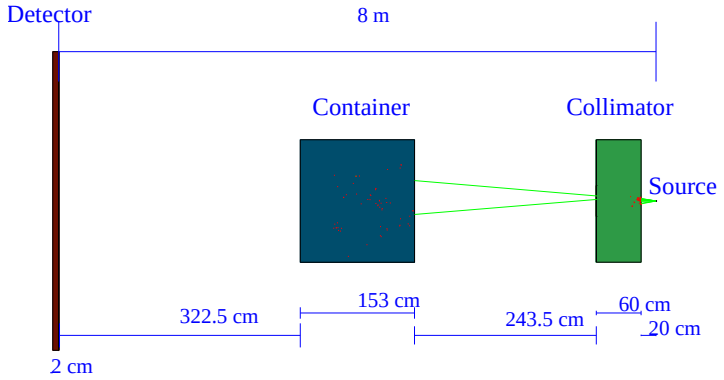

Figure 5.2: Illustration of simulation scenario to scale, side view, with dimensions and gamma-rays blocked by the container. The red rectangle is the detector array, made of smaller LYSO detectors. The green lines are the gamma-rays coming from the source.

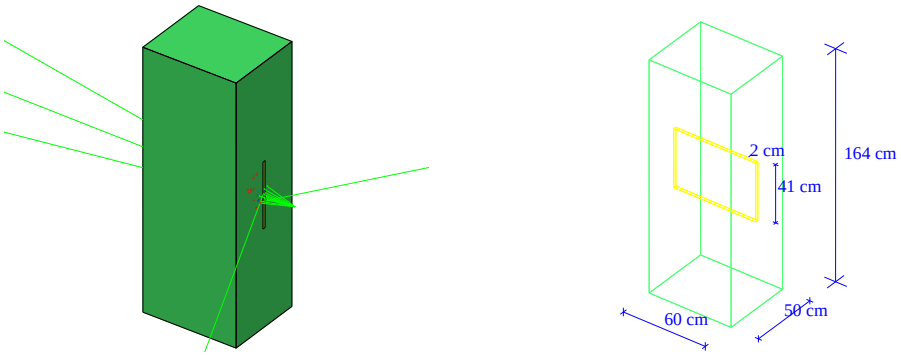

(a) Source emitting γ-rays in the collimator direction (10 γ-rays in this case).

(b) The collimator structure, showing the slit.

Figure 5.3: The simulated gamma-ray source.

The cargo container, illustrated in Fig 5.4, is a cuboid 463×164×153 cm^3 in size, the 153 cm side in the beam direction. In the majority of the simulations the container is filled with cotton that is composed of carbon, hydrogen and oxygen and has a density of 0.63 g/cm^3.

The objects to be detected are placed inside the container as demonstrated in Fig 5.4b. In these simulations we are trying to assess their effect on the transmitted signal. These objects are cuboids, their area in the direction perpendicular to the beam is 10×10 cm^2 and their thickness in the beam direction varies. The different sizes of each such cell is detailed in Fig. 5.4c. These "target" objects are made of a different material in each simulation.

The detector array is 20×400 cm^2 with 2 cm thickness and is positioned 8 meters away from the source. Each individual detector pixel face is 1×1 cm^2, enabling 1 cm^2 resolution. This resolution is consistent with the physical constraint determined by the electron tracks length, ∼0.8 cm for the 15.1 MeV electrons. The detector array is illustrated in Fig. 5.5, where the full array as well as a zoom-in image showing individual detectors are presented. The detectors are made of LYSO crystals with a density of 7.2 g/cm^3.

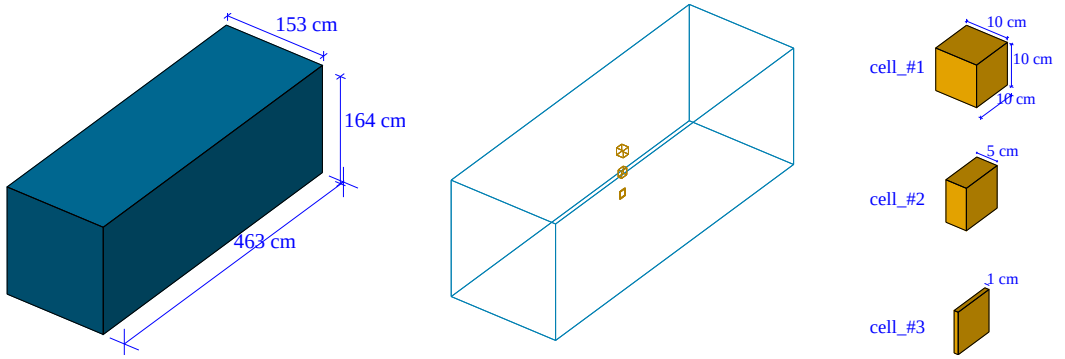

(a) The container. **(b)** The container structre, showing the objects hideen inside. **(c)** The objects.

Figure 5.4: The simulated container geometry.

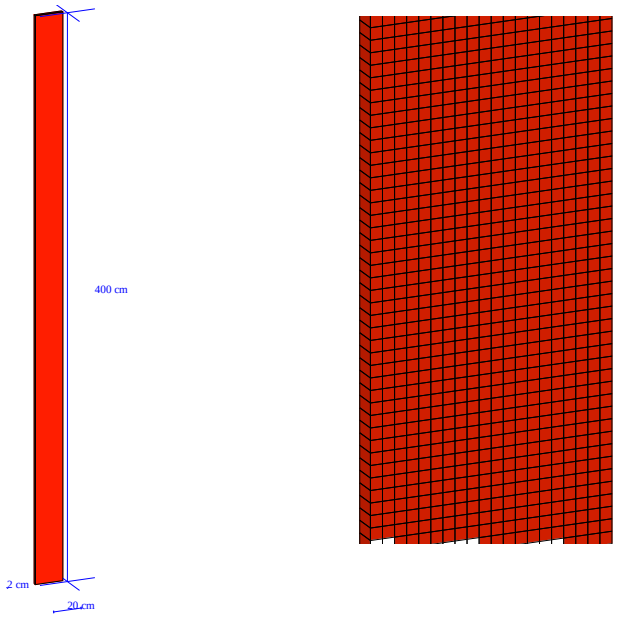

(a) The entire detector. **(b)** Zoom on the detector center.

Figure 5.5: The simulated detector. Each pixel is 1×1 cm^2 with 2 cm thickness.

To emulate a realistic analysis scenario, the deposited energy in each detector is analysed in a simplistic, practical way. Each detector was assigned 2 bins for the two discrete gamma-ray energies. The first bin contains all the events in which the gamma-ray, through secondary particles, deposited energy between 2 and 4.43 MeV, representing the response to 4.43 MeV gamma-rays. The second bin, representing the response to 15.1 MeV gamma-rays, contains all the events in which the deposited energy exceeded 6 MeV. In the analysis of the experimental spectra somewhat different energy bins were used – 3-5 and 8-15.5 MeV for 4.4 and 15.1 MeV gamma-rays, respectively. The different choice of bins was motivated by the different shape of the experimental spectrum and had a minor effect on the measured transmission.

In conclusion, the simulation described above includes the influence of many critical factors on the possibility to detect materials. These factors include the use of this source type with the two simultaneous gamma-rays, the detection technique of choice in this work, the detector response and the scattering from a full container.

5.2 Scattering From the Container

The first goal of the simulations is to estimate the effect of scattered gamma-rays from the cotton-filled container on the gamma-ray spectrum reaching the detector. These scattered gamma-rays may significantly influence the transmission spectrum and destroy, at least to a certain extent, the ability to detect high-Z materials with high contrast. In these simulations the spectra are of gamma-rays arriving at the detector, before interacting with the detector substance. The investigated pixel is a typical 1×1 cm^2 one at the centre of the array, seen in Fig. 5.2.

Three preliminary scenarios were simulated: source and detector, addition of collimator and addition of a cotton-filled container. In this simulation set the source is emitting one gamma energy at each simulation, either 4.4 or 15.1 MeV. The spectra reaching a typical detector pixel are presented in Fig. 5.6a and 5.6b for 4.4 and 15.1 MeV gamma-rays, respectively. The small peak evident in both spectra at 0.511 MeV is the result of annihilation gamma-rays.

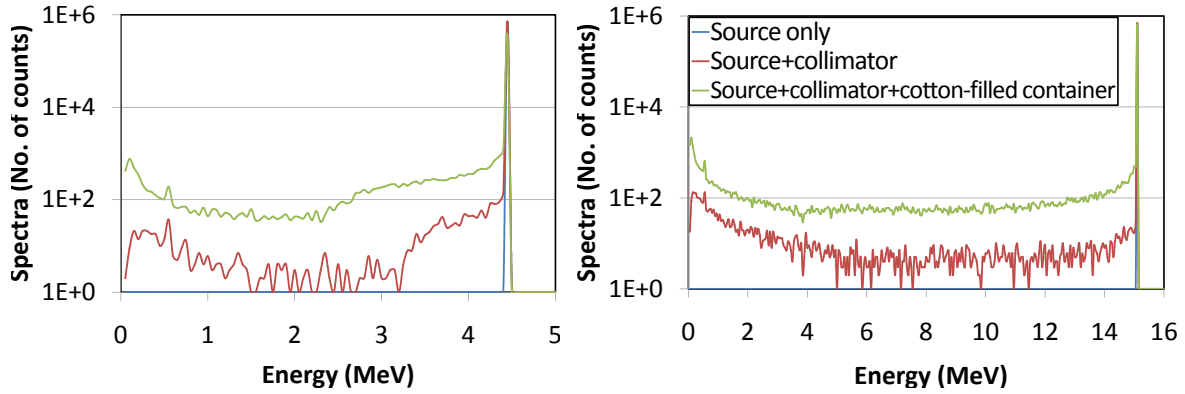

(a) 4.4 MeV gamma-rays. **(b)** 15.1 MeV gamma-rays.

Figure 5.6: Gamma-ray spectra at the detector for different scenarios with a joint legend, seen in (b). The number of primary gamma-rays is 10^9 for all the simulations.

The figure of merit here is the ratio between the scattered gamma-rays and the fraction of gamma-rays in the full-energy peak, which represent the gamma-rays that have not undergone any interaction on their path from the source to the detector. To be more exact, the ratio should be the division of area under the portion of the spectrum that falls within the detection energy bins – above 2 MeV for 4.4 MeV gamma-rays and above 6 MeV for 15.1 MeV gamma-rays (the

simulated energy bins) – by the area under the full energy peak. This ratio is presented in Table 5.1 for the different scenarios.

γ-ray energy	ratio scattered γ-rays/full-E		
	1: Source+detector	2: 1+collimator	3: 2+cotton-filled container
4 MeV	0	0.0019	0.049
15 MeV	0	0.0016	0.026

Table 5.1: Ratio between the fraction of scattered to full energy gamma-rays (above 2 and 6 MeV for 4.4 and 15.1 MeV gamma-rays, respectively) reaching the detector. The simulated statistics is no less than 10^4 events in each region, so the statistical errors are negligible.

The main cause of scattered particles is the cotton filled container that adds a significant 5% to the 4.4 MeV and 3% to the 15.1 MeV gamma-rays. The collimator contribution to the scattering is minor, less than 0.5% of the scattering.

The effect of scattering from the container was quantified by repeating the simulation with the source-detector distance constant and changing the position of the container relative to the detector. The ratio of the scattered gamma-rays/full-energy, presented in Fig. 5.7, drops as the container moves away from the detector as the scattered particles do not reach the detector. For a distance of 3 metres between the detector and the container less than 5% of the events in the detector are due to scattering.

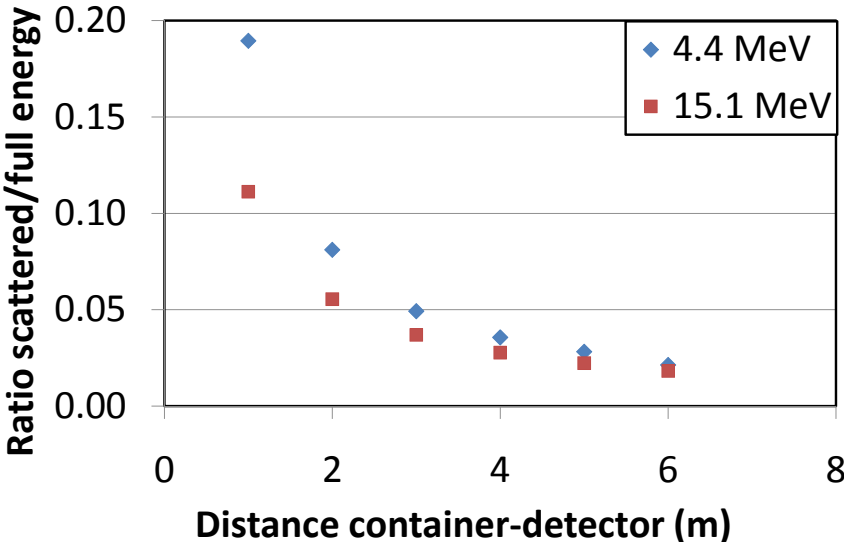

Figure 5.7: Simulated ratio of the scattered gamma-rays/full-Energy at varying distance between the container and the detector.

The detector signals due to 15.1 MeV gamma-rays interacting with the cotton-filled container are distributed from zero energy to the full 15.1 MeV (see Fig. 5.6b). Part of this distribution is below 4.4 MeV and may be mistakenly assumed to represent 4.4 MeV gamma-rays.

To evaluate this effect, the fraction of 15.1 MeV gamma-rays between 2 and 4.4 MeV was divided by the equivalent fraction from the 4.4 MeV spectra multiplied by five, the measured ratio of 4.4 MeV to 15.1 MeV gamma-ray yields in the ^{11}B(d,n+γ)^{12}C reaction. The results in Table 5.2 show that the contribution of scattered 15.1 MeV gamma-rays to the 4.4 MeV gamma-rays signal is insignificant over a wide range of distances between the detector and the

container.

Distance	1 m	2 m	3 m	4 m	5 m	6 m
Fraction	0.00064	0.00083	0.0010	0.0015	0.0028	0.0071

Table 5.2: The interference of the 15.1 MeV with the 4.4 MeV gamma spectrum, estimated by the fraction of 15.1 MeV gamma-ray signals between 2 and 4.4 MeV divided by the equivalent fraction from the 4.4 MeV source energy, multiplied by five, a typical ratio of 4.4 MeV to 15.1 MeV gamma-ray yields in the ^{11}B(d,n+γ)^{12}C reaction.

The transmission through the cotton-filled container is calculated by dividing relevant parts of the spectra from the scenario where the container is present by the same spectra parts from the no-container scenario (used as a "blank"). The theoretical transmissions, calculated from NIST attenuation coefficients [30], are 0.25 and 0.43 for 4.4 and 15.1 MeV gamma-rays, respectively.

The simulated transmission of 15.1 MeV gamma-rays is 0.43 without scattering in the container and 0.44 with scattering. The simulated transmission of 4.4 MeV gamma-rays is 0.25 without scattering in the container and 0.26 with scattering. These results support the viability of the proposed method of inspection, showing that the scattering is sufficiently low that it enables a measurement of the transmission.

5.3 Detector Response

To better understand the simulated results of the full detector array the response of an individual pixel to the incoming gamma-ray spectrum must be studied. The simulated detector response is the energy deposited in the pixel via secondary charged particles created by the primary gamma-rays. The simulated detector response is later used to study the transmission through a container at both gamma-ray energies, so the capability to separate the gamma energies is hereby examined.

The pixel response, presented in Fig. 5.8, shows the full-energy, first and second escape peaks, the result of pair production, on top of the Compton-induced continuum. At low energies the same pattern is observed for the 0.511 MeV annihilation gamma-rays interacting in the detector.

The deposited energy spectra have substantial addition in the Compton continuum area compared to the spectra of gamma-rays reaching the detector, shown in Fig. 5.6. The different shape of the spectra is the result of interaction in the detector, either gamma-rays that transferred only part of their energy to electrons (in a Compton scattering) or electron that left only part of their energy in the inspected pixel.

The number of counts in the areas out of the full energy peaks is larger by an order of magnitude than the number of counts inside the full energy peak – 10 times larger for 15.1 MeV gamma-rays in the container scenario. The detector response is the reason that in the transmission calculation we are using energy windows rather than the full energy peak.

The response of a typical pixel in the centre of the array (the geometry is shown in Fig. 5.2) to a source emitting both gamma-ray energies at a ratio of 5:1 in favour of 4.4 MeV, similar to the realistic yields of the ^{11}B(d,n)^{12}C reaction is presented in Fig. 5.9. The total number of gamma-rays in the scenario with the container is smaller, because many gamma-rays are attenuated in the container.

The calculated transmission through the container with the two-gamma spectrum and after introducing the detector response is 0.27 and 0.44 , compared to 0.24 and 0.43 calculated from

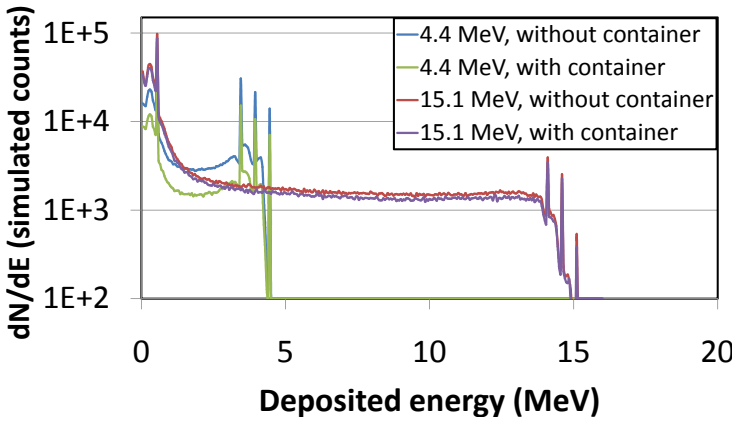

Figure 5.8: Simulated response of a typical individual pixel in the centre of the detector array for both gamma-ray energies and in simulation scenarios with and without the cotton-filled container.

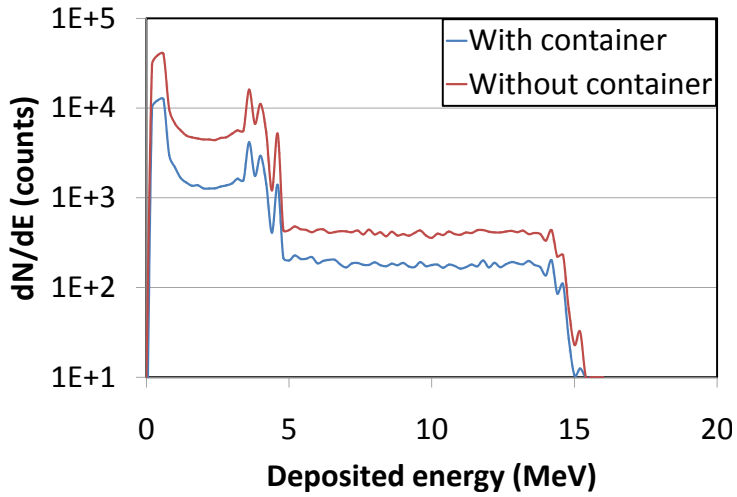

Figure 5.9: Simulated response of a typical pixel in the centre of the detector array with and without a cotton-filled container. The number of primary events in both simulations was 2×10^8.

cross sections, respectively. Comparing to the transmission as calculated for the spectra reaching the detector – 0.26 and 0.44 (see Section 5.2) we see that the detector response does not have a strong effect on the transmission.

5.4 Transmission Through Cargo

The transmission through a cotton-filled container was simulated for scenarios with different materials at varying thicknesses, using the scenario described in Fig. 5.2. To calculate the transmission through the different objects, the number of counts in each energy bin (3-5 and 8-15.5 for 4.4 and 15.1 MeV gamma-rays, respectively) with the object is divided by the counts in the same bins in a scenario without the container.

The total number of primary events (events from the source) in each simulation is 10^{10} and typical counts in an integrated detector area range from 10^6 when only cotton is present to 10^4 when thick high-Z samples cause strong attenuation. Six sample thicknesses were simulated (two simulation runs, three thicknesses in each) for each material: 1, 2, 5, 10, 50 and 100 mm.

The transmission profile - the response of the central line pixels in the array - of the detector array to a container filled with cotton and uranium cubes 1,2, and 5 mm thick inside is plotted

in Fig. 5.10. The transmission is the number of counts in an individual pixel of the detector in a scenario containing a cotton-filled container with target objects inside, divided by the number of counts in the same detector in an empty (no container) simulation scenario.

In Fig. 5.10 there are two transmission profiles that differ by their normalization process. The bottom line (in blue) is the transmission, where the signal of cotton+material (uranium 1,2, and 5 mm thick) was normalized by the signal of the no-container scenario. The top line (in red) is "cotton-normalized" transmission, meaning that the signal of cotton+material was normalized by the signal from the cotton filled container scenario. The cotton-normalized profile shows better contrast than the regular transmission.

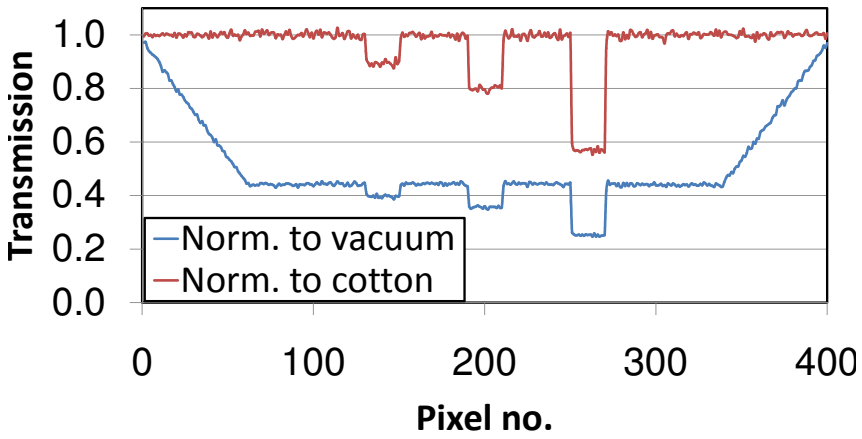

Figure 5.10: Profile of the detector array, showing regular transmission and cotton-normalized transmission

Comparison between simulated and calculated results is presented in Tables 5.3 and 5.4. To calculate the theoretical transmission from cross sections the effect of the cotton was added to the effect of the target objects. As predicted in the previous section, the detector response changes the transmission value somewhat. The errors on the simulated transmission are the statistical errors combined with the effect of the scattering. While the effect of the statistics depends on the object, the scattering adds a constant 8% and 2% to the transmission for 4.4 and 15.1 MeV gamma-rays, respectively.

For uranium and tungsten, 5 cm thickness is sufficient to diminish the signal, not leaving enough counts for a reliable analysis. However, since lead is still visible at 5 cm thickness, separation is possible. At 10 cm thickness the signal is undetectable for all high-Z materials and differentiation is not possible. In an inspection system, strong attenuation will guide the operators to open the inspected container.

When the signal is strongly attenuated (very thick objects in the beam path) the simulated transmission exceeds the calculated value. The effect is stronger at 15.1 MeV where there is up to three orders of magnitude difference between the simulated and calculated transmission. This is caused by scattered gamma-rays that have interacted with the cotton-only part of the container but have been deflected at small angles, hitting the pixels behind the threat objects and "posing" as photons transmitted by the threat.

	1 mm		2 mm		5 mm		10 mm		50 mm		100 mm	
	Calc.	**Simul.**	**Calc.**	**Simul.**	**Calc.**	**Simul.**	**Calc.**	**Simul.**	**Calc.**	**Simul.**	**Calc.**	**Simul.**
Cotton	0.24	0.27	0.24	0.27	0.24	0.27	0.24	0.27	0.24	0.27	0.24	0.27
Fe	0.24	0.26	0.23	0.26	0.22	0.24	0.19	0.21	0.07	0.09	0.02	0.03
Pb	0.23	0.26	0.22	0.25	0.19	0.21	0.15	0.17	0.02	0.03	0.002	0.01
W	0.23	0.25	0.21	0.23	0.17	0.18	0.11	0.12	0.005	0.01	0.0001	0.01
U	0.22	0.25	0.21	0.23	0.16	0.18	0.11	0.12	0.004	0.01	0.0001	0.01

Table 5.3: Transmission values of 4.4 MeV gamma-rays through a cotton-filled container with samples of different thicknesses inside. The simulated transmission is compared to transmission calculated from cross sections.

	1 mm		2 mm		5 mm		10 mm		50 mm		100 mm	
	Calc.	**Simul.**	**Calc.**	**Simul.**	**Calc.**	**Simul.**	**Calc.**	**Simul.**	**Calc.**	**Simul.**	**Calc.**	**Simul.**
Cotton	0.43	0.44	0.43	0.45	0.43	0.44	0.43	0.44	0.43	0.45	0.43	0.44
Fe	0.42	0.43	0.41	0.42	0.38	0.39	0.34	0.35	0.13	0.14	0.04	0.05
Pb	0.40	0.41	0.38	0.39	0.31	0.32	0.23	0.23	0.02	0.03	0.001	0.01
W	0.39	0.40	0.35	0.36	0.26	0.27	0.15	0.16	0.002	0.01	0.00001	0.01
U	0.39	0.39	0.34	0.36	0.25	0.25	0.14	0.15	0.002	0.01	0.00001	0.01

Table 5.4: Transmission values of 15.1 MeV gamma-rays through a cotton-filled container with samples of different thicknesses inside. The simulated transmission is compared to transmission calculated from cross sections.

5.5 Discussion

Summarizing this chapter, simulations of the inspection system were conducted to evaluate its capability to operate in a realistic scenario. The simulations lead to the following conclusions:

Scattering The scattering from a full cargo container may introduce a significant background and dictate a large system size. The simulations show that 3-4 meters between the source and detector are enough to reduce the scattering to less than 5%.

Detector Response The response of a single detector pixel changes the spectrum reaching the detector, but does not have an effect on the simulated transmission.

Transmission Through Cargo The summed effect of these phenomena on the transmission was simulated. The simulations show that the transmission is close to its theoretical value and support the viability of DDEGR for variety of objects.

For high-Z objects thicker than 10 cm, the scattering has a stronger effect than the transmitted signal, and separating benign high-Z materials from SNM will not be possible using DDEGR. However, areas in the radiographic image with very strong attenuation should alert the operator that a high-Z object is present and guide her to open the container.

CHAPTER

6

DETECTION PARAMETERS

6.1 Basics of Materials Separation

Most X-ray inspection techniques of cargo and vehicles are based on Digital Radiography (DR) and its modern version, dual-energy radiography (DER), which acquires two separate images at two different photon energies. Another recent approach is to apply Computed Tomography (CT) to inspect large objects, such as aviation containers.

DR is most widely used, due to its simplicity and high throughput, but its images are cluttered with overlapping objects. CT on the other hand, can provide a cross sectional view of the inspected object, so that each part is separated from the other at a cost to the throughput capacity.

Distinguishing SNM from benign materials by radiographic methods requires detectable Z-dependent features. The strongest Z-dependence of the attenuation is at low energies (less than 150 keV), where the photo-electric effect is the prevailing attenuation mechanism. However, penetrating a massive object such as a loaded cargo container requires photons at higher energies of several MeV, where the Z-dependence is less favourable (Z/A for Compton scattering and Z^2/A for pair production).

Fig. 6.1 displays the energy dependence of the mass attenuation coefficient (denoted μ) of several materials. The mass attenuation coefficient of the materials is similar at energies between 2 and 4 MeV. The mass attenuation coefficient becomes different at higher energies, where the pair production mechanism dominates. DER compares the attenuation at different photon energies to determine the atomic number of the inspected object (specific examples were presented in Section 2.2.2.)

However, as seen in Fig. 6.1, the separation between SNM and benign high-Z materials, such as lead that is a common shielding material, is difficult. The ratio between the mass attenuation coefficients of U, W and Pb at 15 MeV is 1:0.91:0.96.

A significantly better separation between SNM and benign high-Z materials can be obtained by determining the macroscopic attenuation coefficient, also denoted the linear attenuation coefficient or $\mu\rho$ (ρ is the density). Fig. 6.2 shows the macroscopic attenuation coefficient of

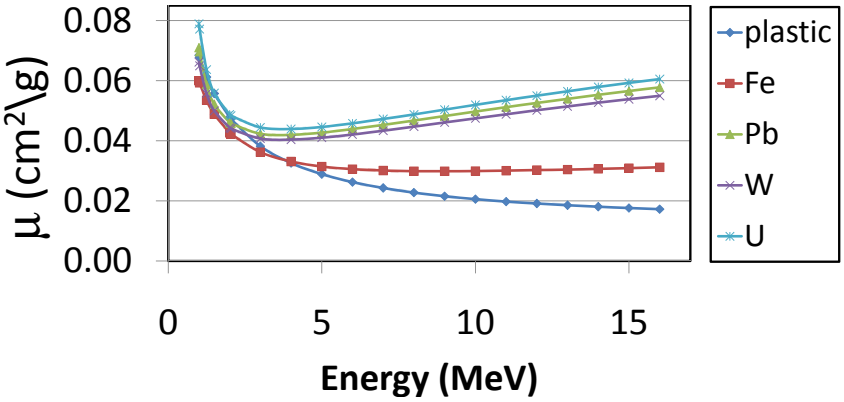

Figure 6.1: Mass attenuation coefficients vs photon energy for different materials.

several materials in the photon energy between 1 and 16 MeV. The ratio between the macroscopic attenuation coefficients of U, W and Pb at 15 MeV is 1:0.93:0.57, enabling better separation.

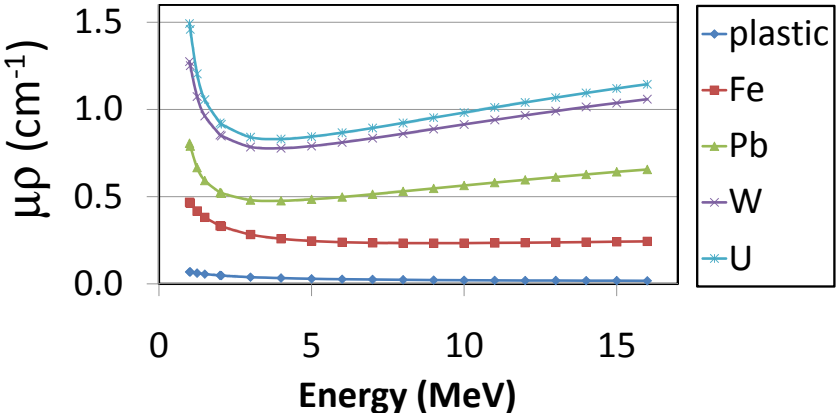

Figure 6.2: Macroscopic attenuation coefficients vs photon energy for different materials.

CT enables determination of the macroscopic attenuation coefficient in every voxel of the inspected object. Indeed, this approach is already routinely employed in inspection of checked passenger baggage in most airports [33]. Recently, high energy, few-view tomography systems for aviation containers have been developed and tested [43,44,196,197]. Other groups attempted to obtain the 3D information by using few-view stereoscopic reconstruction [198–204].

A drawback of CT systems based on one photon energy is their high false alarm rate. To reduce it, two photon energies are used in Dual Energy CT (DECT) techniques, proposed as an explosives detection technique [205]. In addition to density measurements, DECT enables determination of the atomic number of the materials in the inspected object.

6.1.1 DER Materials Separation

Dual-energy photon radiography acquires separate measurements using two different photon energies. A composite image can then be constructed from the ratio of the two images.

For two mono-energetic photon beams denoted by H (high energy) and L (low energy) traversing a single material, the transmission is the ratio of transmitted to incident beam intensity:

$$T_L = \frac{I_L}{I_{L,0}} = e^{-\mu_L \rho t}$$
$$T_H = \frac{I_H}{I_{H,0}} = e^{-\mu_H \rho t} \tag{6.1}$$

where $I_{L,H}$ are the intensities of the signal attenuated by the object, $I_{L,H,0}$ are the intensities of the incident signal, μ is the object mass attenuation coefficient, ρ is the density and t is the object thickness.
By taking the ratio of the natural logarithms of T_L and T_H we obtain R, which is independent of object density and thickness:

$$R = \frac{ln\, T_H}{ln\, T_L} = \frac{\mu_H}{\mu_L} \tag{6.2}$$

In most cases, high-energy Bremsstrahlung sources using electron accelerators with accelerating voltages up to 9 MV are used. These produce broad spectrum radiation with energies up to the accelerating potential. For broad-spectrum radiation produced by such a source, the transmission needs to be replaced with a more complicated expression [2]:

$$T_i = \frac{I_i}{I_{0,i}} = \frac{\int_0^{E_{max}} \Phi(E) e^{-\mu_i(E)\rho t} r(E) dE}{\int_0^{E_{max}} \Phi(E) r(E) dE} \qquad (i = 1, 2) \tag{6.3}$$

where the integrals extend over all radiation energies produced by the source, i values are H or L, $\Phi(E)$ is the energy spectrum of X-ray emitted by the source and $r(E)$ is the relative detector response as a function of X-ray energy.

Because X-ray mass-attenuation coefficients vary strongly with energy, the attenuation of broad-spectrum radiation is no longer strictly exponential and the simple solution for R given in Eq. 6.2 does not strictly apply. However, using the average photon energies of Bremsstrahlung spectra provides a good approximation of the exact attenuation calculation.

Fig. 6.3 shows the calculated R as a function of the atomic number Z for several materials at two pairs of energies: 1.5/3.0 MeV and 4.4/15.1 MeV. The 1.5/3.0 MeV pair corresponds to average photon energies of Bremsstrahlung spectra obtained with 5 and 9 MeV electrons.

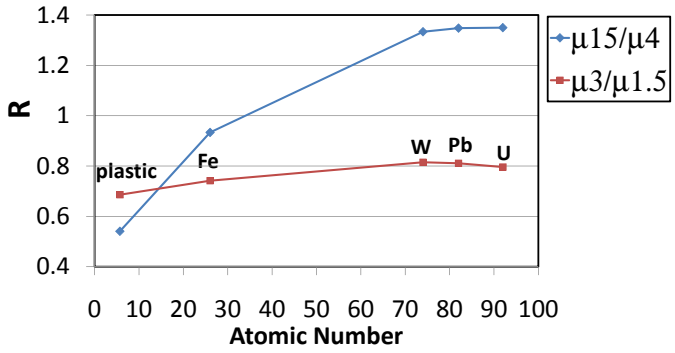

Figure 6.3: Calculated R as a function of the atomic number Z for several materials at two pairs of energies: 1.5/3 MeV and 4.4/15.1 MeV.

The 4.4/15.1 MeV pair is visibly advantageous to the 1.5/3.0 MeV pair. However, SNM remains inseparable from benign high-Z materials such as lead or tungsten.

Material separation based on R is valid only in the case when the traversed object consists of

a single material. Regions of scan images with just one material in view are rare in the typical cluttered air cargo container images.

If two (or more) materials "a" and "b" are traversed by the two beams, we obtain:

$$\begin{aligned} -ln\ T_L &= \mu_{a,L}\rho_a t_a + \mu_{b,L}\rho_b t_b \\ -ln\ T_H &= \mu_{a,H}\rho_a t_a + \mu_{b,H}\rho_b t_b \end{aligned} \tag{6.4}$$

Here the division of the logarithms does not cancel the dependence on constituent densities and thicknesses.

Several investigators attempted to solve this problem by assuming that the nature of the materials is known, as is the case in medical imaging, where soft tissue and bone are imaged [206,207]. This method, called Dual Energy Subtraction (DES) imaging can be used to suppress the clutter and to enhance the contrast of the feature of interest. For example, different pairs of threat and clutter materials can be tried in a sequential manner and then the pair that suppresses the background in the most optimal way can be determined.

By selecting the threat and clutter mass attenuation coefficients for the two energies and using their ratio as weighting factors one can in principle remove from the image either the clutter (a) or the threat material (b).

$$\begin{aligned} \frac{\mu_{a,L}}{\mu_{a,H}}\ ln\ T_H - ln\ T_L &= \rho_b t_b \left(\mu_{b,L} - \mu_{b,H}\frac{\mu_{a,L}}{\mu_{a,H}}\right) \\ \frac{\mu_{b,L}}{\mu_{b,H}}\ ln\ T_H - ln\ T_L &= \rho_a t_a \left(\mu_{a,L} - \mu_{a,H}\frac{\mu_{b,L}}{\mu_{b,H}}\right) \end{aligned} \tag{6.5}$$

Each image calculated from the left hand part of the equation is now dependent on the areal density of a single component.

In spite of the above problems Bentley reported [23] an attempt to use the simplistic single material approach for a detection of a test object consisting of a 100 cm^3 uranium sphere in a lead lined steel box positioned in a fully loaded marine container using 6 and 9 MV cargo inspection system. Using the R map, the test object was easily discernible even when hidden in a highly cluttered machine parts environment. However, judging from the colour coded images presented in the paper, the value of R in the uranium sphere is not distinguishable from that of the lead lined steel box.

6.1.2 DECT Materials Separation

As described earlier, Computed Tomography (CT) basically measures the distribution of the macroscopic attenuation coefficient ($\mu\rho$, in units of cm^{-1}) within the scanned object. Fig. 6.4 shows a plot of the macroscopic attenuation coefficient as a function of the atomic number for two discrete photon energies – 4.43 and 15.1 MeV.

In terms of SNM discrimination from benign materials there is not much difference between the two energies.

The higher energy gamma-rays, 15.1 MeV have a better penetration in typical aviation cargo composed of plastics, aluminium and steel. However, 15.1 MeV gamma-rays are scarce in comparison to the 4.4 MeV gamma rays emitted in the $^{11}B(d,\gamma+n)$ reaction. The measurement times will therefore be shorter with 4.4 MeV gamma-rays, which will also enable a better spatial

resolution.

For each photon energy a threshold can be set such that all low- and medium-Z as well as some of the benign high-Z materials are below the threshold. An image consisting of values above the discrimination threshold will be significantly less cluttered, leaving in only objects composed of SNM and few other materials, such as tungsten, platinum and gold.

The non-SNM materials above the discrimination level are high density rare-earth metals that are of interest to customs in border crossing points, and as such, their detection may be an advantage. The discrimination threshold is 1 cm^{-1} for 15.1 MeV gamma-rays and 0.7 for 4.4 MeV gamma-rays.

A complete separation of SNM from benign high-Z materials can be accomplished by determining material density and atomic number in each voxel of the CT image. This data can be deduced in DECT by decomposing the macroscopic attenuation coefficient into its Compton and pair-production components.

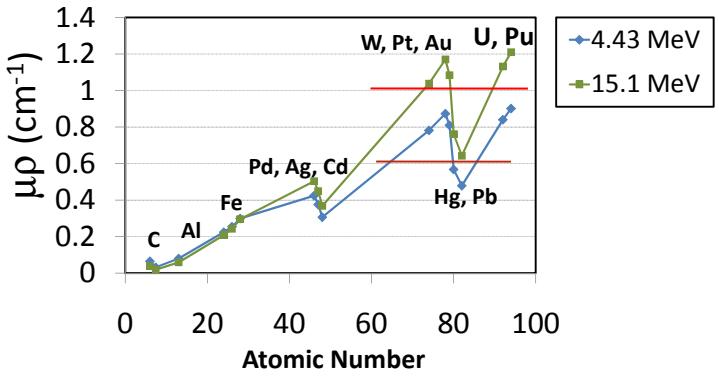

Figure 6.4: Macroscopic attenuation coefficient as a function of the atomic number for two discrete photon energies – 4.43 and 15.1 MeV. The two red horizontal lines are the discrimination levels for 15.1 and 4.4 MeV gamma-rays.

A Dual high-energy CT system using 3 and 6 MV Bremsstrahlung spectra has been described recently by Xing and Duan et al. [43]. They adapted the basis decomposition method developed for medical purposes using dual low-energy X-rays [208].

This method relies on decomposition of the macroscopic attenuation coefficient into its components, in the high energy case Compton and pair production. The decomposition of the CT data enables reconstruction of CT images by density and by atomic number. In their conclusions Xing and Duan et al claim that ignoring the photoelectric effect in their reconstruction introduced large errors for high-Z materials while the low- and medium-Z materials results were satisfactory.

The high-Z error is clearly the result of the incident Bremsstrahlung spectra containing large proportion of photons at low energies (below 1 MeV). In this energy range the photoelectric effect is negligible for low- and medium-Z materials while remaining significant in high-Z substances. Other factors in their work created limited performance, such as uncertainty in electron energy and high-energy accelerator instability. In our approach these issues are avoided and material separation is further enhanced by using two discrete-high energy gamma-rays.

The method described below is based, with some changes, on previous work [43,52,209,210].

The macroscopic attenuation coefficient (cm^{-1}) of a material can be expressed as:

$$\mu(E)\rho = \frac{\sigma(E)\rho N_A}{A} \tag{6.6}$$

where $\sigma(E)$ is the total cross-section of the material (in units of cm^2) at energy E, N_A is Avogadro number and ρ and A are the density and the atomic weight of the material, respectively. At photon energies above 3 MeV, the total cross section is a sum of Compton and the pair-production cross sections, which are proportional to Z and Z^2, respectively.

$$\sigma(E) = a(E)Z + b(E)Z^2 \tag{6.7}$$

The coefficients $a(E)$ and $b(E)$ depend only on the photon energy E and are not dependent on the nature of material. The total macroscopic attenuation coefficient for two different energies can now be written as:

$$\begin{aligned} \mu(E_1)\rho &= [a(E_1) + b(E_1)Z]\left(\frac{Z}{A}\right)\rho N_A \\ \mu(E_2)\rho &= [a(E_2) + b(E_2)Z]\left(\frac{Z}{A}\right)\rho N_A \end{aligned} \tag{6.8}$$

The values of $a(E_1)$, $b(E_1)$, $a(E_2)$ and $b(E_2)$ can be determined by the least-squares method using theoretical or measured macroscopic attenuation coefficients of the two gamma-ray energies for several known materials. Once these coefficients are determined, the unknown Z value of a material can be calculated using the macroscopic attenuation coefficient values obtained from CT. By back-substituting the Z values into the above equations and assuming the Z/A value to be approximately constant, the density of the material can be determined. A map of density vs Z can determine the nature of a material unambiguously.

6.2 Statistical Considerations

The flux of gamma-rays required for a reliable detection of SNM in an aviation container can be calculated for a given configuration. The flux differs between DER and DECT, requiring two different calculations.

Our goal is to detect small amounts of SNM in cargo, ~250 g in a realistic scenario: High Enrichment Uranium (HEU) emits a large number of 186 keV gamma-rays, therefore it is assumed that it will be surrounded by some shielding material such as lead or steel. Another possibility is that it will be hidden within steel machinery of significant thickness. Therefore, the scenario used for calculation includes a cubic HEU block, 2.4×2.4×2.4 cm^3, hidden inside a 5 cm thick steel box covered with a 5 mm thick lead layer. The cross section of this scenario is sketched in Fig. 6.5.

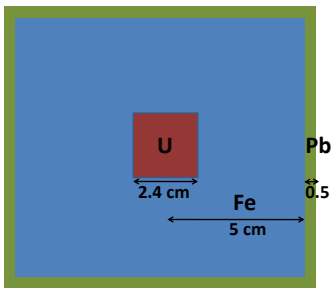

Figure 6.5: Cross section of the scenario used in calculations of material separation.

6.2.1 DER Inspection Configuration

Table 6.1 presents the transmission value for both gamma-ray energies at two different detection configurations - a box with and without uranium inside.

Gamma-ray energy	Steel box configuration	Steel box+U configuration
4.4 MeV	$T_{1,L}$=0.18	$T_{2,L}$=0.043
15.1 MeV	$T_{1,H}$=0.16	$T_{2,H}$=0.019

Table 6.1: Calculated transmission of the two gamma-rays through two configurations: box and box+U

The detection efficiencies for a 2 cm LYSO detector are ϵ_4=0.41 and ϵ_{15}=0.47 for the 4.4 MeV and 15.1 MeV gamma-rays, respectively, and the ratio of gamma-ray production yields is 1:0.2 in favour of the 4.4 MeV gamma-rays.

If the number of incident 4.4 MeV gamma-rays is N_0, the number of detected events in the detector is $N_0\epsilon_4$ outside the object and $N_0\epsilon_4 T_{1,L}$ and $N_0\epsilon_4 T_{2,L}$ in the steel box region and box+HEU, respectively. A similar expression applies for the 15.1 MeV gamma-rays.

In DER the signal is given by Eq. 6.2. By substituting all the numerical values and propagating the errors, values for R and its standard deviation in the two configurations are obtained and presented in Table 6.2.

Determined value	Steel box/lead	Steel box/lead +U
R	1.08	1.27
σ	$3.39/\sqrt{N_0}$	$4.61/\sqrt{N_0}$

Table 6.2: R and its standard deviation in the two configurations.

R in the area of the box where no uranium is present is lower than R in the region of the uranium. However, the fact that a mixture of materials is present in the traversed beam causes the calculated R to be different than that of the pure materials (shown in Fig. 6.3).

To estimate the number of incident 4.4 MeV gamma-rays (N_0) needed for a reliable separation of the lead lined steel box from the uranium, we require Detection Probability (DP) of 99.9% and False Alarm (FA) probability of 0.1%. Therefore, the threshold is positioned 3 standard deviations (3σ) above the steel/lead R and 3σ below R value of uranium.

This leads to the equation:

$$R_{steel/lead} + 3\sigma_{steel/lead} = R_{steel/lead+U} - 3\sigma_{steel/lead+U} \tag{6.9}$$

Substituting the values from Table 6.2 and solving for N_0, the number of 4.4 MeV gamma-rays required for a reliable detection is $N_0=1.7\times10^4$. Considering the effect of scattering, which was assessed to be 5% for a typical scenario by the simulations presented in Section 5.5, adds a negligible number of photons.

Positioning the container (with the object) mid-way between the radiation source and the detector will cause an image magnification of 2. The attenuation corresponding to uranium will take place in all pixels within a 4.8×4.8 cm^2 spot occupied by uranium. The required number of incident 4.43 MeV gamma-rays per cm^2 in the detector (photon fluence) is 740 ph/cm^2. Inspection of the container includes 3-4 views (with 3-4 detector arrays), reducing the fluence to

about 250 ph/cm^2. Scanning a 200 cm long container in 60 s divided into 20 steps (3 s/position) requires a photon flux of about 83 ph/cm^2/s.

Results from our measurements, reported in Chapter 4, indicate that the yield of the 4.43 MeV gamma-rays is about 1×10^{10} photons/str/mC. A solid angle viewed by a 10×10 cm^2 detector positioned at 800 cm from the source will be 1.56×10^{-4} str so the photon intensity on the 10×10 cm^2 detector will be 1.56×10^{6} ph/mC or a flux of 1.56×10^{4} ph/s/cm^2/mA. Thus, the required deuteron current on the target is only 5.3 μA.

It must be stressed that this is an average deuteron current of a pulsed beam. Using a beam pulsing regime of 1.5 ns burst with 500 ns period, the duty factor is only 0.3%. The ion source current must be in the range of 1.8 mA. Using a shorter period or measuring several events per each pulse may reduce this current by a factor of 2-5. Therefore, material separation using DER is feasible with deuteron energies of 4 MeV and higher (see Fig. 4.9). Longer measurements will permit using lower deuteron currents.

6.2.2 DECT Inspection Configuration

In DECT the macroscopic attenuation coefficient $\mu\rho$ is determined in every pixel of an examined CT slice. The precision of the reconstructed value depends on several factors: the chosen algorithm, r- the required spatial resolution, d- the slice thickness, N- the number of transmitted detected events in a projection and M- the number of projections. The expression for the standard deviation is [211]:

$$\sigma^2 \propto \frac{1}{r^3 dNM} \tag{6.10}$$

Statistical properties in computed tomography have been investigated by several groups [212–214].

Using a reconstruction approach based on Gore and Tofts [213] we assume a parallel photon beam and a reconstruction algorithm that employs convolution filtering of the projections, followed by back projections into a reconstructed image. The variance of the reconstructed macroscopic attenuation coefficient in this approach is:

$$\sigma^2 = \frac{\pi^2}{12a^2NM} \tag{6.11}$$

where a is a sampling interval of the projection (detector spacing) and N, M are defined above. Table 6.3 shows the expected macroscopic attenuation coefficients and the standard deviation of the reconstructed value based on 6 views and 0.5 cm detector spacing.

Determined value	**Steel**	**Lead**	**Uranium**
$\mu\rho_{4.4\ \mathrm{MeV}}$	0.25	0.47	0.83
$\sigma(\mathrm{cm}^{-1})$	$4.05/\sqrt{N_0}$	$4.05/\sqrt{N_0}$	$4.05/\sqrt{N_0}$

Table 6.3: The expected macroscopic attenuation coefficients and the standard deviation of the reconstructed value based on 6 views and 0.5 cm detector spacing

Substituting the values from Table 6.3 and solving for N_0 a similar equation to 6.9, the number of 4.4 MeV gamma-rays required for a reliable differentiation of uranium is 3240 and 8500 for iron and lead, respectively. As in the DER calculations, the uranium will occupy a 4.8×4.8 cm^2 spot on the projection image and the required fluence of 4.43 MeV gamma-rays is

140 ph/cm^2.

Following the procedure of Duan et al, the container is first scanned vertically [44], which is repeated for several views. For a 60 seconds inspection time per container and 6 views, the time per vertical scan should be 10 seconds. An array with a 10 cm width (divided into 0.5×0.5 cm^2 pixels), will result in 15 slices for a container of 150 cm height and 0.7 seconds per slice. The required 4.43 MeV gamma-rays flux is therefore 211 ph/s/cm^2, and the deuteron current 13.5 μA.

This is the average deuteron current of a pulsed beam, similarly to the DER case. Under the same conditions (1.5 ns burst with 500 ns period), the ion source current must be in the range of 4.5 mA when using a current of deuterons with energy of 4 MeV or higher (see Fig. 4.9).

The requirements enabling reliable material differentiation with DDEGR are fulfilled by the ^{11}B(d,n+γ) nuclear-reaction source, as calculated here and measured experimentally (see Chapter 4).

Part III

TRECOR Detector

CHAPTER

7

TRECOR DESCRIPTION

7.1 Preamble

TRECOR stands for Time Resolved Event Counting Optical Radiation detector. It uses event-by-event counting, measuring relevant quantities (position, timing and pulse height) for each particle interacting with the scintillator converter.

There are two generations of TRECOR, TRECOR-I and TRECOR-II. The concept of both generations is very similar, differing only by the scintillator screen (the converter of particle energy into light) and the readout electronics.
TRECOR-I is a flexible gamma-ray/neutrons detector, sensitive only to one particle type at a time. It is suitable for a DDEGR detection system.
TRECOR-II detects both particle types simultaneously, making it suitable for the combined explosive/SNM detection system.

This chapter will start with a description of the concept of each generation and continue with detailed description of the different components.

7.2 Concept

7.2.1 TRECOR-I

The TRECOR detector is based on a time resolved event-by-event counting optical technique. TOF serves to separate the gamma-rays from the neutrons emitted in the same nuclear reaction (and to determine neutrons energies when relevant). The first-generation TRECOR concept, TRECOR-I, is sketched in Fig. 7.1 and images are presented in Figs. 7.2 and 7.3.
It is based on a scintillator converter (#1 in Fig. 7.2) that transforms the incoming particle energy into light. The converter is a high-Z scintillator block, which is a good gamma-converter and interacts weakly with neutrons. The light is emitted isotropically and is read simultaneously from the scintillator side and front. The scintillator side (the part of the scintillator that is parallel to the beam) is optically coupled to a light guide and a PMT that reads the pulse-height and TOF.

The light exiting the scintillator back is reflected by a front-coated bending mirror (98% reflectivity) positioned at an angle of 45° relative to the incoming beam direction (#2 in Fig. 7.2) towards a large aperture lens (#3 in Fig. 7.2). The lens focuses the image onto the photocathode of an Event Counting Image Intensifier (ECII) that is able to measure the position of each detected particle and its TOF (#4 in Fig. 7.2).

In TRECOR-I gamma detection mode, the PMT pulses are used to separate gamma-rays from neutrons by the TOF technique. The same pulses are used for gamma-ray spectroscopy by measuring the pulse height. The position of each interaction is determined by the ECII in coincidence with the PMT, enabling imaging.

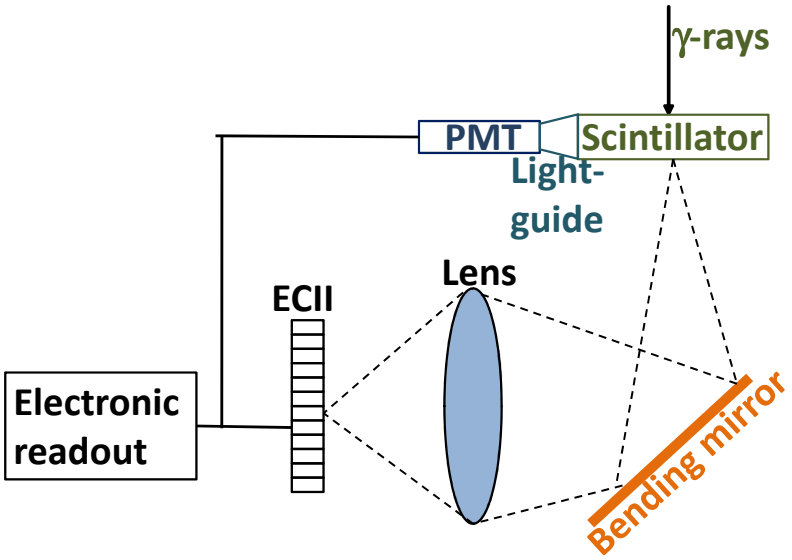

Figure 7.1: Illustration of the TRECOR-I concept.

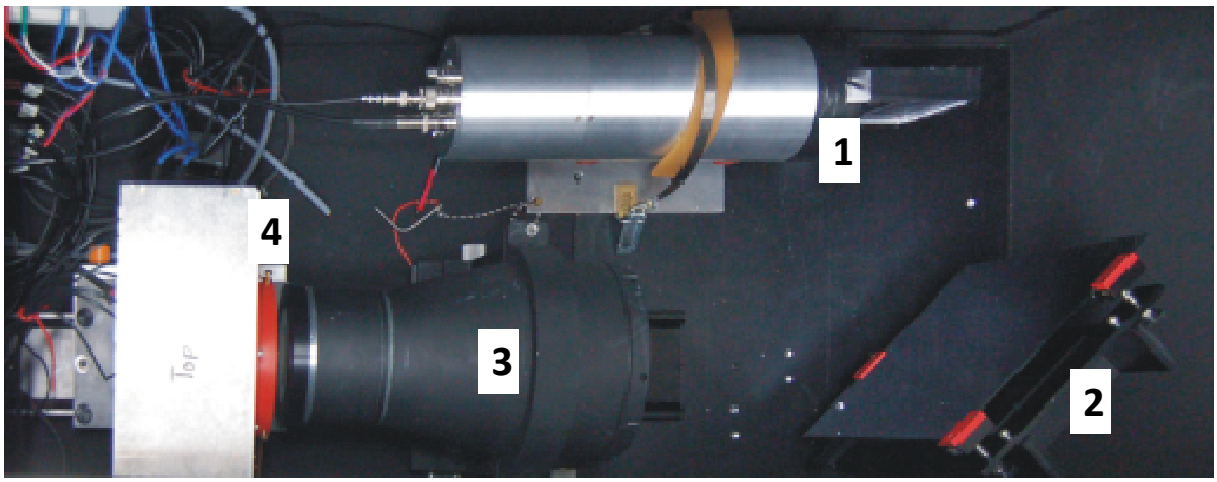

Figure 7.2: TRECOR-I from above, #1: scintillator converter attached to a PMT, #2: bending mirror, #3: lens, #4: ECII.

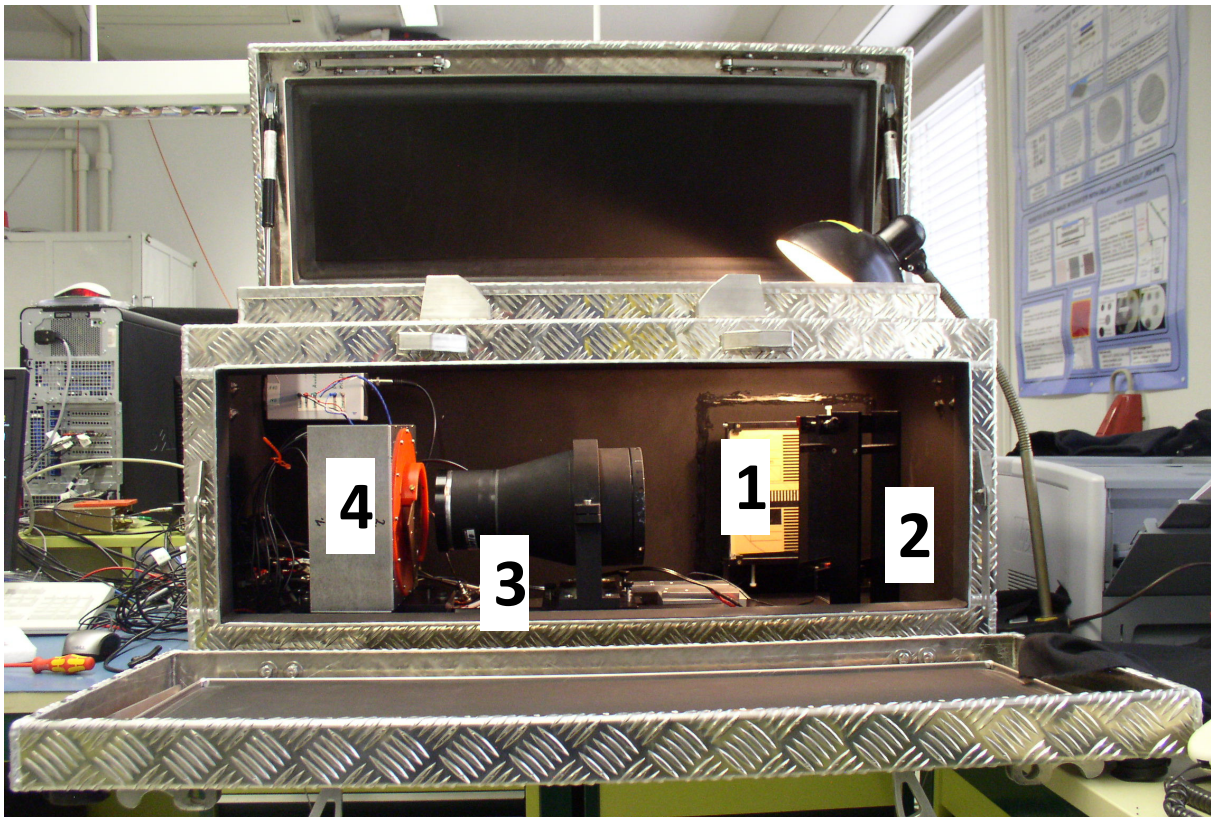

Figure 7.3: TRECOR-I from the side. #1- a metal frame with a pattern used for focusing is positioned instead of the scintillator converter attached to a PMT, #2: bending mirror, #3: lens, #4: ECII.

7.2.1.1 TRECOR-I Neutron Detection Mode

TRECOR-I can be switched from a gamma detector into a neutron detector by replacing the scintillator converter (including the PMT) and adjusting the electronics. The concept, illustrated in Fig. 7.4 is that the ECII provides all the signals: TOF for neutron/gamma separation and neutron spectroscopy and position measurement for imaging. The PMT is redundant in the neutron detection mode since the spectroscopy is based on TOF instead of pulse-height.

The scintillator converter is a plastic scintillator fibre-screen instead of the high-Z scintillator block in the gamma-detection mode. Scintillating optical fibres are used, rather than a plain scintillator slab, in order to maintain position resolution independent of screen thickness. A mirror positioned at the beam end of the scintillator screen reflects the light reaching it, which doubles the light intensity at the readout end of the fibre.

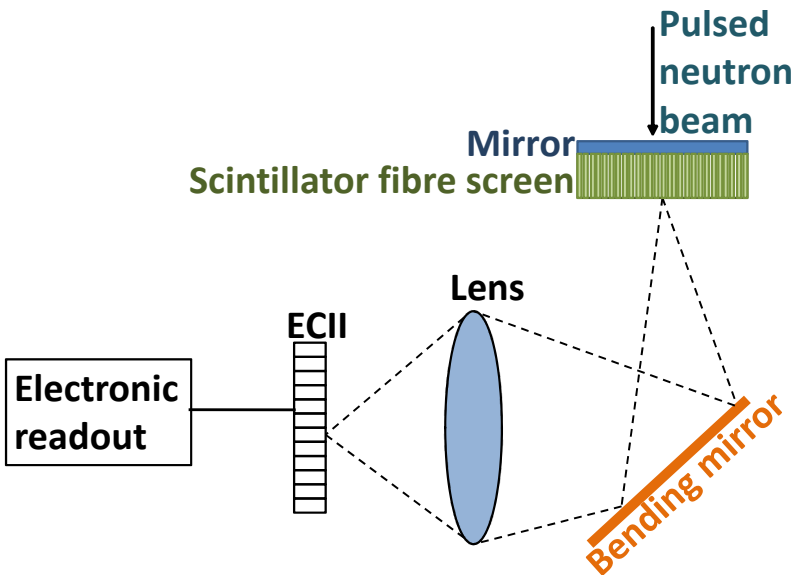

Figure 7.4: Illustration of TRECOR-I as a neutron detector – The high-Z scintillator block has been replaced by a plastic scintillator fibre screen and the electronics have been modified accordingly.

7.2.2 TRECOR-II

TRECOR-II is the second generation of TRECOR detector. It is suitable for the combined DDEGR/FNRR system because it can simultaneously detect gamma-rays and neutrons.

The concept of TRECOR-II is illustrated in Fig. 7.5 and an image of TRECOR-II is presented in Fig. 7.6. It is similar to TRECOR-I, with the scintillator converter and the following electronics adjusted. While in TRECOR-I detection of different particle types required substitution of the scintillator converter, in TRECOR-II both particle types are detected simultaneously.

The converter is composed of two parts: the first is a high-Z scintillator block (LYSO) that is directly attached to a light guide and a PMT through its side. The second part of the converter is a plastic scintillator block that is also read by the PMT through the LYSO block, as the LYSO has low absorption at 420 nm, which is the peak emission wavelength of both the plastic and the LYSO scintillators.

As in TRECOR-I, the light exiting the scintillator back is reflected by a bending mirror positioned at an angle of 45° relative to the incoming beam direction towards a broad-aperture lens. The lens focuses the image onto the photo-cathode of an ECII that measures the position of each detected particle.

In TRECOR-II the PMT pulses are used to separate gamma-rays from neutrons by the TOF technique. The same pulses are used for neutron spectroscopy via TOF and for gamma spectroscopy via pulse-height analysis. The position of each interaction is determined by the ECII (in coincidence with the PMT) for both gamma-rays and neutrons. Gamma and neutron images are acquired separately based on their TOFs.

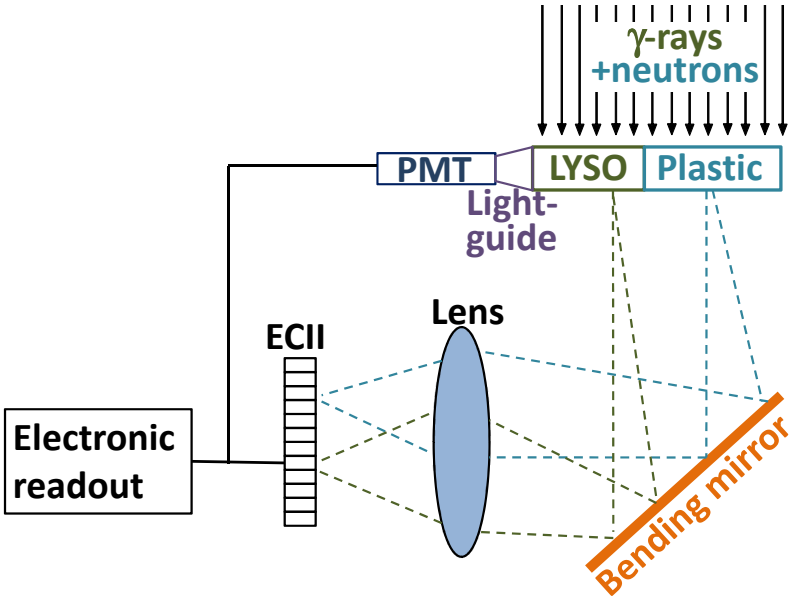

Figure 7.5: Illustration of the TRECOR-II concept.

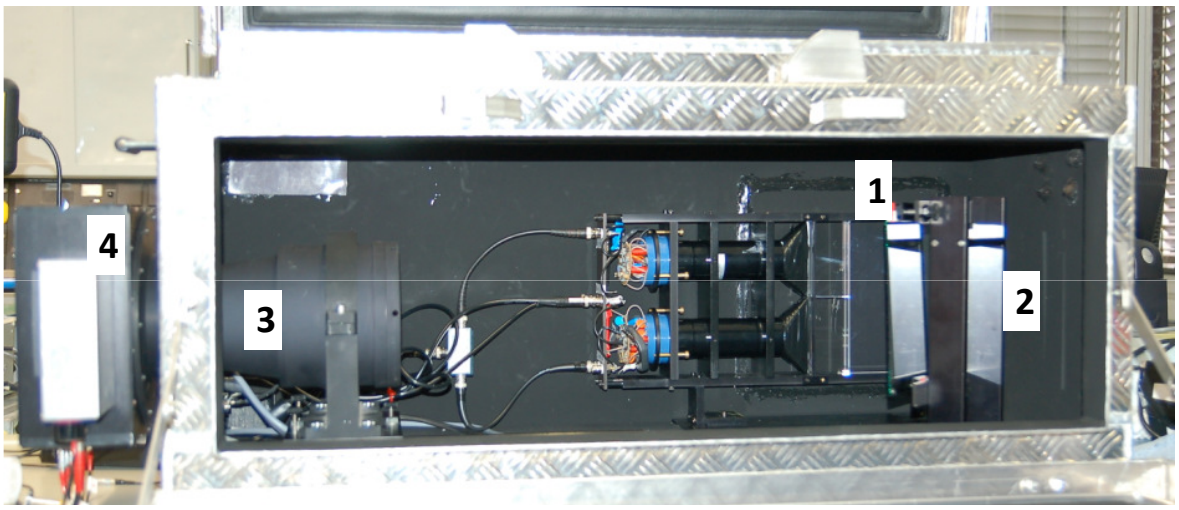

Figure 7.6: Image of TRECOR-II. #1: scintillator converter, #2: bending mirror, #3: lens, #4: ECII.

7.3 Components

7.3.1 Scintillator Converter

7.3.1.1 TRECOR-I Gamma Scintillator

Using TRECOR-I as a spectroscopic gamma-ray detector requires a high-Z scintillator converter that is sensitive to gamma-rays. The converter of choice was a $10\times5\times2$ cm^3 LYSO block (LYSO properties are detailed in Table 8.1). The LYSO was purchased from Omega-Piezo [215] and is shown in Fig. 7.7a. At 2 cm thickness, the efficiency of interaction is 41% for 4.4 MeV gamma-rays and 47% for 15.1 MeV gamma-rays.

A gamma-ray that interacts with the scintillator does so electromagnetically, with the dominating process depending on its energy - Compton and pair-production for 4.4 and 15.1 MeV gamma-rays, respectively. These processes create energetic electrons and positrons, which transfer their energy to the scintillator in a series of collisions with the scintillator molecules. These

molecules are excited and in their decay process scintillation light is emitted isotropically.
Separating gamma-rays of different energies requires a method to read the amount of light deposited in the scintillator - a pulse-height measurement. For that purpose, a light guide was designed to optically connect the LYSO block to a PMT. The light guide side, as seen in Fig. 7.7b, is covered with a Teflon reflector.
The LYSO sides were covered with a layer of Teflon above a layer of reflective paint. The entire LYSO–light guide–PMT combination is presented in Fig. 7.7c and inside TRECOR-I in Fig. 7.2. The PMT is Photonis-XP 2020 [216].

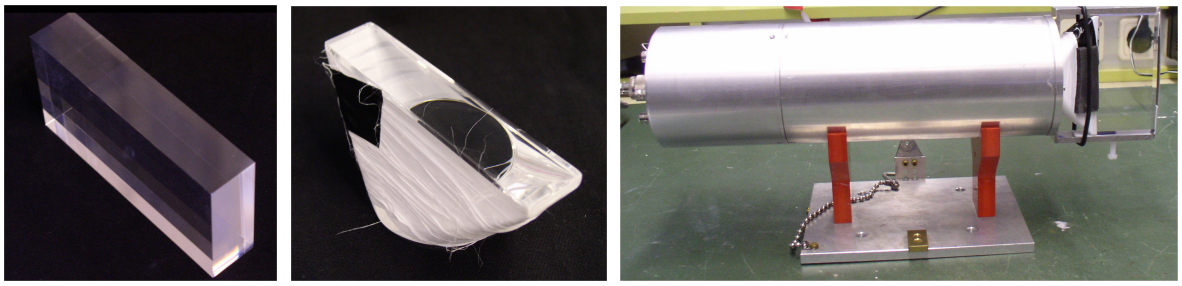

(a) LYSO block **(b)** Light guide **(c)** LYSO attached to PMT

Figure 7.7: The LYSO scintillator block, the light guide and the setup attached to the PMT.

7.3.1.1.1 TRECOR-I Neutron Scintillator

The plastic scintillator screen converter is composed of a matrix of square fibres, each 0.7×0.7 mm^2 face area and 5 cm thickness. Each fibre is wrapped in a reflective layer 0.016 mm thick and an absorbing layer, 0.02 mm thick. The fibre screen can be seen in Fig. 7.8.
A neutron that interacts in a fibre transfers part or all of its energy to protons, mostly via elastic collisions with hydrogen nuclei. In turn, the proton generates scintillations in the fibre, emitting light isotropically. A fraction of this light travels along the fibre in each direction and is emitted at its ends, creating a light image on the face of the screen.
Scintillating optical fibres are used rather than a plain scintillator slab in order to maintain position resolution, independent of screen thickness. In a fibre matrix scintillation photons are emitted from the fibre screen surface, while in a plain slab they are emitted all along its thickness, causing significant blurring due to the small depth of field in the following broad-aperture optics.

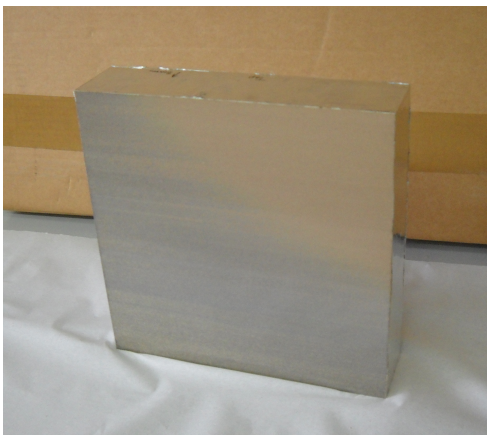

Figure 7.8: Image of the plastic scintillator fibre-screen used for neutron detection.

7.3.1.2 TRECOR-II Scintillator

The scintillator in TRECOR-II is split into a high-Z scintillator for gamma-ray detection and a plastic scintillator for neutron detection. The scintillators are read by the ECII and by two PMTs optically attached to the high-Z scintillator. The high-Z scintillator side of the screen is composed of 2 LYSO blocks, $5\times10\times2$ cm^3 each. The plastic scintillator block is $10\times20\times2$ cm^3. The scintillators are contained by a metal frame. The scintillator setup is presented in Fig. 7.9.

The setup uses two PMTs, one for each LYSO block, to ensure a uniform light collection. The same PMT's are used to read the pulse height from the LYSO and to trigger events from the plastic scintillator. The almost identical emission wavelength of both scintillators (420 nm) permits the light from the plastic scintillator to pass through LYSO unabsorbed and reach the PMT.

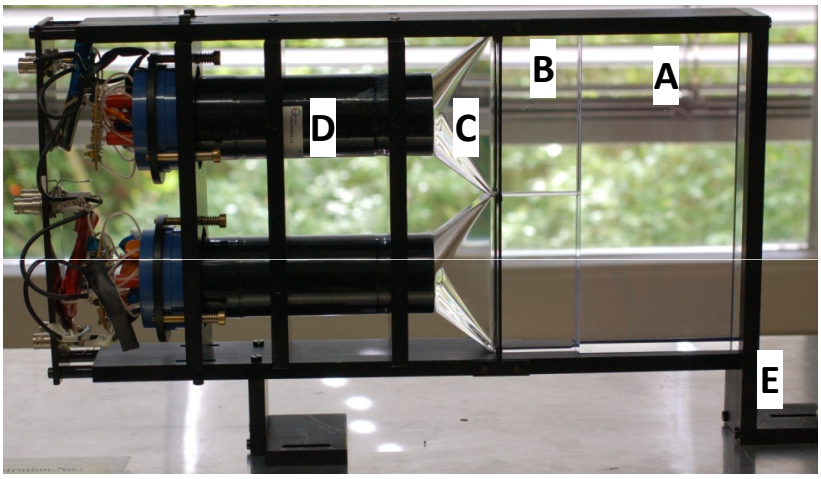

Figure 7.9: The scintillators setup of TRECOR-II. A: the plastic scintillator block, B: The LYSO scintillator blocks, C: light guides D: PMTs E: Iron frame.

7.3.2 Optical Path

To protect the sensitive system components (ECII and electronics) from radiation damage, these components were moved out of the accelerator beam path, as shown in Fig. 7.5. Thus, a bending mirror was positioned at 45° facing the scintillator to deflect the scintillation light toward the F#=0.95 lens and onward. The mirror (3.3 mm thick), manufactured by Praezisions Glas & Optik GmbH [217], is composed of a borosilicate substrate front-coated by a multi-layer dielectric thin-film. The mirror exhibits reflectance of >99% for single wavelengths, high mechanical resistivity and high temperature stability.

The large aperture lens has $F_{\#}$=0.95, focal length = 120 mm and diameter = 126 mm. This lens is not commercially available and was originally designed for another detector developed by our group [14].

7.3.3 Event Counting Image-Intensifier (ECII)

The ECII is based on a patented technique developed by RoentDek [218], described in detail in [11, 219, 220]. The active ECII diameter is 40 mm, its quantum efficiency is 10% at 420 nm and its temporal resolution is ∼1 ns. It is combined of two parts: A Resistive Screen Photo-Multiplier Tube (RS-PMT) enclosured in a vacuum tube and a delay-line readout anode.

The RS-PMT operation principle is similar to that of a conventional image intensifier, the main difference being the replacement of the phosphor screen used in conventional image intensifiers by a ceramic wall with a resistive coating.
In the RS-PMT, the screen resistivity is chosen so that nearly 100% of the collected charge from the MCP avalanche creates an induced signal in a metal electrode (the delay-line readout anode) placed on the rear wall outside the sealed tube. The Resistive screen is made of a thin film of Germanium. It was manufactured by Photek LTD in the UK.

The schematic structure of the ECII is presented in Fig. 7.10. The photo-cathode, which is located on the glass entrance window, converts incoming photons into electrons. After multiplication in a high-gain triple MCP stack the electron cloud reaches the resistive screen. The MCP stack and the resistive screen are both inside a sealed PMT vacuum enclosure.
The readout electrode is placed outside the rear wall, in contact with it. The moving electron charge inside the tube induces a signal on the electrodes that is coded by suitable electronic circuitry to preserve its two-dimensional position and timing information. By measuring the time sequence of the signals using appropriate readout electronics, the position and absolute arrival time (the TOF) of each particle can be registered and stored at MHz count rates.

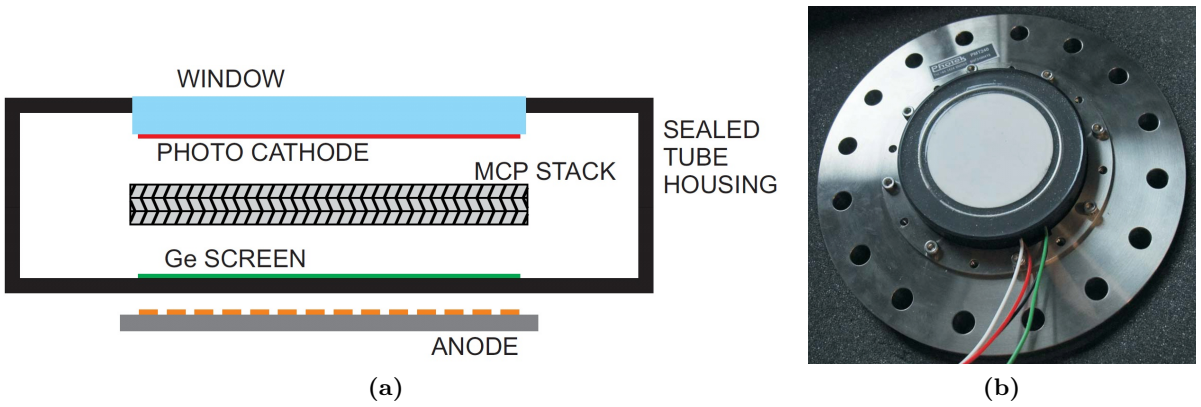

Figure 7.10: ECII schematics and image. 7.10a: Schematics of the ECII. The photo-cathode on the glass entrance window, a triple MCP stack and a thin film of Germanium on a ceramic rear wall are inside a sealed PMT vacuum housing. The readout electrode (anode) is placed outside near the rear wall. There, the image charge is naturally spread to a few mm footprint size enabling high resolution COG averaging with delay-line readout anodes. 7.10b: Rear view of a 40 mm active ECII (here: mounted on a flange) [220].

The delay-line anodes used behind the RS-PMT are standard multi-layer Printed-Circuit Boards (PCB) consisting of rows of diamond-shaped pads connected along one direction. These rows are interconnected on one end via serpentine tracks (meander delay-line), as can be seen in Fig. 7.11.
This method introduces a certain delay for induced signals after emerging from the rows and travelling along the so formed delay-lines in both directions towards the terminals. Since the image charge is spread over more than one row, Centre-Of Gravity (COG) averaging enables a spatial precision that is not limited by the row-to-row distance (anode pitch). At least two such layers are needed for a two-dimensional detection of the incoming particle or photon. Unlike anodes for direct charge collection, the layers for each dimension are separated by a continuous insulating sheet.

The delay-line variant used in TRECOR is denominated Hexanodes and is made of three such delay-line layers oriented 60° to each other, as shown in Fig. 7.12b. It enables three linear independent position measurements so each two-dimension position is over-determined, which

can be used for online correction of position distortions. The spatial resolution was found to be 0.1 mm FWHM or better [220, 221].
The pad sizes in the multi-layer PCB grow with the layer distance from the resistive screen to compensate for the diminishing image charge on more distant layers. The delay line anode module in the TRECOR-I ECII module is presented in Fig. 7.12a.

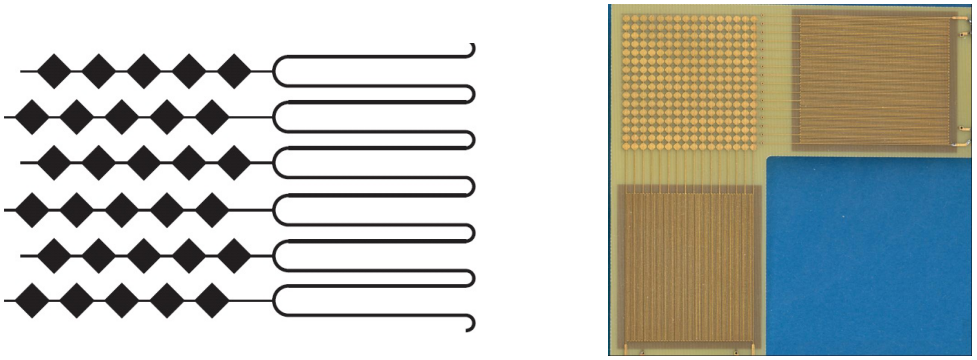

(a) Illustrasion.

(b) Image of a two-dimentional meander delay-line readout.

Figure 7.11: Delay-line layers formed by a meandering track. Rows of interconnected pads pick up the image charge signal and guide it along delay-lines to terminals for further signal processing [220].

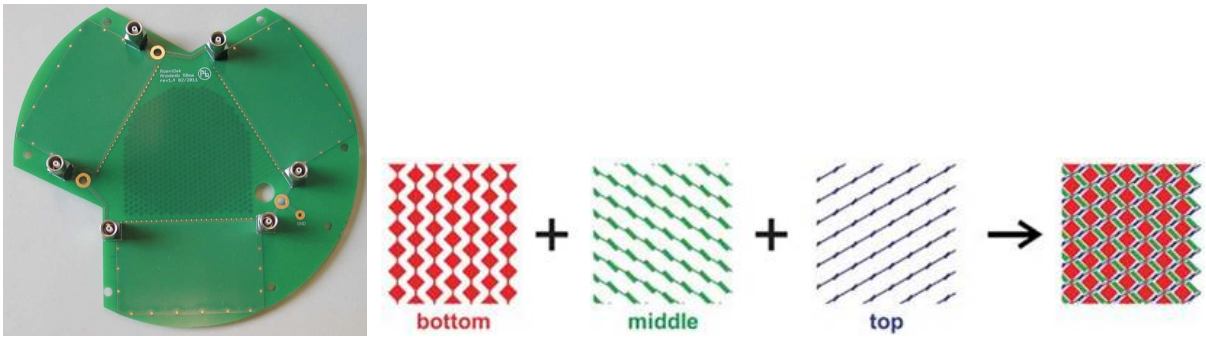

(a) The meander hexanode delay-line anode. The transmission lines are covered between ground planes in the multi-layer PCB.

(b) structures and orientation of the pickup pad rows for the three-layer Hexanode geometry.

Figure 7.12: Reprinted from [220].

7.3.4 Electronics

The electronics was designed and manufactured by RoentDek [218] and by Dr. V. Dangendorf from PTB Braunschweig and his group. The main concepts are common to both TRECOR generations and the differences will be explained here. A detailed description of the electronics is provided in Appendix B.

The electronics setups are presented in Figs. 7.13 and 7.14 for TRECOR-I and TRECOR-II, respectively. The two setups are similar but not identical.

Each event initiates eight signals: six position signals from the ECII, the anode signal from the ECII and the pulse-height signal from the PMT. These are translated into ten signals entering the RoentDek TDC8HP unit (Time to Digital Converter) that transforms them into a digital form.

This TDC was designed as the interface between the ECII and its electronic circuitry and the computer. It translates the time-differences between the start-signal, called here the common start, and up to eight stop signals to digital words with a resolution of 25 ps.
The common start is the time reference to which all other signals to the TDC are measured. Channels 1-6 in the TDC are open for one hit in each detector event (used for position measurement) and channels 7 (pulse-height) and 8 (TOF) are open for two hits in each detector event, the value being the second hit ("stop") minus the first hit ("start"). The first hit of channel 8 of the TDC is the common start.
To avoid an overflow of unanswered start signals from the accelerator, the start is from the detector and is matched with a stop from the next accelerator pulse.

The TDC card is hosted in a powerful work station that operates the data acquisition system "COBOLD", also from Roentdek, for on-line data analysis and list-mode data storage. The computer can directly accumulate images related to specific particle types, energies, etc. and at the same time transfer the full particle-event information in so-called list-mode files for a flexible off-line analysis.

The main consideration in the design of the detector electronics is the timing. The future application will have data rates of 2–5 MHz at 2 MHz pulse frequency requiring multiple events measured within an accelerator spill, demanding minimum time spent on each event. The following method has the added value that it enables use of the TDC as the single connector between the measurement system and the computer.

The signal of a LYSO scintillator has a decay constant of 42 ns, short comparing to other high-Z crystals, but long comparing to the approximately 4 ns decay constant of plastic scintillators. To expedite the pulse-height measurement, instead of measuring pulse-height with a pre-amplifier that integrates over the signal charge (usually extends over approximately 1 μs) a dedicated electronic module was built by RoentDek – the CFDx.
The CFDx unit is a combination of a constant fraction discriminator and a converter of pulse-height to time. It translates the two cut-offs of the constant fraction (at the beginning of the rise and at its end) into two NIM signals, "start" and "stop", with the time difference between their leading edges proportional to the analogue input signal (the pulse-height). This method was designed to measure the amplitude as fast as possible at the expense of linearity and resolution.

The different setups of TRECOR electronics differ by how events are triggered. When pulse-height information is required a measurement will be triggered by the PMT anode.

In TRECOR-I, events are triggered by the CFDx first output signal that is also used as veto on the ECII measurement, enabling the position information to be delivered to the TDC only when a measurement was triggered. The same CFDx start signal is the first signal in pulse-height measurement.
In TRECOR-I neutron detection mode, where pulse-height information is not required and the PMT is removed from the system, events are triggered by the ECII.

In TRECOR-II, events are always triggered by the ECII, which is vetoed by the signal from the PMT. Since both LYSO and plastic are optically attached to the PMT, this veto is sufficient to ensure that events reaching the TDC will always have both position, timing and pulse-height information. The pulse height start and stop signal are delayed accordingly. The accurate TOF is calculated by software as a subtraction of the accelerator pulse time from the CFDx start signal.

At this stage of development only one event per accelerator pulse is measured, so once an event was triggered a logic loop is used to block the TDC common start for 500 ns.

The 6 position information signals are pre-amplified and sent to a constant fraction discrim-

inators and then to the TDC. The constant fractions are vetoed by the PMT signal.

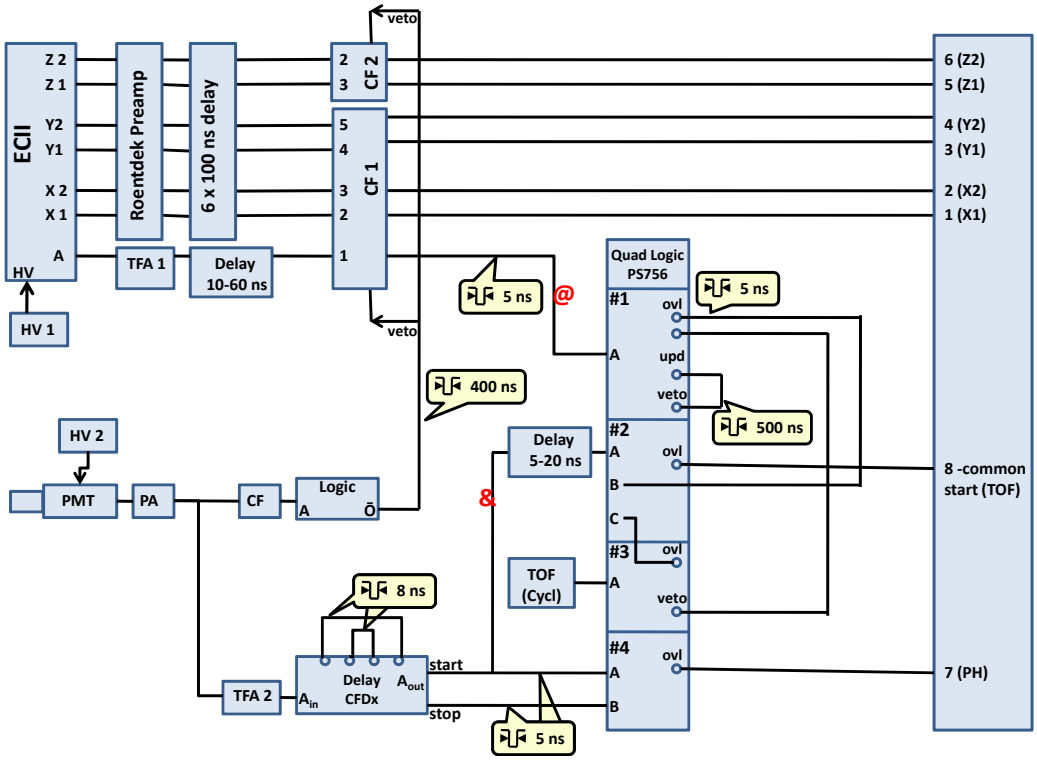

Figure 7.13: Electronic setup of TRECOR-I. The electronic circuit presented here shows the electronics of the gamma-detector mode and the neutron-detector mode simultaneously. Gamma-detector mode requires disconnection at the points marked by a @ sign and neutron-detector mode requires disconnection at the points marked by a & sign.

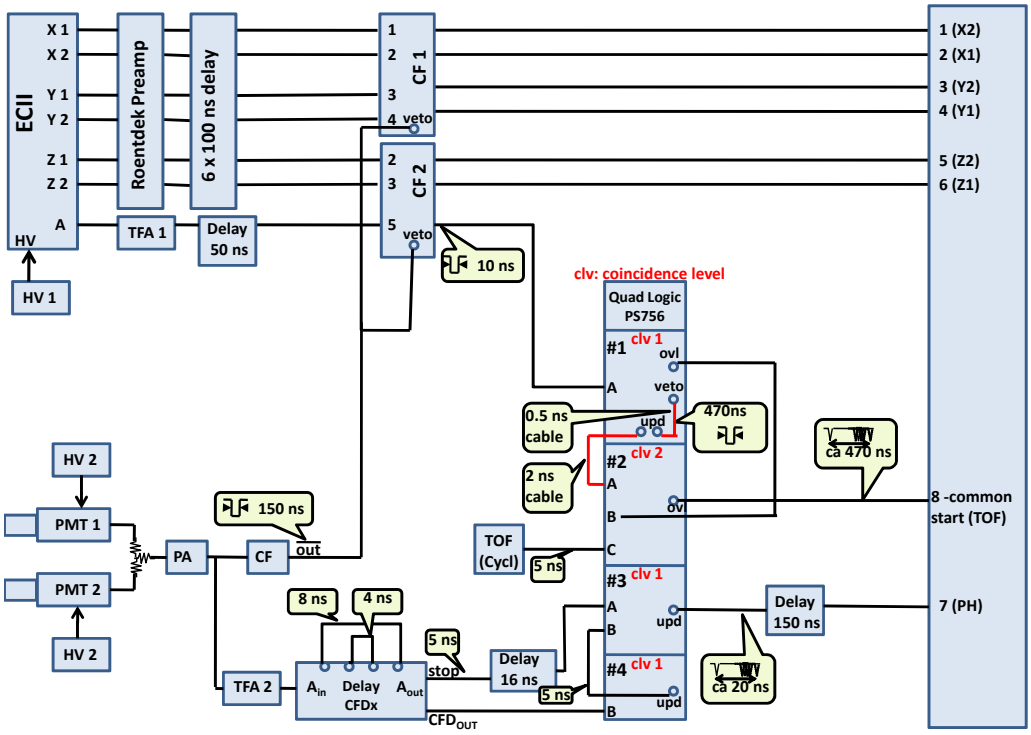

Figure 7.14: Electronic setup of TRECOR-II.

CHAPTER

8

TRECOR DESIGN CONSIDERATIONS

8.1 Selection of Scintillator Converter

The high-Z scintillator was selected based on two main requirements: a wavelength similar to that of plastic scintillator (to enable a joint readout) and availability of large single-crystals (to enable a large area detector). The two main candidates were LYSO and LSO. Their desirable properties include, in addition to the reasons above, high density, fast decay time, high light output and relatively low cost.

LYSO ,$Lu_{2(1-x)}Y_{2x}SiO_5 : Ce^{3+}$, is a Ce^{3+}-doped scintillator that was developed for positron emission tomography (PET) [222] along with LSO, Lu_2SiO_5 [223]. The two scintillators have almost identical properties, detailed in Table 8.1, but the cost of LYSO is lower, therefore it was chosen. The absorption, emission and luminescence spectra of LYSO are presented in Fig. 8.1.

A drawback of using LYSO is that natural lutetium contains 2.6% of the isotope ^{176}Lu that is radioactive and adds to LYSO an inherent radiation of about 240 count/s/cm^3 [224, 225]. Another source of background intrinsic to LYSO is radiation-induced phosphorescence that has a decay time constant of 2.53 h. A similar phosphorescence can be caused by exposure to room light [226]. To avoid this phosphorescence, the scintillator has to be kept in a light-tight enclosure for several hours before use.

The plastic scintillator is BC400, and its properties and suitability were discussed in previous publications by our group [10, 14].

	Effective atomic no.	Density (g/cm^3)	Index of refraction	Light yield (% of NaI(Tl))	Peak emission (nm)	Decay constant (ns)
LYSO	62	7.2	1.81	80	420	42
LSO	66	7.4	1.82	75	420	40

Table 8.1: Properties LYSO and LSO high-Z scintillators [110].

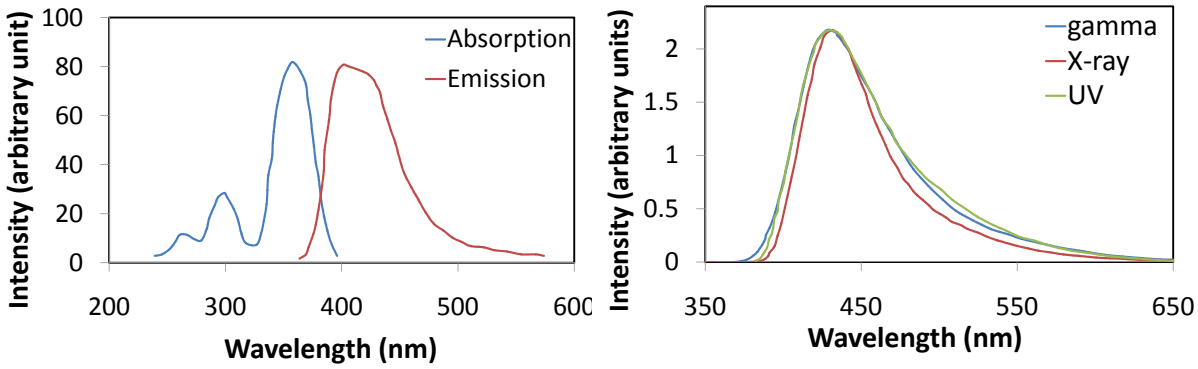

(a) UV-absorption and emission spectra of LYSO, from [226]

(b) luminescence spectra of LYSO excited by gamma-rays (667 keV), X-rays (60 keV) and UV light, from [227]

Figure 8.1: LYSO properties.

8.2 Simulations of Energy Deposition

Simulations with GEANT4 [192] enable prediction of the part of the detector response that includes the gamma-ray interactions with the scintillator and the energy deposition in the scintillator via secondary charged particles (electrons and positrons).

The average deposited energy in such a slab is detailed in Table 8.2 for two scintillator thicknesses.

	Deposited energy (MeV)	
LYSO thickness (mm)	**4.43 MeV γ-rays**	**15.1 MeV γ-rays**
20	3.3	10.9
30	3.5	11.8

Table 8.2: Average energy deposited in a 100×50×Thickness mm^3 LYSO slab by 4.43 and 15.1 MeV gamma-rays.

The simulated deposited energy spectra created by 4.4 and 15.1 MeV gamma-rays impinging on the centre of a 100×50×20 mm^3 LYSO slab are presented in Fig. 8.2. This slab is larger than the 10×10×20 mm^3 pixel in the detector array simulated in Section 5.3. The full energy, single and double escape peaks are dominant in both spectra. However, the spectra contain a non-negligible energy continuum extending from full-range to zero.

Only 7% of the 15.1 MeV spectrum extends below the 4.4 MeV peak. The ratio of 4.4 to 15 MeV gamma-rays produced in the intended ^{11}B(d,γ) reaction source is approximately 5 to 1 (the exact ratio depends on the deuterons energy). Considering the multitude of 4.4 MeV gamma-rays comparing to the 15.1 MeV gamma-rays, the 7% background sums up to a negligible amount.

The Continuous Slowing Down Approximation (CSDA) range is an approximation to the average path length travelled by a charged particle as it slows down to rest. The rate of energy loss at every point along the track is assumed to be equal to the total stopping power, while energy-loss fluctuations are neglected. The CSDA range of electrons at energies between 1-20 MeV as calculated from NIST [30] data is presented in Fig. 8.3.

The range of electrons at an energy of 10.9 MeV, the average energy deposited in a 100×50×20

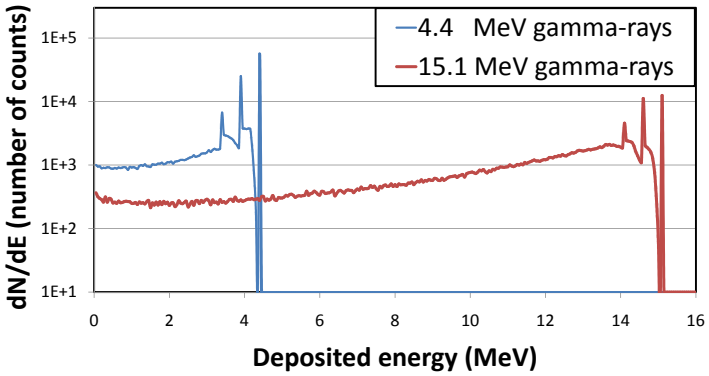

Figure 8.2: Simulated (GEANT4) spectra of energy deposited by gamma-rays impinging on the centre of 100×50×20 mm^3 LYSO slab.

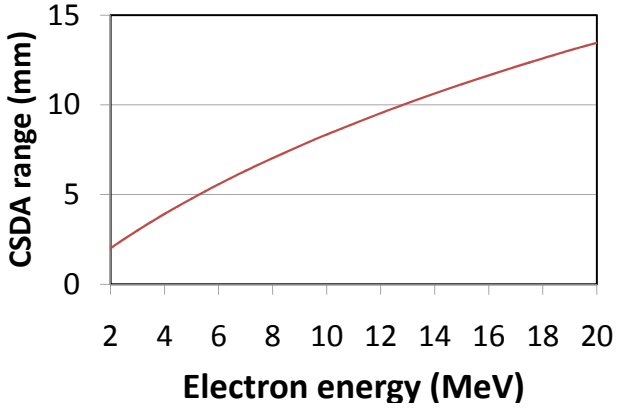

Figure 8.3: Electron stopping range in LYSO [30].

mm^3 LYSO slab by 15.1 MeV gamma-rays, is 8.3 mm. The range of electrons at an energy of 15.1 MeV, the full energy electrons, is 11.1 mm. These ranges limit the spatial resolution, but this is not the end of the story.

A high energy gamma-ray does not simply create one electron through which all the energy is deposited. As explained in Chapter 3, the deposition of energy in high-Z scintillators is the result of a combination of processes, involving, for example, an electron and a positron, the positron creating two annihilation photons that further interact with the scintillator. Both electrons and positrons may create an emission of a Bremsstrahlung photon, which may or may not be re-absorbed.

Six such tracks, each created by one 15.1 MeV gamma-ray in a LYSO scintillator slab, as projected in the two dimensions relevant to imaging, are presented in Fig. 8.4. The 100×100×2 mm^3 simulated LYSO slab was divided into 1000×1000 virtual pixels, and the energy deposited in each track was counted. The location in which the gamma-ray has interacted with the scintillator for the first time is always (x,y) = (5,5). The tracks are spread over several centimetres and are discontinuous as the annihilation and Bremsstrahlung photons do not deposit energy in the scintillator, thus creating gaps.

In the neutron detector, fibres are used to create a light image at the face of the screen without losing resolution to the depth-of-focus. Early in the project we considered using a similar high-Z scintillator fibre-screen. Assuming the lens is focused on the LYSO centre, the LYSO is 600 mm from the lens whose diameter is 130 mm, so the maximal blur from de-focus is 2.2 mm. Therefore, the loss of resolution due to the wide tracks is the main limitation on spatial resolution for gamma-rays, which renders the fibre-screen superfluous and thus reducing

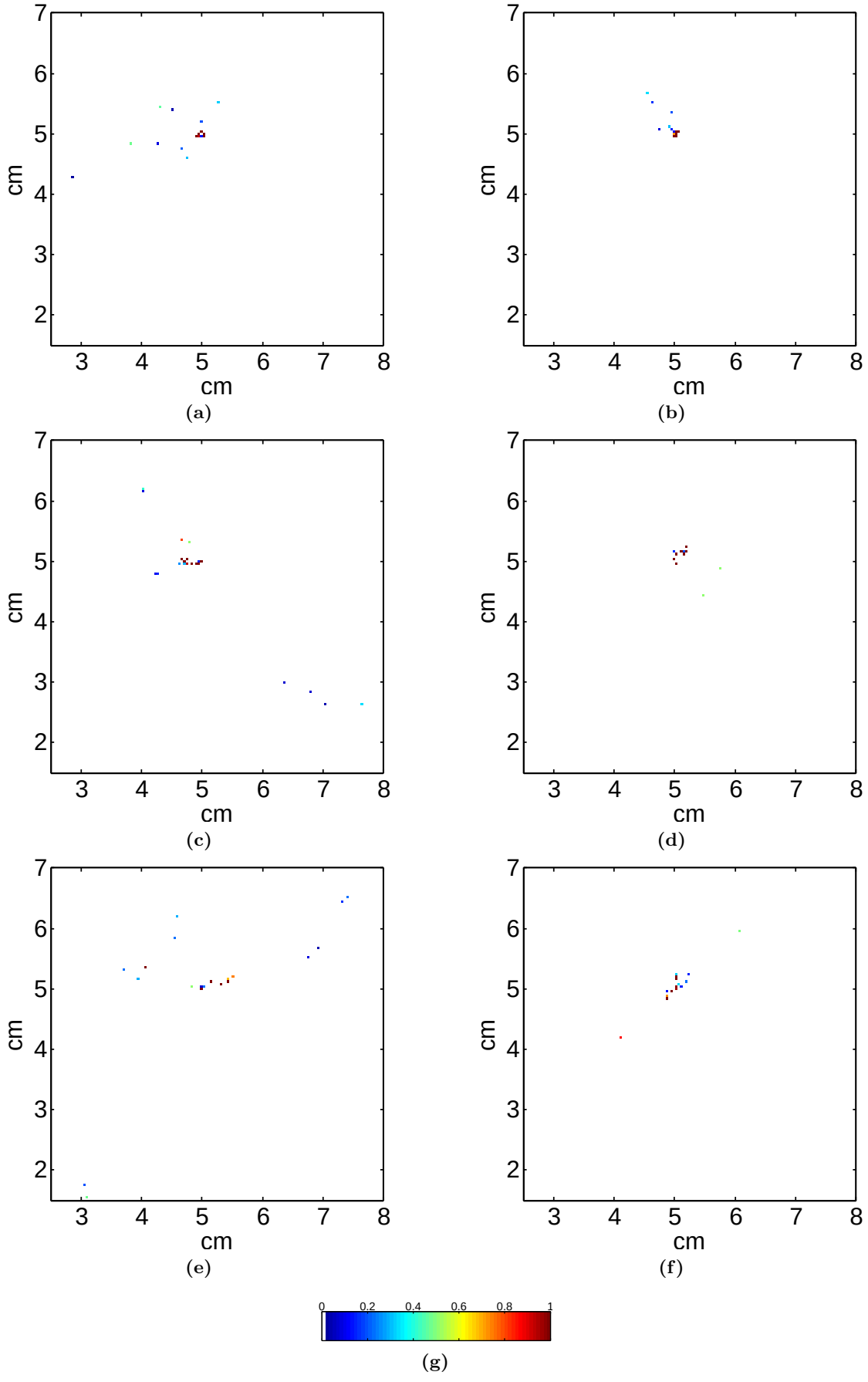

Figure 8.4: Simulated tracks created by six randomly chosen 15.1 MeV gamma-rays in a LYSO slab, each frame represents one gamma-ray. The dots represent positions where energy was deposited and their colour is linearly related to the amount of energy deposited at that point. The location of the first interaction of the gamma-ray is always at (x,y) = (5,5). The colour legend represents the relative amount of energy deposited at each point of the track.

cost.

8.3 Light Collection

The light that is created in the scintillator is emitted isotropically. It is collected simultaneously by the PMT and by the ECII as illustrated in Fig. 8.5.

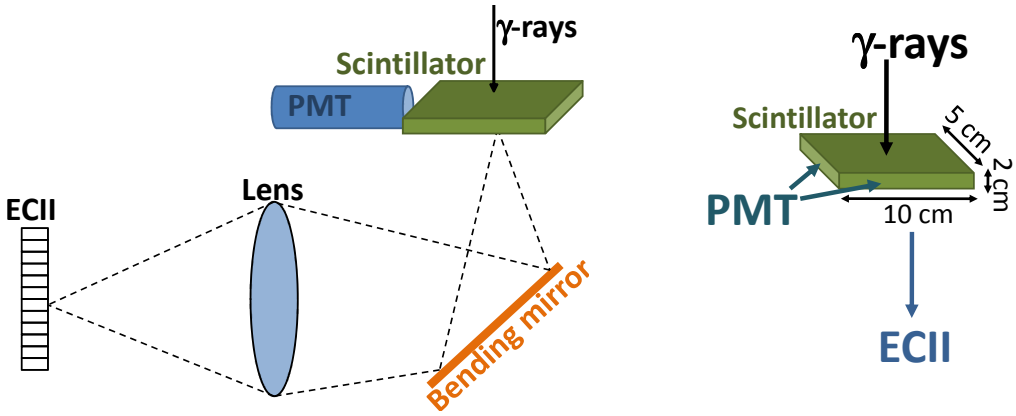

(a) full light collection path of the PMT and the ECII

(b) The PMT can be attached to one of the narrow LYSO sides and the ECII collects the light from the LYSO wide face.

Figure 8.5: Light collection paths of the PMT and ECII. The PMT is attached to the LYSO, either by a light guide or in direct contact. The ECII collects the light from the scintillator face via a bending mirror and a lens.

The ECII is the imaging device and therefore it views the back of the LYSO, the wide face opposing the gamma-rays arrival direction, whose dimensions are 10×5 cm^2.

The PMT is connected directly to the LYSO and can be attached either to the 5×2 cm^2 side or to the 10×2 cm^2 side, leaving the wide face to the ECII. The PMT can be attached directly or via a light guide. A third option that was considered was to connect the PMT with a wavelength shifter slab, but a quick laboratory test proved this technique to be inefficient.

8.3.1 PMT Light Collection

Several options for collecting light were compared with ZEMAX [228] optical design software, using the non-sequential photon tracing module. The LYSO slab size in these calculations is $100\times50\times20$ mm^3, the refractive index is 1.83 and the wavelength is 420 nm.

The first, simple, option was to attach the PMT directly to a 50×20 mm^2 face, presented in Fig. 8.6 alongside the simulation results in Table 8.3. The simulation included the LYSO slab and a 3 mm thick glass window representing the PMT entrance window. The light is emitted isotropically from a point source positioned at different locations within the slab, 5 mm from either the top, side or bottom LYSO narrow faces.

The fraction of light reaching the PMT is approximately 0.2 for all light source locations, with and without reflector on the narrow faces of the LYSO. Given that the light yield of LYSO is 25,000 optical photons/MeV and the average gamma-ray energy is about 3 MeV (for 4.4 MeV gamma-rays), we expect 15,000 optical photons reaching the photo-cathode per gamma-ray. Assuming the PMT photocathode quantum efficiency is 0.2 (not to be confused with QE=0.14 for the ECII), about 3000 photoelectrons.

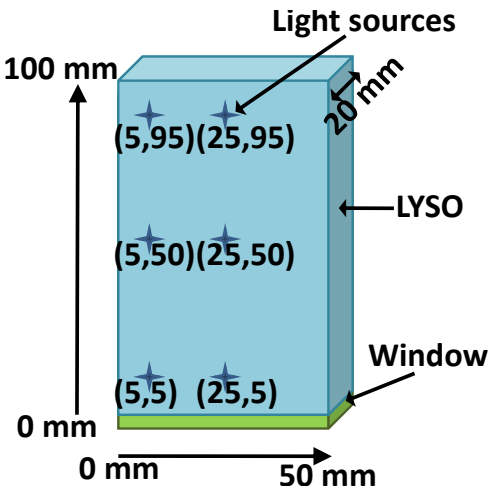

Figure 8.6: The geometry of the Zemax configuration including the LYSO slab and the PMT entrance window. In the 20 mm LYSO dimension, all the sources are at the centre, 10 mm from each side.

Source position	Bare LYSO	Reflectors on narrow faces
Top centre (25,95)	0.18	0.20
Top side (5,95)	0.18	0.20
Centre centre (25,50)	0.19	0.21
Centre side (5,50)	0.20	0.21
Bottom centre (25,5)	0.21	0.23
Bottom side (5,5)	0.22	0.23

Table 8.3: Fraction of the light reaching the PMT window for light sources located in different parts of the slab, with and without reflectors on the narrow faces of the slab (calculated with ZEMAX)

The next simulated geometry included a perspex light-guide that connects the LYSO to the PMT. The light guide simulated is similar to the one used in the experiment, an inverted truncated pyramid having a 100×20 mm^2 top and a 48×48 mm^2 bottom, as illustrated in Fig. 8.7. The light-guide is coupled to a 48 mm diameter cylinder 1 mm thick used to calculate the fraction of light reaching the PMT window.

The light was emitted from a point source positioned 5 mm from either the top, side or bottom of the LYSO narrow faces. Two cases were investigated, with and without specular reflectors covering the narrow faces of the LYSO and the light-guide sides. The results are presented in Table 8.4. The uniformity of the light collection from different locations in the LYSO is better with the specular reflector.

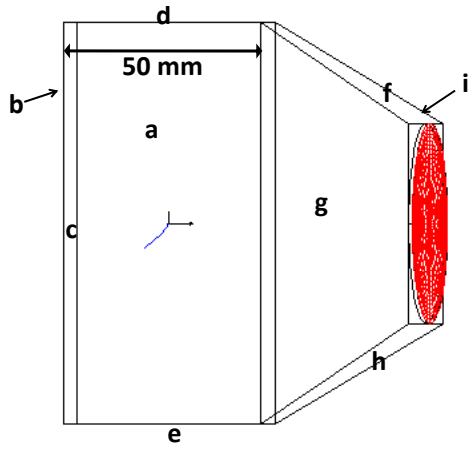

Figure 8.7: The geometry of the Zemax configuration including the LYSO slab and light guide. The letters mark different surfaces of the LYSO and light guide.

source position	Bare LYSO	LYSO+Reflector
Top centre (25,95)	0.09	0.18
Top left (5,95)	0.16	0.25
Centre centre (25,50)	0.11	0.19
Centre left (5,50)	0.16	0.24
Bottom centre (25,5)	0.14	0.22
Bottom left (5,5)	0.13	0.22

Table 8.4: Fraction of light reaching the PMT in the configuration presented in Fig. 8.7 with and without specular reflectors on the LYSO narrow faces and on the light-guide sides (calculated with ZEMAX).

Next, the effect on light collection uniformity of a specular reflector was compared to that of a diffusive reflector. The configuration is identical to the previous one, with the coating entirely specular or entirely diffusive. The results, presented in Table 8.5, show that the uniformity is

better when using a diffusive reflector. Therefore, the narrow faces of the LYSO and the light guide sides in TRECOR-I were covered with diffusive reflectors.

Distance from										(centre)		standard
edge (mm)	5	10	15	20	25	30	35	40	45	50	mean	deviation
Specular	0.25	0.24	0.23	0.22	0.21	0.21	0.20	0.19	0.18	0.18	0.21	0.03
Diffusive	0.31	0.31	0.30	0.30	0.30	0.30	0.30	0.29	0.29	0.28	0.30	0.01

Table 8.5: Comparison of the fraction of light reaching the PMT in the configuration presented in Fig. 8.7 with specular and diffusive reflectors (calculated with ZEMAX).

The final design was therefore composed of the PMT attached to the 20×100 mm^2 side of the LYSO via a light guide. The light guide sides were covered with Teflon, a diffusive reflector.

8.3.2 ECII Light Collection

The ECII is not in direct contact with the scintillator. Light is emitted in the scintillator isotropically and a fraction of it reaches the scintillator face. As illustrated in Fig. 8.5, it is bent by 90° into a focusing lens with $F_{\#}$=0.95 and focused on the ECII, which has a 40 mm diameter.

The solid angle of the lens with respect to a light point source determines the fraction of optical photons that reach the ECII. The schematic geometry is illustrated in Fig. 8.8, with the exact position of the point source inside the scintillator neglected. The portion of the light reaching the detector from the point source can be expressed with the relative solid angle (divided by 4π) of the lens Ω, which is subtended by:

$$\Omega = \frac{1}{2}\,(1 - cos\,\alpha) \tag{8.1}$$

and α can be derived from Snell's law:

$$sin\,\alpha = \frac{sin\,\theta}{n_{LYSO}} \tag{8.2}$$

with n_{LYSO}=1.8 is the refractive index of LYSO and θ is calculated from its tangent. Substituting the values from Fig. 8.8, the calculated values are θ=5.99°, α=3.29° and the relative solid angle is Ω=8.2×10^{-4}.

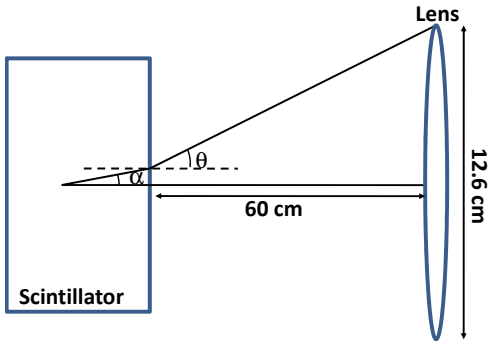

Figure 8.8: Illustration of the geometry used to calculate the fraction of optical photons reaching the lens.

In Section 8.3, the average deposited energy in a LYSO slab of this size was simulated to be 3.3 and 10.9 MeV for 4.4 and 15.1 MeV gamma-rays, respectively. The average number of optical photons reaching the ECII is therefore 68 and 223, respectively (the number of created optical photons is 25,000 photon/MeV). The mechanism of photo-electron creation on the ECII photo-cathode is dominated by binomial distribution and the quantum efficiency of the ECII is QE = 0.14. Thus, the probability that an event will be registered is practically 100% for both energies. The average number of photo-electrons created in the photo-cathode is 10 and 32 for 4.4 and 15.1 MeV gamma-rays, respectively.

The light collection onto the ECII is therefore sufficient and this design, where the lens collects the light into the ECII, enables detection and position determination of the ^{11}B(d,n+γ) gamma-rays.

8.4 Random Coincidences

LYSO contains approximately 2.6% of ^{176}Lu. ^{176}Lu decays by β^- emission to ^{176}Hf, which decays to its ground state by a cascade of 3 gamma-rays (307 keV, 202 keV and 88 keV). The spectrum of the combined β-gamma activity is a broad continuum and in a large bulk of LYSO it is expected to have an average energy of about 1 MeV [224]. The natural activity of ^{176}Lu in LYSO is quoted to be approximately 240 counts/s/cc.

The LYSO slab has volume of 100 cc. The expected scintillation rate from the internal activity is therefore 2.4×10^4 events/s. The calculated light collection (the fraction of created light reaching the ECII) is 9×10^{-4}, resulting in 22 optical photons reaching the ECII for each such event. The probability of creating 1 photo-electron or more in the photo-cathode with 14% quantum efficiency is thus 98%. The ECII is operated at a high gain near the saturation point, prohibiting pulse-height discrimination with the ECII.

The internal activity is distributed evenly over time, so in a 5 ns window 1.2×10^{-4} events will be created in the ECII. At a 2 MHz accelerator pulse frequency the random coincidence rate will be $1.2\times10^{-4} \cdot 2\times10^6 = 240$ event/s.

The number of events in the ECII from reaction gamma-rays ("true events") at 5 MeV deuteron energy is approximately 1×10^{11} γ/mC/sr, which is 1.3×10^9 γ/μC created at the target. At 1 μA accelerator current and 12 meters distance between the detector and the target (approximately isotropic emission), 69 γ/s/cm^2 reach the detector 50 cm^2 face. With a 40% detection efficiency in the LYSO, the rate of real events is 1390 events/s. Thus, the rate from random coincidences is 17% of the true events rate and constitutes a significant background under the conditions used in the experiments.

In a realistic inspection system, the true events rate will be increased by positioning the detector nearer to the target and by using higher current, in the mA range. Assuming 8 meters and 1 mA, 3.1 $\times10^6$ events/s are expected from true events, overpowering the random coincidence rate. However, in the experiments testing the detectors the random coincidence background had to be removed. Since the pulse-height (gamma energy) measurement with the PMT enables using a threshold on energy, setting the threshold at 1 MeV effectively removes most of the LYSO counts while leaving the true events rate un-effected.

CHAPTER

9

TRECOR PERFORMANCE

9.1 Experimental Setup

The experiments took place at the cyclotron accelerator located at the Physikalisch-Technische-Bundesanstalt (PTB) in Braunschweig, Germany. It is a CV-28 variable-energy compact cyclotron, manufactured by TCC (The Cyclotron Corp.). The cyclotron accelerates deuterons up to energy of 13.5 MeV, and current up to 80 μA. The cyclotron is equipped with a fast (ns) internal beam-pulsing system, that provides the capability to choose between a wide range of pulse repetition rates, 2 kHz to 6 MHz [229, 230].

In our experiments the rate had to be restricted to a pulsing frequency of about 2 MHz (500 ns separation between consecutive pulses), to prevent the less-energetic neutrons from arriving at comparable times to the most energetic neutrons of the next burst (frame overlap).

The cyclotron is located in a room inside a low scattering collimation system defining 5 different neutron beam-lines, each consisting of a set of massive polyethylene, water and concrete collimators combined with steel, described in Fig. 9.1. TRECOR detector was positioned 12 m from the target in beam-line d3, indicated in Fig. 9.1.

The deuteron beam structure was determined with the help of a Čerenkov detector positioned at a large distance (approximately 30 meters from the target). This detector, which has low sensitivity to neutrons, measures the flash of gamma rays emitted during the deuteron interaction with the target. The temporal resolution will be addressed in more detail later.

Another measurement of the radiation spectra was conducted with a 2"×4" NE213 liquid scintillator coupled to a PMT detector that was positioned on a movable stand, at a distance of 1000 cm from the target. The detector was easily moved in and out of the beam.

In a typical measurement setup, depicted in Fig. 9.2, a sample is located in the path of the gamma-rays/neutrons arriving from the target towards the detector. In Fig. 9.2 the sample is a Styrofoam box filled with liquid nitrogen.

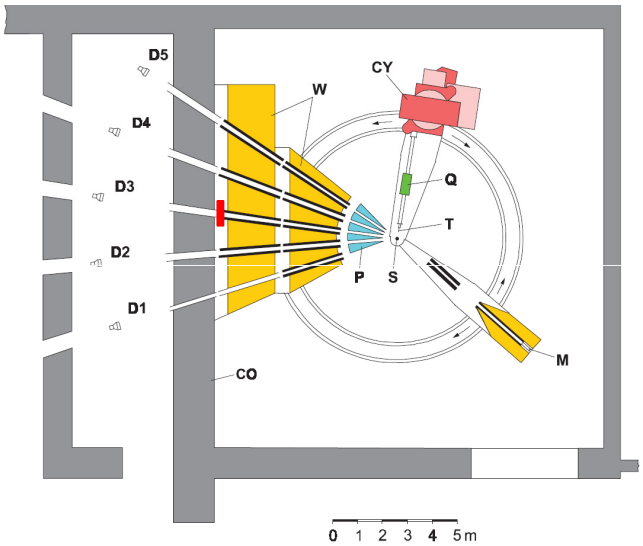

Figure 9.1: The PTB cyclotron and experimental hall. The experiments took place in beam-line d3, TRECOR detector position is marked with a red rectangle.

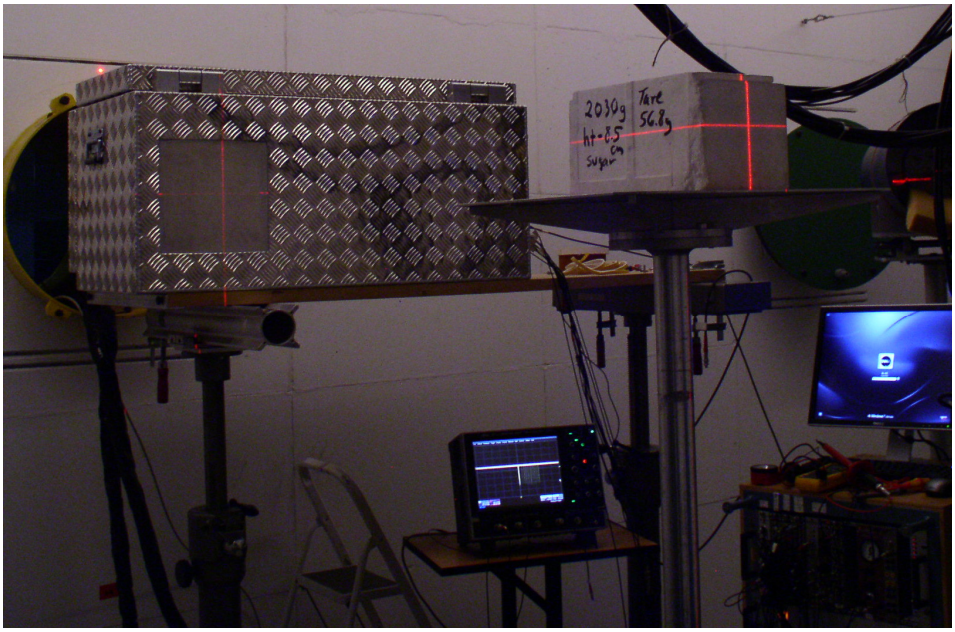

Figure 9.2: Setup of TRECOR in the beam line at the PTB cyclotron facility. The photo shows the Aluminium box of TRECOR (both generations were encompassed by the same box), the data acquisition and electronics setup (lower right corner) and in the beam line, marked with the red laser cross, a sample made of a liquid nitrogen filled Styrofoam box.

The work described here includes results from three experiments. In the first experiment, in June 2010, we used an early version of TRECOR-I as a neutron detector. The second experiment took place in August 2011 and included runs with TRECOR-I at its gamma-detection mode and at its neutron-detection mode. The third experiment took place in June 2012 and included TRECOR-II as a simultaneous gamma/neutron detector.

In the 2010 experiment and the 2011 neutron-detection experiment the source was the ^{9}Be(d,n) reaction with pulsing rate of 2 MHz that implies 500 ns between bursts, each burst 1.5 ns long. The deuterons energy upon hitting the target was 11.8±0.2 MeV and the current was 1.2 μA. The Be target was made of solid Be, 3 mm thick. The ^{9}Be(d,n) produces a broad-energy

neutron spectrum [231].

In the 2012 experiment and the 2011 gamma-detection experiment the source was the ^{11}B(d,γ+n)^{12}C reaction. The deuteron beam current was 1.2 – 1.5 μA, impinging on the target at 7.4±0.12 MeV. The pulsing rate was 1.5 MHz that implies 667 ns between bursts, each burst 1.5 ns long.

The boron target, presented in Fig. 9.3, was made of B enriched to 96% ^{11}B, diameter 8 mm and 3 mm thickness. The ^{11}B powder was supplied by Ceradyne Boron Products, USA. The size of the powder grains is less than 22 μ in diameter. The target was produced by RHP-Technology, Austria. It was sintered at high temperatures and pressure to achieve a bulk density of about 85% of solid B. The final target dimensions were reached by grinding the sintered B-plate, after which it was bonded at a high temperature with a Cu/Ag solder to the Mo backing. The vacuum compatibility of the target as well as the thermal conductivity and homogeneity of the B contact with the Mo backing were tested [232].

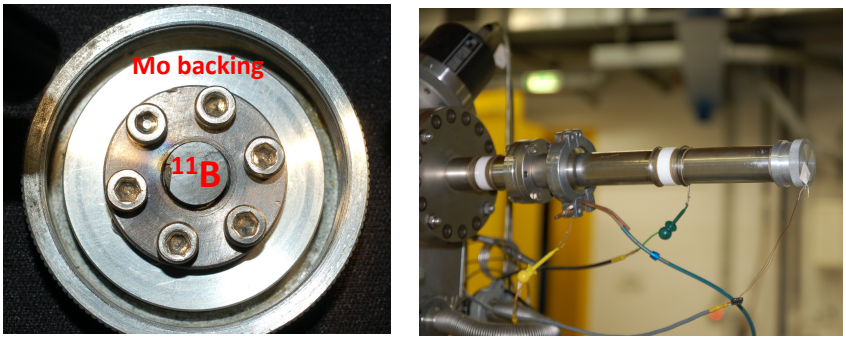

(a) The ^{11}B target after irradiation. **(b)** The mounted target.

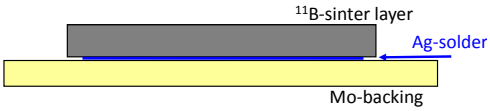

(c) The ^{11}B target sketch

Figure 9.3: The ^{11}B target, alone and mounted in the beam-line.

9.2 Energy Resolution

The fast pulse-height measurement method (described in Chapter 7) results in some non-linearity in the energy spectrum, making a precise energy calibration difficult. However, as the gamma-ray spectrum does not include any complicated features, it is sufficient to determine that the 4.4 and 15.1 MeV-related peaks are correctly identified and located.

A pulse-height spectrum measured with TRECOR-I and a ^{11}B(d,n+γ)^{12}C source is presented in Fig. 9.4 along with a 4.4 MeV gamma-ray spectrum emitted from a ^{241}AmBe gamma source. The overlap between the two peaks validates that both peaks are indeed located at 4.4 MeV.

The 15.1 Mev peak is the cleanest peak in the spectrum with no adjacent energy peaks and no higher energy peaks adding to its signal (The 4.4 peak is on top of the Compton continuum of the the 15.1 MeV peak). Therefore, the energy resolution is calculated from the 15.1 MeV

peak by [49]:

$$\text{Energy resolution} = \frac{\text{FWHM}}{E_{peak}} = \frac{3.1}{15.1} = 0.20 \tag{9.1}$$

resulting in energy resolution of 20%, double the intrinsic LYSO energy resolution of 10% [233]. The widening could be the result of the crystal size, the light collection quality and the electronic setup.

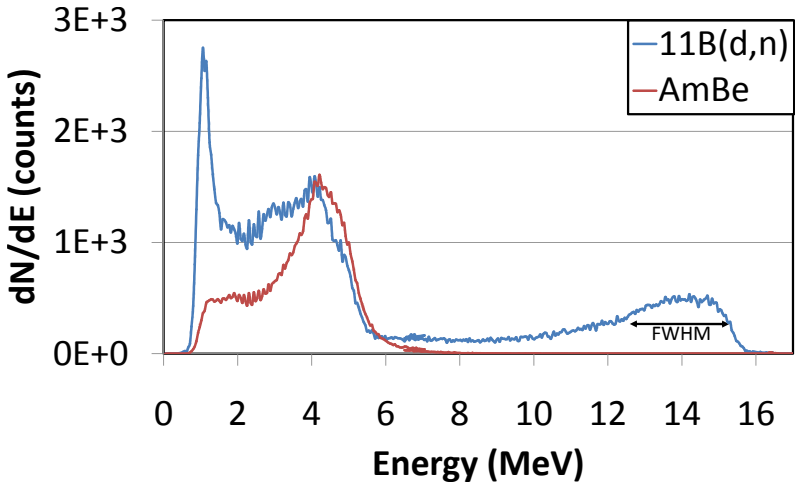

Figure 9.4: Pulse-height from the ^{11}B(d,n+γ)^{12}C source and the ^{241}AmBe source measured with TRECOR-I in the 2011 experiment with the AmBe 4.4 MeV peak height adjusted so that it can be compared to the ^{11}B(d,n+γ)^{12}C peak. The FWHM of the 15.1 MeV peak is marked.

9.3 Timing Resolution

The separation between particle types is based on Time Of Flight (TOF), which depends on the distance between the detector and the target. At 12 metres, the gamma-rays arrive at the detector after 40 ns, while the fastest neutrons, with an energy of approximately 20 MeV, arrive after about 200 ns.

The separation of gamma-rays from neutrons required for DDEGR is achieved with a crude timing resolution of about 100 ns. The combined DDEGR-FNRR system requires a timing resolution of several ns to distinguish the main features of the neutron transmission spectra.

The timing resolution is determined by the gamma peak of the TOF spectrum, in which all the effects of the combined accelerator-detector systems are manifested. It is compared to the timing resolution of a Čerenkov detector that indicates the accelerator's timing resolution since it is sensitive only to gamma-rays. The timing resolution of both TRECOR generations, with LYSO and plastic scintillators, is presented in Table 9.1 and the definitions of the different scintillators of TRECOR-II are given in Fig. 9.5.

The gamma peaks of the LYSO spectra are plotted in Fig. 9.6a. Some of the spectra show a smaller peak to the left of the main gamma peak, caused by a satellite of the main beam that was present in some of the experiments. The presence of the satellite peak in the Čerenkov detector spectrum indicates that it is indeed coming from the accelerator beam and not from the detectors. The TOF profile of both TRECOR generations is plotted in Fig. 9.6b, showing that gamma-neutron separation is accomplished for both generations.

Detector	Scintillator	Source	FWHM (ns)
Čerenkov		^{11}B(d,γ+n)	2.0
TRECOR-I	LYSO	^{11}B(d,γ+n)	2.3
TRECOR-II	LYSO (top)	^{11}B(d,γ+n)	3.9
TRECOR-II	LYSO (bottom)	^{11}B(d,γ+n)	3.9
TRECOR-II	plastic	^{11}B(d,γ+n)	4.0
Čerenkov		^{9}Be(d,n)	1.7
TRECOR-I	plastic	^{9}Be(d,n)	4.5

Table 9.1: Timing resolution of both TRECOR generations, compared to the timing resolution of the Čerenkov detector with the same radiation source. The TRECOR-II different scintillators are marked in Fig. 9.5.

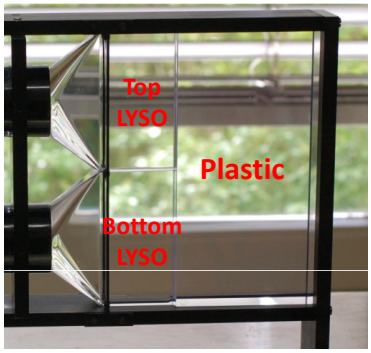

Figure 9.5: TRECOR-II different scintillator parts.

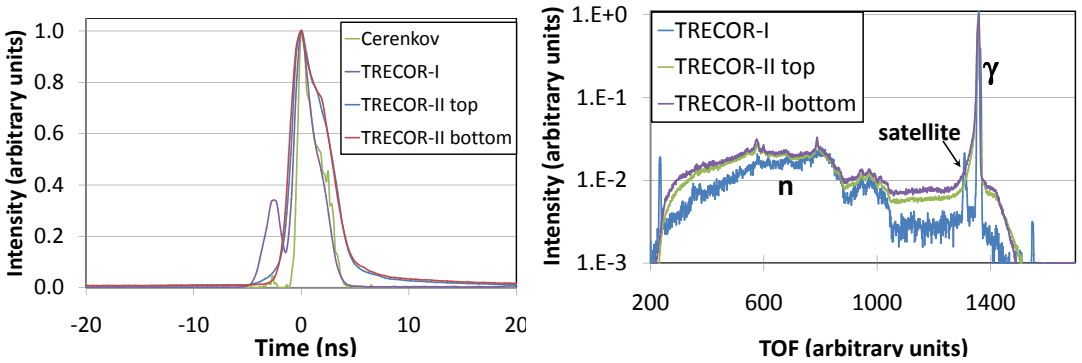

(a) The gamma TOF peak compared to a Čerenkov detector.

(b) TOF profile with the ^{11}B(d,γ+n) reaction as a radiation source.

Figure 9.6: Timing properties of both TRECOR generations - gamma detection mode (TRECOR-I) and LYSO scintillator area (TRECOR-II).

Detection of neutrons in TRECOR-I is completely separate from the detection of gamma-rays. The neutron detection mode of TRECOR-I was tested with the ^{9}Be(d,n) reaction as a neutron source. The gamma peaks of TRECOR-I and the Čerenkov detector, measured with a ^{9}Be(d,n) source are presented in Fig. 9.7a.

TRECOR-II detects gamma-rays and neutrons in parallel so its timing resolution was measured with the ^{11}B(d,γ+n) reaction as a radiation source. The gamma peaks of TRECOR-II and a Čerenkov detector measured with ^{11}B(d,γ+n) source are presented in Fig. 9.7b.

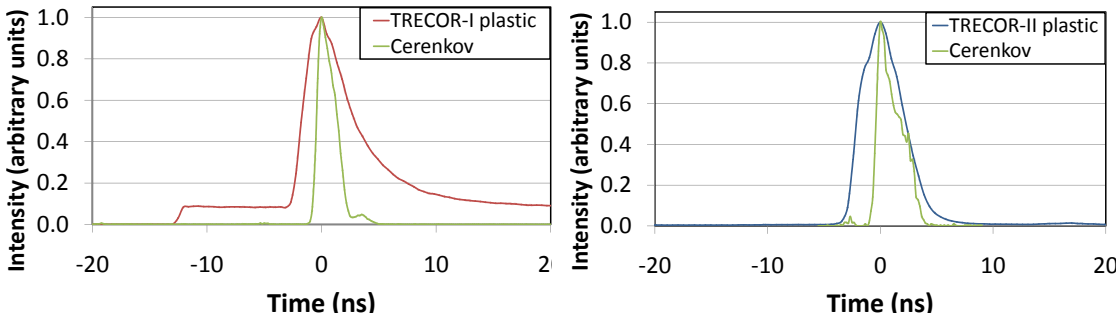

(a) ^{9}Be(d,n) source, TRECOR-I

(b) ^{11}B(d,γ+n), TRECOR-II

Figure 9.7: The gamma TOF peak of both TRECOR generations in neutron detection mode (TRECOR-I) and relevant scintillator area (TRECOR-II) compared to a Čerenkov detector.

The timing resolution of TRECOR-I differs between the gamma (2.3 ns) and neutron (4.5 ns) detection modes. The gamma detection mode triggers events through a PMT connected to the LYSO scintillator bulk, in which the scintillation light travels freely and can be collected by the PMT. The neutron detection mode triggers events through the ECII which collects the light from the plastic scintillator fibres. Less than 10% of the light created in a fibre is emitted at its end, and considering the solid angle between the fibre and the lens shows that only a single photon will reach the ECII photocathode.

Therefore, detection of most of the events is based on a single scintillation photon, making the timing resolution dependant on the light decay properties of the scintillator. The plastic scintillator decay times (and corresponding intensities) are 2.5 ns (95%), 12 ns (2.5%) and 68 ns (0.2%). This effect is seen in Fig. 9.7a, in which the plastic scintillator decay is clear on the right side of the peak.

In TRECOR-II, both the LYSO and the plastic scintillators are bulk scintillators, and both are attached to the PMT. The timing resolution is therefore identical for both (4 ns) and it is double the beam timing resolution (2 ns).

TRECOR-II is similar to TRECOR-I gamma detection mode in its readout method, but TRECOR-II timing resolution is almost double that of TRECOR-I (4 ns comparing to 2.3 ns) because of the different electronic setup.

In TRECOR-I gamma mode the events are triggered by the PMT anode through the CFDx first output, which doubles as the TOF measurement start signal.

In TRECOR-II, the ECII is responsible for the start signal. The ECII anode signal, which is vetoed by the PMT, is fed into a constant fraction unit where a blocking logic is applied to stop a second event from coming while the first is being measured. Because of this blocking logic, two outputs are fed into a second constant fraction unit, from the update and overlap outputs of the first unit. To fit both outputs into the same time window a 2 ns delay is added to the update output. When both signals coincide in the second unit, it sends the start signal to the TDC. The variances in the timing between the two signals arriving to the second constant fraction unit effect the TOF resolution.

TOF spectra of transmission through carbon as measured with TRECOR-I (with a ^{9}Be(d,n) radiation source) and TRECOR-II (with a ^{11}B(d,γ+n) radiation source) are compared to TOF calculated from cross section [234] in Fig. 9.8. As expected, the typical transmission spectrum is seen in both, but the timing resolution does not enable measuring the fine (less than 1 ns) features.

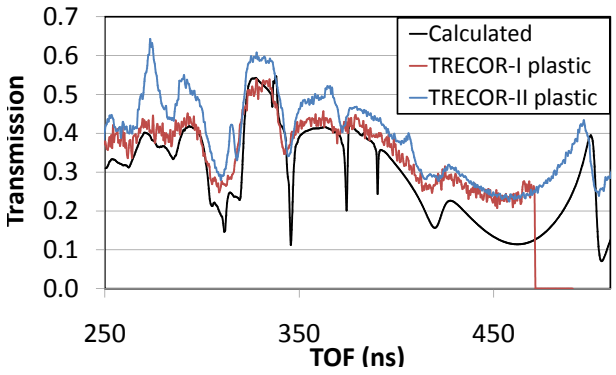

Figure 9.8: TOF spectra of transmission through Carbon as measured with TRECOR-I (with a ^{9}Be(d,n) radiation source) and TRECOTR-II (with a ^{11}B(d,γ+n) radiation source) compared to TOF calculated from cross section [234].

9.4 Spatial Resolution

9.4.1 Position Calculation

The spatial resolution of the detector is determined by a combination of the responses of the system parts and specifically by the scintillator and the optical components. As discussed in earlier sections, the electron tracks generated by the 15.1 MeV gamma-rays set the limit on spatial resolution, as they are the broadest tracks generated when using a ^{11}B(d,n+γ) source.

The position is determined in the ECII by calculating the Centre-Of-Gravity (COG) of the emitted light (see Fig. 8.4). The COG is calculated by:

$$R_{COG} = \frac{\sum E_i X_i}{\sum E_i} \tag{9.2}$$

where R_{COG} is the location of the COG and E_i is the energy deposited in position X_i.

The hit location is the place in which the gamma-ray has first interacted with the scintillator. Two examples of simulated tracks created by individual 15.1 MeV gamma-rays are presented in Fig. 9.9. On each track the hit position, the COG and the distance between them are marked. Even though track projections are broad, the COGs are relatively close to the hit position for both cases.

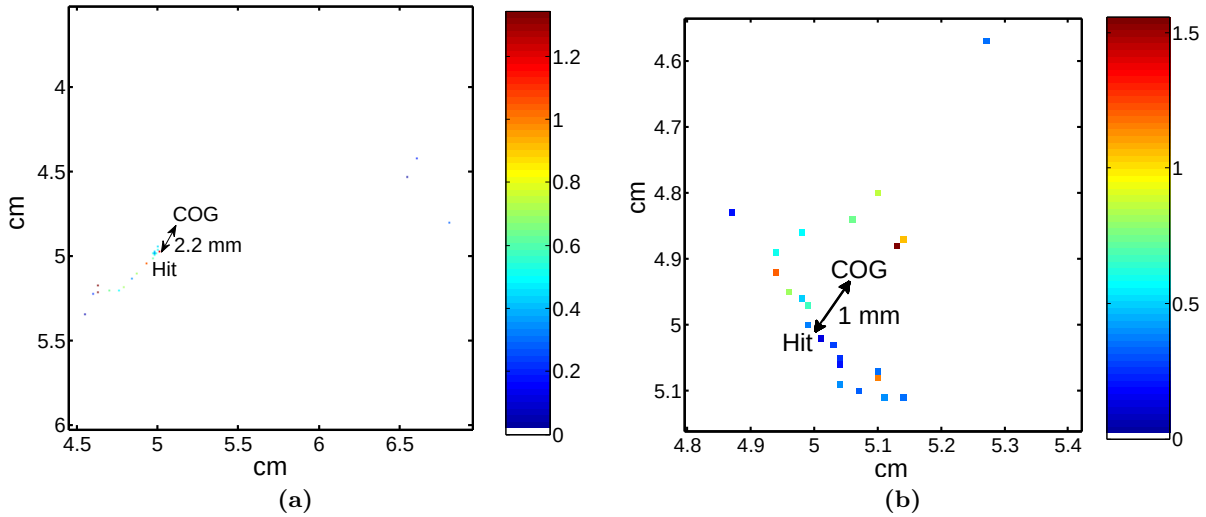

Figure 9.9: Demonstration of the COG concept. Two tracks created by individual 15.1 MeV gamma-rays. The coloured areas are locations where energy was deposited, where the colour represents the amount of deposited energy. The hit (the location where the gamma-ray first interacted) and the COG locations are marked, along with the distance between them. The tracks were simulated with GEANT4.

Fig. 9.10 shows a scatter plot of the simulated hit-COG distance and the deposited energy for 15.1 MeV gamma-rays. The scatter plot shows that gamma-rays that deposit more energy are more likely to have a large hit-COG distance: average track distances are 0.3, 0.9 and 2 mm for 1, 4, and 15 MeV gamma-rays, respectively.

Gamma-rays deposit energy via electrons, which deposit a constant amount of energy per distance unit, independent of their initial energy. Thus, energetic electrons will deposit their energy over larger distances, creating larger tracks and increasing the probability of a large hit-COG distance, reducing the accuracy of the COG calculation.

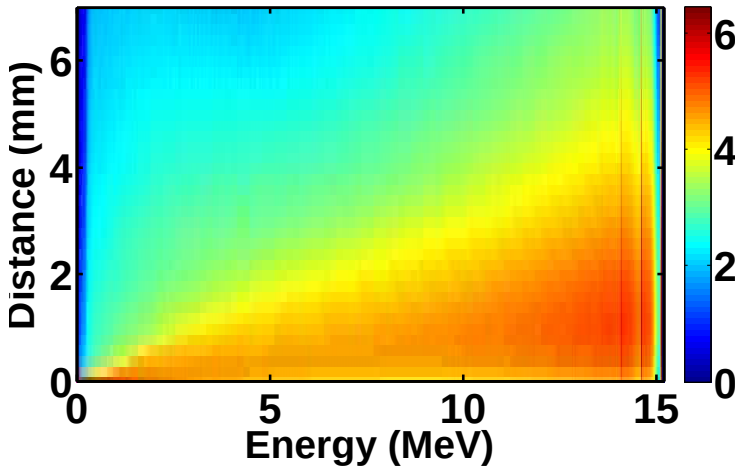

Figure 9.10: A scatter plot of the simulated hit-COG distance and the deposited energy for 15.1 MeV gamma-rays. The colour scale represents number of counts, where the simulation included 10^9 primary gamma-rays. The colour scale is logarithmic.

The hit-COG distance integrated over all energies is presented in Table 9.2 and graphically in Fig. 9.11. Table 9.2 details the percentage of tracks whose COG fall within a given distance from the hit position. Fig. 9.11 shows the distribution of the distance between the hits and the COG locations for 20 mm thick LYSO, for 4.4 and 15.1 MeV gamma-rays, with a ratio of 5:1 in favour of the first (the experimentally measured ratio of these gamma-rays) and the joint distribution of both energies. The distributions peaks are at 2-3 mm, with tails that continue into the cm range. Thus, a spatial resolution of about 2 mm can be expected, as the majority of events are below 2 mm.

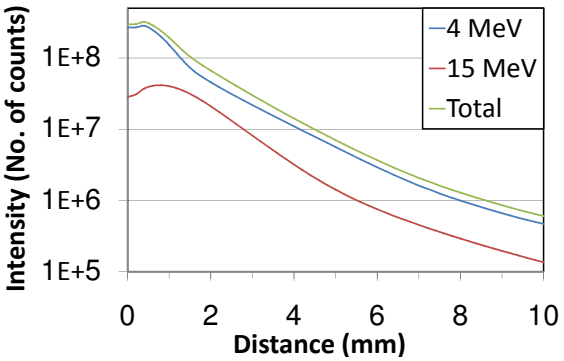

Figure 9.11: Distribution of the distance between the hit and the COG locations for 2 cm thick LYSO.

up to	4.4 MeV	15.1 MeV	Total
1 mm	68%	46%	64%
2 mm	85%	77%	84%
3 mm	92%	90%	92%
4 mm	96%	95%	96%
5 mm	98%	97%	98s%

Table 9.2: Percentage of tracks in which the distance between the hit and the COG locations falls within the specified range, for 20 mm thick LYSO slab and both gamma-rays energies.

The main optical cause for loss of resolution is from the depth-of focus effect, because the focus of the lens is set to be in the middle of the 20 mm thick scintillator. The resulting blur is a circle of 2.2 mm diameter. Therefore, the blurs from the optical system and from the electron tracks in the scintillator are similar, leading to an expected spatial resolution of 2.5 mm.

9.4.2 Contrast Transfer Function

The Contrast Transfer Function (CTF) provides a way to evaluate the spatial resolution of the detectors. It is a measure of how well the detector reproduces the true contrast of a test object at different spatial frequencies. In this case the test object was a steel mask, 10×10 cm^2 with slits at increasing spatial frequencies. A photograph of this CTF mask is presented in Fig. 9.12. The mask is 2 cm thick in the centre and 1 cm thick on the top and bottom sides.

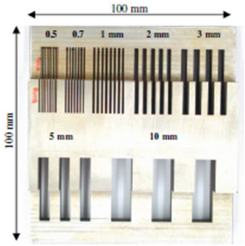

Figure 9.12: A photograph of the iron CTF mask used in the experiment and simulations. The mask is 2 cm thick in the centre and 1 cm thick on the top and bottom sides.

The spatial resolution is inversely related to gamma-ray energy. Therefore, the 15.1 MeV gamma-rays (the highest energy in the radiation source spectrum) are expected to have the worst spatial resolution. A simulated radiographic image is presented in Fig. 9.13, divided into the side of the mask with narrow slits and the side of the mask with broad slits. Experimental radiographic images with all gamma-rays energies in the spectrum are presented in Fig. 9.14. These images were measured with TRECOR-II in the LYSO scintillator side, which is the gamma-converter side of the scintillator screen. The neutrons detected by the LYSO were eliminated by a condition on the TOF spectrum.

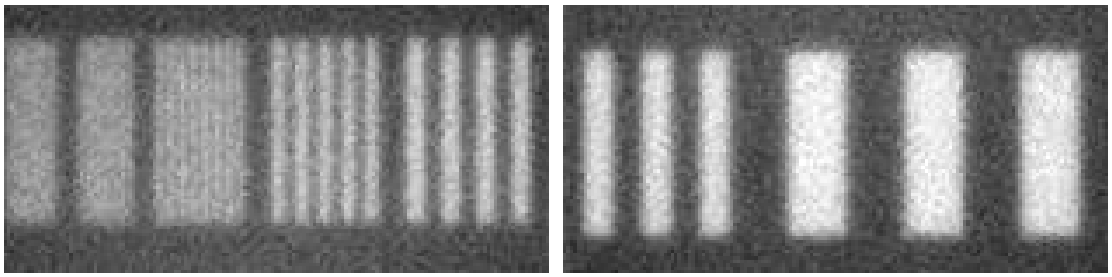

(a) Narrow slits side **(b)** Broad slits side

Figure 9.13: A simulated radiography image of the CTF mask with 15.1 MeV gamma-rays.

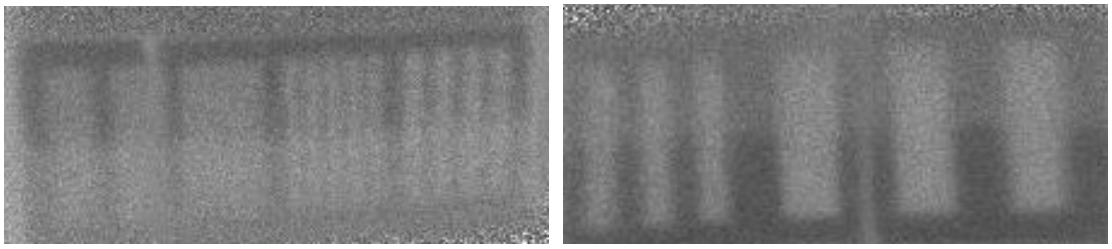

(a) Narrow slits side **(b)** Broad slits side

Figure 9.14: A normalized experimental radiography image of the CTF mask with TRECOR-II with all gamma energies. In the experimental CTF two CTF mask thicknesses are visible, contrary to the simulated image.

Profiles along these images are presented in Fig. 9.15. In this analysis of the experimental results the 2 cm thick part was used and therefore a 2 cm thick CTF mask was simulated. The simulation does not include the optical effects that are expected to limit the spatial resolution to 2 mm. Therefore, the smallest visible slits are 1 mm. In the experimental profiles, limited by the depth-of-focus effect, the smallest visible slits are 3 mm.

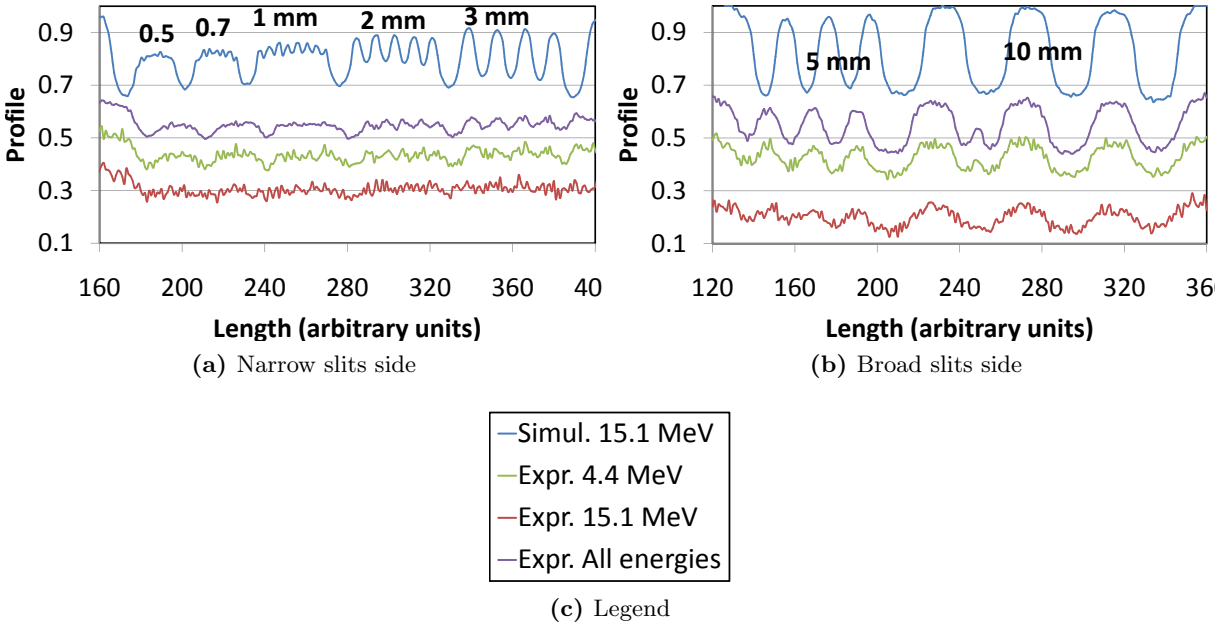

(a) Narrow slits side

(b) Broad slits side

(c) Legend

Figure 9.15: Profiles of the radiographic images of the CTF mask. The Y-axes of the profiles are in arbitrary units and do not represent transmission directly, as they were shifted to enable a clear representation of all profiles on the same graph.

The %CTF function is used to quantify the spatial resolution. It is defined by:

$$\%\ CTF = \frac{\left(\frac{T(w)_{max} - T(w)_{min}}{T(w)_{max} + T(w)_{min}}\right)_{m}}{\left(\frac{T(w)_{max} - T(w)_{min}}{T(w)_{max} + T(w)_{min}}\right)_{expect}} \tag{9.3}$$

$T(w)_{max}$ and $T(w)_{min}$ are the transmission values at maximum and minimum points of the transmission spectrum for each spatial frequency w, respectively. The indices m and *expect* stands for measured and expected values. The spatial frequency is measured in line-pairs per mm (lp/mm). For example, 2 mm slits compose a 4 mm line-pair, which transforms into 1/4=0.25 lp/mm.

The spatial resolution of the detector is determined by a combination of all the responses of system parts, the major issues being the scintillator screen, the optical components and the statistics.

The %CTF is presented in Fig. 9.16 and detailed in Table 9.4. If we set the accepted limit of 10% as the lowest value that is still detectable, the spatial resolution of the simulated 15.1 MeV gamma-rays is 0.5 lp/mm, or 1 mm slits. The measured %CTF of 15.1 MeV gamma-rays is just above 0.17 lp/mm (3 mm slits), significantly different than the expected 0.25 lp/mm (2 mm slits).

The combination of the fast timing electronics with the long decay of the LYSO is the probable cause for the reduction in resolution. The ECII timing does not permit integration

over the entire LYSO signal and instead uses just one photon to determine the position.

To calculate the %CTF (see Eq.9.3), we need to first calculate the theoretical transmission. However, the all-energies transmission is hard to calculate theoretically, since we need to know the exact composition of the gamma-ray spectrum reaching the detector. Instead, the empty areas of the CTF image, areas of the image with no slits or with no mask, provide experimental measurement of the all-energies spectrum transmissions $T(w)_{min,expect}$ and $T(w)_{max,expect}$, respectively.

The best experimental CTF is the all-energies CTF, which includes all the available gamma-rays, including low energy gamma-rays present in the spectrum (see Fig. 9.4). The spatial resolution is inverse to the gamma-ray energy, so these low energy gamma-rays improve the spatial resolution. These low energy gamma-rays will be used for the image presented to system operator but do not take part in the material separation process. Moreover, because of their low energy they will be strongly attenuated in the cargo container, resulting in lower abundance.

The spatial resolution available with all gamma-ray energies is just above 2 mm, consistent with 2.2 mm limit from depth-of-focus effect. The spatial resolution available with 4.4 MeV gamma-rays is below 3 mm, sufficient for the 5 mm resolution defined as a requirement for the DDEGR system detector (see Section 3.1).

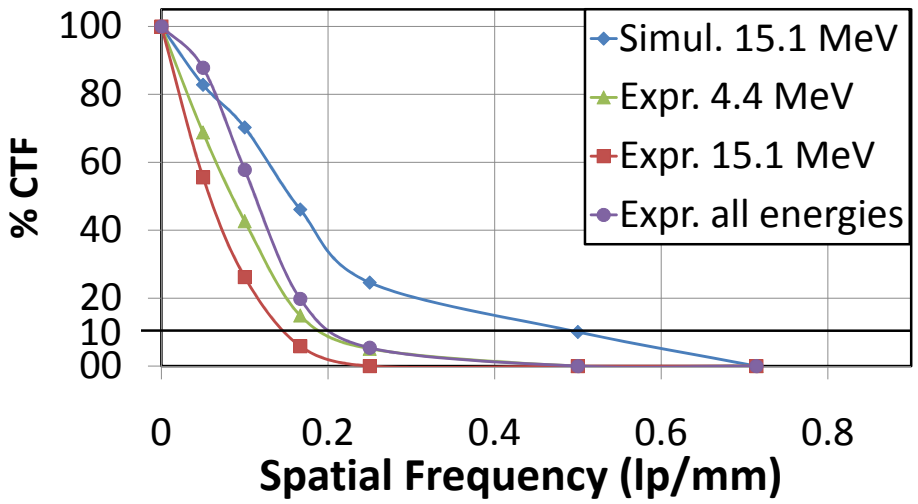

Figure 9.16: Gamma %CTF, simulated and experimental.

Width		Simulated	Experimental % CTF		
(mm)	lp/mm	15.1 MeV	15.1 MeV	4.4 MeV	All energies
inf	0	100	100	100	100
10	0.05	83	56	69	88
5	0.1	70	26	43	58
3	0.17	46	6	15	20
2	0.25	25	0	5	5
1	0.5	10	0	0	0
0.7	0.7	0	0	0	0

Table 9.3: Gamma %CTF, simulated and experimental.

9.4.2.1 Neutron CTF

The same CTF mask was used to measure the neutron-induced spatial resolution of TRECOR-I and TRECOR-II. In TRECOR-II, the neutron spatial resolution is measured in the plastic scintillator, which is the neutron converter side of the scintillator screen (see Fig. 9.5).

Radiographic images of the CTF mask as measured with 7.5 MeV neutrons are presented in Figs. 9.17 and 9.18 for TRECOR-I and TRECOR-II, respectively. Profiles of the 7.5 MeV neutrons are presented in Fig. 9.19 and the %CTF is presented in Fig. 9.20.

Images of the CTF mask that include all neutron energies, containing a high number of events, are presented in Figs. 9.21 and Fig. 9.22 for TRECOR-I and TRECOR-II, respectively.

The 7.5 MeV neutron images are characterised by reduced statistics compared to the all-energies images, but they have a defined transmission that enables calculation of the %CTF. 7.5 MeV is approximately the average energy of neutrons in the spectrum, so it enables comparison to previous works [13].

Neutrons deposit energy in the scintillator mainly via elastic collisions with hydrogen atoms, creating energetic recoil protons that deposit energy in a series of collisions. A 7.5 MeV proton will have a range of approximately 0.5 mm. Multiple scattering of neutrons inside the scintillator may also add to the background [13].

TRECOR-I's neutron converter is a plastic fibre scintillator screen, where each fibre has lateral dimensions of 0.7×0.7 mm^2. The limit on the spatial resolution is the size of an individual fibre, which is larger than the proton tracks.

TRECOR-II's neutron converter is a plastic bulk scintillator. The expected loss of resolution from neutron tracks is much less than the 2 mm optical resolution loss from Depth-of-focus.

The spatial resolution of TRECOR-I is better than that of TRECOR-II, because of TRECOR-I's fibre screen. Both spatial resolutions are as expected, approximately 1 mm for TRECOR-I (just above the 0.7 from the fibres) and approximately 2 mm for TRECOR-II, dictated by the optical effects and the statistics.

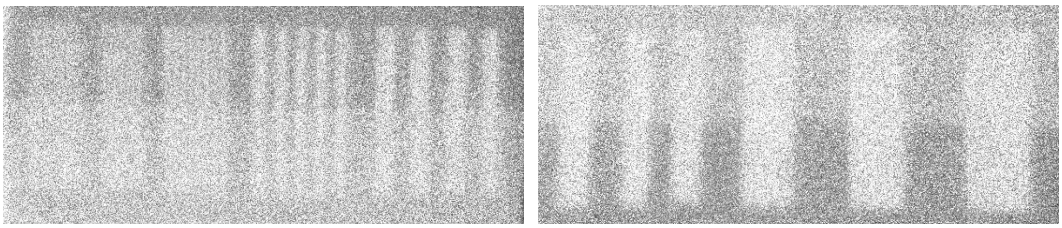

(a) Narrow slits side **(b)** Broad slits side

Figure 9.17: A TRECOR-I normalized experimental radiography image of the CTF mask with 7.5 MeV neutrons.

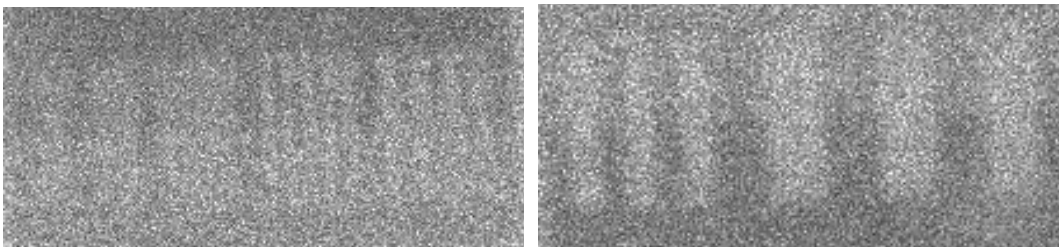

(a) Narrow slits side **(b)** Broad slits side

Figure 9.18: A TRECOR-II normalized experimental radiography image of the CTF mask with 7.5 MeV neutrons.

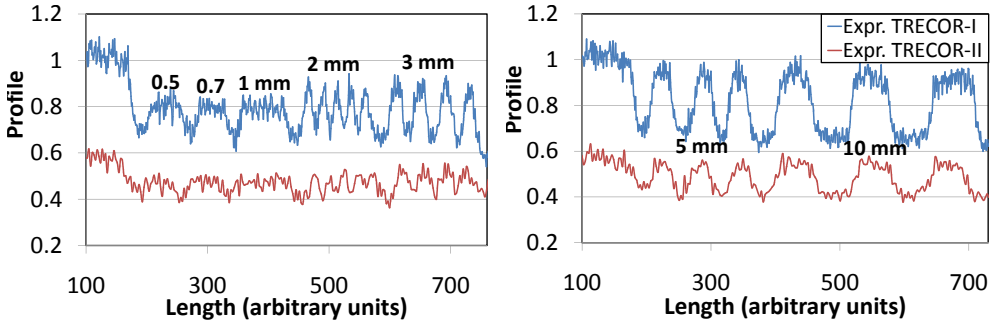

(a) Narrow slits side **(b)** Broad slits side

Figure 9.19: Profiles of the radiographic image of the CTF mask with 7.5 MeV neutrons. The Y-axes of the profiles are in arbitrary units and do not represent transmission directly, as they were shifted to enable a clear representation of all profiles on the same graph.

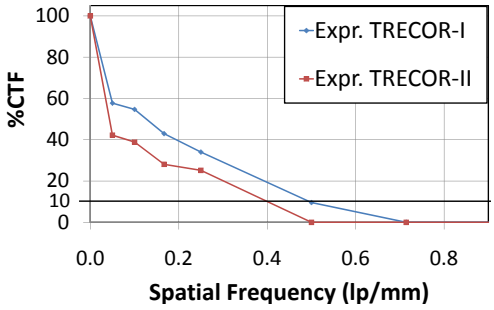

Figure 9.20: Experimental %CTF of TRECOR-I and II with 7.5 MeV neutrons.

Width		7.5 MeV neutrons	
(mm)	lp/mm	TRECOR-I	TRECOR-II
inf	0	100	100
10	0.05	58	42
5	0.1	55	39
3	0.17	43	28
2	0.25	34	25
1	0.5	10	0
0.7	0.7	0	0

Table 9.4: Neutron experimental %CTF.

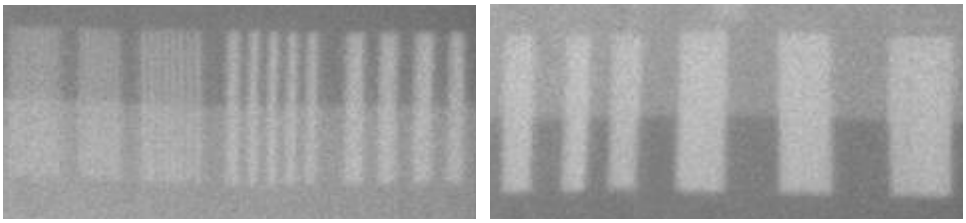

(a) Narrow slits side **(b)** Broad slits side

Figure 9.21: A normalized experimental radiography image of the CTF mask with TRECOR-I, integrated over all neutron energies. TRECOR-I's neutron converter is a plastic fibre scintillator screen. The radiation source in this measurement was the ^{9}Be(d,n) reaction.

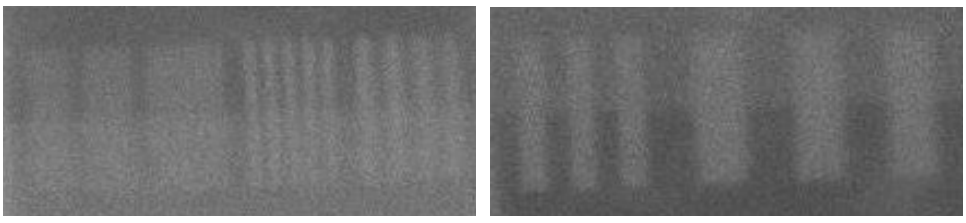

(a) Narrow slits side **(b)** Broad slits side

Figure 9.22: A normalized experimental radiography image of the CTF mask with TRECOR-II, integrated over all neutron energies. TRECOR-II's neutron converter is a plastic scintillator bulk. The radiation source in this measurement was the ^{11}B(d,γ+n) reaction.

Part IV

Experimental DDEGR Demonstration

CHAPTER

10

MATERIAL SEPARATION

10.1 Transmission Through Samples

The transmission of gamma-rays through a sample is calculated by dividing the number of gamma-rays measured with and without the sample in the beam path to the detector. Each measurement is normalized to the integrated charge of the accelerator beam. The different gamma-ray energies in the spectrum have to be separated in order to get the correct transmission for each gamma-ray energy.

The measured spectrum is that of the energy deposited in the detector. Since gamma-rays do not necessarily deposit all their energy at every interaction the detector response to each gamma-ray energy will be a continuum of energies spreading from the full gamma-ray energy to zero. However, the effect on the transmission calculation should be minor due to the small size of the contribution.

If we assume that the 4.4 and 15.1 MeV gamma-rays dominate the spectrum, the transmission of each point in the spectrum should be that of the 15.1 or 4.4 MeV gamma-ray. Such a "transmission spectrum" is presented in Fig. 10.1 for a 10 cm thick carbon sample. The spectrum measured with a carbon sample was divided by the spectrum measured without any sample, both normalized to the integrated charge of the accelerator beam.

The per-channel transmission remains constant over large parts of the transmission spectrum. The 4.4 MeV transmission is constant between 3-5 MeV with 7% standard deviation, resulting from the number of events per channels. Below 3 MeV, lower energy gamma-rays prevail and the transmission drops.

The 15.1 MeV transmission is affected by inferior statistics, but the transmission remains constant between 8-15 MeV with 15% standard deviation.

To improve the statistics, the following transmission calculations will integrate over larger energy bins, presented in Fig. 10.2. The bins are 3-5 MeV and 8-15.5 MeV for 4.4 and 15.1 MeV gamma-rays, respectively. The typical number of events in such energy bins results in a standard deviation of about 1%.

Comparison of the experimental transmission to the expected transmission, calculated from

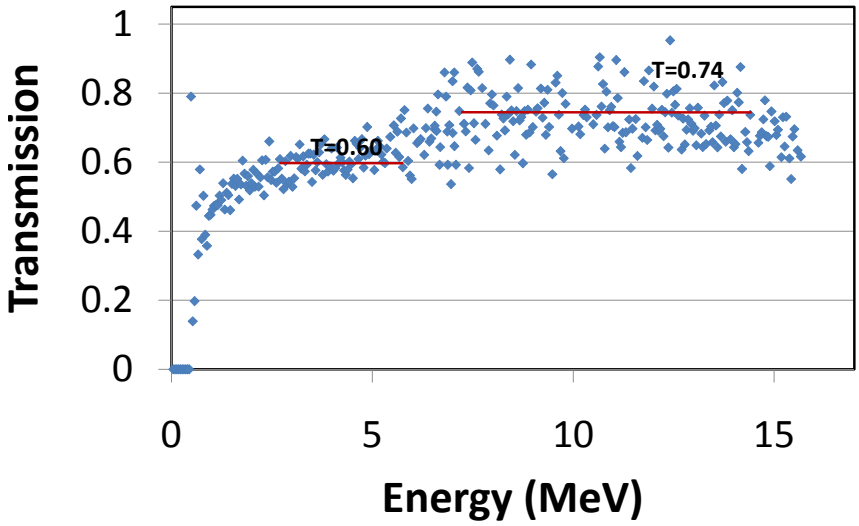

Figure 10.1: A "transmission spectrum" of a 10 cm carbon sample. The spectrum measured with a carbon sample was divided by the spectrum measured without any sample, both normalized to the integrated charge of the accelerator beam.

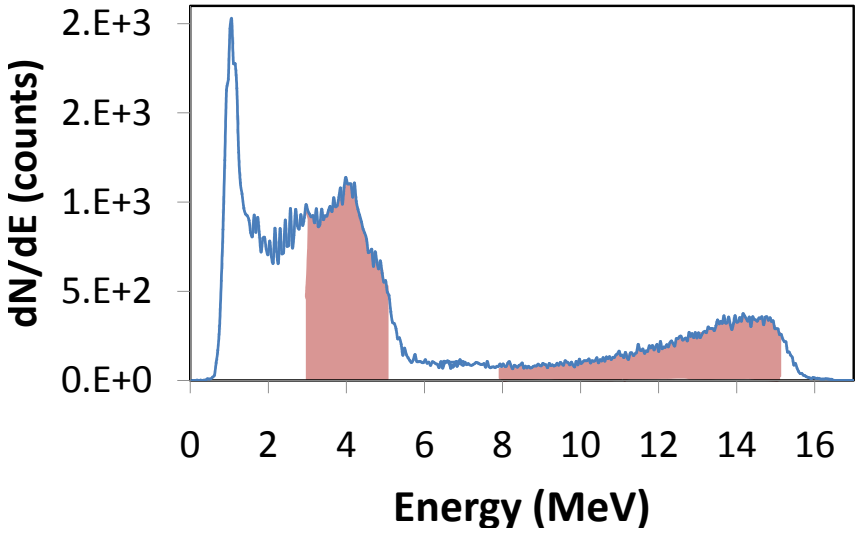

Figure 10.2: The energy bins integrated upon in the transmission calculations.

cross-sections [30], for 4.4 and 15.1 MeV gamma-rays is presented in Table 10.1. The experimental transmission is always higher than the expected transmission, by an average 6%. This may be the result of background in the experiment, discussed in Appendix A.

10.2 DDEGR Laboratory Prototype

The DDEGR system laboratory prototype was built in the PTB cyclotron experimental hall. The radiation source was the ^{11}B(d,γ+n)^{12}C reaction, the object was mounted on a scanning device suited for large objects and the detector used was TRECOR-II. The schematics of the DDEGR prototype is presented in Fig. 10.3.

		4.43 MeV			15.1 MeV		
	X (cm)	**Theory**	**Expr.**	±	**Theory**	**Expr.**	±
C	10	0.60	0.62	0.04	0.74	0.76	0.11
Al	8.0	0.53	0.56	0.04	0.62	0.67	0.10
Fe	1.1	0.76	0.80	0.06	0.76	0.82	0.12
Fe	2.2	0.59	0.61	0.04	0.60	0.65	0.10
Fe	5.2	0.28	0.30	0.02	0.29	0.31	0.05
Cu	2.9	0.43	0.44	0.03	0.43	0.45	0.07
Pb	1.0	0.64	0.60	0.04	0.54	0.53	0.08
Pb	2.0	0.41	0.43	0.03	0.30	0.33	0.05
W	0.6	0.67	0.65	0.05	0.59	0.59	0.09
W	1.1	0.43	0.44	0.03	0.33	0.36	0.05

Table 10.1: Transmission values calculated from cross section (Theory) and measured experimentally (Expr.)

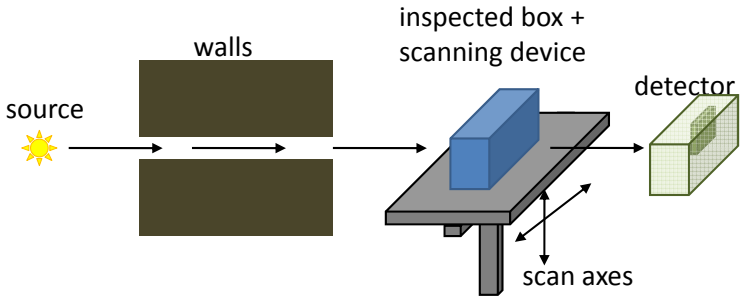

Figure 10.3: Schematics of the DDEGR prototype

The scanning device, seen in Fig. 10.4, is basically a table capable of movement in two dimensions, horizontal and vertical. The two translations permit to systematically scan a side of a container. The scanner was controlled from a remote computer that enabled determination of the final coordinates of the table and the velocity with which it moves to that location.

The scanned object is an aluminium box 60×28×35 cm^3, seen in Fig 10.5a. It was filled with the objects listed in Table 10.2. The objects were arranged side-by-side, their arrangement demonstrated in Fig. 10.5b. The box was filled with 20 mm thick polystyrene foam panels (density = 0.03 g/cm^3), stacked on top of each other. Holes with the appropriate shapes were cut in each panel to enable the positioning of the standards. The scan of the container side was composed of 14 measurements with 4 cm translation between them.

The standards were selected to demonstrate the DDEGR system capabilities and the neutron detection capability of the combined system (which is not a part of this work). The DDEGR demonstration is based on the medium and high-Z standards, namely copper, iron, lead and an uranium cylinder.

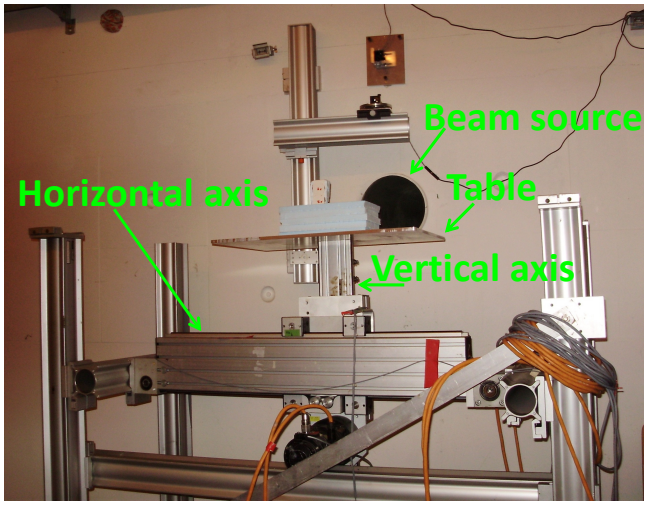

Figure 10.4: The scanning device positioned in the experimental hall. The object on the scanning device table is set to be irradiated. TRECOR detector is behind the camera.

(a) The aluminium box used as a mini-container.

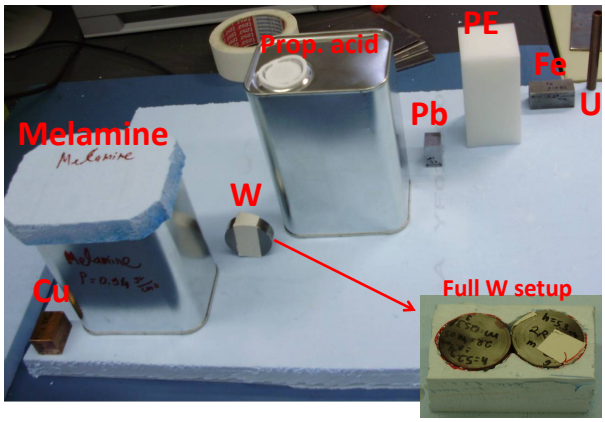

(b) Standards orgenized in a pattern similar to the one inside the mini-container.

Figure 10.5: The scanned box and standards inside it. The dimensions and content of the standards are detailed in Table 10.2. Only half of the tungsten sample is seen in the large photograph. The final tungsten setup, including two large coins (4 cm diameter) is presented in the bottom right side of the image. The two coins were positioned on top of each other inside the box.

Material	Cu	Melamine	W	W	Propionic acid	Pb	Polyethylen (PE)	Fe	U
Thickness (cm)	2.9	7.7	0.5	1.1	7.7	2.0	5.0	2.0	1*
Density (g/cm^3)	8.9	0.94	19.1	19.1	1.0	11.2	0.97	7.8	18.9
Z	29	6.4	74	74	6.6	82	5.2	26	92

Table 10.2: List of the objects that were used as standards inside the mini-container and their thickness in the beam direction. For U, this value is diameter of the cylinder.

10.2.1 Transmission Through the Container

The scan of the entire box is composed of different images, each individual image contributing a slice. The vertical lines in the scan image are the borders between these slices. The different images were taken at 4 cm steps while the LYSO scintillator is 5 cm wide, intending to have some overlap between the images that will enable a composed scan image that is smooth.

However, the edges of each image were blurred as a result of reflections from the interface with the plastic scintillator from the one side and the light guide from the other. The actual image acquired in each step was therefore smaller and the composed image is discontinuous. A composed image is presented in Fig. 10.6a, where the horizontal line is the seam between the top and bottom LYSO blocks.

After composing a scan image, a normalization was required to produce a transmission image. The transmission was achieved by dividing the composed scan image by an image measured with an empty scene (a 'flat'). Each pixel in the scan image and the 'flat' image was divided by the integrated charge of the accelerator beam. After the normalization, the value inside each pixel of the transmission image equals the transmission of the object seen in it. The transmission images of 4.4 and 15.1 MeV gamma-rays are presented in Figs. 10.6b and 10.6c, respectively. As expected, the 4.4 MeV image has a better statistics and resolution.

The transmission image is affected by the statistics and by the gamma-ray energy, where lower energy gamma-rays will result in better spatial resolution. Therefore, the best transmission image is that of all gamma-ray energies, seen in Fig. 10.6a. It includes a large number of gamma-rays at low energies (1-2 MeV) and has the highest statistics.

The average transmission through the standards was extracted from the image by averaging the transmission value over many pixels. An example of such an integration area, for the iron standard, is presented by the red square marked "standard" in Fig. 10.6a. The integration area is always smaller than the actual standard to eliminate edge effects.

Each transmission value was further normalized to the average transmission in an empty area of image, called "side flat" – an empty area of the image representing the transmission through the aluminium box and the Styrofoam. An example of such a side flat, used for the iron sample, is presented in Fig. 10.6a. The side flat should preferably be in the same LYSO slab as the standard.

The average transmission of the standards is presented in Table 10.3. No transmission values are presented for the uranium cylinder as its thickness in the beam path is not uniform and the statistics was too poor to permit a reliable estimation. The average transmission values have deviations of up to 10% from theoretical values that could be explained by a non-uniformity in the light collection from the scintillator. Comparison of several side flats in a single image that showed up to 35% difference supports this explanation.

The errors were evaluated considering the uncertainty on each object's thickness and density, the alignment of the box in the beam direction and a 5% uncertainty in the gamma-ray energy for 4.4 MeV gamma-rays, which determines the mass attenuation coefficient.

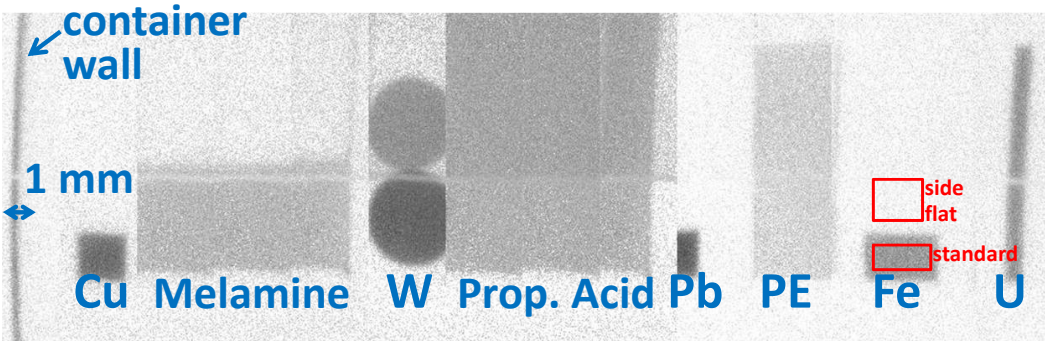

(a) Transmission image with all gamma-rays energies.

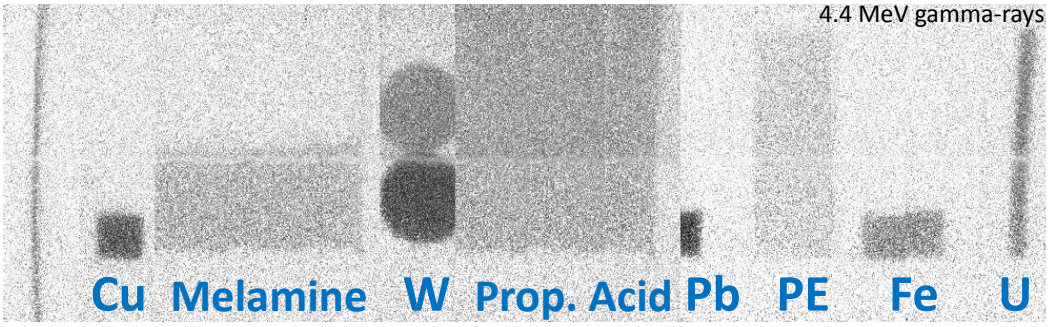

(b) Transmission image with 4.4 MeV gamma-rays.

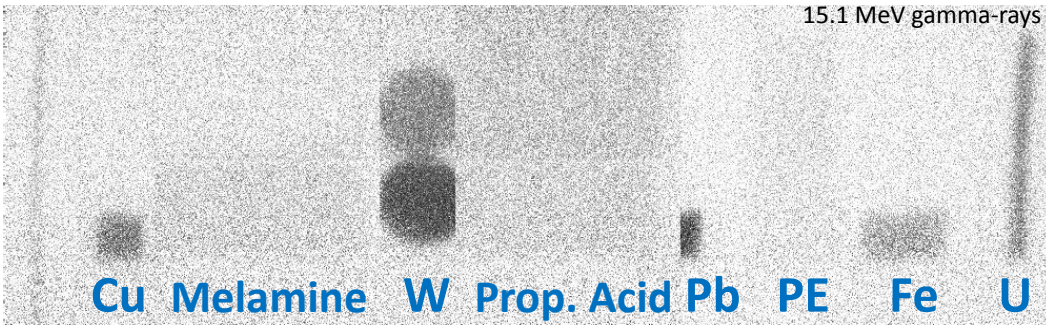

(c) Transmission image with 15.1 MeV gamma-rays.

Figure 10.6: Transmission images at different gamma-ray energies.

	4.43 MeV			15.1 MeV		
Material	**Theory**	**Expr.**	±	**Theory**	**Expr.**	±
Cu	0.43	0.47	0.12	0.43	0.46	0.04
Melamine	0.80	0.79	0.17	0.88	0.83	0.02
W1	0.67	0.64	0.16	0.59	0.56	0.04
W2	0.43	0.46	0.10	0.33	0.35	0.04
propionic acid	0.79	0.76	0.14	0.87	0.84	0.02
Pb	0.39	0.40	0.09	0.28	0.31	0.04
Polyethylen	0.86	0.82	0.10	0.92	0.86	0.01
Fe	0.61	0.67	0.14	0.62	0.69	0.04
U	N/A	N/A		N/A	N/A	

Table 10.3: The measured average transmission through standards inside the mini-container after normalization.

10.2.2 Material Discrimination with R

Separation of materials into different groups, which is based on the simple DER principles, relies on the discrimination parameter R, defined by $R = \frac{\mu_{High}}{\mu_{Low}}$, in this case $R = \frac{\mu_{15.1}}{\mu_{4.43}}$ (defined in Section 6.1.1). It enables separation of high-Z elements from low- and medium-Z ones, reducing the clutter in the image and thus making detection of high-Z objects easier.

Experimentally, R was calculated from the transmission images, per pixel, and the composed image is presented in Fig. 10.7. The three images in Fig. 10.7 are for three different threshold values: no threshold, R_{min}=0.5 and R_{min}=0.9. The clutter in the image decreases as the threshold value increases.

In Fig. 10.7a, where no threshold is applied, all the objects are visible. When the threshold is set to R_{min}=0.5, the low-Z objects (melamine, polyethylene and propionic acid) disappear from the image and the medium- (iron and copper) and high-Z (tungsten, lead and uranium) objects are still visible. Further increasing the threshold to R_{min}=0.9, the medium-Z elements disappear and the image is no longer cluttered: only high-Z materials are visible.

Average R parameters, calculated over the same image areas as in Table 10.3, are presented in Table 10.4. Although the average R of uranium cannot be extracted, the uranium cylinder is detectable in the images, especially in Fig. 10.7c that shows only the high-Z objects.

The standard deviations over each object are typically close to 70% because of the low statistics in each pixel. However, the average experimental values are similar to the theoretical ones and visually the objects are easily distinguished.

Material	**R Theory**	**R Expr.**	±
Cu	1.0	1.0	0.2
Melamine	0.6	0.7	0.1
W	1.3	1.4	0.2
W	1.3	1.3	0.2
Propionic acid	0.6	0.7	0.1
Pb	1.4	1.3	0.2
Polyethylene (PE)	0.6	0.4	0.2
Fe	1.0	1.0	0.1
U	N/A	N/A	

Table 10.4: Average R values, experimentally measured, compared to values calculated from cross sections [30]. The experimental values are averaged over the area of each object in the scan image.

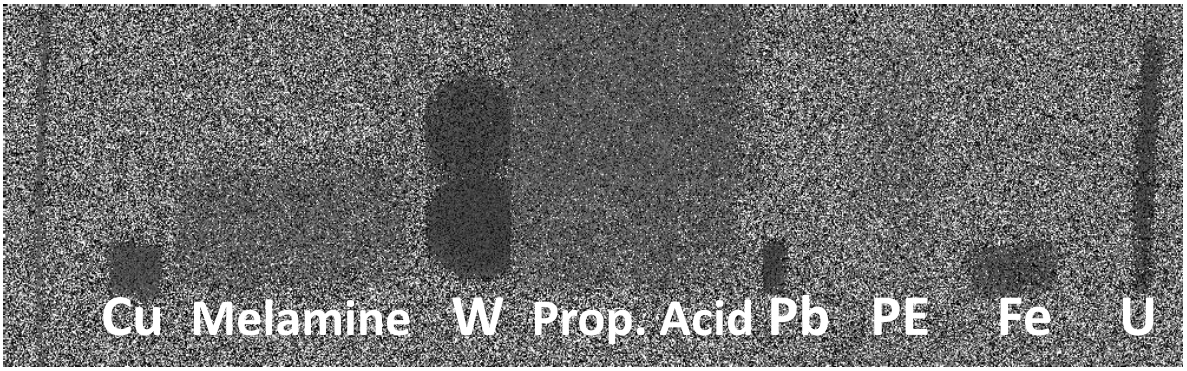

(a) Scan image of R with no lower threshold.

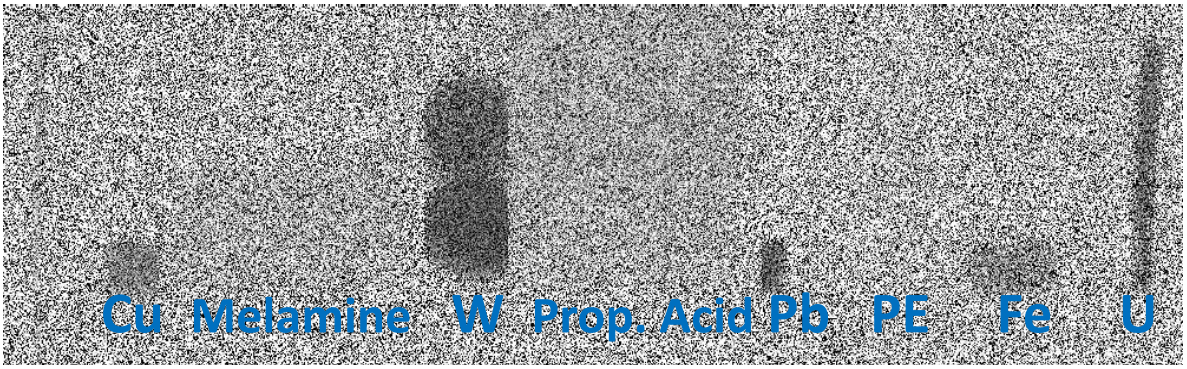

(b) Scan image of R with lower threshold R_{min}=0.5.

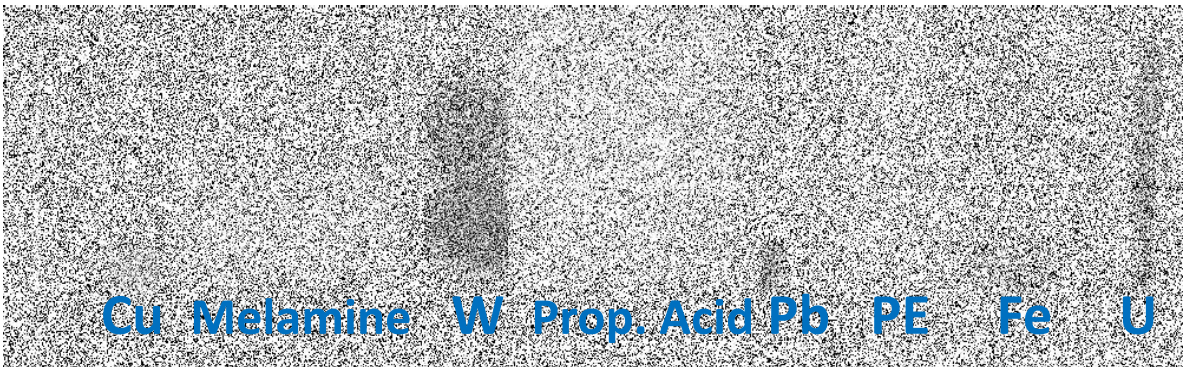

(c) Scan image of R with lower threshold R_{min}=0.9.

Figure 10.7: Scan images of the discrimination parameter R with different lower thresholds.

10.2.3 Material Discrimination with $\mu\rho$

Separation based on the macroscopic attenuation coefficient $\mu\rho$ enables separation between benign high-Z materials and materials that are suspected as SNM (as explained Section 2.2.2) as well as separation of high-Z from low- and medium-Z materials (which can be achieved with the simpler separation based on R).

The parameter $\mu\rho$ was calculated from the transmission values for each image pixel using the equation:

$$\mu_i\rho = -\frac{ln\,(T_i)}{d} \tag{10.1}$$

where T is the measured transmission, d is the thickness of each object and i is the gamma-ray energy - 4.4 or 15.1 MeV.

Ideally, tomography should be implemented to reconstruct the thickness of the objects ap-

pearing in each pixel, as described in Section 6.1.2. However, in our experiment only one view of the container was measured, requiring that the pre-known thicknesses of the objects will be used in the analysis.

In the analysis the scan image was divided into slices, each slice containing a single object. Fig. 10.8 shows one such slice, with a copper object. Each slice was divided by the thickness of the object seen in it, including the empty parts of the image (the backdrop). For example, in the slice seen in Fig. 10.8 the copper object thickness was d=2.9 cm, so for the calculation of $\mu\rho$, the natural logarithm of the transmission in each pixel was divided by 2.9, for all the pixels in this slice (following Eq. 10.1).

After the $\mu\rho$ calculation, all the slices were recombined, creating the image seen in Fig. 10.9a. This analysis enables correct calculation of the $\mu\rho$ values of the objects but also results in large differences in the backdrop (the empty, no-object parts of the image) that are the result of the artificial division between slices.

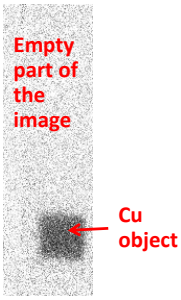

Figure 10.8: A slice of the transmission image with 4.4 MeV gamma-ray, used in the calculation of $\mu\rho$.

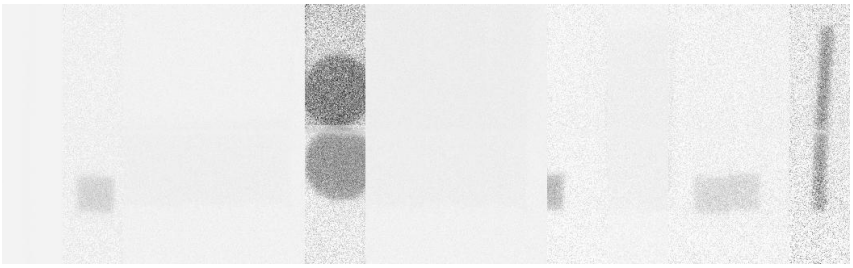

(a) Scan image of $\mu\rho_{4.4}$ before background clearing.

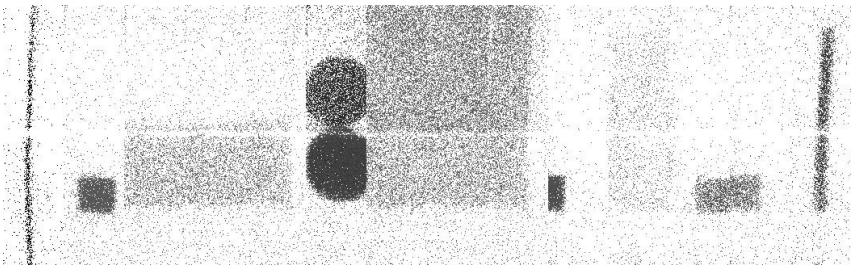

(b) Scan image of $\mu\rho_{4.4}$ after background clearing.

Figure 10.9: Scan image of $\mu\rho_{4.4}$ before and after background clearing.

To better understand the artificial slicing effect, we must remember that $\mu\rho$ is calculated from the transmission (see Eq. 10.1). In the transmission images, Figs. 10.6b and 10.6c, the pixels in the empty part of the image should have a transmission close to one (there are no attenuating objects in the image). Substituting T_i=1 in Eq. 10.1, the pixels in the empty areas of the image should have a value of zero, regardless of the thickness substituted for d.

However, in reality the transmission in the empty areas does not equal one, since a small amount of attenuating objects is present – the aluminium box and the styrofoam. Thus, Eq. 10.1 results in values different than zero for the pixels in the empty part of the image that are affected by the value we substitute for d. The artificial division into slices means that in each slice, the backdrop (the empty part of the image) is divided by a different d, dictated by the thickness of the object in that slice. The thickness difference can be quite large - the thin tungsten object is only 0.5 cm thick while the propionic acid and melamine are 7.7 cm thick. Thus, the backdrop is visibly different between different slices.

To remove the backdrop differences the following condition was applied to each pixel in the transmission image (before the $\mu\rho$ calculation): if the value in that pixel was higher than a threshold (for example 0.98) the value of that pixel was changed to one. This condition was applied to all the pixels, including the pixels in the area of the image representing objects. Since the transmission value in the object pixels is lower than 0.95 in all cases, this condition has effected mainly the pixels in the backdrop. Then, when using Eq. 10.1 for the image, the backdrop pixels equalled zero in all the slices. The image after this clearing is presented in Fig. 10.9b, showing that the artificial differences between the different slices have disappeared.

	4.43 MeV			**15.1 MeV**		
Material	$\mu\rho$ **Theory**	$\mu\rho$ **Expr.**	$\pm$	$\mu\rho$ **Theory**	$\mu\rho$ **Expr.**	$\pm$
Cu	0.29	0.26	0.04	0.29	0.27	0.03
Melamine	0.03	0.03	0.01	0.02	0.02	0.01
W	0.78	0.89	0.16	1.03	1.16	0.19
W	0.78	0.72	0.10	1.03	1.04	0.11
Propionic acid	0.03	0.04	0.01	0.02	0.02	0.01
Pb	0.47	0.46	0.06	0.64	0.59	0.07
Polyethylen (PE)	0.03	0.04	0.01	0.02	0.03	0.01
Fe	0.25	0.22	0.04	0.24	0.19	0.03
U	N/A	N/A		N/A	N/A	

Table 10.5: Average $\mu\rho$ values of the objects, experimentally measured, compared to values calculated from cross sections [30] for 4.4 and 15.1 MeV gamma-rays. The experimental values are averaged over the area of each object in the scan image.

The material separation is demonstrated in Table 10.5 showing the average values $\mu\rho$ of the objects and in Figs. 10.10 and 10.11, demonstrating the material separation by increasing the threshold level $\mu\rho_{min}$. At each increment, more material groups disappear until the scan image shows only materials recognised as SNM. The first image in each figure (Figs. 10.10a and 10.11a) shows the $\mu\rho$ scan image after clearing with no threshold on $\mu\rho$ values. In the next image, Figs. 10.10b and 10.11b, the threshold is set above the value of the low-Z material showing medium and high-Z materials. When the $\mu\rho_{min}$ is increased further, only high-Z materials remain in the images (Figs. 10.10c and 10.11c).
Finally, with the $\mu\rho_{min}$ value above the lead value, 0.6 and 0.7 for 4.4 and 15.1 MeV gamma-rays, respectively, only uranium and tungsten are visible in the images, Figs. 10.10d and 10.11d.

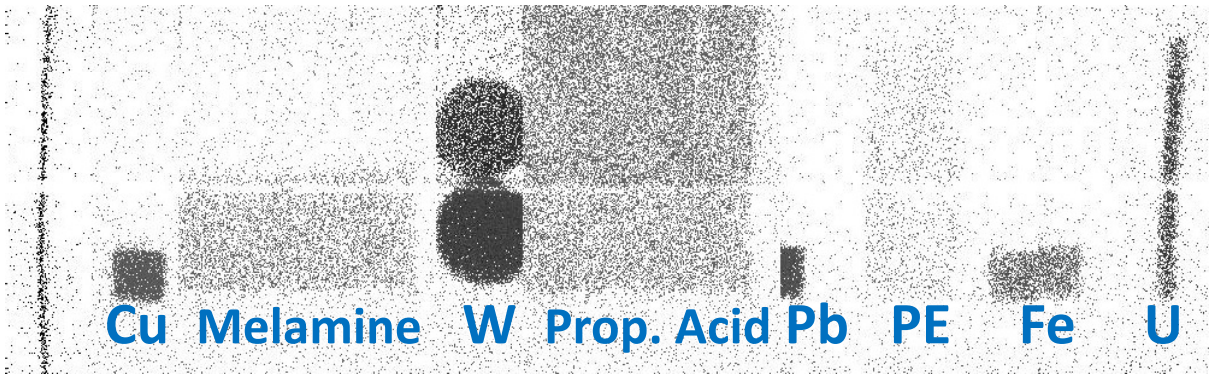

(a) Scan image of $\mu\rho_{4.4}$ with no lower threshold.

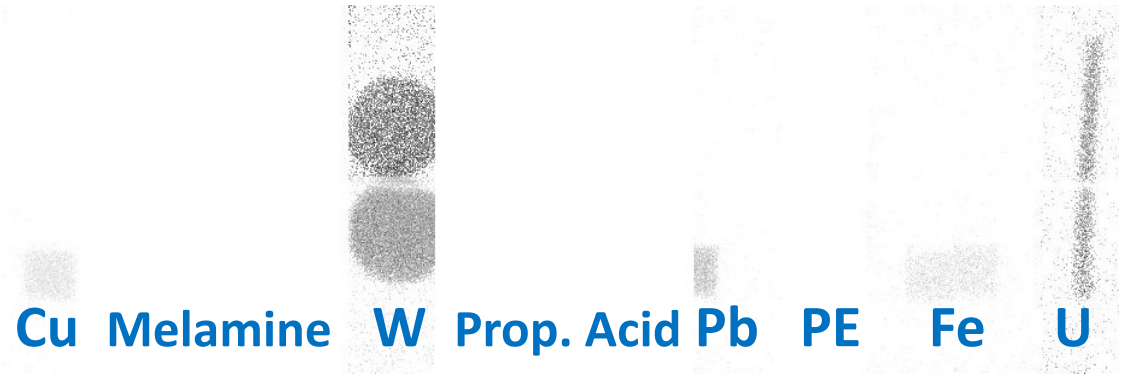

(b) Scan image of $\mu\rho_{4.4}$ with lower threshold $\mu\rho_{4.4,min}$=0.1.

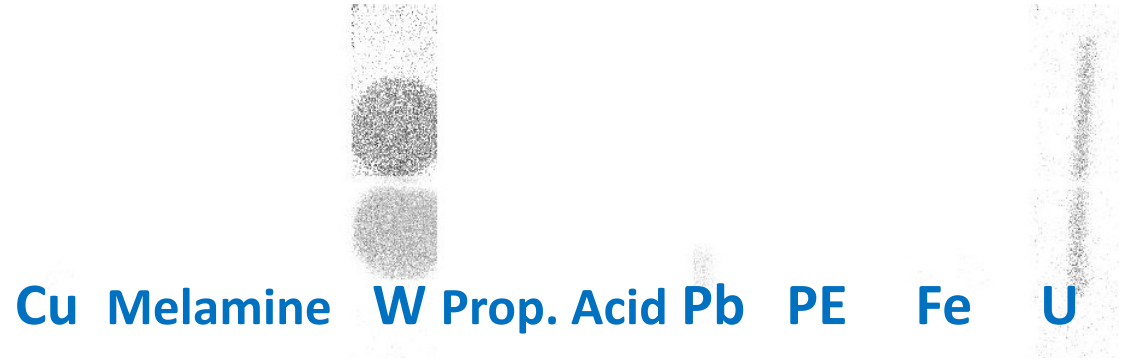

(c) Scan image of $\mu\rho_{4.4}$ with lower threshold $\mu\rho_{4.4,min}$=0.4.

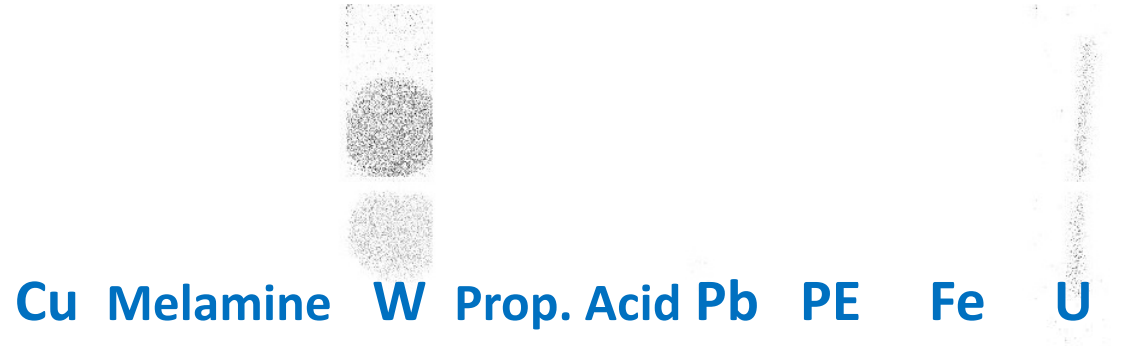

(d) Scan image of $\mu\rho_{4.4}$ with lower threshold $\mu\rho_{4.4,min}$=0.6.

Figure 10.10: Scan images of the macroscopic attenuation coefficient of 4.4 MeV gamma-rays $\mu\rho_{4.4}$ with different lower thresholds.

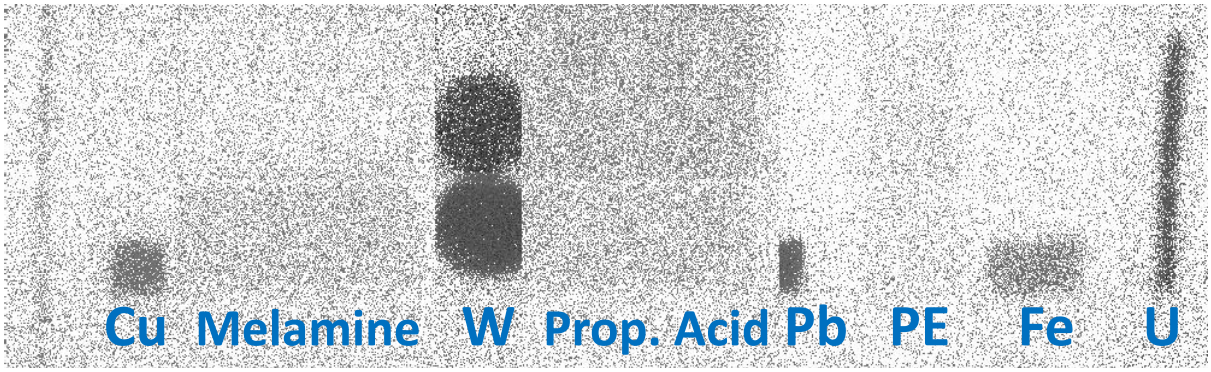

(a) Scan image of $\mu\rho_{15.1}$ with no lower threshold.

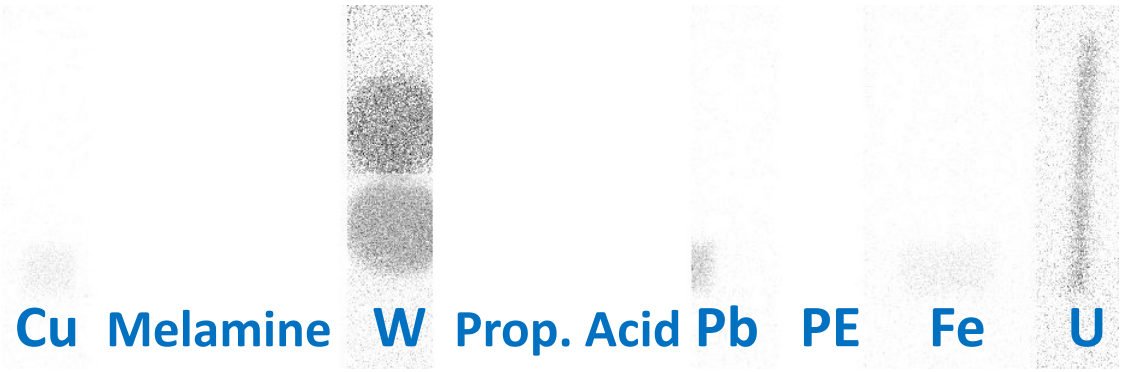

(b) Scan image of $\mu\rho_{15.1}$ with lower threshold $\mu\rho_{15.1,min}$=0.1.

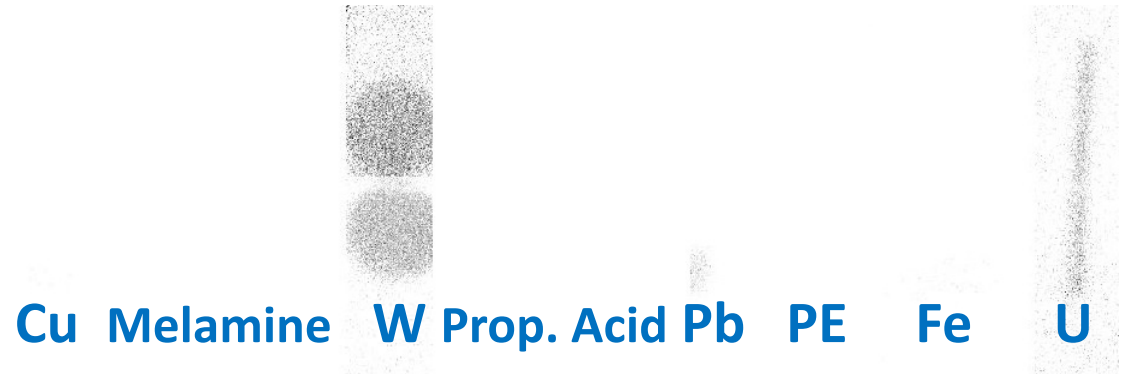

(c) Scan image of $\mu\rho_{15.1}$ with lower threshold $\mu\rho_{15.1,min}$=0.3.

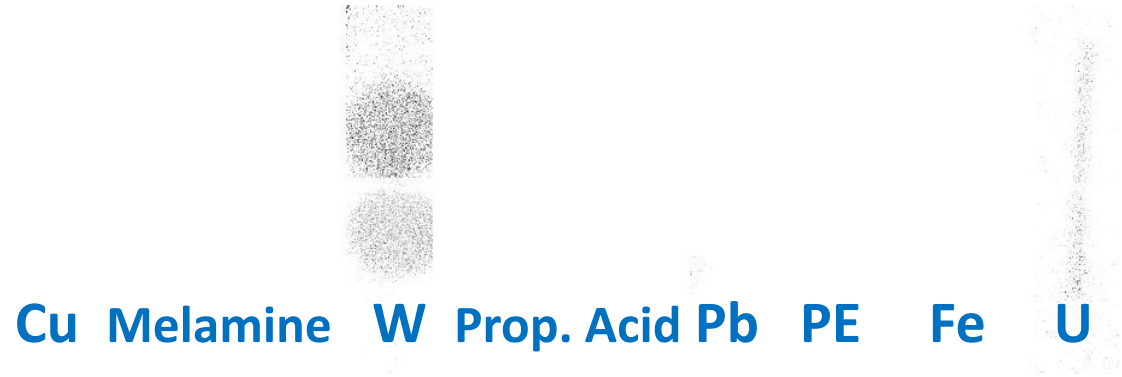

(d) Scan image of $\mu\rho_{15.1}$ with lower threshold $\mu\rho_{15.1,min}$=0.7.

Figure 10.11: Scan images of the macroscopic attenuation coefficient of 15.1 MeV gamma-rays $\mu\rho_{15.1}$ with different lower thresholds.

CHAPTER

11

SUMMARY AND CONCLUSIONS

11.1 DDEGR Proof-of-Principle

DDEGR proof-of-principle is based on many investigated aspects, discussed in Chapters 4, 5, 6 and 10.

First, the experimental measurement of gamma-ray (and neutron) yields from the ^{11}B(d,n)^{12}C reaction at different deuteron energies was described. The yields from deuterons with 3–12 MeV energy are 2–20$\times10^{10}$ N_γ/sr/mC 4.4 MeV gamma-rays and 2–5$\times10^{9}$ N_γ/sr/mC 15.1 MeV gamma-rays.

A simplified inspection system that was simulated with GEANT4 is described in Chapter 5. The effect of scattering on the signal reaching the detector and measured in it was simulated as well as the transmission through a container with a variety of objects inside. The simulations show that the scattering in large containers is expected to add up to 5% background to the signal in a system with a 4 metres distance between the detector and the container. The overall effect of the background was estimated to be acceptable and support the viability of the proposed DDEGR inspection method.

Next, the practical issues of material separation with a DDEGR system were analysed based on existing work in dual energy radiography and computed tomography. Considering the reaction gamma yields, the estimated required deuteron current for scanning an entire container within 60 s at 99.9% detection probability and 0.1% false alarms is 1.8 mA for a single radiography image, which enables separation of high-Z materials from medium- and low-Z materials. A tomographic reconstruction of the linear attenuation coefficient within the same time and detection probability requires higher current – 4.5 mA, but it enables the additional capability of separating benign high-Z materials from SNM.

Finally, a DDEGR system laboratory prototype was assembled at the PTB accelerator facility and used to demonstrate material separation, as described in Chapter 10. The ^{11}B(d,n)^{12}C nuclear reaction was used as a dual energy gamma source, and TRECOR-II was used to scan a small container with several low-, medium- and high-Z objects, including uranium. Separation of SNM from benign high-Z materials was demonstrated, as well as separation of high-Z materials

from low and medium-Z materials.

At the very beginning of this thesis, in Section 1.1.1, a list of requirements from an inspection system was presented. Based on this work, a DDEGR system can fulfil most of them: it can inspect cargo containers in 1-2 minutes with sufficient statistics for SNM detection, it can present a good quality image (under 5 mm resolution) and it can separate low- and medium-Z materials from high-Z materials. Two aspects that were not investigated are the safety and cost of such a machine, which should be dealt with at later stages of the development process.

Material separation enables de-cluttering of the result images, leaving only SNM objects in the images or highlighting them. Using DER, the system can separate high-Z from low-Z materials. Relying CT, the system can separate SNM and some rare earth metals from benign high-Z materials. Using an advanced decomposition technique detailed in Chapter 6, the atomic number and density can be determined thus identifying the material unambiguously.

The separation algorithm proposed in Section 6.1.2 is based on a method recently published by Xing et al. [43], demonstrating reconstruction of density and atomic number for a cargo container. This algorithm resulted in large errors for high-Z materials when using Bremsstrahlung beams, because of the high flux of low energy gamma-rays. Implementing the Xing algorithm in a full size DDEGR system prototype is promising, because of the inherent significant reduction in low energy gamma-rays in this method

An example of a highlighted image that can be achieved with CT is presented in Fig. 11.1. The system can therefore detect SNM threats automatically and does not need to rely on the judgement of human operator, but can still present a good quality image to the operator, which is the standard market demand.

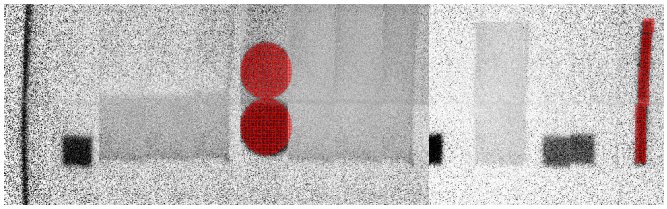

Figure 11.1: Good resolution scan image, with SNM-suspected objects highlighted in red, relying on CT for material separation.

11.2 Detector Development

The main part of the work was development of a detector suitable for a DDEGR system — Time Resolved Event Counting Optical Radiation (TRECOR) detector. TRECOR detector is a novel spectroscopic imaging detector for gamma-rays within the MeV energy range that uses the event counting image intensifier with gamma-rays for the first time. The second generation detector is also capable of detecting gamma-rays and neutrons in parallel.

TRECOR-I detector uses the event-by-event counting technique to measure the relevant quantities: position, timing and pulse-height (energy) for each interacting particle. The detector, its design and its performance are described in Chapters 7,8 and 9.

The position is measured by the ECII and a PMT is used to determine the timing and energy. TOF serves to separate the gamma-rays from the neutrons emitted in the same nuclear reaction and to determine neutron energies when relevant.

A second generation detector, TRECOR-II, is capable of detecting gamma-rays and neutrons

in parallel, separating them to create particle-specific images and energy-specific images for each particle, thus enabling simultaneous implementation of the SNM/explosives inspection methods. The first stage of its development consisted of converting TRECOR-I into a neutron detector by replacing the scintillator screen and adapting the electronic setup – this detector is referred to as TRECOR-I neutron detection mode.

The requirements from TRECOR-I (gamma-ray detector for a DDEGR system) were listed in Section 3.1. The list of requirements from a gamma-ray detector designed for a DDEGR system compared to the final specifications of TRECOR-I and TRECOR-II is presented in Table 11.1 and the list of requirements from a gamma/neutron detector designed for a combined DDEGR/FNRR system is presented in Table 11.2.

Requirement		**TRECOR-I**	**TRECOR-II**	**Comments**
Gamma-ray energy resolution	∼3 MeV	20%	20%	∼3 MeV for 15.1 MeV gamma-rays
Image resolution	5-10 mm	3 mm	3 mm	With 4.4 MeV gamma-rays
Timing resolution	50 ns	2.3 ns	4 ns	
Ability to work at high event rates	up to 0.5 MHz	0.5 MHz	0.5 MHz	
Large area detector	10×10 cm^2	5×10 cm^2	5×20 cm^2	

Table 11.1: List of requirements from gamma-ray detector designed for a DDEGR system compared to the final specifications of TRECOR-I and TRECOR-II detectors.

Requirement		**TRECOR-I**	**TRECOR-II**
Simultaneous detection of γ-rays and neutrons		Easy transformation from γ-ray to neutron detection	Yes
Timing resolution for neutron spectroscopy	5 ns	4.5 ns	4 ns
Neutron imaging resolution	∼2 mm	1 mm	2 mm

Table 11.2: List of additional requirements (to Table 11.1) from gamma/neutron detector designed for a combined DDEGR/FNRR system compared to the final specifications of TRECOR-I and TRECOR-II detectors.

The presence of radioactive ^{176}Lu in the LYSO scintillator introduces internal background to the detector that will be insignificant in the final inspection system, using a high current accelerator. However, in the experiments described in this work the background was significant and the spectroscopic capability of the detector was used to remove it based on its average energy (see Chapter 8 for more details).

11.3 Conclusions

In conclusion, many aspects of a DDEGR system were discussed, simulated, measured and demonstrated. The results support the viability of the proposed DDEGR inspection method and constitute a proof-of-principle.

Two generations of detectors were developed, one for a DDEGR system and the second anticipating the requirements of the broader-ability SNM/explosives inspection system. The second generation detector, TRECOR-II, was used in the DDEGR laboratory prototype.

The objectives of this work, as defined in Section 1.3, included proof-of-principle of the DDEGR method, development of a gamma-ray detector suitable for such a system and development of a gamma/neutron detector for the combined SNM/explosives inspection system. All three objectives were accomplished.

Future work should include demonstration of DDEGR with a full-sized system, including several detector arrays and the scanning of an LD3 container. The scanning of such a large object requires higher deuteron current than available in the PTB cyclotron. To that effect, a collaboration was initiated with the RFQ accelerator group in iThemba LABS in South Africa [235].

Appendices

APPENDIX

A

BEAM-INDUCED BACKGROUND

A.1 Simulated Scattering

A.1.1 Scattering From the Sample

In an experimental measurement a sample (an object of interest) is positioned in the beam path to the detector. In the case of gamma-rays, their interaction with the sample results in some scattered radiation in the form of energetic electrons and scattered gamma-rays, of which some reach the detector and increase the measured transmission. Some interactions also occur in the 12 m of air between the target (the gamma-ray source) and the detector, generating electrons that are partially stopped in the air and in the sample on their path.

Simulations describing a simplistic experimental scenario were conducted with different sample materials at different thicknesses.

The simulated scenario is illustrated in Fig. A.1 for a LYSO crystal slab $5\times10\times2$ cm^3 as the detector. An aluminium sheet, $5\times10\times0.1$ cm^3, is positioned 5 cm in front of the LYSO, representing the wall of the detector box. A sample is positioned about 1.5 m (depending on its thickness) from the aluminium wall. The gamma-rays are emitted from a square source, 5×10 cm^2, 12 m away from the LYSO detector.

The simulated samples are listed in Table A.1. Selected energy spectra of particles arriving at the detector are presented in Figs. A.2a-A.2b.

The first simulated scenario (marked "No sample, no air" in Table A.1) includes the detector, which is composed of the LYSO block and the aluminium wall, surrounded by vacuum. The scattered particles reaching the LYSO in this scenario are the results of gamma interactions in the aluminium wall.

By comparing this scenario to a similar one, with air instead of vacuum (marked "No sample" in Table A.1), we can estimate the effect of scattering in the air, adding 5-15% to the scattering. However, the addition is insignificant compared to the number of events reaching the detector - less than 0.5%.

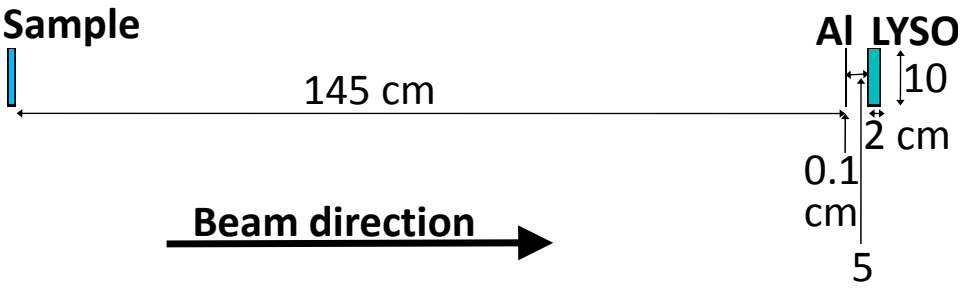

(a) A cross-section of the simulated scenario. The source is 12 m away from the detector in the same direction as the sample. The third dimension, not visible in the image, is 5 cm for all objects.

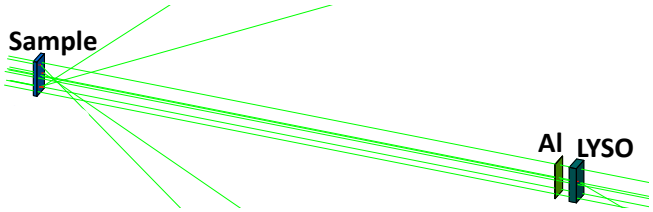

(b) A rotated view of the simulated scenario. The green lines describe gamma-rays.

Figure A.1: The simulated scenario approximating a simplistic experimental scenario, to scale, including a sample, an aluminium wall of the detector box in front of the LYSO detector and the LYSO scintillator detector. The absorbing sample thickness and material were varied between simulations.

The effect of the air becomes negligible when a sample is introduced in the beam path. The incoming gamma-rays (primary and scattered by air) and scattered electrons interact with the sample. Thicker samples reduce the number of scattered particles reaching the LYSO. Carbon has a weaker effect than the higher-Z, higher-density lead.

The effect of the scattered particles on the measured transmission is measured by the percentage of the scattered particles per primary gamma-rays reaching the detector. This has a significant effect when a strongly absorbing object is introduced in the beam path, such as a thick lead block.

	Electrons				**Scattered γ-rays**			
	No. of scattered particles		**% of scattered particles of primary γ-rays**		**No. of scattered particles**		**% of scattered particles of primary γ-rays**	
	4.4 MeV	**15.1 MeV**	**4.4 MeV**	**15.1 MeV**	**4.4 MeV**	**15.1 MeV**	**4.4 MeV**	**15.1 MeV**
No sample, no air	50,139	51,705	0.5	0.5	29,232	18,254	0.3	0.2
No sample	54,694	61,671	0.5	0.6	30,589	20,937	0.3	0.2
C 1 cm	51,521	62,817	0.5	0.3	30,241	23,313	0.7	0.2
C 5 cm	39,680	55,363	0.5	0.4	27,048	29,329	0.7	0.4
C 10 cm	29,142	45,544	0.6	0.4	22,934	31,530	0.7	0.5
Pb 1 cm	33,751	33,739	0.5	0.4	22,744	29,300	0.6	0.6
Pb 5 cm	5,221	2,949	0.6	0.6	5,599	8,569	0.8	2.2
Pb 10 cm	558	628	0.7	1.0	772	1,058	4.1	6.9

Table A.1: Number of scattered particles reaching the LYSO detector for different simulation scenarios and their percentage of primary gamma-rays reaching the detector. In all scenarios, 10^7 primary gamma-rays were simulated. Unless stated explicitly, in all scenarios the environment is composed of air.

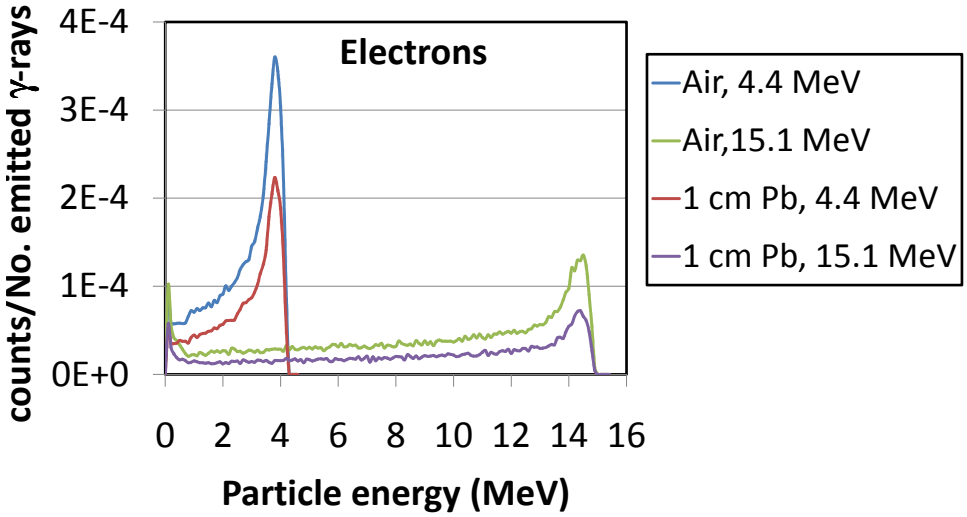

(a) Spectra of electrons reaching the detector.

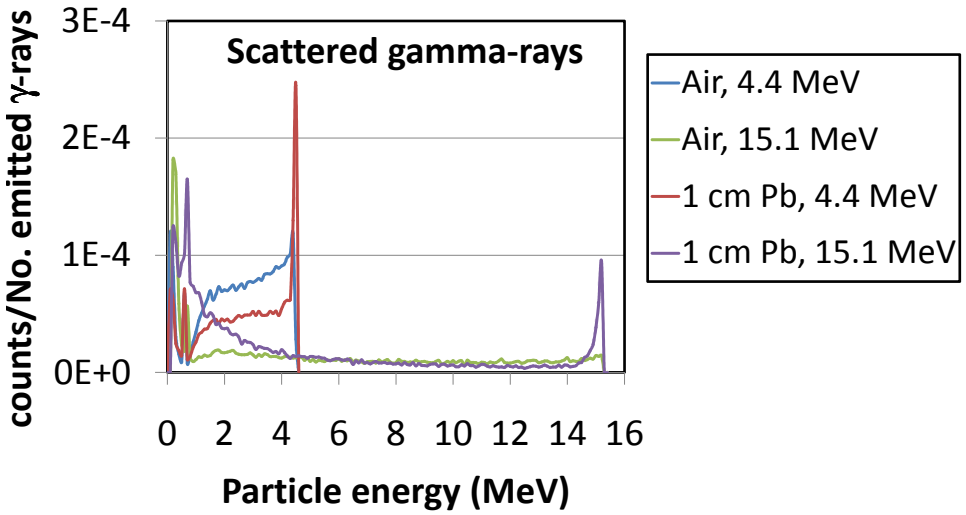

(b) Spectra of scattered gamma-rays reaching the detector.

Figure A.2: Simulated spectra of scattered particles reaching the detector with the simplistic geometry described in Fig. A.1. The spectra are normalized to the number of primary gamma-rays emitted from the source.

A.1.2 Scattering From the Environment

The effect of scattering was further investigated by a more detailed simulation, including the entire experimental hall at PTB. The simulation details are presented in Fig. A.3.

The source emits gamma-rays in a solid angle slightly larger than the one subtended by the opening in the first attenuating wall, assuming that gamma-rays at larger angles will be stopped and will not contribute significantly to the signal in the detector. The scattering of 4.4 and 15.1 MeV gamma-rays was simulated separately for each gamma-ray energy. We assume that the scattered 4.4 and 15.1 MeV gamma-rays cause the main background since the neutrons are being separated by TOF.

Energy spectra of scattered particles reaching the detector are presented in Fig. A.4, separated into electrons (Fig. A.4a) and scattered gamma-rays (Fig. A.4b) for a scenario with no sample in the beam path. The low energy gamma-rays seen in the scattered gamma spectrum are the 0.511 annihilation gamma-rays.

Table A.2 shows the number of scattered particles reaching the detector, given as a percentage

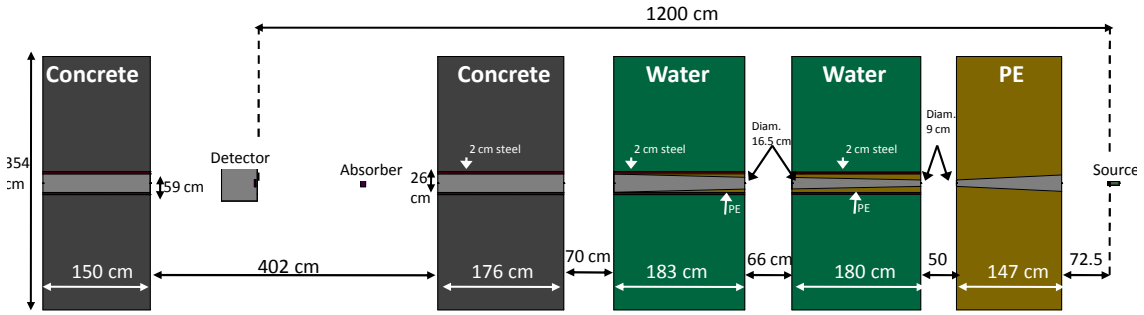

(a) A cross section of the simulated scenario, to scale. Missing details from the diagram: the detector is composed of a 50×50×147 cm^3, aluminium box with a 0.2 cm wall and a 5×10×2 cm^3 LYSO slab, the 2 cm is its thickness in the beam path. Air is filling the gaps between the objects.

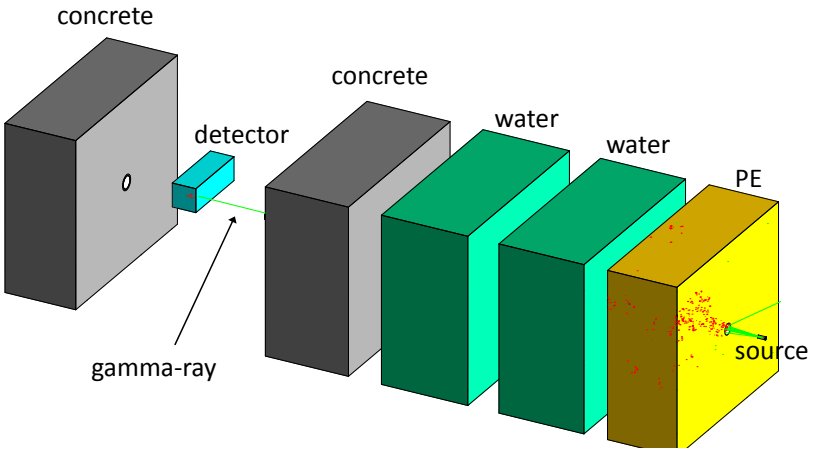

(b) A rotated view of the simulated scenario with 10 primary gamma-rays (the inner features are hidden). The green lines represent gamma-ray tracks and the red lines represent electron tracks.

Figure A.3: The simulated scenario approximating the PTB experimental scenario, to scale.

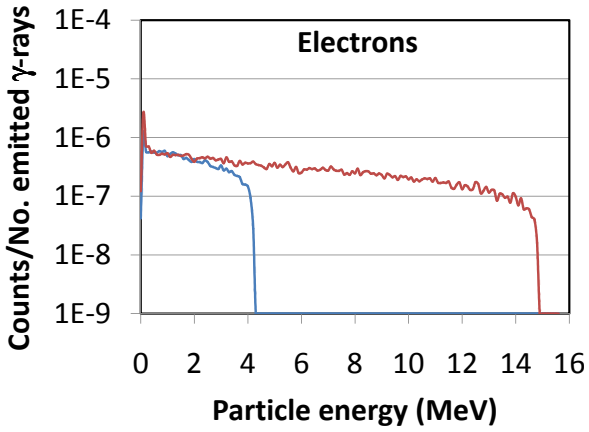

(a) Spectra of electrons reaching the detector.

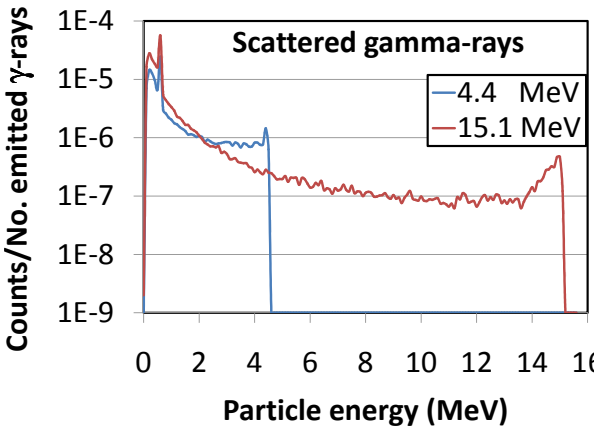

(b) Spectra of scattered γ-rays reaching the detector.

Figure A.4: Simulated spectra of scattered particles reaching the detector with the full PTB accelerator experimental hall geometry described in Fig. A.3. The spectra are normalized to the number of primary gamma-rays emitted from the source.

of the primary gamma-rays reaching the detector for the different simulated scenarios. The contribution of the scattered particles is large, especially the scattered gamma-rays contribution.

	Electrons (%)		Scattered γ-rays (%)	
	4.4 MeV	**15.1 MeV**	**4.4 MeV**	**15.1 MeV**
No sample	5	11	32	56
10 cm C	5	12	37	60
1 cm Pb	5	12	36	65

Table A.2: Number of scattered particles reaching the detector, given as a percentage of the primary gamma-rays reaching the detector at different simulation scenarios. In all scenarios, 5×10^8 primary gamma-rays were simulated.

However, most of the scattering contribution is at energies below 1 MeV, a part of the spectra that is discriminated when calculating the transmission. In fact, in calculating the transmission specific energy windows were used, 3-5 and 8-15.5 MeV for 4.4 and 15.1 MeV gamma-rays, respectively (see section 10.1). Table A.3 presents the percentage of scattered particles from primary gamma-rays when considering only gamma-rays above 1 MeV and when considering gamma-rays within the energy windows. The scattering contribution is reduced but remains significant.

Another observation from these numbers is that the beam induced background from the room is higher than the sample-related beam induced background.

	Electrons		Scattered γ-rays	
	4.4 MeV	**15.1 MeV**	**4.4 MeV**	**15.1 MeV**
Above 1 MeV				
No sample	3	9	9	11
10 cm C	3	10	10	12
1 cm Pb	3	10	10	13
In the energy windows				
No sample	3	8	8	9
10 cm C	3	8	9	10
1 cm Pb	3	8	9	10

Table A.3: Percentage of scattered particles with energy above 1 MeV and within the energy windows from primary gamma-rays reaching the LYSO detector at different simulation scenarios.

A.2 Measured Beam-Induced Background

A.2.1 Particle Separation via TOF and PSD

In previous sections the contribution of neutrons to the gamma-ray measurements was assumed negligible after separation of particles by TOF. This assumption was experimentally tested using an NE213 detector, a ^{9}Be source and a two-dimensional TOF-PSD electronic circuit. The resulting two-dimensional image allows separation of the TOF spectrum into its gamma-ray and neutron components. Particles reaching the detector at a "wrong" time will be mistaken in the TOF spectrum for another particle type, creating background.

Fig A.5 show a two dimensional presentation of PSD vs. TOF for the NE213 detector positioned in and out of the beam. The two horizontal bands represent the separation of the

TOF spectrum into gamma-rays and neutrons. Gamma-rays constitute the lower, thinner band and neutrons constitute the upper band, expanded in two regions.

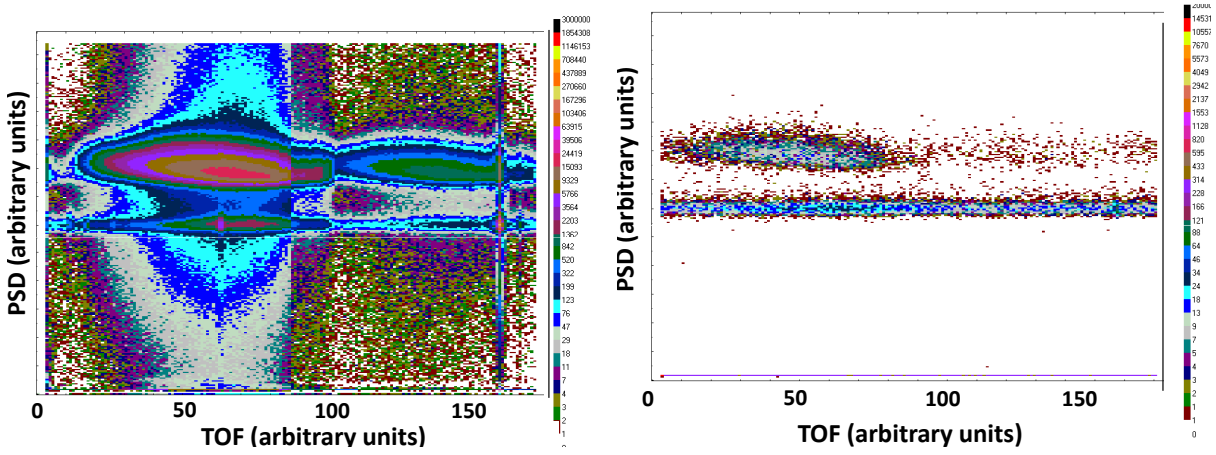

(a) Detector in-beam **(b)** Detector out-of-beam

Figure A.5: NE213 TOF-PSD spectrum.

A profile of each band is presented in Fig. A.6, which is the TOF spectrum separated by particle type. The out-of-beam TOF spectrum is dominated by gamma-rays and some scattered neutrons.

The gamma-ray in-beam component follows to some extent the fast neutron TOF spectrum. This behaviour suggests that these gamma-rays are created in the detector, most probably by inelastic neutron scattering on carbon – that is why they appear with a neutron TOF but with light decay properties (or PSD) of gamma-rays.

The peak at the gamma-ray position in the in-beam neutron spectrum is 23% of the gamma-ray peak in the same position. The origin is likely a misclassification of events by the PSD system, . The two-dimensional images above support this assumption, showing a significant number of counts at the TOF-determined gamma-rays position for every PSD value.

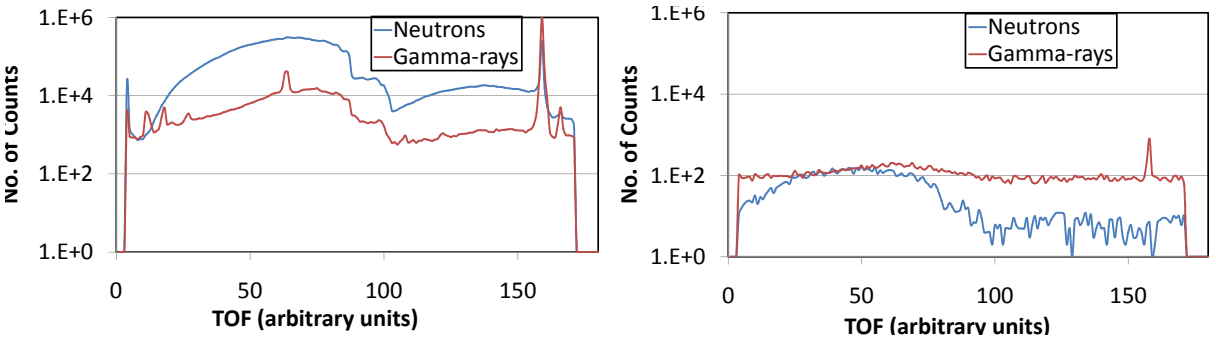

(a) Detector in-beam **(b)** Detector out-of-beam

Figure A.6: TOF spectra separated by particles. These spectra are presented in arbitrary units rather than ns, to maintain the same positions of peaks as in Fig. A.5

A.2.2 Neutron Background

During experiments, samples are positioned at least 1 m away from the detector, which is usually a sufficient distance to reduce the contribution of neutrons scattered from the sample to a negligible level.

The contribution of scattered neutrons from different samples to the neutron spectrum has been experimentally tested using an NE213 detector and a ^{9}Be source.

An NE213 detector was added to the regular experimental setup, placed right between TRECOR detector and the source. Different samples were positioned in the beam to add scattered neutrons. For each sample, the NE213 detector was first positioned in the beam and then out of the beam. The ratio between these two measurements for each sample is the room background. Such NE213 TOF spectra, measured in and out of the beam with a water sample in the beam path, are presented in Fig. A.7.

As seen in Table A.4, the beam-induced background is negligible when there is no sample. In the presence of samples the background is elevated by an order of magnitude, but remains lower than 10%, which is the contribution of background in TRECOR-I experiments.

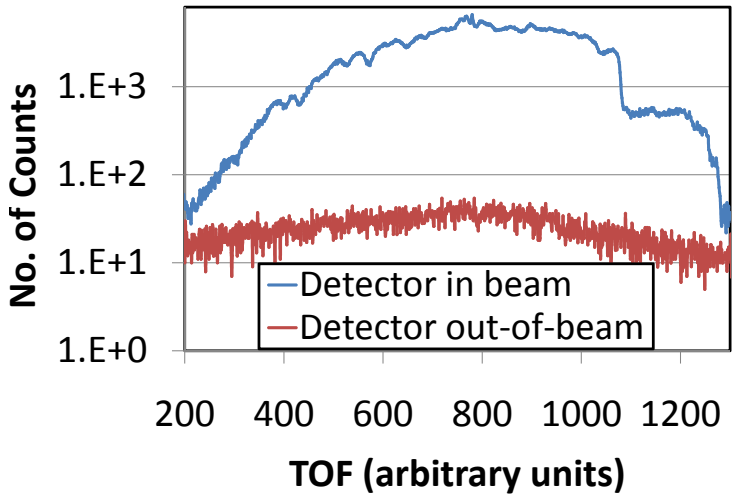

Figure A.7: NE213 TOF spectrum in and out of the beam with a water sample in the beam path.

Sample	Average Bckg. (%)
No sample	0.3
10 cm carbon	2
8 cm water	3

Table A.4: Room background measured with an NE213 detector with different samples in the beam path. The background here is the neutron part of the TOF spectrum.

APPENDIX

B

DETAILED DESCRIPTION OF ELECTRONICS

B.1 TRECOR-I

TRECOR-I has two detection modes, one for gamma-ray detection and one for neutron detection. The electronic setup diagram is presented in Fig. 7.13 and marks in red show the difference between the two detection modes. This section will discuss the gamma-detection mode first and then follow with the adjustments made for neutron detection.

The High-voltage module CAEN-1470 supplies HV to the PMT and the ECII divider chains: 1800–2000 V to the PMT and 4100–4250 V to the ECII. The ECII has 6 position output channels, fed by the delay line anodes and the ECII-common output channel, which is fed by the MCP anode.

The position signals X1, X2, Y1, Y2, Z1, Z2 are pre-amplified and sent to a constant fraction discriminator (CD1 and CD2) and then to the TDC. To suppress unnecessary data load and excess dead-time in the TDC, the constant fractions are vetoed by the PMT. When the PMT detects a signal, the position measurement is enabled for 400 ns. The delay cables in the position signal paths are required to adjust the time windows for the veto.

The PMT anode output is amplified and split by a Phillips Scientific 6950 pre-amplifier of variable gain, 1-10 fold and 2 parallel outputs. One signal is fed to a logic branch and generates the veto on all the ECII output channels.

When an event is measured both in the PMT and the ECII, the ECII-common signal is fed into unit #1 of a Philips Scientific 756 (PS756) logic module. By using the stretched update (upd) output and feeding it back to the same channel's veto input the signal is self-vetoed, blocking more events for a period of 500 ns (for 2 MHz frequency), which is one measurement cycle. The overlap (ovl) output of the logic module unit #1 is fed into input A of the logic module unit #2.

The second signal from the PMT is used for the anode pulse-height measurement, measuring the energy deposited in the scintillator. The signal is amplified and shaped by a Timing Filter

Amplifier and then fed to the Roendek CFDx emitting two timing signals.

As explained in Section 7.3.4, the CFDx unit is a combination of a constant fraction discriminator and a converter of pulse-height to time, which translates the two cut-offs of the constant fraction (at the beginning of the rise and at its end) into two NIM signals, "start" and "stop", with the time difference between their leading edges proportional to the analogue input signal (the pulse-height).

The outputs of the CFDx must be less than 5 ns apart. Both the CFDx start and stop outputs are combined at unit #4 of a Philips Scientific 756 (PS756) logic module and fed to channel #7 of the TDC. Channel #7 of the TDC is operated in dual-hit mode, taking 2 subsequent hits and subtracting their time stamps, calculating the pulse height.

The start output of the CFDx is branched off to input B of logic unit #2 of the PS756 logic module. The A (from the ECII-common) input and B (from the CFDx start) are combined in a coincidence logic, so only if both are present a signal is passed through to the TDC common start on channel 8. This is the first hit of the TDC channel 8.

The second hit is the stop, coming from the cyclotron pulse-selector, fed to the system via the PS756 logic module unit #3. Unit #3 is vetoed by the system common, permitting a stop only in cases where a start was presented. The signal from unit #3 is fed into unit #2 input C. Since the signal in unit #2 input is coming from unit #1 ovl output that is stretched over 500 ns, the gate is open for the signal from the pulse-selector for the same period of time.

This time period should span the relevant TOF regime to measure gamma-rays and the full neutron spectrum. Furthermore, the delay of the TOF-cyclotron signal must be adjusted in a way that the TOF spectrum includes all the relevant neutron energies and the gamma peak.

This method relies on constant fraction logic to measure the pulse-height signal, rather than the integral over the entire pulse area commonly used with a PMT. In the latter method, the connection between the energy deposited in the detector and the pulse-height is mostly linear [236]. Using the difference between the high and low edges of the constant fraction is much less so, but is required to achieve a common start fast enough for high-rate measurements. This non-linearity has a marginal effect on the transmission, which is determined by a ratio of spectra in well-identified gamma energies.

In the neutron-detector mode there is no pulse height measurement, so events are triggered by the ECII-common. The ECII-common is responsible for the veto on the ECII position channels and the line between the PMT and the ECII veto is disconnected.

The common start is provided by the ECII-common, via unit #1 of the PS756 logic module. The ECII-common signal is self-vetoed in #1 unit of the PS756 logic module using the stretched update output and feeding it back to the same channel's veto input. This method prohibits re-triggering since it permits only one common start signal to pass and initiate a measurement cycle (usually 500 ns in a 2 MHz cyclotron frequency).

B.2 TRECOR-II

Contrary to TRECOR-I, TRECOR-II has only one detection mode that measures gamma-rays and neutrons in parallel. The electronics was adjusted accordingly and the new electronics diagram is presented in Fig. 7.14. The ECII voltage divider circuit is unchanged with respect to that of TRECOR-I. The detector measures position, TOF and pulse-height for all events.

The first adjustment from TRECOR-I is that in TRECOR-II the scintillator is read by two PMTs instead of one. They require two high voltage supplies (HV2 and HV3) that are provided

from an ISEG module no. NHQ223m-K, operated at 1800-2000 V and up to 2 mA. The two signals are combined and then amplified, split etc. in an identical manner to TRECOR-I.

The position and pulse height use the same electronics principles as in TRECOER-I. Events are triggered in channel 8 of the TDC, which is operated in a dual-hit mode, as in TRECOR-I.

The main difference in the electronics is the triggering of events. The common start of the TDC (hit 1 of Channel 8) is provided by the ECII-common signal via CF2/Ch1 and the following logic. The ECII-common is fed into unit #1 of the PS756 logic module.

The ECII-common signal is fed from unit #1 of the logic module into unit #2 in two ways. The update output is fed with an approximately 2 ns delay to unit #2 input A and the overlap output is fed into unit #2 input B. The cable delay helps to fit both outputs into the same time window.

Logic unit #2 is operated with coincidence level 2, meaning that if at least 2 signals coincide the signal is permitted to pass. Since upd (update) and ovl (overlap) of logic unit #1 are always in coincidence with each other, this signal (originating from the ECII-common) always goes through and creates the first hit in the TDC common start (channel 8).

After the first hit from the ECII-common, logic unit #2 remains open for as long as the signal is self blocking (470 ns) (one measurement cycle). Input C of logic unit #2 is fed by a signal from the cyclotron pulse selector, creating the second hit of TDC channel 8. This period should span the TOF range necessary to measure gamma-rays and the full neutron spectrum.

The TOF is calculated by subtracting the first hit of the TDC channel 7 from the second hit of the TDC channel 8.

BIBLIOGRAPHY

[1] J. Medalia, *Detection of Nuclear Weapons and Materials : Science , Technologies , Observations*, Tech. Rep. 7–5700, Congressional Research Service (2010).

[2] Y. Liu, B. D. Sowerby, J. R. Tickner, *Comparison of Neutron and High-Energy X-Ray Dual-Beam Radiography for Air Cargo Inspection*, Appl. Radiat. Isot. 66 (2008) 463–473.

[3] M. A. Descalle, D. Manatt, D. Slaughter, *Analysis of Recent Manifests for Goods Imported Through US ports*, Tech. rep., Lawrence Livermor National Laboratory, UCRL-TR-225708 (2006).

[4] *The Practicality of Pulsed Fast Neutron Transmission Spectroscopy for Aviation Security for Aviation Security*, National Academy Press (1999).

[5] *Assessment of the Practicality of Pulsed Fast Neutron Analysis for Aviation Security*, National Academy Press, 2002.

[6] J. C. Overley, et al., *Explosives Detection via Fast Neutron Transmission Spectroscopy*, Nucl. Instr. and Meth. B 251 (2) (2006) 470–478.

[7] A. Buffler, J. R. Tickner, *Detecting Contraband Using Neutrons: Challenges and Future Directions*, Radiat. Meas. 45 (10) (2010) 1186–1192.

[8] B. D. Sowerby, J. R. Tickner, *Recent Advances in Fast Neutron Radiography for Cargo Inspection*, Nucl. Instr. and Meth. A 580 (1) (2007) 799–802.

[9] V. Dangendorf, et al., *Detectors for Energy Resolved Fast Neutron Imaging*, Nucl. Instr. and Meth. A 535 (1) (2004) 93–97.

[10] D. Vartsky, et al., *Time Resolved Fast Neutron Imaging: Simulation of Detector Performance*, Nucl. Instr. and Meth. A 542 (2005) 206–212.

[11] V. Dangendorf, et al., *Detectors for Time-Of-Flight Fast-Neutron Radiography 1. Neutron-Counting Gas Detector*, Nucl. Instr. and Meth. A 542 (2005) 197–205.

[12] D. Vartsky, *Prospects of Fast-Neutron Resonance Radiography and Its Requirements for Instrumentation*, in: Proc. of Int. Workshop on Fast Neutron Detect. and Appl., South Africa, 2006.

[13] I. Mor, et al., *Parameters Affecting Image Quality with Time-Resolved Optical Integrative Neutron (TRION) Detector*, Nucl. Instr. and Meth. A 640 (2011) 192–199.

[14] I. Mor, et al., *High Spatial Resolution Fast-Neutron Imaging Detectors for Pulsed Fast-Neutron Transmission Spectroscopy*, JINST4 P05016.

[15] V. Dangendorf, C. Kersten, D. Vartsky, M. B. Goldberg, *Time-Resolved, Optical-Readout Detector, for Neutron and Gamma-Ray Imaging*, World Patent No. WO2006048871 (2006).

[16] *United States Nuclear Regulatory commission* , `http://www.nrc.gov/materials/sp-nucmaterials.html`, accessed June 19, 2012.

[17] J. Mark, et al., *Can Terrorists Build Nuclear Weapons?*, Report Prepared for the International Task Force on the Prevention of Nuclear Terrorism (1986).

[18] V. A. Orlov, *llicit Nuclear Trafficking and the New Agenda*, IAEA Bulletin 46/1 (2003).

[19] R. C. Runkle, L. E. Smith, A. J. Peurrung, *The Photon Haystack and Emerging Radiation Detection Technology*, J. of Appl. Phys. 106 (4) (2009) 1101–1121.

[20] J. Medalia, *Terrorist Nuclear Attacks on Seaports: Threat and Response*, Tech. Rep. Order Code RS21293, Congressional Research Service (2002).

[21] J. Medalia, *Nuclear Terrorism: A Brief Review of Threats and Responses*, Tech. Rep. Order Code RL32595, Congressional Research Service (2002).

[22] M. B. Goldberg, et al., *Detecting Small Amounts of SNM in Cargo-Containers/Vehicles via Dual-Discrete-E gamma Ray Radiography Following* $^{11}B(d,n)^{12}C$, in: 9th Intl. Conf. on Appl. of Nucl. Tech., Crete, 2008.

[23] R. Bentley, *Database of High-Z Signatures in Cargo*, in: IEEE Int. Conf. on Technol. for Homel. Secur., Massachusetts, 2011, pp. 379–383.

[24] B. J. Quiter, et al., *A Method for High-Resolution X-Ray Imaging of Intermodal Cargo Containers for Fissionable Materials*, J. of Appl. Phys. 6 103 (064910).

[25] *Nordisk Aviation Products*, `http://www.nordisk-aviation.com/default.aspx?Cat=101`, accessed June 20, 2012.

[26] *American Airliner Cargo Aircraft Containers*, `http://https://www.aacargo.com/tools/ld3.jhtml?selection=4`, accessed June 20, 2012.

[27] J. E. Eberhardt, et al., *Fast-Neutron/Gamma-Ray Radiography Scanner for the Detection of Contraband in Air Cargo Containers*, in: Proc. of SPIE: Non-Intrusive Insp. Technol., Vol. 6213, Orlando, 2006, p. 03.

[28] R. Runkle, et al., *Photon and Neutron Interrogation Techniques for Chemical Explosives Detection in Air Cargo: A Critical Review*, Nucl. Instr. and Meth. A 603 (3) (2009) 510–528.

[29] A. Buffler, *Contraband Detection with Fast Neutrons*, Radiat. Phys. and Chem. 71 (3-4) (2004) 853–861.

[30] *Physical Reference Data, National Institute of Standards and Technology*, http://physics.nist.gov/PhysRefData/XrayMassCoef/cover.html, accessed June 30, 2012.

[31] *American Science and Engineering (ASE)*, http://www.as-e.com/products_solutions/z_backscatter.asp, accessed May 12, 2012.

[32] *Science Applications International Corporation (SAIC) mobile*, http://www.saic.com/products/security/mobile-vacis/, accessed May 12, 2012.

[33] *L-3 Communications*, http://www.sds.l-3com.com/products/aircargo.htm, accessed June 25, 2012.

[34] *Safran Morpho*, http://www.morpho.com/detection/transports-publics-310/?lang=en, accessed April 4, 2012.

[35] *Nuctech Ltd.*, http://www.nuctech.com/templates/T_Second_EN/index.aspx?nodeid=838&page=ContentPage&contentid=467, accessed June 26, 2012.

[36] *Rapiscan Systems*, http://www.rapiscansystems.com/en/products/cvi, accessed April 4, 2012.

[37] M. Goldberg, S. NRC, U.S. Patent No. 7,381,962 (2008).

[38] *Science Applications International Corporation (SAIC) RPMs*, https://www.saic.com/products/security/at-980/, accessed September 29, 2012.

[39] *Varian*, http://www.varian.com/us/security_and_inspection/products/accelerators/linatron_k9.html, accessed June 26, 2012.

[40] W. G. J. Langeveld, et al., *Neutron-Based Material Categorization System for the Rapiscan Eagle MAX*, in: 2nd Int. Workshop on Fast Neutron Detect. and Appl., Israel, 2011.

[41] K. Lee, et al., *Design and Experiment of Dual-Energy X-Ray Material Recognition Using a 950 keV X-band Linac*, Nucl. Instr. and Meth. A 637 (1) (2010) s54–s56.

[42] D. Sheukh-Bagheri, D. W. O. Rogers, *Monte Carlo Calculation of Nine Megavoltage Photon Beam Spectra Using the BEAM Code*, Med. Phys. 29 (2002) 391–402.

[43] Y. Xing, et al., *A Reconstruction Method for Dual High-Energy CT With MeV X-Rays*, IEEE Trans. Nucl. Sci. 58 (2) (2011) 537–546.

[44] X. Duan, et al., *X-Ray Cargo Container Inspection System with Few-View Projection Imaging*, Nucl. Instr. and Meth. A 598 (2) (2009) 439–444.

[45] D. Vartsky, V. Dangendorf, M. B. Goldberg, *Automatic Contraband in Cargo Interrogation System*, Proposal to the Joint German-Israeli Research Program (2009).

[46] M. Brandis, et al., *Nuclear-Reaction-Based Radiation Source for Explosives- and SNM-Detection in Massive Cargo*, in: 21th Int. Conf. on Accel. Appl. in Res. and Ind., Vol. 1336, Texas, 2010, pp. 711–716.

[47] M. Brandis, et al., *Detector for Simultaneous Detection of Explosives and Special-Nuclear-Materials*, in: 26th Conf. of the Nucl. Soc., Israel.

[48] G. Zentai, *X-Ray Imaging for Homeland Security*, Signal and Imaging Syst. Eng. 3 (1).

[49] G. F. Knoll, *Radiation Detection and Measurments*, Wiley and Sons, New York, 2000.

[50] J. I. Katz, G. S. Blanpied, K. N. Borozdin, C. Morris, *X-Radiography of Cargo Containers*, Sci. and Global Secur. 15 (1) (2007) 49–56.

[51] W. G. J. Langeveld, C. Condron, M. Elsalim, M. Ingle, *Noise Spectroscopy: Z-Determination by Statistical Count-Rate Analysis (Z-scan)*, Nucl. Instr. and Meth. A 652 (2011) 79–83.

[52] R. E. Alvarez, A. Macovski, *Energy Selective Reconstructions in X-Ray Computerized Tomography*, Phys. Med. Biol. 21 (1976) 733–744.

[53] R. F. Eilbert, K. D. Krug, *Aspects of Image Recognition in Vivid Technology's Dual-Energy X-Ray System for Explosive Detection*, in: Appl. in Opt. Sci. and Eng., Vol. 1824, 1993, pp. 127–143.

[54] W. W. Neale, J. G. Rushbrooke, R. E. Ansorge, U.S. Patent No. 5,524,133 (1996).

[55] J. G. Rushbrooke, et al., *High Energy Material Discrimination (HEMD) in the X-Ray Imaging of Cargo Containers at Linac Energies*, in: Harnessing Technol. to Support the Natl. Drug Control Strategy, Chicago, 1997, pp. 6–19.

[56] P. J. Bjorkholm, U.S. Patent No. 6,069,936 (2000).

[57] D. Perion, International Patent No. WO 00/43760 (2000).

[58] S. A. Ogorodnikov, V. L. Petrunin, *Processing of Interlaced Images in 4–10 MeV Dual Energy Customs System for Material Recognition*, Phys. Rev. Spec. Top. Accel. Beams 5.

[59] V. L. Novikov, S. A. Ogorodnikov, V. I. Petrunin, *Dual Energy Method of Material Recognition in High Energy Introscopy Systems*, in: Int. Workshop on Charged Particle Linear Accel., 1999, pp. 93–95.

[60] S. A. Ogorodnikov, V. I. Petrunin, M. F. Vorogushin, *Application of High-Penetrating Introscopy Systems for Recognition of Materials*, in: 7th Eur. Particle Accel. Conf., Vienna, 2000, pp. 2583–2585.

[61] S. A. Ogorodnikov, V. I. Petrunin, *Processing of Interlaced Images in 4–10 MeV Dual Energy Customs System for Material Recognition*, in: Proc. of the 6th Int. Computional Accel. Phys. Conf., Germany, 2000.

[62] P. J. Bjorkholm, *Dual Energy Detection of Weapons of Mass Destruction*, Port Technol. Int. 22 (2004) 155–158.

[63] P. J. Bjorkholm, *WMD Detectionn*, Cargo Security Int. (2005) 22–25.

[64] G. J. Budner, *Dual Energy Detection of Weapons of Mass Destruction*, in: Nonintrusive Insp., Struct. Monit. and Smart Syst. for Homeland Secur., Vol. 61780G, San Diego, 2006.

[65] Z. Chen, X. Wang, *Cargo X-Ray Imaging Technology for Material Discrimination*, Port Technol. Int. 30 (2006) 163–165.

[66] C. Tang, *Low Energy Linacs and Their Application in Tsinghua University*, in: Proc. of LINAC, 2006, pp. 256–258.

[67] X. W. Wang, *Material Discrimination by High-Energy X-Ray Dual-Energy Imaging*, High Energy Phys. and Nucl. Phys. 31 (11).

[68] Y. Gil, Y. Oh, M. Cho, W. Namkung, *Radiography Simulation on Single-Shot Dual-Spectrum X-Ray for Cargo Inspection System.*, Appl. Radiat Isot. 69 (2) (2011) 389–393.

[69] G. Chen, *Understanding X-Ray Cargo Imaging*, Nucl. Instr. and Meth. B 637 (1) (2005) 810–815.

[70] D. Chen, G. Bennett, D. Perticone, *Dual-Energy X-Ray Radiography for Automatic High-Z Material Detection*, Nucl. Instr. and Meth. B 261 (2007) 356–359.

[71] *Accuray*, `http://www.accuray.com/`, accessed September 20, 2012.

[72] V. J. Orphan, *Lessons Learned in Developing the VACIS Products*, in: AIP Conf. Proc.: 21 Int, Conf. on App. of Accel. in Res. and Ind., Vol. 1336.

[73] J. Gerl, F. Ameil, I. Kojouharov, A. Surowiec, *High-Resolution Gamma Backscatter Imaging for Technical Applications*, Nucl. Instr. and Meth. A 525 (1–2) (2004) 328–331.

[74] *Passport Systems Inc.*, `http://www.passportsystems.com/nrf.htm`, accessed May 12, 2012.

[75] W. Bertozzi, S. Korbly, R. Ledoux, W. Park, *Nuclear Resonance Fluorescence and Effective Z Determination Applied to Detection and Imaging of Special Nuclear Material, Explosives, Toxic Substances and Contraband*, Nucl. Instr. and Meth. B 261 (1-2) (2007) 331–336.

[76] *DNDO Programs*, `http://www.dhs.gov/files/programs/dndo-snar.shtm`, accessed May 12, 2012.

[77] G. Harding, *Potential of X-Ray Diffraction for Detecting Special Nuclear Materials (SNMs)*, in: Conf. Proc. Penetrating Radiat. Syst. and Appl. IX, Vol. 7080, 2008.

[78] G. Harding, *X-Ray Diffraction Imaging - a Multi-Generational Perspective.*, App. Rad. Iso. 67 (5) (2009) 287–295.

[79] G. Harding, *On Screening for Special Nuclear Materials (SNMs) with X-Ray Diffraction*, Rad. Phys. Chem. 79 (5) (2010) 597–602.

[80] R. T. Kouzes, et al., *Passive Neutron Detection for Interdiction of Nuclear Material at Borders*, Nucl. Instr. and Meth. A 584 (2007) 383–400.

[81] D. Cester, et al., *Special Nuclear Material Detection with a Mobile Multi-Detector System*, Nucl. Instr. and Meth. A 663 (2011) 55–63.

[82] R. C. Runkle, D. L. Chichester, S. J. Thompson, *Rattling Nucleons: New Developments in Active Interrogation of Special Nuclear Material*, Nucl. Instr. and Meth. A 663 (2012) 75–95.

[83] *Evaluated Nuclear Data Files*, `http://www.nndc.bnl.gov`, accessed April 4, 2010.

[84] D. K. Wehe, H. Yang, H. Jones, *Observation of ^{238}U Photofission Products*, IEEE Trans. on Nucl. Sc. NS53 (2006) 1430–1434.

[85] D. R. Slaughter, et al., *The Nuclear Car Wash: a Scanner to Detect Ilicit SNM in Cargo Containers*, IEEE Sens. J. 5 (2005) 560–564.

[86] D. Slaughter, et al., *Detection of SNM in Cargo Containers Using Neutron Interrogation*, Tech. rep., Lawrence Livermore National Laboratory (2003).

[87] H. Rennhofer, J. M. Crochemore, E. Roesgen, B. Pedersen, *Detection of SNM by Delayed Gamma-Rays from Induced Fission*, Nucl. Instr. and Meth. A 652 (1) (2011) 140–142.

[88] J. Hall, et al., *The Nuclear Car Wash: Neutron Interrogation of Cargo Containers to Detect Hidden SNM*, Nucl. Instr. and Meth. B 261 (2007) 337–340.

[89] J. M. Hall, et al., *Modeling the Production of Beta-Delayed Gamma-Rays for the Detection of SNM*, Tech. rep., Lawrence Livermore National Laboratory (2005).

[90] N. Kikuzawa, et al., *Non-Destructive Detection of Heavily Shielded Materials by Using Nuclear Resonance Fluorescence with a Laser-Compton Scattering Gamma-Ray Source*, Appl. Phys. Express 2 (3) (2009) 6502.

[91] H. Yang, D. K. Wehe, *Detection of Concealed Special Nuclear Material Using Nuclear Resonance Fluorescence Technique*, in: IEEE Nucl. Sci. Symp. Conf., 2009, pp. 898–903.

[92] J. Pruet, et al., *Detecting Clandestine Material with Nuclear Resonance Fluorescence*, J. of Appl. Phys. 99 (12) (2006) 123102–123102.

[93] M. S. Johnson, et al., *Searching for Illicit Materials Using Nuclear Resonance Fluorescence Stimulated by Narrow-Band Photon Sources*, Nucl. Instr. and Meth. B 285 (2012) 72–85.

[94] W. L. Myers, C. A. Goulding, C. L. Hollas, C. E. Moss, *Photon and Neutron Active Interrogation of Highly Enriched Uranium*, in: Int. conf. on Nucl. data for Sci. and Tech., Vol. 769, 2005, pp. 1688–1692.

[95] Y. P. Bogolubov, et al., *Method and System Based on Pulsed Neutron Generator for Fissile Material Detection in Luggage*, Nucl. Instr. and Meth. B 213 (2004) 439–444.

[96] P. Kerr, et al., *Active Detection of Small Quantities of Shielded Highly-Enriched Uranium using Low-Dose 60-keV Neutron Interrogation*, Nucl. Instr. and Meth. B 261 (1) (2007) 347–350.

[97] B. D. Sowerby, et al., *Recent Developments in Fast Neutron Radiography for the Interrogation of Air Cargo Containers*, in: IAEA Conf. Proc., Vienna, 2009, pp. 4–8.

[98] N. G. Cutmore, Y. Liu, J. R. Tickner, *Development and Commercialization of a Fast-Neutron/X-Ray Cargo Scanner*, in: IEEE Int. Conf. on Technolog. for Homel. Secur., 2010, pp. 330–336.

[99] Y. Liu, J. R. Tickner, *Image Processing and Display Systems for the CSIRO Air Cargo Scanner*, in: IEEE Nucl. Sci. Symp., Vol. 5, 2007, pp. 77–81.

[100] J. Eberhardt, et al., *Fast Neutron and Gamma-Ray Interrogation of Air Cargo Containers*, in: Proceedings of Science, International Workshop on Fast Neutron Detectors, Cape Town, 2006, p. 92.

[101] J. E. Eberhardt, et al., *Fast Neutron Radiography Scanner for the Detection of Contraband in Air Cargo Containers*, Appl. Radiat. and Isot. 63 (2) (2005) 179–188.

[102] J. E. Eberhardt, et al., *Fast Neutron and Gamma-Ray Detectors for the CSIRO Air Cargo Scanner*, in: Proc. of Int. Workshop on Fast Neutron Detect. and Appl., South Africa, 2006, p. 74.

[103] P. J. Rothschild, *Combined X-Ray CT/neutron Material Identification System, U.S. Patent No. 7,551,714* (2009).

[104] J. Stevenson, et al., *Linac Based Photofission Inspection System Employing Novel Detection Concepts*, Nucl. Instr. and Meth. A (2011) 124–128.

[105] T. Gozani, et al., *Combined Photoneutron And X Ray Interrogation Of Containers For Nuclear Materials*, in: 21th Int. Conf. on Accel. Appl. in Res. and Ind., Vol. 1336, Texas, 2010, pp. 686–692.

[106] J. B. Birks, *The Theory and Practice of Scintillation Counting*, Pergamon Press, 1964.

[107] H. A. Bethe, J. Ashkin, *Passage of Radiations Through Matter*, Vol. 1 of *Experimental Nuclear Physics*, Wiley and Sons, New York, 1953.

[108] T. E. Peterson, L. R. Furenlid, *SPECT Detectors: the Anger Camera and Beyond.*, Phys. Med. Bio. 56 (2011) R145–R182.

[109] M. J. Weber, *Scintillation: Mechanisms and New Crystals*, Nucl. Instr. and Meth. A 527 (1) (2004) 9–14.

[110] T. K. Lewellen, *Recent Developments in PET Detector Technology*, Phys. Med. Bio. 53 (17) (2008) R287–R317.

[111] C. L. Melcher, *Scintillation Crystals for PET*, J. Nucl. Med. 41 (6) (2000) 1051–1055.

[112] H. Kume, S. Muramatsu, M. Iida, *Position Sensitive Photomultiplier Tubes for Scintillation Imaging*, IEEE Trans. Nucl. Sci. 33 (1986) 359–363.

[113] T. K. Lewellen, *The Challenge of Detector Designs for PET*, Am. J. of Roentgenology 195 (2) (2010) 301–309.

[114] R. Pani, et al., *Evaluation of Flat Panel PMT for Gamma-Ray Imaging*, Nucl. Instr. and Meth. A 504 (2003) 262–268.

[115] D. Brust, *Band-Theoretic Model for the Photoelectric Effect in Silicon*, Phys. Rev. 139 (A) (1965) 489–500.

[116] C. Degenhardt, et al., *The Digital Silicon Photomultiplier a Novel Sensor for the Detection of Scintillation Light*, in: IEEE Nucl. Sci. Symp. Conf. Rec. (NSS/MIC), Orlando, 2010, pp. 2383–2386.

[117] M. Gersbach, et al., *A Parallel 32×32 Time-to-Digital Converter Array Fabricated in a 130 nm Imaging CMOS Technology*, in: IEEE Proc. Eur. Solid-State Circuits Conf., Athens, 2009, pp. 196–199.

[118] J. Richardson, et al., *A 32×32 50 ps Resolution 10 Bit Time to Digital Converter Array in 130 nm CMOS for Time Correlated Imaging*, in: IEEE Cust. Integr. Circuits Conf., San Jose, 2009, pp. 77–80.

[119] S. K. Madan, B. Bhaumik, J. M. Vasi, *Experimental Observation of Avalanche Multiplication in Charge-Coupled Devices*, IEEE Trans. Electron Devices 30 (1983) 694–699.

[120] P. Jerram, et al., *The LLCCD: Low-Light Imaging Without the Need for an Intensifier*, in: Sens. and Camera Syst. for Sci., Ind., and Digit. Photogr. Appl. II, Vol. 4306, San Jose, 2001, pp. 178–186.

[121] G. A. Johansen, C. B. Johnson, *Operational Characteristics of an Electron-Bombarded Silicon-Diode Photomultiplier Tube*, Nucl. Instr. and Meth. A 326 (1-2) (1993) 295–298.

[122] E. Albrecht, et al., *First Observation of Čerenkov Ring Images Using Hybrid Photon Detectors*, Nucl. Instr. and Meth. A 411 (2-3) (1998) 249–264.

[123] Z. Fraenkel, et al., *A Hadron Blind Detector for the PHENIX Experiment at RHIC*, Nucl. Instr. and Meth. A 546 (2005) 466–480.

[124] A. Breskin, et al., *A Novel Liquid-Xenon Detector Concept for Combined Fast-Neutrons and Gamma Imaging and Spectroscopy*, JINST 7 (2012) C06008.

[125] L. Lanca, A. Silva, *Digital Radiography Detectors A Technical Overview: Part 1*, Radiogr. 15 (1) (2009) 58–62.

[126] L. Lanca, A. Silva, *Digital Radiography Detectors A Technical Overview: Part 2*, Radiogr. 15 (2) (2009) 134–138.

[127] V. C. Spanoudaki, C. S. Levin, *Photo-Detectors for Time of Flight Positron Emission Tomography (ToF-PET)*, Sens. 10 (11) (2010) 10484–10505.

[128] W. W. Moses, *Recent Advances and Future Advances in Time-Of-Flight PET*, Nucl. Instr. and Meth. A 580 (2) (2007) 919–924.

[129] S. Seifert, H. Van-Dam, T. Schaart, R. Dennis, *The Lower Bound on the Timing Resolution of Scintillation Detectors.*, Phys. Med. Bio. 57 (7) (2012) 1797–1814.

[130] A. Del Guerra, et al., *Advances in Position-Sensitive Photodetectors for PET Applications*, Nucl. Instr. and Meth. A 604 (1-2) (2009) 319–322.

[131] M. A. Descalle, et al., *Detector Design for High-Resolution MeV Photon Imaging of Cargo Containers using Spectral Information*, Nucl. Instr. and Meth. A 624 (3) (2010) 635–640.

[132] W. W. Moses, S. E. Derenzo, *Prospects for Time-of-Flight PET using LSO Scintillator*, IEEE Trans. Nucl. Sci. NS-46 (1999) 474–478.

[133] T. Moriya, T. Omura, M. Watanabe, T. Yamashita, *Development of a Position-Sensitive Detector for TOF-PET*, IEEE Trans. Nucl. Sci. 55 (5) (2008) 2455–2459.

[134] H. O. Anger, *Use of a Gamma-Ray Pinhole Camera for In-Vivo Studies*, Nat. 170 (1952) 200–201.

[135] P. Dorenbos, J. T. M. De-Haas, C. W. E. Van-Eijk, *Non-Proportionality in the Scintillation and the Energy Resolution with Scintillation Crystals*, IEEE Trans. Nucl. Sci. 42 (6) (1995) 2190–2202.

[136] S. Surti, J. S. Karp, *Imaging Characteristics of a 3-Dimensional GSO Whole-Body PET Camera*, J. Nucl. Med. 45 (2004) 1040–1049.

[137] S. Surti, et al., *Performance of Philips Gemini TF PET/CT Scanner with Special Consideration for its Time-Of-Flight Imaging Capabilities*, J. Nucl. Med. 46 (2007) 471–480.

[138] V. V. Nagarkar, et al., *Structured CsI(Tl) Scintillators for X-Ray Imaging Applications*, IEEE Trans. Nucl. Sci. 45 (1998) 492–496.

[139] V. V. Nagarkar, et al., *A CCD-Based Detector for SPECT*, IEEE Trans. Nucl. Sci. 53 (2006) 54–58.

[140] M. P. Tornai, et al., *Investigation of Microcolumnar Scintillators on an Optical Fiber Coupled Compact Imaging System*, IEEE Trans. Nucl. Sci. 48 (2001) 637–644.

[141] A. Del Guerra, N. Belcari, *State-of-the-Art PET Scanners for Small Animal and Breast Cancer Imaging*, Nucl. Instr. and Meth. A 580 (2) (2007) 910–914.

[142] A. Del Guerra, N. Belcari, *State-of-the-Art of PET , SPECT and CT for Small Animal Imaging*, Nucl. Instr. and Meth. A 583 (2007) 119–124.

[143] N. Inadama, et al., *Performance of 256ch Flat Panel PS-PMT with Small Crystals for a DOI PET Detector*, in: IEEE Nucl. Sci. Symp. Conf. Record, Vol. 4, 2003, pp. 2486–2490.

[144] J. Benlloch, et al., *Design and Calibration of a Small Animal PET Scanner Based on Continuous LYSO Crystals and PSPMTs*, in: IEEE Nucl. Sci. Symp. Conf. Record, Vol. 4, 2006, pp. 2328–2332.

[145] C. Domingo-Pardo, et al., *A Position Sensitive Gamma-Ray Scintillator Detector with Enhanced Spatial Resolution, Linearity, and Field of View*, IEEE Trans. Med. Img. 28 (12) (2009) 2007–2014.

[146] R. A. Ramirez, et al., *A Lower-Cost High-Resolution LYSO Detector Development for Positron Emission Mammography (PEM)*, IEEE Trans. Nucl. Sci. 56 (5) (2009) 2621–2627.

[147] H. Alva-Sanchez, et al., *Initial Characterization of a Benchtop Micro-PET System Based on LYSO Crystal Arrays and Hamamatsu H8500 PS-PMTs*, in: Proc. of the 8th Int. Conf. on Position Sensitive Detect., Vol. 604, 2009, pp. 335–338.

[148] E. Yoshida, et al., *Basic Performance of a Large Area PET Detector with a Monolithic Scintillator*, Rad. Phys. Tech. 4 (2) (2011) 134–139.

[149] A. Bieberle, J. Kronenberg, E. Schleicher, U. Hampel, *Design of a High-Resolution Gamma-Ray Detector Module for Tomography Applications*, Nucl. Instr. and Meth. A 572 (2) (2007) 668–675.

[150] A. Braem, et al., *High Precision Axial Coordinate Readout for an Axial 3-D PET Detector Module Using a Wavelength Shifter Strip Matrix*, Nucl. Instr. and Meth. A 580 (3) (2007) 1513–1521.

[151] A. Braem, et al., *Wavelength Shifter Strips and G-APD Arrays for the Readout of the Z-Coordinate in Axial PET Modules*, Nucl. Instr. and Meth. A 586 (2) (2008) 300–308.

[152] P. Beltrame, et al., *The AX-PET Demonstrator - Design, Construction and Characterization*, Nucl. Instr. and Meth. A 654 (1) (2011) 546–559.

[153] T. Yamaya, et al., *A SiPM-Based Isotropic-3D PET Detector X'wtal Cube with a Three-Dimensional Array of 1 mm^3 Crystals*, Phys. Med. Biol. 56 (2011) 6793–6807.

[154] T. Kato, et al., *A Novel Gamma-Ray Detector with Submillimeter Resolutions using a Monolithic MPPC Array with Pixelized Ce:LYSO and Ce:GGAG crystals*, Nucl. Instr. and Meth. AIn press.

[155] S. K. Moore, W. C. J. Hunter, L. R. Furenlid, H. H. Barrett, *Maximum-Likelihood Estimation of 3D Event Position in Monolithic Scintillation Crystals: Experimental Results*, in: IEEE Nucl. Sci. Symp. Conf. Record, 2007, pp. 3691–3694.

[156] T. Ling, n. T. K. Lewelle, R. S. Miyaoka, *Depth of Interaction Decoding of a Continuous Crystal Detector Module*, Phys. Med. Biol. 52 (2007) 2213–2228.

[157] M. Carles, et al., *Performance of a DOI-Encoding Small Animal PET System with Monolithic Scintillators*, Nucl. Instr. and Meth. A 695 (2012) 317–321.

[158] D. R. Schaart, et al., *SiPM-Array Based PET Detectors with Depth-of- Interaction Correction*, in: IEEE Nucl. Sci. Symp. Conf. Record, 2008, pp. 3581–3585.

[159] D. R. Schaart, et al., *A Novel, SiPM-Array-Based, Monolithic Scintillator Detector for PET*, Phys. Med. Bio. 54 (2009) 3501–3512.

[160] H. T. van Dam, et al., *Improved Nearest Neighbor Methods for Gamma Photon Interaction Position Determination in Monolithic Scintillator PET Detectors*, IEEE Trans. Nucl. Sci. 58 (2011) 2139–2147.

[161] G. Llosá, et al., *First PET Imaging Results with Continuous LYSO Crystals and Monolithic, 64-Pixel SiPM Matrices*, in: IEEE Nucl. Sci. Symp. Conf. Record, 2010, pp. 3376–3379.

[162] W. M. Gibson, *The Neutrons Emitted in the Bombardment of ^{10}B and ^{11}B by Deuterons*, in: Proc. Phys. Soc. A, Vol. 62, 1949, p. 586.

[163] J. G. Rutherglen, E. R. Rae, R. D. Smith, *Gamma-Rays from Deuteron Bombardment of Boron and the Proton Bombardment of Aluminium*, Proc. Phys. Soc. A 64 (10) (1951) 906–914.

[164] J. Terrell, G. C. Phillips, *Gamma-Rays from Deuteron Bombardment of* B^{10}, B^{11}, N^{14}, *and* F^{19}, Phys. Rev. 83 (1951) 703–708.

[165] W. M. Gibson, *A Study of the Reaction $^{11}B(d,n)^{12}C$ by an Improved Photographic Method*, Phil. Mag. series 7 44 (350) (1953) 297–303.

[166] A. Ward, P. G. Grant, *The Reaction $^{11}B(d,n)^{12}C$*, in: Proc. Phys. Soc. A, Vol. 68, 1955, p. 637.

[167] M. A. Ihsan, *An Investigation of $^{7}Li(d,\ n)^{8}Be$ and $^{11}B(d,\ n)^{12}C$ Nuclear Reactions*, in: Proc. Phys. Soc. A, Vol. 68, 1955, p. 393.

[168] E. J. Price, *Yield and Angular Distribution from the $^{11}B(d,n)^{12}C$ and $^{9}Be(\alpha,n)^{12}C$ Reactions*, Ph.D. thesis, The Rice Institute, Texas (1956).

[169] E. E. Maslin, J. M. Calvert, A. A. Jaffe, *An Investigation of the Reactions: $^{10}B(d,n)^{11}C$ and $^{11}B(d,n)^{12}C$*, in: Proc. Phys. Soc. A, Vol. 69, 1956, p. 754.

[170] R. W. Kavanagh, C. A. Barnes, *Boron plus Deutron Reactions*, Phys. Rev. 112 (2) (1958) 503–511.

[171] B. Zeidman, J. M. Fowler, *Angular Distributions from Deuteron Bombardment of Beryllium and Boron*, Phys. Rev. 112 (6) (1958) 2020–2026.

[172] J. B. Garg, N. H. Gale, J. M. Calvert, *Neutron-Gamma Angular Correlations Studies of the $^{11}B(d,n\gamma)^{12}C$ Reaction*, Nucl. Phys. 23 (1961) 630–647.

[173] J. R. Risser, P. R. Almond, *Differential Cross Sections at 0^{o} and Angular Distributions of Resolved Neutrons from ^{11}B+d*, Nucl. Phys. 72 (1965) 436–448.

[174] G. U. Din, M. A. Nagarajan, R. Pollard, *The Study of $^{10}B(d,n)^{11}C$ and $^{11}B(d,n)^{12}C$*, Nucl. Phys. A93 (1967) 190–200.

[175] J. W. Tepel, M. Cosack, R. Felst, B. Zeitnitz, *A Study of the Mechnism of the $^{11}B(d,n)^{12}C$ Reaction by Means of Neutron-Gamma Correlation Measurments*, Nucl. Phys. A113 (1968) 332–352.

[176] G. S. Mutchler, et al., *The (d,n) Reaction on 1p Shell Nuclei at E_d=11.8 MeV*, Nucl. Phys. A172 (1971) 469–488.

[177] D. Hilscher, R. C. Davis, P. A. Quin, *Vector Analysing Power of (d,n) Reactions on ^{11}B, ^{12}C, ^{15}N*, Nucl. Phys. A174 (1971) 417–425.

[178] M. B. Goldberg, et al., *A Dual-Purpose Ion-Accelerator for Nuclear-Reaction-Based Explosives-and SNM-Detection in Massive Cargo*, in: Proc. of Topical Meeting on Nucl. Res. Appl. and Utilization of Accel., Vienna, 2009.

[179] R. C. Lanza, et al., *Low Dose Transmission Radiography for Detection of SNM using Monoenergetic Gamma-Rays*, in: Proc. of Topical Meeting on Nucl. Res. Appl. and Utilization of Accel., 2009.

[180] G. A. Sziki, *Gamma Ray Production Cross-Sections of Deuteron Induced Nuclear Reactions for Light Element Analysis*, Nucl. Instr. and Meth. B 251 (2) (2006) 343–351.

[181] M. A. Norsworthy, et al., *Active Interrogation Source Based on Deuteron Reactions*, in: Nucl. Sc. Sym., 2011, pp. 1362–1366.

[182] Goodfellow
, `http://www.goodfellow.com/csp/active/gfPDetail.csp?result=8&UpdateParam=8~~`.

[183] SRIM/TRIM, http://www.srim.org/, accessed November 4, 2012.

[184] F. Ajzenberg-Selove, T. Lauritsen, *Energy Levels of Light Nuclei A=12*, Nucl. Phys. A 114, revised September 2012.

[185] E. Adelberger, R. Marrs, K. Snover, J. Bussoletti, *Radiative Transitions and Isospin Mixing in* ^{12}C, Phys. Rev. C 15 (2) (1977) 484.

[186] W. Olsen, W. Dawson, G. Neilson, J. Sample, *The Alpha-Particle Breakup of the 12.71 and 11.83 MeV Levels in* ^{12}C, Nucl. Phys. 61 (1965) 625–640.

[187] G. Neuschaefer, S. Tabor, *Decays of High-Lying States in* ^{12}C, Phys. Rev. C 31 (2) (1985) 334.

[188] S. J. Skorka, J. Hertel, T. W. Retz-Schmidt, *Compilation of Electromagnetic Transition Rates in Light Nuclei* $A \leq 40$, Nucl. Data Sheets A 2 (4) (1966) 347–401.

[189] D. Alburger, D. Wilkinson, *Gamma-Ray Decay of the 15.11-MeV T= 1 State of* ^{12}C, Phys. Rev. C 5 (2) (1972) 384.

[190] J. Sample, G. Neilson, G. Chadwick, J. Warren, *Gamma-Rays from the Deuteron Bombardment of Boron 10*, Canadian J. of Phys. 33 (12) (1955) 828–840.

[191] *TUNL compilation*, http://www.tunl.duke.edu/nucldata/.

[192] *Geant4 Toolkit for the Simulation of the Passage of Particles Through Matter* , http://geant4.cern.ch/, accessed July 9, 2012.

[193] G. Baur, D. Trautmann, *The Coulomb Break-up of the Deuteron*, Nucl. Phys. A 191 (2) (1972) 321–331.

[194] M. A. Mcmahan, *Neutron Beams from Deuteron Breakup at the 88-Inch Cyclotron at Lawrence Berkeley National Laboratory*, in: Int. Conf. on Nucl. Data for Sci. and Technol., 2007, pp. 411–414.

[195] *Geant4 Physics Reference Guide*, http://geant4.web.cern.ch/geant4/UserDocumentation/UsersGuides/PhysicsReferenceManual/fo/PhysicsReferenceManual.pdf, accessed July 9, 2012.

[196] E. Y. Sidky, C. M. Kao, X. Pan, *Accurate Image Reconstruction from Few-Views and Limited-Angle Data in Divergent-Beam CT*, J. of X-Ray Sci. and Technol. 14 (2) (2006) 119–139.

[197] L. Pizarro, D. Mery, R. Delpiano, M. Carrasco, *Robust Automated Multiple View Inspection*, Pattern Anal. Appl. 11 (1) (2008) 21–32.

[198] F. L. Roder, *X-Ray or Gamma-Ray Examination Device for Moving Objects* (US Patent 4,064,440, 1977).

[199] J. Evans, *Stereoscopic Imaging Using Folded Linear Dual-Energy X-Ray Detectors*, Meas. Sci. Technol. 13 (9) (2002) 1388.

[200] H. W. Hon, J. P. O. Evans, *Multiple-View Line-Scan Imaging*, in: IEEE Proc. Optoelectron., Vol. 149, IET, 2002, pp. 45–50.

[201] O. Abusaeeda, J. Evans, D. Downes, J. Chan, *View Synthesis of KDEX Imagery for 3D Security X-Ray Imaging*, in: 4th Int. Conf. on Imaging for Crime Detec. and Prevention, 2011, pp. 1–6.

[202] J. Evans, Y. Liu, J. Chan, D. Downes, *View Synthesis for Depth From Motion 3D X-Ray Imaging*, Pattern Recognit. Letters 27 (15) (2006) 1863–1873.

[203] T. Wang, J. Evans, *Stereoscopic Dual-Energy X-Ray Imaging for Target Materials Identification*, in: IEEE Proc.: Vision, Image and Signal Processing, Vol. 150, 2003, pp. 122–130.

[204] W. L. Khoo, T. Jordan, D. G. Stork, Z. Zhu, *Reconstruction of a Three-Dimensional Tableau from a Single Realist Painting*, in: IEEE 15th Int. Conf. on Virtual Syst. and Multimedia, 2009, pp. 9–14.

[205] Z. Ying, R. Naidu, C. R. Crawford, *Dual Energy Computed Tomography for Explosive Detection*, J. of X-Ray Sci. and Technol. 14 (4) (2006) 235–256.

[206] W. R. Brody, G. Butt, A. Hall, A. Macovski, *A Method for Selective Tissue and Bone Visualization Using Dual Energy Scanned Projection Radiography*, Med. Phys. 8 (1981) 353.

[207] T. Gomi, M. Nakajima, *Dual-Energy Subtraction X-Ray Digital Tomosynthesis: Basic Physical Evaluation*, Open J. of Med. Imaging 2 (3) (2012) 111–117.

[208] L. A. Lehmann, et al., *Generalized Image Combinations in Dual KVP Digital Radiography*, Med. Phys. 8 (1981) 659.

[209] B. Heismann, J. Leppert, K. Stierstorfer, *Density and Atomic Number Measurements with Spectral X-Ray Attenuation Method*, J. of Appl. Phys. 94 (3) (2003) 2073–2079.

[210] C. Rizescu, C. Beşliu, A. Jipa, *Determination of Local Density and Effective Atomic Number by the Dual-Energy Computerized Tomography Method with ^{192}Ir Radioisotope*, Nucl. Instr. and Meth. A 465 (2) (2001) 584–599.

[211] *Technical Aspects of Computed Tomography*, Vol. 5 of *Radiology of the Skull and Brain*, Mosby, 1981, p. 3870.

[212] R. A. Brooks, G. Di Chiro, *Statistical Limitations in X-Ray Reconstructive Tomography*, Med. Phys. 3 (4) (1976) 237.

[213] J. Gore, P. Tofts, *Statistical Limitations in Computed Tomography*, Phys. Med. Bio. 23 (6) (1978) 1176.

[214] K. E. Bennett, R. L. Byer, *Fan-Beam-Tomography Noise Theory*, J. Opt. Soc. of Am. A 3 (5) (1986) 624–633.

[215] *Omega Piezo Technologies Inc.*, `http://www.omegapiezo.com/crystal\_scintillators.html`, accessed April 4, 2012.

[216] *Photonis*, `http://www.datasheet4u.com/datasheet/X/P/2/XP2020_Photonis.pdf.html`, accessed September 30, 2013.

[217] *Praezisions Glas & Optik GmbH*, `http://www.pgo-online.com/intl/katalog/shd_cold_mirror.html`, accessed September 30, 2013.

[218] *RoentDek Handels GmbH*, http://www.roentdek.com/, accessed October 27, 2012.

[219] O. Jagutzki, et al., *A Position-and Time-Sensitive Photon-Counting Detector with Delay-Line Read-Out*, in: Int. Congr. on Opt. and Optoelectron., 2007, p. 65851C.

[220] S. Schossler, et al., *Time and Position Sensitive Single Photon Detector for Scintillator Read-Out*, JINST 7 (02) (2012) C02048.

[221] O. Jagutzki, et al., *Multiple Hit Readout of a Microchannel Plate Detector with a Three-Layer Delay-Line Anode*, IEEE Trans. Nucl. Sci. 49 (5) (2002) 2477–2483.

[222] D. W. Cooke, et al., *Crystal Growth and Optical Characterization of Cerium-Doped* $Lu_{1.8}Y_{0.2}SiO_5$, J. Appl. Phys. 88 (12) (2000) 7360–7362.

[223] C. L. Melcher, J. S. Schweitzer, *A Promising New Scintillator: Cerium-Doped Lutetium Oxyorthosilicate*, Nucl. Instr. and Meth. A (1992) 212.

[224] J. S. Huber, W. W. Moses, W. F. Jones, C. C. Watson, *Effect of* ^{176}Lu *Background on Singles Transmission for LSO-Based PET Cameras*, Phys. Med. Bio. 47 (19) (2002) 3535.

[225] A. J. Wojtowicz, et al., *Scintillation Properties of Selected Oxide Monocrystals Activated with Ce and Pr*, Opt. Mat. 28 (2006) 85–93.

[226] J. Chen, L. Zhang, R. Y. Zhu, *Large Size LYSO Crystals for Future High Energy Physics Experiments*, IEEE Trans. Nucl. Sci. 52 (6) (2005) 3133–3140.

[227] R. Mao, L. Zhang, R. Y. Zhu, *Emission Spectra of LSO and LYSO Crystals Excited by UV Light, X-Ray and Gamma-Ray*, IEEE Trans. Nucl. Sci. 55 (3) (2008) 1759–1766.

[228] *Zemax - optical design program*, http://www.radiantzemax.com/en/design/, Accessed May 15, 2012.

[229] V. Dangendorf, et al., *Fast Neutron Resonance Radiography in a Pulsed Neutron Beam*, in: 7th World Conf. on Neutron Radiography, 2002.

[230] *Physikalisch-Technische-Bundestalt (PTB)*, http://www.ptb.de/index_en.html, Accessed April 10, 2012.

[231] H. J. Brede, et al., *Neutron Yields from Thick Be Targets Bombarded with Deuterons or Protons*, Nucl. Instr. and Meth. A 274 (1) (1989) 332–344.

[232] V. Dangendorf, *Testreport of 11B Target from October 2011*, private communication (2011).

[233] W. Chewpraditkul, et al., *Scintillation Properties of LuAG:Ce, YAG:Ce and LYSO:Ce Crystals for Gamma-Ray Detection*, IEEE Trans. Nucl. Sci. 56 (6) (2009) 3800–3805.

[234] NRESP, http://www.oecd-nea.org/tools/abstract/detail/nea-0700/, accessed November 5, 2012.

[235] *iThemba Laboratory for Accelerator Based Sciences, Cape Town, South Africa.*, http://www.tlabs.ac.za/, accessed September 30, 2013.

[236] T. Novotny, L. Buermann, S. Guldbakke, H. Klein, *Response of NE213 Liquid Scintillation Detectors to High-Energy Photons (7 MeV* $< E_\gamma <$ *20 MeV)*, Nucl. Instr. and Meth. A 400 (2) (1997) 356–366.

בתמונה 1 ניתן לראות את תמונת ההעברה של המיכל עם כל אנרגיות קרני הגאמה, שעליה מסומנים באדום האובייקטים שזוהו כחומרים גרעיניים. תמונה כזו תוצג למפעיל המכונה כשהיא מסתמכת על זיהוי אוטומטי של איומים במקום על שיפוט המפעיל האנושי.

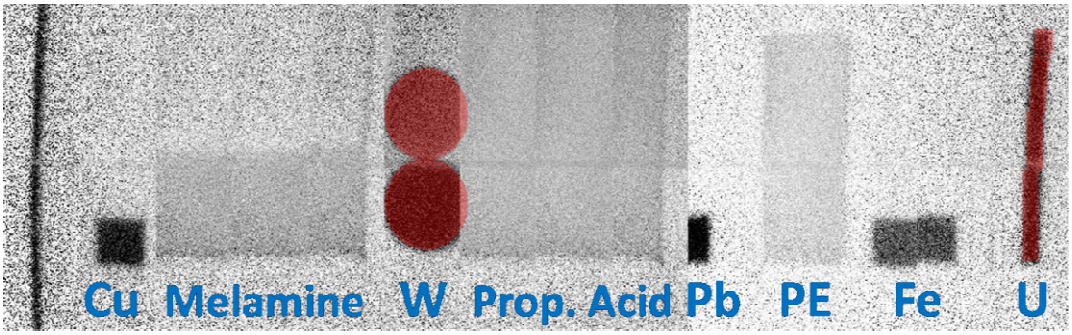

תמונה 1: תמונת העברה של המיכל המוקטן שנסרק בניסוי ההדגמה. על התמונה מסומנים סוגי האובייקטים השונים בכחול, ובאדום האובייקטים שאותם המערכת מזהה כחומרים גרעיניים.

5. מסקנות

במסגרת עבודה זו נבחנו היבטים רבים של מערכת DDEGR כולל שיטת ההפרדה, סימולציות של המערכת, מדידות ניסיוניות והדגמה של אב טיפוס מעבדתי. התוצאות של עבודה זו תומכות בכך ששיטת DDEGR ניתנת ליישום ומהוות הוכחת ישימות של DDEGR.

פיתוח שני דורות של גלאים התבצע בהצלחה. הדור הראשון הוא גלאי קרני גאמה המתאים למערכת DDEGR ואילו הדור השני הוא גלאי גאמה/ניוטרונים המתאים למערכת עתידית משולבת לגילוי חומרים גרעיניים וחומרי נפץ במקביל.

לסיכום, שלושת המטרות של עבודה זו כפי שהוגדרו בפרק הראשון הוגשמו בהצלחה. מטרות אלה כללו הוכחת ישימות של שיטת DDEGR, פיתוח גלאי קרני גאמה מתאים לשימוש במערכת DDEGR וכן פיתוח גלאי גאמה/ניטרונים המתאים למערכת משולבת לגילוי חומרים גרעיניים וחומרי נפץ במקביל.

עבודה עתידית צריכה לכלול הדגמה של DDEGR בעזרת אב-טיפוס בגודל מלא שיכלול מספר מערכי גלאים ויוכל לסרוק מיכל LD3, מהסוג המשמש היום למעבר מטען אוירי. סריקה של עצם בגודל כזה דורשת מאיץ המפיק זרם בעוצמה גבוהה מזו המופקת כיום במאיץ של PTB (ששימש לניסויים המתוארים בעבודה זו). לצורך כך, מתקיים בימים אלה שיתוף פעולה עם קבוצת מאיץ ה-RFQ שבמעבדות אייטמבה בדרום אפריקה [232].

דרישה		טרקור-1	טרקור-2	הערות
כושר הפרדה עבור אנרגיית קרני גאמה	3 מא"ו	20%	20%	כ-3 מא"ו עבור קרני גאמה באנרגיה של 15.1 מא"ו
כושר הפרדה חזותי	5-10 מ"מ	3 מ"מ	3 מ"מ	עבור קרני גאמה באנרגיה של 4.4 מא"ו
כושר הפרדה זמני	50 ננושניות	4 ננושניות	2.3 ננושניות	
עבודה בקצבים גבוהים	עד 0.5 מגה-הרץ	0.5 מגה-הרץ	0.5 מגה-הרץ	
שטח גילוי גדול	10×10 סמ"ר	5×10 סמ"ר	20×20 סמ"ר	

טבלה 1: רשימת הדרישות מגלאי למערכת DDEGR בהשוואה למפרט הסופי של גלאים טרקור-1 וטרקור-2.

דרישה		טרקור-1	טרקור-2
גילוי של גאמה/ניטרונים בו-זמנית.			כן
כושר הפרדה זמני הנדרש לביצוע ספקטרוסקופיית ניטרונים	5 ננושניות	4.5 ננושניות	4 ננושניות
כושר הפרדה חזותי בתמונת הניטרונים	כ-2 מ"מ	1 מ"מ	2 מ"מ

טבלה 2: רשימת דרישות נוספות מגלאי המתאים למערכת משולבת לגילוי חומרים גרעיניים וחומרי נפץ בו-זמנית, בהשוואה למפרט הסופי של גלאים טרקור-1 וטרקור-2.

4. הדגמת השיטה בעזרת אב-טיפוס מעבדתי

אב טיפוס מעבדתי של מערכת DDEGR הוקם במאיץ החלקיקים שב-PTB. אב טיפוס זה כלל את הריאקציה הגרעינית $^{11}B(d,n)^{12}C$ בתור מקור קרינה, את גלאי טרקור-2 ומתקן סריקה שעליו הונח מיכל מוקטן. אוסף של חומרים בעלי מספרים אטומיים שונים הונח במיכל המוקטן שנסרק ע"י הגלאי בצעדים של 4 ס"מ.

הודגמה הפרדה בין חומרים בעלי מספר אטומי גבוה לחומרים בעלי מספר אטומי נמוך באמצעות מבט אחד על המיכל. בעזרת הנחת ידיעת עובי הפריטים, גודל שניתן למדוד באמצעות ביצוע טומוגרפיה ממוחשבת, הודגמה גם הפרדה נוספת בין סוגים שונים של חומרים בעלי מספר אטומי גבוה: אלה הנמדדים במערכת כחומרים תמימים (פריטים מעופרת) ואלה המהווים התראה של המערכת (פריטים מאורניום ומטונגסטן).

עבור מבט אחד על המיכל המאפשר הבחנה בין חומרים בעלי מספר אטומי גבוה לחומרים בעלי מספרים אטומיים נמוכים ובינוניים בשיטת הפרדה בשתי אנרגיות נדרש זרם דיטרונים של 1.8 מיליאמפר.

על מנת לאפשר הפרדה בין חומרים תמימים בעלי מספר אטומי גבוה לחומרים גרעיניים מיוחדים יש להשתמש בטומוגרפיה ממוחשבת הדורשת מספר מבטים על המכל. בשיטה זו הזרם הדיטרונים הדרוש גבוה יותר - 4.5 מיליאמפר. גם בשיטה זו ישנם מספר חומרים בעלי מספר אטומי גבוהה שיזוהו בטעות כחומרים גרעיניים – בינהם טונגסטן.

3. פיתוח הגלאי

החלק העיקרי של עבודה זו הוא פיתוח גלאי מתאים למערכת DDEGR – גלאי טרקור-1. הגלאי מסוגל לבצע דימות, ספקטרוסקופיית גאמה וכן מדידת זמן תעופה. הגלאי מורכב ממסך נצנץ בעל מספר אטומי גבוה, מראה המכופפת את האור בתשעים מעלות לתוך עדשה הממרכזת את האור על מגביר-תמונה המסוגל לעבוד בשיטת המאורעות הנפרדים ומודד מיקום וזמן תעופה של כל מאורע.

הדור שני של הגלאי, טרקור-2, מסוגל לגלות קרני-גאמה וניטרונים במקביל וליצור תמונות נפרדות עבור סוגי חלקיקים שונים ואנרגיות שונות של כל חלקיק. כך, גלאי טרקור-2 מאפשר יישום של שתי שיטות הגילוי במערכת אחת. ההבדל העיקרי בין הדור הראשון לשני הוא במסך הנצנץ, שבטרקור-2 מכיל נצנץ פלסטיק לצד הנצנץ בעל המספר האטומי הגבוה.

שני הגלאים נבחנו ואופיינו בסדרה של שלושה ניסויים במאיץ החלקיקים שב-PTB בבראונשוויג, גרמניה.

רשימת הדרישות מהגלאים וכן המפרט הסופי של שני דורות הגלאים מוצגים בטבלה 1. השלב השני של הפיתוח, פיתוח גלאי גאמה/ניטרונים המתאים למערכת משולבת לגילוי חומרים גרעיניים וחומרי נפץ בו-זמנית מוסיף מספר דרישות, המפורטות בטבלה 2 יחד עם החלקים הרלוונטיים מן המפרט הסופי של טרקור-1 וטרקור-2.

הגלאים עומדים במפרט הנדרש ומאימים לשימוש במערכות המתוארות להלן.

תקציר

1. מבוא

עבודה זו עוסקת בפיתוח גלאי למערכת גילוי חומרים גרעיניים מיוחדים (אורניום ופלוטוניום) במיכלי מטען אוירי. שיטת הגילוי היא רדיוגרפיה בשתי אנרגיות גאמה דיסקרטיות (DDEGR). בשיטה זו משקפים את המקור בעזרת שתי גאמות המגיעות מן הריאקציה בה דיטרונים פוגעים במטרת בורון 11 הפולטת בתגובה קרני-גאמה וניטרונים ($^{11}B(d,n)^{12}C$). ריאקציה זו פולטת קרני-גאמה בשתי אנרגיות – 4.4 ו-15.1 מגה-אלקטרון-וולט (מא"ו).

בשיטות דומות משתמשים במקורות שפולטים קרינת ברמשטרלונג, כך שהאנרגיה הנפלטת היא בעלת ספקטרום רציף שרק חלק קטן ממנו מתאים לרדיוגרפיה. הספקטרום הנקי וההפרדה הטובה בין קרני-הגאמה המשמשות את השיטה החדשה מאפשרים רגישות גבוהה וגילוי כמויות קטנות של חומרים גרעיניים.

החלק המרכזי של העבודה הוא פיתוח גלאי מתאים למערכת DDEGR, גלאי קרינה בעל רגישות זמנית בשיטת מאורע-לאחר-מאורע, או בשמו העברי, טרקור-1.

ניטרונים הנפלטים באותה ריאקציה מאפשרים גילוי של חומרי נפץ בעזרת שיטה הנקראת רדיוגרפיה רזוננטית של ניטרונים מהירים. שיטה זו אינה נידונה בעבודה זו, אך מתואר כאן פיתוח של גלאי המסוגל לגלות קרני גאמה וניטרונים בו זמנית, טרקור-2.

2. חקירת שיטת הגילוי

החלק הראשון של העבודה דן בשיטת הגילוי DDEGR על פניה השונים. בשלב הראשון נמדדו תנובות קרני הגאמה והניטרונים המופקים בריאקציה הגרעינית עבור דיטרונים בטווח האנרגיה שבין 3 ו-12 מא"ו. תנובת קרני הגאמה המדודה היא 10^{10}×2-20 קרני גאמה/סטרדין/מיליקולומב עבור קרני-גאמה באנרגיה של 4.4 מא"ו ו-10^{9}×2-5 קרני גאמה/סטרדין/מיליקולומב עבור קרני-גאמה באנרגיה של 15.1 מא"ו.

סימולציות של מערכת גילוי מופשטת בעלת מטען כותנה טיפוסי בוצעו בתכנת Geant4. ההשפעה של הפיזורים ממיכל הכותנה על האות המגיע לגלאי הוערכה בפחות מ-5% עבור מערכת שבה הגלאי מוצב במרחק 4 מטרים מהמקור. תוצאות הסימולציות וההערכה של סך ההשפעה של רקעים שונים על ההעברה הנמדדת בגלאים מעידים על כך שהשיטה ניתנת ליישום.

לאחר דיון בשאלה כיצד השיטה מאפשרת להבדיל בין חומרים שונים ובהתבסס על התנובות שנמדדו ניסיונית מחושבת הערכה של עוצמת זרם הדיטרונים הנדרש לגילוי. דרישות המערכת הן שסריקה מלאה של מיכל תתבצע תוך 60 שניות עם הסתברות גילוי של 99.9% והסתברות לאזעקת שווא של 0.1%.

עבודה זו נעשתה בהדרכתם של:

ד"ר דוד ורצקי, ממ"ג שורק

פרופ' אליהו פרידמן, האוניברסיטה העברית בירושלים

ד"ר ישראל מרדור, ממ"ג שורק

פיתוח גלאי גאמות לדימות רדיוגרפי הרגיש למספר אטומי

חיבור לשם קבלת תואר דוקטור לפילוסופיה

מאת

מיכל ברנדיס

הוגש לסנט האוניברסיטה העברית בירושלים

נובמבר 2013